



저작자표시-비영리-변경금지 2.0 대한민국

이용자는 아래의 조건을 따르는 경우에 한하여 자유롭게

- 이 저작물을 복제, 배포, 전송, 전시, 공연 및 방송할 수 있습니다.

다음과 같은 조건을 따라야 합니다:



저작자표시. 귀하는 원저작자를 표시하여야 합니다.



비영리. 귀하는 이 저작물을 영리 목적으로 이용할 수 없습니다.



변경금지. 귀하는 이 저작물을 개작, 변형 또는 가공할 수 없습니다.

- 귀하는, 이 저작물의 재이용이나 배포의 경우, 이 저작물에 적용된 이용허락조건을 명확하게 나타내어야 합니다.
- 저작권자로부터 별도의 허가를 받으면 이러한 조건들은 적용되지 않습니다.

저작권법에 따른 이용자의 권리는 위의 내용에 의하여 영향을 받지 않습니다.

이것은 [이용허락규약\(Legal Code\)](#)을 이해하기 쉽게 요약한 것입니다.

[Disclaimer](#)

Doctoral Thesis

Human and Biological Skin-Inspired Electronic
Skins for Advanced Sensory Functions and
Multifunctionality

Youngoh Lee

Department of Energy Engineering

Graduate School of UNIST

2020

Human and Biological Skin-Inspired Electronic Skins
for Advanced Sensory Functions and
Multifunctionality

Youngoh Lee

Department of Energy Engineering

Graduate School of UNIST

Human and Biological Skin-Inspired Electronic Skins for Advanced Sensory Functions and Multifunctionality

A thesis/dissertation
submitted to the Graduate School of UNIST
in partial fulfillment of the
requirements for the degree of
Doctor of Philosophy

Youngoh Lee

01. 08. 2020

Approved by

Advisor

Hyunhyub Ko

Human and Biological Skin-Inspired Electronic Skins for Advanced Sensory Functions and Multifunctionality

Youngoh Lee

This certifies that the thesis/dissertation of Youngoh Lee is approved.

01. 08. 2020

signature

Advisor: Hyunhyub Ko

signature

Jae Joon Kim

signature

Sang Kyu Kwak

signature

Chunggi Baig

signature

Jiseok Lee

Abstract

The electronic skin (e-skin) technology is an exciting frontier to drive next generation of wearable electronics owing to its high level of wearability to curved human body, enabling high accuracy to harvest information of users and their surroundings. Although various types of e-skins, based on several signal-transduction modes, including piezoresistive, capacitive, piezoelectric, triboelectric modes, have been developed, their performances (i.e. sensitivity, working range, linearity, multifunctionality, etc.) should be improved for the wearable applications. Recently, biomimicry of the human and biological skins has become a great inspiration for realizing novel wearable e-skin systems with exceptional multifunctionality as well as advanced sensory functions. As an ideal sensory organ, tactile sensing capabilities of human skin was emulated for the development of e-skins with enhanced sensor performances. In particular, the unique geometry and systematic sensory system of human skin have driven new opportunities in multifunctional and highly sensitive e-skin applications. In addition, extraordinary architectures for protection, locomotion, risk indication, and camouflage in biological systems provide great possibilities for second skin applications on user-interactive, skin-attachable, and ultrasensitive e-skins, as well as soft robots. Benefitting from their superior perceptive functions and multifunctionality, human and biological skins-inspired e-skins can be considered to be promising candidates for wearable device applications, such as body motion tracking, healthcare devices, acoustic sensor, and human machine interfaces (HMI).

This thesis covers our recent studies about human and biological skin-inspired e-skins for advanced sensory functions and multifunctionality. First, chapter 1 highlights various types of e-skins and recent research trends in bioinspired e-skins mimicking perceptive features of human and biological skins. In chapter 2, we demonstrate highly sensitive and tactile-direction-sensitive e-skin based on human skin-inspired interlocked microdome structures. Owing to the stress concentration effect, the interlocked e-skin experiences significant change of contact area between the interlocked microdomes, resulting in high pressure sensitivity. In addition, because of the different deformation trends between microstructures in mutual contact, the interlocked e-skin can differentiate and decouple sensor signals under different directional forces, such as pressure, tensile strain, shear, and bending. In chapter 3, interlocked e-skins were designed with multilayered geometry. Although interlocked e-skin shows highly sensitive pressure sensing performances, their pressure sensing range is narrow and pressure sensitivity continuously decreases with increasing pressure level. The multilayer interlocked microdome geometry can enhance the pressure-sensing performances of e-skins, such as sensitivity, working range, and linearity. As another approach of e-skin with multilayered geometry, we demonstrate multilayered e-skin based on conductivity-gradient conductive materials in chapter 4. The conductive polymer composites with different conductivity were coated on the microdome pattern and

designed as interlocked e-skin with coplanar electrode design, resulting in exceptionally high pressure-sensing performances compared with previous literatures. In chapter 5, inspired by responsive color change in biological skins, we developed mechanochromic e-skin with a hierarchical nanoparticle-in-micropore architecture. The novel design of hierarchical structure enables effective stress concentration at the interface between nanoparticle and porous structure, resulting in impressive color change under mechanical stimuli. In chapter 6, we emulate ultrahigh temperature sensitivity of human and snake skin for temperature-sensitive e-skin. The thermoresponsive composite based on semi-crystalline polymer, temperature sensor shows ultrahigh temperature sensitivity near the melting point of semi-crystalline polymer. In addition, integration of thermochromic composite, mimicking biological skins, enables dual-mode temperature sensors by electrical and colorimetric sensing capabilities. Finally, in chapter 7, we summarize this thesis along with future perspective that should be considered for next-generation e-skin electronics. Our e-skins, inspired by human and biological skin, can provide a new paradigm for realizing novel wearable electronic systems with exceptional multifunctionality as well as advanced sensory functions.

Contents

Abstract	1
Contents	4
List of Figures	6
List of Tables	21
Nomenclature	22
Chapter 1. Introduction	25
1.1 Electronic skin	25
1.2 Working mechanisms of various electronic skins.....	28
1.2.1. Transduction modes for mechanical stimuli-sensitive e-skins	28
1.2.2. Transduction modes for temperature-sensitive e-skins	31
1.2.3. Other working mechanisms	32
1.3 Bio-inspired electronic skins	33
1.3.1. Limitation of conventional electronic skins	33
1.3.2. Human skin-inspired electronic skins	35
1.3.3. Biological skin-inspired electronic skins	39
1.4 Applications of electronic skins	41
1.4.1. Wearable motion sensors	41
1.4.2. Healthcare devices	43
1.4.3. Prosthesis	46
1.5 Challenges of current electronic skins	48
Chapter 2. Highly sensitive and multidirectional electronic skins based on human skin-inspired interlocked microdome structure	50
2.1 Introduction	50
2.2 Experimental Details	52
2.3 Results and Discussion	54
2.4 Conclusions	71
Chapter 3. Human skin-inspired multilayered ferroelectric skins with ultrahigh pressure sensitivity and linear response over exceptionally broad pressure range	72
3.1 Introduction	72

3.2 Experimental Details	74
3.3 Results and Discussion	76
3.4 Conclusions	98
Chapter 4. Human skin-inspired multilayered flexible electronic sensors with tunable sensitivity and linearity	99
4.1 Introduction	99
4.2 Experimental Details	102
4.3 Results and Discussion	103
4.4 Conclusions	128
Chapter 5. Biological skin-inspired mechanochromic electronic skin for visualization of mechanical stimuli	129
5.1 Introduction	129
5.2 Experimental Details	131
5.3 Results and Discussion	133
5.4 Conclusions	166
Chapter 6. Human and biological skin-inspired electronic skin for deformation-insensitive flexible and highly sensitive dual-mode temperature sensor	167
6.1 Introduction	167
6.2 Experimental Details	169
6.3 Results and Discussion	171
6.4 Conclusions	196
Chapter 7. Summary and Future perspective	197
7.1 Summary	197
7.2 Future perspective	200
References	205
Appendix A: List of Achievements	233
Acknowledgements	237

List of Figures

Figure 1.1. Personalized healthcare monitoring system based on Internet of Medical Things (IoMT) technology.

Figure 1.2. Wearable devices and sensors with self-powered systems and multifunctional abilities.

(left) Self-powered wearable electronic skins based on piezoelectric, triboelectric, and thermoelectric harvest mechanical and thermal energy from the human body. Through the physical movements of various body parts and the heat dissipation from the body, high power of several to tens of watts are generated. (right) Multifunctional electronic skins based on resistive, capacitive, triboelectric, piezoelectric accurately monitor the user's biological signals, including the EEG, EMG, and various physiological signals as well as physical movements and motions. (bottom) Ubiquitous healthcare systems through wireless network and feedback system (J. Park et al. *J. Mater. Chem. B* **2016**, *4*, 2999).

Figure 1.3. Transduction modes for mechanical stimuli-sensitive e-skins. (a) Piezoresistive e-skins based on PSR. (b) Capacitive e-skins of a parallel-plate capacitor. (c) Piezoelectricity generated in single film-based e-skins. (d) Triboelectricity generated in e-skins during contact/separation cycles.

Figure 1.4. Conventional e-skins with planar sensor design. (a-c) E-skins combined with PSR and field-effect transistors. (K. Takei et al. *Nat. Mater.* **2010**, *9*, 821, C. Wang et al. *Nat. Mater.* **2013**, *12*, 899, T. Someya et al. *Proc. Natl. Acad. Sci. U.S.A.* **2014**, *111*, 12998). (d) Piezoresistive e-skin based on planar structure. (B. C.-K. Tee et al. *Nat. Nanotech.* **2012**, *7*, 825).

Figure 1.5. Bioinspired e-skin systems for wearable devices. Human skin: Dermal-epidermal structure (K. J. Busam, *Dermatopathology E-Book: A Volume in the Series: Foundations in Diagnostic Pathology* **2014**, *1*, M. Ha et al. *ACS Nano* **2018**, *12*, 3964) Mechanoreceptor. (M. L. Jin et al. *Adv. Mater.* **2017**, *29*, 1605973) Fingerprint. (J. Park et al. *Sci. Adv.* **2015**, *1*, e1500661). Nerve. (C. Wan et al. *Adv. Mater.* **2018**, *30*, e1801291). Self-healing. (J. Kang et al. *Adv. Mater.* **2018**, *30*, e1706846). **Smart biological skin:** Visualization. (C. Wang et al. *Nat. Mater.* **2013**, *12*, 899). Adhesion. (Y. Park et al. *Adv. Mater.* **2017**, *29*, 1606453). Crack. (D. Kang et al. *Nature* **2014**, *516*, 222). Environmental adaption. (S.A. Morin et al. *Science* **2012**, *337*, 828).

Figure 1.6. Human tactile perception system. The mechanoreceptors in human skin encode the applied tactile stimuli into action potentials, which are sent along the chain of afferent axons to synapse. The action potentials from multiple presynaptic neurons are processed in the biological synapses to obtain multilevel features of tactile perception.

Figure 1.7. Human skin-inspired e-skins. (a) Detection of multiple stimuli with e-skins composed of

interlocking nanofibers (C. Pang et al. *Nat. Mater.* **2012**, *11*, 795). (b) Hierarchical and interlocked e-skins with gradient stiffness (M. Ha et al. *ACS Nano* **2018**, *12*, 3964). (c) Skin-inspired multifunctional e-skins based on ferroelectric and conductive composite with interlocked geometry (J. Park et al. *Sci. Adv.* **2015**, *1*, e1500661). (d) Multifunctional e-skins with interlocked and hierarchical geometry (M. Ha et al. *Adv. Funct. Mater.* **2015**, *25*, 2841). (e) Fingerprint-inspired texture sensors with MEMS microforce sensors (J. Scheibert et al. *Science* **2009**, *323*, 1503). (f) 3D, reconfigurable and multimodal e-whiskers for high-fidelity surface mapping (J. T. Reeder et al. *Adv. Mater.* **2018**, *30*, 1706733).

Figure 1.8. Biological skin-inspired e-skins. (a) Visualized e-skin combined with electrochromic materials and piezoresistive sensor (H.-H Chou et al. *Nat. Commun.* **2015**, *6*, 8011). (b) Smart medical patch based on octopus sucker inspired dry adhesive pad (M. K. Choi et al. *Adv. Healthcare Mater.* **2016**, *5*, 80). (c) Spider-inspired strain sensors based on nanoscale crack junction (D. Kang et al. *Nature* **2014**, *516*, 222).

Figure 1.9. Applications for wearable motion sensor. (a) Differentiation of various motions using e-skins with interlocked microdome structure (J. Park et al. *NPG Asia Mater.* **2018**, *10*, 163). (b) Monitoring of finger movement using dual-mode wearable motion sensors (H. Park et al. *Nanoscale* **2017**, *9*, 7631). (c) Wireless-controlled interactive system with crack-inspired e-skins for HMI technology (S. Han et al. *NPJ Flexible Electron.* **2018**, *2*, 16.).

Figure 1.10. Applications for healthcare device. (a) Microtopography-guided conductive e-skins for skin conformal sensors (Y. Park et al. *Adv. Mater.* **2017**, *29*, 1606453). (b) Temperature-dependent evaluation of vascular health based on pulse signals from multifunctional interlocked e-skins (J. Park et al. *Sci. Adv.* **2015**, *1*, e1500661). (c) Gecko-inspired conductive dry adhesives for reliable monitoring of ECG under extreme human motions T. Kim et al. *ACS Nano* **2016**, *10*, 4770). (d) Metal-based temperature sensor (D.-H. Kim et al. *Science* **2011**, *333*, 838). (e) Pyroresistive flexible temperature sensor for wearable e-skins (J. Park et al. *Sci. Adv.* **2015**, *1*, e1500661).

Figure 1.11. E-skins for prosthesis. (a) Robotic hands with pressure, strain, and pressure sensor arrays for perception of hand gestures (H.-J. Kim et al. *Sci. Adv.* **2017**, *3*, e1701114). (b) Dual-mode smart prosthesis based on triboelectric-photonic skins (T. Bu et al. *Adv. Mater.* **2018**, *30*, 1800066). (c) Human skin-like prosthetic hands with multidirectional e-skins (C. M. Boutry et al. *Sci. Robot.* **2018**, *3*, eaau6914). (d) Prosthetics for sensory feedback and a pain reflex feedback control system (L. E. Osborn et al. *Sci. Robot.* **2018**, *3*, eaat3818).

Figure 2.1. Electronic skin based on carbon nanotube–poly(dimethylsiloxane) (CNT–PDMS) composite films with interlocked microdome arrays. (a) Schematic of human skin structure showing interlocked epidermal–dermal layers and mechanoreceptors (MD: Merkel disk; MC: Meissner corpuscle; PC: Pacinian corpuscle; RE: Ruffini ending). (b) Schematic of an interlocked microdome

array. (c) Tilted SEM image of a composite film with microdome arrays (diameter: $\sim 3 \mu\text{m}$; height: $\sim 3.5 \mu\text{m}$; pitch: $6 \mu\text{m}$). Scale bar: $5 \mu\text{m}$. (d) Cross-sectional SEM image of an interlocked composite film. Scale bar: $5 \mu\text{m}$. (e) Schematic of a stress-direction-sensitive electronic skin for the detection and differentiation of various mechanical stimuli including normal, shear, stretch, bending, and twisting forces.

Figure 2.2. Schematic illustration of the micromoulding process for the fabrication of CNT–PDMS composite elastomers with microdome arrays.

Figure 2.3. Lateral-stretch-sensing capability of electronic skins. (a) Schematic of the stretch-sensing mechanism of interlocked microdome arrays. (b) SEM images of microdome arrays showing the deformation of the array pattern from hexagons to elongated hexagons under different stretch ratios (0, 30, 60, and 120%). Scale bar: $5 \mu\text{m}$. (c) Finite-element analysis showing the contact pressure and the contact points between interlocked microdome arrays with the increase of uniaxial stretch. (d) FEA calculated results of the change of contact area between interlocked microdome arrays as a function of stretch. (e) Comparison of stretch-sensing capabilities of interlocked microdome arrays (black) and planar films (red). (f) Comparison of response and relaxation times of interlocked microdome arrays (black) and planar films (red) exposed to a stretching ratio of 50% and stretching speed of 3 mm s^{-1} . The CNT concentration in the composite was 7 wt% and curing temperature was $60 \text{ }^\circ\text{C}$. CNT concentration is 7 wt% for all the results.

Figure 2.4. Variation in resistance of the interlocked microdome arrays as a function of lateral stretch for (a) different CNT concentrations (6–8 wt%) and (b) different curing temperatures (60, 70, and $80 \text{ }^\circ\text{C}$).

Figure 2.5. Change in piezoresistance of interlocked microdome arrays with lateral stretch for the loading and unloading cycles at 130% lateral strain. The interlocked microdome arrays were prepared with a CNT concentration of 7 wt% and curing temperature of $60 \text{ }^\circ\text{C}$.

Figure 2.6. Normal- and shear-force-sensing capabilities of electronic skins. (a) Schematic of the deformation of interlocked microdomes during successive applications of normal and shear forces. (b) Relative electrical resistance of electronic skin sample as a function of normal force. (c) Comparison of shear-force sensitivities of interlocked microdomes (black) and planar (red) films under a normal pressure of 58.8 kPa. (d) Comparison of shear-force sensitivities of interlocked microdome arrays under different normal pressures. (e) Finite-element analysis (FEA) showing the deformation and local stress distribution of interlocked microdome arrays with increasing shear force at a normal pressure of 45 kPa. (f) Calculated FEA results of the inverse contact area as a function of shear force under different normal pressures. The CNT concentration was 7 wt% in all electronic skins used for the measurements.

Figure 2.7. (a) Variation in normalized resistance for the pulling and retracting cycles under different shear forces (0.196, 0.392, 0.588 N). (b) Reliability of interlocked microdome composite films through cycles of repeated pulling and retraction under a shear force of 1.96 N.

Figure 2.8. Change in relative resistance of interlocked microdome arrays as a function of shear force for electronic skins with different CNT concentrations.

Figure 2.9. Stress-direction-sensitive electronic skins for the detection and differentiation of multiple mechanical stimuli. (a) Real-time monitoring of changes in the relative resistance of interlocked microdome arrays subjected to different normal and shear forces. (b–d) Change in relative electrical resistance of an electronic skin attached on the front of a human wrist under different types of wrist movements: (b) forward bending; (c) backward bending; (d) torsion. The electronic skin showed different signal patterns in response to different wrist movements. (e–j) Change in relative electrical resistance of electronic skins in response to different mechanical stimuli: (e) normal force; (f) shear force; (g) lateral stretch; (h) forward bending; (i) backward bending; (j) torsion.

Figure 2.10. (a) Photographic images of bending tests of electronic skins with interlocked microdome arrays. (b) Variation in relative resistance of interlocked microdome arrays as a function of radius of curvature for electronic skins with different CNT concentrations (6–8 wt%) and cured at 80 °C. (c) Variation in relative resistance of interlocked microdome arrays as a function of radius of curvature for electronic skins prepared with 7 wt% CNTs at different curing temperature (60, 70, 80 °C). The decrease of curing temperature results in the decrease of elastic modulus and thus the increased deformability in response to mechanical stress, resulting in the increased sensitivity.

Figure 2.11. Stress-direction-sensitive electronic skins for directional sensing of mechanical stimuli applied in three axial directions. (a) Schematic of sensor arrays, where interlocked microdome arrays are sandwiched between the electrodes and PDMS protection layers. (b) Spatial pressure mapping capability of electronic skin for the detection of finger touch on two different pixels (R1-C3, R3-C1). (c) Detection of different finger-pushing directions: left (L), right (R), up (U), down (D). (d) Detection of different directions of fluid flow (left, right, diagonal). (e) Detection of the location of applied vibration and the gradual damping of vibration.

Figure 3.1. Various applications to show highly sensitive and large range pressure sensing of multilayered e-skins. (b) Schematic illustration of multilayered e-skins. (c) Cross-sectional scanning electron microscopy (SEM) image of microdome-patterned rGO/PVDF composite film with multilayer stacked structures. (d) Cross-sectional SEM image of interlocked microdome geometry of rGO/PVDF composite film. (e) Tilted SEM image of microdome array of rGO/PVDF composite film.

Figure 3.2. X-ray diffraction (XRD) spectroscopy of (a) a pure PVDF film, 2 wt% GO/PVDF,

and 2 wt% rGO/PVDF composite films; and (b) pure PVDF and 0.3, 0.5, and 1 wt% rGO/PVDF composite films.

Figure 3.3. Sheet resistance of rGO/PVDF composite films as a function of the loading concentration of rGO.

Figure 3.4. Circuit diagram of triple multilayer e-skins. piezoresistive properties of multilayer e-skins mainly depend on the bulk film resistance (R_f) and contact resistance between neighboring interlocked microdomes (R_c), which are connected in series.

Figure 3.5. Piezoresistive static pressure-sensing performances of multilayer interlocked microdome e-skins. (a) Relative current of e-skins with multilayer geometry with different numbers of stacked layers and planar geometry in response to the applied pressure. (b) Pressure sensitivity of e-skins converted from Figure 2a. (c) Comparison of the sensitivity and linear sensing performances based on this work and previous reports. (d) Finite element calculation of the contact area change as a function of pressure for different numbers of stacked layers. (e) Finite element calculations of the local stress distribution for different numbers of interlocked layers showing the concentrated and amplified stress at the small spot between interlocked microdomes under a pressure of 355 kPa. (f) Real-time pressure monitoring of e-skins at an applied pressure of 54, 108, 163, 217, 272, and 326 kPa. (g) Response and relaxation times for multilayer e-skins under different pressures of 10 and 200 kPa. (h) Cyclic stability test of multilayer e-skins under repetitive high-pressure loading of 272 kPa at a frequency of 0.5 Hz.

Figure 3.6. Static pressure-sensing performances of multilayer e-skins over three layers.

Figure 3.7. Finite-element calculation showing the stress distribution in multilayer e-skins with single, double, and triple layers. (a) Model systems with different number of interlocked layers. (b) Stress distribution of multilayer e-skins with single, double, and triple layers under different applied pressure.

Figure 3.8. (a) Static pressure-sensing performances of single-interlocked e-skins with different rGO loading concentrations. (b) Static pressure-sensing performances of triple-interlocked e-skins with different rGO loading concentrations. (c) Initial resistance of single- and triple-interlocked e-skins using 1 and 2 wt% rGO/PVDF composite films.

Figure 3.9. Pressure-sensing performances of multilayer e-skins based on different size of microdomes. Cross-sectional SEM images of microdome arrays with (a) 10, 15, and 4 μm , (b) 25, 30, and 10 μm , (c) 50, 60, 20 μm in diameter, pitch, and height, respectively. Relative current of multilayer e-skins based on microdomes with (d) different pitch size and (e) different diameter.

Figure 3.10. Application of weak pressure on multilayer e-skins. (a) Schematic illustration showing the detection of weak air flow by multilayer e-skins. (b) Relative current change of multilayer e-skins as a

function of gas flow rate. (c) Real-time monitoring of gas flow by multilayer e-skins. (d) Piezoelectric dynamic pressure-sensing performances of e-skins with different multilayer structure geometries with different stacked layers and planar structures. (e) Schematic of sound wave detection by multilayer e-skins. (f) Detection of the sound wave with single frequency for planar, single-interlocked, and multilayer interlocked microdome e-skins. (g) Sound waveforms and corresponding spectrograms converted by STFT from the original sound source (black), signals recorded from multilayer e-skins (red), and planar e-skins (blue). (h) Expanded frequency spectrograms in Figure 3g.

Figure 3.11. Applied pressure due to weak gas flow with a flow rate of 3 L/min. Considering the size of the multilayer e-skins, the applied pressure due to gas flow with a flow rate of 3 L/min is ≈ 1.3 Pa.

Figure 3.12. (a) Dynamic pressure-sensing performances of single-interlocked e-skins with 1 and 2 wt% rGO/PVDF composite films. (b) Dynamic pressure-sensing performances of triple-interlocked e-skins with 1 and 2 wt% rGO/PVDF composite films.

Figure 3.13. Piezoelectric single sound frequency detection performances of (a) multilayer e-skins and (b) planar e-skins.

Figure 3.14. (a) Sound waveforms and corresponding spectrograms converted by STFT of the original sound from a piano, guitar, and electric guitar (black). (b) Recorded piezoelectric waveforms and corresponding spectrograms from multilayer e-skins, converted by STFT of sound from a piano, guitar, and electric guitar (red).

Figure 3.15. Application of medium pressure on multilayer e-skins. (a) Photograph showing the detection of human breath by attaching multilayer e-skins to the nostril of a volunteer. (b) Monitored real-time signals of weak and deep breathing detected by multilayer e-skins. (c) Photograph showing the pulse pressure detection after attaching multilayer e-skins to wrist skin. (d) Real-time monitoring of the pulse signals and expanded pulse wave containing three peaks, *i.e.*, P_1 (incident wave), P_2 (tidal wave), and P_3 (diastolic wave), recorded by multilayer e-skins. (e) Schematic of the 3×3 sensor array for the multilayer e-skins with an ability to perceive the magnitude and spatial distribution of the applied pressure. (f–h) Schematics of the detection of applied pressure from different shapes and weights of loads and their corresponding pressure maps.

Figure 3.16. Application of high pressure to multilayer e-skins. (a) Schematic of the smart insole consisting of 4×8 pixel arrays of multilayer e-skins, patterned electrodes, and supporting PET layers. (b) Photograph of 4×8 pixel arrays of multilayer e-skins with pressure applied by an upside-down petri dish. (c) Corresponding pressure map. (d) Schematics of five walking motions on the smart insole to monitor the foot pressure distribution and their corresponding pressure maps.

Figure 4.1. Comparison of the electrode with sandwiched structure and coplanar structure (Upper) A scheme of the sandwiched electrode which experiences both of contact resistance and bulk film resistance and affects change of total resistance (Bottom) A scheme of the coplanar electrode which only is affected by the contact resistance.

Figure 4.2. Design and functional mechanism of the flexible multi-layered e-skin. (a,b) Scheme of sensor with multi-layered poly(3,4-ethylenedioxythiophene):poly(styrene sulfonate)/ polyurethane dispersion (PEDOT:PSS/PUD) composite and an interdigitated electrode. (c) Multi-layered PEDOT:PSS/PUD composite with different conductivities on the microdome-patterned polydimethylsiloxane (PDMS) layer. (d) Pressure-sensing mechanism of the multi-layered sensor. (e) Limitations of single-layered sensors with co-planar electrodes. (f) Sensing profiles of the multi-layered e-skin.

Figure 4.3. Fabrication process of the e-skins. (a) Schematic of multi-layered pressure sensor. (b) Fabrication process of the upper active layer; on the microdome patterned PDMS, PEDOT:PSS/PUD composite with different conductivity is coated successively. (c) Fabrication process of the bottom electrode layer; on the microdome patterned TPU, Pt is sputtered and AgNWs are spray-coated under the interdigitated mask.

Figure 4.4. Control of the sheet resistance of PEDOT:PSS depending on the amount of ethylene glycol and PUD addition (50 wt%) (a) Scheme indicating single layered PEDOT:PSS/PUD film on the microdome PDMS. (b) The sheet resistance of the PEDOT:PSS with addition of 0 and 100 μL of ethylene glycol in 10 mL of PEDOT:PSS solution. (b) The sheet resistance of the PEDOT:PSS with addition from 200 to 800 μL of ethylene glycol in 10 mL of PEDOT:PSS solution.

Figure 4.5. SEM image of the surface of PEDOT:PSS/PUD coated microdome depending on the amount of the Polyurethane Dispersion (PUD). (upper) The SEM image showing microdome surface before pushing test. (Below) The SEM image showing microdome surface after pushing test with 10 kPa of the pressure.

Figure 4.6. The sensing performance in resistance with single layered sensor with 30 nm of thickness. (a) Resistance change in single layered sensor with different resistance. (b-d) Relative current change of single layered sensor with different sheet resistance 300 $\text{k}\Omega/\text{sq}$, 2 $\text{k}\Omega/\text{sq}$ and 226 Ω/sq in response to applied pressure.

Figure 4.7. (a) The scheme of the single layered PEDOT:PSS/PUD on the microdome PDMS with 45 nm of thickness (b) SEM image showing whole microdome's cross section. (c) Enlarged SEM image showing valley between microdomes with thickness of the 320 nm. (d) Enlarged SEM image showing upper section of the microdome with thickness of the 45 nm.

Figure 4.8. Sensing performance and sensitivity of pressure sensors. (a,b) Resistive pressure-sensing performance and sensitivity of multi-layered pressure sensors with different number of layers. (c) Resistive pressure-sensing performance of multi-layered pressure sensors with different structures. (d) Real-time monitoring of pressure sensor at pressure loads of 0.5, 1, 2.5, 5, 10, 50, and 100 kPa. (e) Response and relaxation times of pressure sensor at 0.5 and 10 kPa. (f) Cyclic stability test of e-skin under repetitive pressure loading of 20 kPa at a frequency of 0.25 Hz. (g) Resistance change in multi-layered pressure sensor at different applied voltage biases (0.1 to 5 V). (h) Sensitivity and linear sensing performance obtained in present study and previous reports.

Figure 4.9. Resistance change depending on the number of layers (a) Multi-layering condition with different resistance in each layer. (b) Resistance change under the pressure from 0 to 100 kPa. (c) Enlarged graph in the pressure range from 0 to 10 kPa showing released saturation trends of resistance as the number of layers increase. (d) Enlarged graph in the pressure range from 0 to 0.2 kPa showing increase of the initial resistance as the resistance of the outermost layer increases.

Figure 4.10. Scheme and sensing performance in resistance and current change indicating the effect of multi-layering. (a) Scheme of the conductive gradient PEDOT:PSS/PUD film by multi-layered structure and uniformly conductive film. (b) Resistance change of the sensors with conductive gradient and non-gradient composite. (c-d) Current change of the sensors with conductive gradient and non-gradient composite.

Figure 4.11. Sensing performance depending on the structure of the sensors. (a) Scheme of the sensor with different structures; Planar, single dome, and interlocked structure (b) Resistance change depending on the structure of the multi-layered sensor (c) Sensitivity depending on the structure of the multi-layered sensor.

Figure 4.12. Structural contribution to the sensing performance. (a) Local stress distribution in the interlocked microdome structure with PDMS-PDMS layers at different pressures. (b) Local stress distribution in the interlocked microdome structure with PDMS-TPU layers at different pressures. (c,d) Contact stress and contact area as a function of pressure for top and bottom substrates with different moduli. (e,f) Deformation degrees of different moduli and SEM images of (upper) microdome-patterned PDMS layer with Pt and AgNWs, microdome-patterned PDMS layer with Pt and (bottom) microdome-patterned TPU layer with Pt and AgNWs, microdome-patterned TPU layer with Pt. (g) Resistance change in multi-layered pressure sensor with top and bottom layers characterized by different moduli.

Figure 4.13. The electrical sensing performance with different modulus of active and electrode layer. (a) The current change. (b) Sensitivity.

Figure 4.14. Applications of multi-layered pressure sensor characterized by high sensitivity and linearity (a) Scheme of sensing weak gas flow by multi-layered e-skin. (b) Real-time monitoring of resistance variation for different gas flow rates. (c) Glove with multi-layered sensor on the fingertip and real-time pressure sensing for varying weights of water (25, 50, 100, 150, 200, and 250 g). (d) Photograph and illustration of multi-layered sensor on human neck for detection of carotid artery signal. (e) Monitored real-time pulse signals for carotid artery with characteristic peaks, i.e., P_1 (incident wave), P_2 (tidal wave), and P_3 (diastolic wave). (f) Photograph and illustration of multi-layered sensor on volunteer facing slightly left for detection of internal jugular vein signal. (g) Monitored real-time pulse signals for internal jugular vein with characteristic peaks, i.e., A (atrial contraction), C (tricuspid bulging, ventricular contraction), and V (systolic filling of atrium), and two descents, i.e., X (atrial relaxation) and Y (early ventricular filling).

Figure 4.15. Photograph of the weighing of weak gas flow (~ 3 L/min)

Figure 4.16. Application of multi-layered pressure sensor for detection of spatial distribution on a 3×3 sensor array. (a,b) Scheme and photograph of the fabricated 3×3 sensor array. (c–e) Detection of spatial distribution for different locations and weights on the multi-layered 3×3 sensor array. (f,g) Ar and N_2 gases on the multi-layered sensor and detected spatial distributions for different air densities.

Figure 5.1. Hierarchical NP-MP architecture in porous mechanochromic composites. (a) Schematic of the working mechanism of porous mechanochromic composites with hierarchical NP-MP architecture. (b) Photograph and SEM images of porous (pore-5) mechanochromic composites comprising PDMS, SP and 300-nm SNPs (SNP-300). The SEM images show uniform spherical pores and SNPs decorated on the inner pore surfaces. (c) Stress–strain behaviours of the stretchable mechanochromic polymers with planar, porous and SNP-decorated porous structures.

Figure 5.2. Schematic of the fabrication procedure for porous mechanochromic composites with PDMS/SP/SNPs. SP, PDMS and SNPs are mixed in hydrophilic co-solvents (water and ethanol) and solvents are evaporated during the hydrosilylation curing process.

Figure 5.3. (a) Scanning electron microscope (SEM) image of a porous mechanochromic composite with an average pore size of $5 \mu\text{m}$ before freeze-drying. SEM images of a fabricated porous mechanochromic composite after three days before (b) and after (c) freeze-drying. Due to the capillary force-induced pore closure during solvent evaporation, freeze-drying is required to completely evaporate the solvent and obtain uniform pores.

Figure 5.4. (a) Schematic of the mechanism of pore formation in composites based on the addition of hydrophilic solvents. (b) Cross-sectional SEM images of porous PDMS/SP composites with different mixed solvent ratios (PDMS:water:ethanol = 3:2:0, 3:1.5:0.5 and 3:1:1). The lower row shows

magnified SEM images. (c) Pore size distributions of porous PDMS/SP composites with different mixed solvent ratios.

Figure 5.5. (a) Simulated surface areas of porous mechanochromic composites with different pore sizes based on face-centered cubic (FCC) unit cell arrays. The porous structures are modelled according to average pore sizes of 25, 10 and 5 μm with the same porosity (26%) based on FCC unit cell arrays. Volume is determined as the total material volume, excluding the pore volume. Area is the total surface area of the porous structure. (b) Material densities of the fabricated porous mechanochromic composites with different pore sizes. (c) Porosity and surface area of porous mechanochromic composites as functions of pore size.

Figure 5.6. (a) Schematic of SNP decoration on the inner pore surfaces of a mechanochromic composite during heat-induced solvent evaporation. (b) Cross-sectional SEM images of porous PDMS/SP composites (pore size = 5 μm) with different SNP sizes (20, 100 and 300 nm). (c) Magnified SEM images showing that the SNPs are uniformly decorated on the inner pore surfaces.

Figure 5.7. (a) Strain–stress curves of porous PDMS/SP composites with different pore sizes. (b) S–S curves of porous PDMS/SP composites (pore size = 5 μm) with different SNP sizes.

Figure 5.8. Schematic of a measurement system using a spectroradiometer for investigating the colour transition properties of porous mechanochromic composites in response to tensile strain.

Figure 5.9. Properties of porous mechanochromic composites under tensile strain. (a) Photographs of mechanochromic polymers with different structures exhibiting colour changes in response to tensile strain. (b) Colour change of the pore-5/SNP-300 mechanochromic composite at the first and 100th stretching and releasing cycles. (c) Changes in the average colour coordinates of the mechanochromic polymers with different structures under applied tensile strain. (d) Normalised luminance as a function of wavelength for the pore-5/SNP-300 mechanochromic composite under tensile strains up to 400%.

Figure 5.10. Photographs showing the colourimetric strain sensing properties of porous mechanochromic composites with different pore sizes.

Figure 5.11. Photographs showing the colourimetric strain sensing of porous PDMS/SP composites (pore size = 5 μm) decorated with SNPs with different sizes: (a) 20 nm. (b) 100 nm. and (c) 300 nm.

Figure 5.12. Strain–stress curves of a porous mechanochromic composite (pore size = 5 μm ; SNP size = 300 nm) under repeated loading/unloading strain of up to 250%.

Figure 5.13 (a) Average colour coordinates of planar mechanochromic composites under loading tensile strain. (b) Average colour coordinates of porous mechanochromic composites with different pore sizes under loading tensile strain. (c) Average colour coordinates of mechanochromic composites with

different SNP sizes under loading tensile strain.

Fig. 5.14. Recovery time of a porous mechanochromic composite (pore size = 5 μm , SNP size = 300 nm) under different tensile strains. (a) Time-dependent tensile strains of 125%, 150% and 175% (top) and the corresponding change in relative intensity (I_{Rel}) of green colour in response to loading strain (bottom). (b) Relaxation under a loading/unloading strain of 175% depending on exposure to white light.

Figure 5.15. Effect of SNPs with different polarity on the mechanochromic property of polymer composites (pore size = 5 μm , SNP size = 100 nm). SEM images of porous PDMS/SP composites with (a) hydrophilic SNPs and (b) hydrophobic SNPs. Average colour coordinates of porous PDMS/SP composites with (c) hydrophilic SNPs and (d) hydrophobic SNPs.

Figure 5.16 Variation in colour component intensities (R, G and B) of porous mechanochromic composites under loading strain at different wavelengths: (a,b) 488 nm. (c,d) 544 nm. and (e,f) 612 nm. The intensity of each colour component initially increases because of the decrease in light absorption caused by the concurrent decrease in film thickness. The intensity subsequently decreases because of the colouration of SP.

Figure 5.17 Structure-dependent strain sensitivity of porous mechanochromic composites. (a) Normalised colour intensity ratio as a function of strain for mechanochromic polymers with different pore sizes (left) and with different SNP sizes at a pore size of 5 μm (right). The colour intensity in response to strain is measured by spectroradiometer. (b) Enlarged plot from a in the strain range 20%–100%. (c) Strain sensitivity [$S = (\Delta C/C_0)/(\Delta \epsilon)$, where C is the colour intensity ratio and ϵ is the applied strain] of mechanochromic polymers with different structures. Sensitivity is estimated from the plot in a for the linear regimes of mechanochromic response. (d) Finite-element analysis (FEA)-determined stress distributions of mechanochromic polymers with different pore sizes (left) and with 300-nm SNPs and a 5- μm pore size (right) under a tensile strain of 50%. (e,f) FEA-determined maximum localised stress near the pore surface in porous mechanochromic polymers with e different pore sizes and f different SNP sizes and a pore size of 5 μm as a function of strain.

Figure 5.18. Stress distributions of porous PDMS/SP composites with different pore sizes (25, 10 and 5 μm) placed under 50% tensile strain calculated numerically using ABAQUS software. For simplicity, the elastic modulus is set to 1 MPa with the same porosity (26%) for all porous composites.

Figure 5.19 Stress distribution of porous PDMS/SP composites (pore size = 5 μm) decorated with SNPs with different sizes (300, 100 and 20 nm) placed under 50% tensile strain calculated numerically using ABAQUS software. For simplicity, to understand the role of the SNPs at the pore walls, the elastic modulus of the porous matrix is set to 0.24 MPa. The elastic modulus of the SNPs is set to a general

value of 180 GPa for all sizes.

Figure 5.20. (a) Measurement system used to evaluate the colour transition properties of porous mechanochromic composites in response to normal stress. (b) Photographs of the mechanochromic composites with different porous structures under a loading normal stress of 6 N.

Figure 5.21. Normal force detection capabilities of porous mechanochromic composites. (a) Relative intensities of the colour components (red, green and blue) of mechanochromic polymers with different structures as functions of normal force. The colour intensity in response to normal force is measured by I-phone camera and colour picker program. (b) Relative green intensity as a function of normal force for mechanochromic polymers with different pore sizes and different SNP sizes with 5- μm pores. (c) Optical images showing the local colour distributions of the porous mechanochromic composites after contact with various objects (microtips and needle).

Figure 5.22. (a) Relative colour changes of porous PDMS/SP composites with different pore sizes in response to applied normal pressure. (b) Finite-element analysis-determined stress distributions in porous PDMS/SP composites with different pore sizes under applied normal pressure.

Figure 5.23. (a) Relative colour intensities of porous PDMS/SP composites (pore size = 5 μm) decorated with SNPs of different sizes (20, 100, 300 nm) as functions of pressure. (b) Finite-element analysis-determined stress distributions at the surfaces of pores in porous PDMS/SP composites with SNPs under applied pressure.

Figure 5.24. Applications of porous mechanochromic composites in wearable e-skins and dual-mode static/dynamic touch and audio sensors. **a**, Images of wearable mechanochromic e-skins for the detection of various hand gestures (folding/unfolding, rock, scissor and grasp). **b**, Schematic of a dual-mode mechanochromic and triboelectric force sensor that enables the spatiotemporal detection of both writing force and speed. **c**, Waveforms of the sound sources of the words ‘electronic’ and ‘skin’: waveforms of the detected read-out signals (left) and short-time Fourier transform of the sound source along with the read-out signals from the dynamic force sensor (right). These applications are based on the pore-5/SNP-300 porous mechanochromic composite.

Figure 5.25. Schematic of the working mechanism of the single-electrode triboelectric sensor, which comprises a porous mechanochromic composite and silver nanowire-based electrode. Object is the plastic pen in this work.

Figure 5.26. (a) Output triboelectric current of a mechanochromic composite in response to normal pressure. The sensitivity is $0.18 \mu\text{A kPa}^{-1}$ below 0.4 kPa and $0.002 \mu\text{A kPa}^{-1}$ in the range 1–108 kPa. (b) Triboelectric output voltage and (c) power density of porous PDMS/SP composites with 5- μm pores and 300-nm SNPs as functions of applied pressure. (d) Output current of the porous mechanochromic

composite in response to dynamic normal pressure with different loading frequencies (0.1–4 Hz).

Figure 5.27. Schematic showing the setup used to detect dynamic acoustic waves.

Figure 6.1. Thermoresponsive composite film based on a semi-crystalline polymer. (a) Photograph of a flexible rGO–PEO–PVDF composite film with large area ($15 \times 15 \text{ cm}^2$). (b) SEM image of rGO–PEO–PVDF composite film. (c) High-magnification SEM image of rGO–PEO–PVDF composite film with PEO microdomains. (d) Schematic showing the temperature-sensing mechanism of rGO–PEO–PVDF composite film based on the melt-induced volume expansion of PEO microdomains. The hexagons represent rGO sheets; the blue spheres represent PEO microdomains.

Figure 6.2. Temperature-sensing properties of flexible and highly sensitive temperature sensors based on a rGO/–PEO–PVDF composite film. (a) Schematic illustration of flexible temperature sensor. (b) Relative resistance as a function of temperature (20–60 °C) of temperature sensors with different loadings of PEO (0 to 20 wt%). (c) Real-time temperature monitoring of temperature sensors as the temperature was increased from 32 °C in steps of 0.1 °C. (d) AFM phase image of a rGO–PEO–PVDF composite film at a temperature of 25 °C. (e) AFM phase image of a rGO–PEO–PVDF composite film at a temperature of 40 °C. (f) Temperature-dependent Raman spectra of rGO–PEO–PVDF composite films; a magnified view of the Raman spectra is shown on the right.

Figure 6.3. Hysteresis curve of temperature sensors with different PEO concentration.

Figure 6.4. TCR values of temperature sensors with and without PEO microdomains

Figure 6.5. (a) Relative resistance of temperature sensors with different loadings of rGO as a function of temperature. (b,c) SEM images of rGO–PEO–PVDF composite films with 5 wt% rGO.

Figure 6.6. Decrease in resistance of temperature sensor as the applied temperature was increased in steps of 0.2 °C.

Figure 6.7. (a,b) Confocal laser microscopy image and 3D profile for surface morphology of rGO–PEO–PVDF composite at 20 °C. (c,d) Confocal laser microscopy image and 3D profile for surface morphology of rGO–PEO–PVDF composite at 40 °C.

Figure 6.8. (a) Temperature-dependent Raman spectra of pure PEO. (b, c) Magnified view of the Raman spectra in (a).

Figure 6.9. Raman spectra of (a) rGO and (b) PVDF.

Figure 6.10. (a) DSC thermo-diagrams of PEO with molecular weight (M_w) of 1000, 1500, and 4000. (b) DSC thermo-diagrams of rGO–PEO–PVDF composites with PEO molecular weights of 1000, 1500, and 4000.

Figure 6.11. (a) Relative resistance as a function of temperature of temperature sensors with different PEO molecular weights (1000, 1500, or 4000). Relative resistance as a function of temperature of temperature sensors with PEO molecular weights of (b) 1000, (c) 1500, and (d) 4000.

Figure 6.12. Temperature-sensing performances in the presence of a warm object at a distance and deformation-insensitive behavior of temperature sensors for wearable application. (a) Schematic illustration of temperature sensing in the presence of a warm object at a distance. (b) Changes in relative resistance of temperature sensors when a warm object at 30 °C was located at a varying distance from the temperature sensors. (c) Relative resistance of temperature sensors as a function of the distance from the warm object; the measurements were repeated when the temperature of the warm object was set to different values. (d) Relative resistance of temperature sensors with different temperature as a function of pressure. (e) Relative resistance of temperature sensors as a function of the bending curvature. (f) Cycling stability of temperature sensors under repetitive temperature change from 20 to 60 °C. (g) A photograph of deformation-insensitive flexible temperature sensor attached on the back of hand. The inset shows enlarged photograph of temperature sensor. (h) Body temperature change detected by the wearable temperature sensor (black) and surface thermometer (red). (i) Enlarged plot in Figure 4h showing temperature accuracy of our temperature sensor and surface thermometer.

Figure 6.13. Real-time monitoring of relative resistance of temperature sensors when the warm objects with temperature of 30, 40, and 50 °C were located at a distance of 3 to 30 cm.

Figure 6.14. Pressure sensitivity of temperature sensors with different electrode designs.

Figure 6.15. (a) Temperature-sensing performances of temperature sensors in different bending states. (b) Relative resistance as a function of temperature of temperature sensors after 0–1000 bending cycles.

Figure 6.16. Relative resistance as a function of temperature of a temperature sensor. The data was fitted with a power-law equation, $y = ax^{-b}$, where a is 11264.48 and b is -3.11 .

Figure 6.17. Dual-mode temperature sensors for electrical and colorimetric temperature sensing. (a) Schematic illustration of dual-mode temperature sensors. (b) Intensities of the color components (red, green, blue) as a function of temperature of thermochromic composite films. (c) Changes in the CIE 1931 color space chromaticity diagrams of thermochromic composite films when the temperature was changed from 28 to 39 °C in steps of 1 °C. (d) Photographs of the thermochromic composite films in 1 °C increments. (e) Time-dependent relative resistance of pyroresistive temperature sensors after the release of a warm water droplet and temperature variation of warm water droplet, obtained by infrared camera. (f) Magnified variations in relative resistance and temperature shown in (e). (g) Color

changes of thermochromic composite films after the release of a warm water droplet and temperature mapping images, obtained by infrared camera, of warm water droplet.

Figure 6.18. (a–c) Thermochromic color change of three thermochromic inks with different color and response temperature.

Figure 6.19. Luminance as a function of wavelength for thermochromic composite film as the temperature was changed from 28 to 39 °C in steps of 1 °C.

Figure 6.20. RGB values of thermochromic composite films when warm water droplets with temperature of 50, 40, and 30 °C were released on the film surface.

Figure 6.21. 8 × 8 dual-mode temperature-sensor arrays. (a) Schematic illustration of 8 × 8 pixel arrays of temperature sensors. (b) Magnified schematic illustration showing components of temperature-sensor arrays. (c) Photograph of flexible pyroresistive temperature sensors in 8 × 8 pixel arrays. (d) Scheme for the temperature-measurement setup of temperature sensors in 8 × 8 pixel arrays on the heating–cooling plate. (e) Relative resistance of 8 × 8 pixel arrays (blue) and a single temperature sensor (red) as the temperature was changed from 20 to 60 °C. (f–h) Pyroresistive temperature mapping images of three metal plates with temperatures of 30, 32, and 40 °C and photographs of corresponding color mapping of the thermochromic composite film.

Figure 6.22. Layer-by-layer schematic illustration of 8 × 8 pixel arrays of temperature sensors.

Figure 7.1. Current and Future challenges for the demonstration of skin electronics. Current challenges: Linearity controlled by macroscopic and microscopic structure modification. (Bae et al. *Adv. Mater.* **2016**, *28*, 5300-5306). Self-powered e-skins based on piezoelectric, triboelectric, pyroelectric, thermoelectric and ionic properties. (Lee et al. *Adv. Mater.* **2014**, *26*, 765, Zhao et al. *Nat. Commun.* **2017**, *8*, 14214). Integration with stretchable electronic components controlled by extrinsically modified structure and intrinsically modified materials. (Kim et al. *Science* **2011**, *333*, 838, Wang et al. *Nature* **2018**, *555*, 83). Biocompatible and biodegradable electronics. (Lei et al. *Proc. Natl. Acad. Sci. U.S.A.* **2017**, *114*, 5107, Kange et al. *Nature* **2016**, *530*, 71). **Future challenges:** Transmission. (Gao et al. *Nature* **2016**, *529*, 509) Perception. (Rudovic. Et al. *Sci. Robot.* **2018**, *3*, eaao6760). Display. (Ryu et al. *Sci. Rep.* **2018**, *8*, 4555).

List of Tables

Table 1.1. Summary of specific roles and location of various mechanoreceptors in human skin.

Table 3.1. Summary of pressure sensors with linear pressure responses and their performances.

Table 4.1. Summary of recent pressure sensors with linear pressure responses and their key parameters.

Table 5.1. Summary of recently reported mechanophore systems.

Table 6.1. Summary of resistive temperature sensors and their performances.

Nomenclature

E-skin	Electronic skin
PSR	Pressure sensitive rubbers
CNT	Carbon nanotube
MWNT	Multi-walled carbon nanotube
AgNW	Silver nanowire
ITO	Indium tin oxide
PET	Polyethylene terephthalate
PEN	Polyethylene naphthalate
FFT	Fast fourier transform
STFT	Short-time fourier transform
MD	Merkel disk
MC	Meissner corpuscle
PC	Pacinian corpuscle
RE	Ruffini ending
SP	Spiropyran
MC	Merocyanine
SNP	Silica nanoparticle
NP-MP	Hierarchical nanoparticle-in-micropore
FEA	Finite element analysis
GF	Gauge factor
PDMS	Polydimethylsiloxane
PVDF	Poly(vinylidene fluoride)
P(VDF-TrFE)	Poly(vinylidene fluoride-trifluoroethylene)
PZT	Lead zirconium titanate
rGO	Reduced graphene oxide
DMF	Dimethyl formamide
PUD	Polyurethane dispersion
TPU	Thermoplastic polyurethane
PEO	Polyethylene oxide
PVA	Polyvinyl alcohol
EG	Ethylene glycol
PEDOT:PSS	Poly(3,4-ethylenedioxythiophene):poly(styrenesulfonate)

PANI	Polyaniline
PPy	Polypyrrole
P3HT	Poly(3-hexylthiophene-2,5-diyl)
OLED	Organic light-emitting diode
FET	Field-effect transistor silicon complementary metal-oxide semiconductor
CMOS	Complementary metal-oxide semiconductor
MEMS	Microelectromechanical system
PSR	Pressure-sensitive rubber
R_b	Bulk film resistance
R_c	Contact resistance
P₁	Incident wave
P₂	Tidal wave
P₃	Diastolic wave
AI_r	Radial augmentation index
DAI_r	Diastolic augmentation index
ΔT_{DVP}	Digital volume pulse time
NTC	Negative temperature coefficient
PTC	Positive temperature coefficient
TCR	Temperature coefficient of resistance
S_T	Seebeck coefficient
RIE	Reactive ion etching
DRIE	Deep reactive ion etching
SAM	Self-assembled monolayer
SEM	Scanning electron microscopy
TEM	Transmission electron microscope
AFM	Atomic force microscope
UV-vis	Ultraviolet-visible
XRD	X-ray diffraction
IR	Infrared
M_w	Molecular weight
RGB	Red-green-blue
PAI	Pressure augmentation index
IoT	Internet of Things
ECG	Electrocardiogram
EMG	Electromyography

IoMT	Internet of medical Things
IoMT	Internet of medical Things
VR	Virtual reality
AI	Artificial intelligent

Chapter 1. Introduction.

1.1 Electronic skin (E-skin)

The ever-increasing demand for improved quality of daily life promotes the rapid evolution of wearable electronics that can be mounted on the human body to collect various personal and environmental information.¹ In particular, the recent development of the Internet of Things (IoT) has made wearable electronics drive the next wave of the global economy by creating new markets, products, and consumers.²⁻³ Figure 1.1 shows one sort of IoT application in healthcare, which is the Internet of Medical Things (IoMT). As data sources in IoT space, wearable sensors play a key role in realizing seamless and intimate integration of wearable electronics with the human body and harvesting medical information from users and their surroundings, which were collected in a cloud computing or medical station. When the wearable sensors find the early signs of abnormal body condition, stored medical data can be sent to physician's office for therapeutic feedback, thus the users can be diagnosed in early state. However, wearable sensors with conventional electronics currently face a huge challenge because of their rigid and brittle nature, preventing conformal mounting on the rough surface of human skin for collecting accurate biosignals. Therefore, the ideal wearable system requires a novel design of materials characterized by light weight, flexibility, user comfort, and the ability to be miniaturized as wearable sensors.⁴⁻⁶

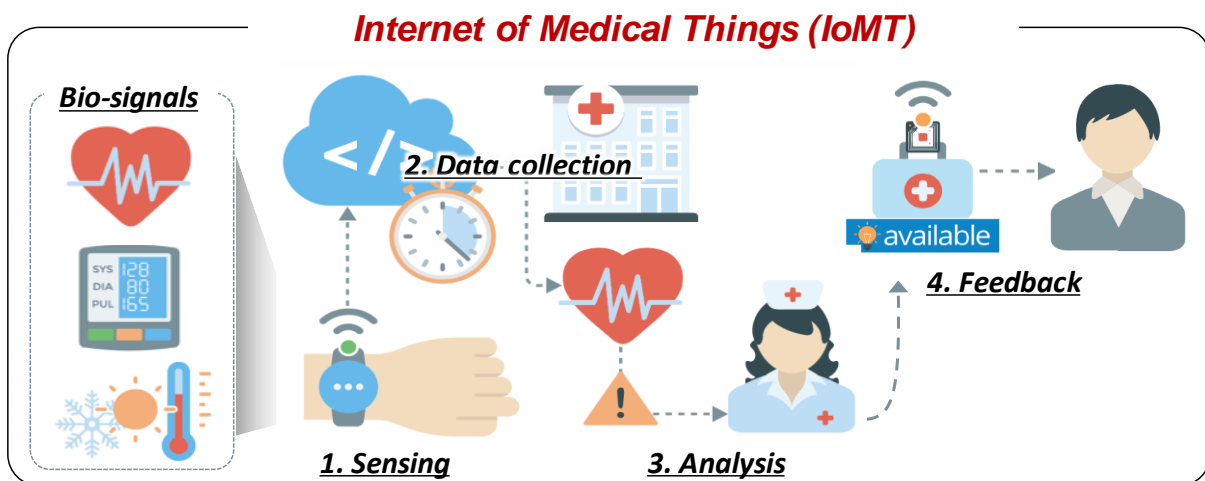


Figure 1.1. Personalized healthcare monitoring system based on Internet of Medical Things (IoMT) technology.

E-skin technology, which mimics the perceptive features of human skin, paves the way for the successful integration of wearable sensors with the human body for applications in health monitoring,

human-machine interfaces, intelligent robots, and prostheses. According to working mechanisms, recent advances in wearable e-skins can be categorized into two types, which are self-powered e-skins and multifunctional e-skins. Firstly, self-powered e-skins are the promising platforms, which can generate electrical signals by itself in response to stimuli from environment (Figure 1.2, left).⁷ Particullary, when they are applied to wearable applications, they can harvest renewable energy from various body motions or temperature, as well as monitor mody motions or various medical information without external power sources, providing promising solution for battery-free and miniaturized smart skins. As another platform, multifunctional e-skins can perceive multidirectional tactile stimuli, such as pressure, bending, stretching, textures, and temperature differences (Figure 1.2, right).⁷ By employing various signal-tranduction modes properly according to the sensing targets, the multifunctional e-skins accurately monitor the user’s biosignals and various physiological signals, enabling applications of healthcare, prosthesis, and robotics.

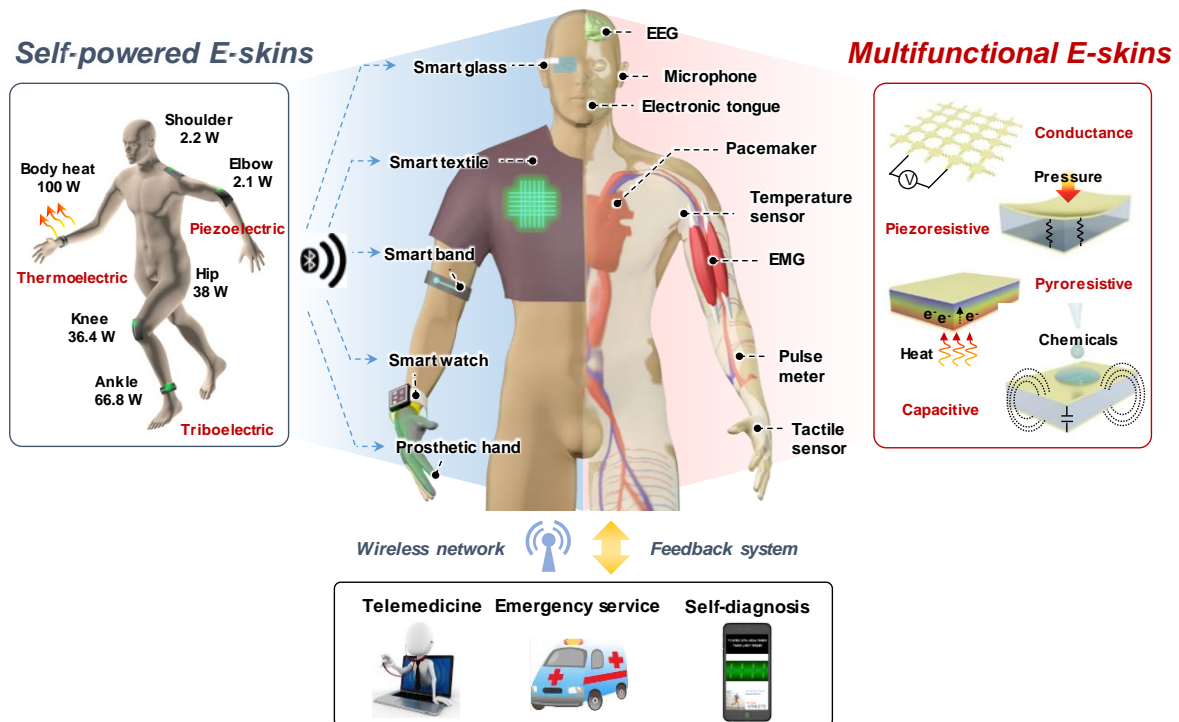


Figure 1.2. Wearable devices and sensors with self-powered systems and multifunctional abilities. (left) Self-powered wearable electronic skins based on piezoelectric, triboelectric, and thermoelectric harvest mechanical and thermal energy from the human body. Through the physical movements of various body parts and the heat dissipation from the body, high power of several to tens of watts are generated. (right) Multifunctional electronic skins based on resistive, capacitive, triboelectric, piezoelectric accurately monitor the user’s biological signals, including the EEG, EMG, and various physiological signals as well as physical movements and motions. (bottom) Ubiquitous healthcare systems through wireless network and feedback system (J. Park et al. *J. Mater. Chem. B* **2016**, 4, 2999).

Although various types of wearable e-skins based on novel materials, fabrication techniques, and sensing mechanisms have been introduced, there are still challenges in their practical application. For example, e-skins for smart robots and prostheses should possess the ability to perceive and differentiate multidirectional forces such as normal, tensile, shear, and bending forces without crosstalk.⁸ In addition, the medical diagnosis using wearable e-skins should be based on the precise and expeditious analysis of monitored signals from health events, which could be achieved by ultrasensitive and skin-attachable materials.⁹ Furthermore, instantaneous and intuitive recognition of applied stimuli can be achieved through the immediate change in color or shape, thus enhancing applications in user-interactive devices and human-machine interfaces.¹⁰⁻¹¹

To address these issues, this thesis suggests novel types of e-skins mimicking human and biological skins. Inspired by unique structures and functionalities in human skin, we designed nano/microstructured e-skins based on flexible and functional polymer composites, enabling high-performance e-skins with high sensitivity and multifunctionality in response to tactile stimuli. In particular, introduction of multilayer geometry further enhances performances of human skin-inspired e-skins, including ultrahigh sensitivity and unexceptionally large working range with linear response to stimuli. Moreover, multidimensional architectures inspired by the responsive color change in biological skins provide unique ability of enhanced mechanochromic sensing capability for stimuli visualization to e-skins. We believe that our bioinspired e-skins provide a great potential of electronic skins in various application fields of wearable sensors and soft electronics.

1.2 Working mechanisms of various electronic skins

In order to perceive various stimuli, the e-skins should convert them into an measurable signals. Therefore, it is necessary to employ proper working mechanism according to the sensing targets. The working mechanisms of the conventional e-skins were mainly dependent on electrical outputs in response to applied stimuli. As a result, the working mechanisms of conventional e-skins can be classified into two categories depending on target stimuli; transduction modes for mechanical stimuli-sensitive e-skins and transduction modes for temperature-sensitive e-skins. Recently, novel e-skins, which can perceive applied stimuli by colorimetric working mechanisms, have been studied. In this section, we will briefly introduce various transduction modes for the conventional e-skins and working mechanisms of novel colorimetric skins.

1.2.1 Transduction modes for mechanical stimuli-sensitive e-skins

Piezoresistivity: Piezoresistivity is the change in the resistance of materials caused by mechanical stimuli. As one of the most widely used transduction modes, piezoresistive e-skins can detect various mechanical stimuli by transducing them into changes in resistance. There are several types of piezoresistive e-skins based on polymer composites, where piezoresistivity is derived from a change in the band structure of semiconductors,¹² modification of tunneling resistance between conductive fillers,¹³ and break up and reforming of percolating pathways.¹⁴ Figure 1.3a shows the conventional piezoresistive e-skins based on pressure-sensitive rubber (PSR), composed of elastomeric polymer matrix and conductive carbon materials, such as graphite, carbon nanotube (CNT), and graphene. When the mechanical stress is applied to the piezoresistive e-skins, deformation of PSR modulates conductive networks between conductive fillers and decreases bulk film resistance (R_b), enabling piezoresistive sensing. In this mechanism, piezoresistive e-skins show the highest sensing performances near the percolation threshold of the conductive fillers in the elastomeric polymer matrix. Recently, introduction of microstructures in the PSRs have attracted much attentions because of much enhanced sensor performances, including sensitivity, response time, durability, etc.⁷ In general, contact resistance (R_c) between microstructured piezoresistive polymer composite and electrode is several orders higher than R_b owing to small contact area. Therefore, overall sensor resistance highly depends on the variation in R_c rather than that in R_b , although both R_c and R_b decreases with applied mechanical stress. Since the microstructured e-skins can be designed to have high variation in contact area between microstructured piezoresistive polymer and electrode, the R_c of them can be decreases from almost insulating state to conductive state near R_b , resulting in much enhanced sensor performances than PSR-based e-skins.¹⁵ To further maximize variation in R_c , various nano/microstructures (such as interlocked, porous, hierarchical, and crack structures), which emulate biostructures, have been introduced for the high performance piezoresistive e-skins.⁷

Capacitance: Capacitive e-skins have been widely researched owing to the advantages of high sensitivity, simple device structure, compatibility with static force detection, and low power consumption. They transduce various mechanical stimuli into a change in the capacitance of the device. The capacitance (C) of a parallel plate capacitor is defined as $C = \epsilon A/d$, where ϵ is the dielectric constant, A is the area of electrode, and d is the distance between electrodes. The pressure sensing mechanism of typical capacitive e-skins is shown in Figure 1.3b. In the early stage, the working mechanism of capacitive e-skins depends on the variation in A or d in response to applied mechanical stimuli, which results in a change in capacitance. Recently, various researches about pressure-dependent dielectric constant have intensively studied because of their high sensitivity to mechanical stimuli.¹⁶ One of the effective methods to assign the pressure-dependent dielectric constant in capacitive e-skins is introduction of nano/microstructures in dielectric layer, which show high variation in effective dielectric constant in response to mechanical stimuli.

Piezoelectricity: Piezoelectricity refers to the ability of piezoelectric materials to generate electrical potential in response to mechanical stimuli, because of non-centrosymmetric crystal structures of them. Therefore, piezoelectric e-skins can produce electric potential in response to mechanical stress based on inorganic materials such as ZnO, lead zirconium titanate (PZT), and BaTiO₃, and organic materials such as PVDF, PVDF-based copolymers, poly-L-lactide, MoS₂, and non-synthetic biocompatible protein (Figure 1.3c).¹⁷ Owing to their high flexibility, the polymer-based materials (PVDF, PVDF-based copolymers, and PVDF-based composite) have mainly studied for the flexible piezoelectric sensors. Because the piezoelectric e-skins can generate and quantify stress-responsive electric potential, they have been utilized as energy harvesting devices, as well as self-powered e-skins. In addition, owing to instantaneous generation of electric signals, piezoelectric e-skins can detect dynamic forces with high frequency, such as vibrations, sound, and slip. Because piezoelectricity can be generated by changing the polarization state of piezoelectric materials, the piezoelectricity highly depends on the crystalline phase of them, where higher polar phase induces higher polarization state.¹⁸⁻
¹⁹ The classical way to transform the phase of piezoelectric materials from nonpolar to polar phase is applying high electric fields through the film, which is known as electric poling method. However, it requires too high applying voltage and their high piezoelectric performances continuously decrease over time, addressing need of new strategy for high-performance piezoelectric materials.²⁰⁻²¹ Recently, introduction of nanomaterials with oxygen-containing functional groups to piezoelectric polymers can possess high piezoelectricity without electric poling process.^{20,22-23} In those piezoelectric polymer composites, the steric effect between nanomaterials and piezoelectric polymers through hydrogen bond restrict and order the PVDF chain segments, transforming phase of piezoelectric polymers from nonpolar σ -phase to polar β -phase. The other method to further improve the piezoelectric performance is introduction of surface micropatterns (e.g., dome, pyramid, and pillar) and bioinspired structures (e.g.,

interlocking, hierarchical, porous), which can enable a large localized stress in the nano/microstructures and large surface area, resulting in significant piezoelectricity compared to planar e-skins^{22,24}

Triboelectricity: Triboelectric e-skins convert mechanical energy to electrical energy through a conjugation of triboelectrification and electrostatic induction, caused by various contact motions such as vertical touch, shear friction from sliding motion, and torsional stress (Figure 1.3d).²⁵ Since the triboelectric output critically relies on differences in triboelectric polarity between two contacting materials and contacting surface areas, the most important factor for high-performane triboelectric e-skin is a rational design of materials in reference to triboelectric series.²⁶ Although two contacting materials have similar position in triboelectric series, chemically modified surface charge by self-assembled monolayers using an end-fluorine terminated group, thiol with a different head group, and atomic-level halogens and amines influences the surface potential and surface-charge density, enhancing triboelectric outputs.¹⁷ Because the triboelectrification occurs at the surfaces of two different materials, modification of surace morphologies can highly enhance the triboelectric performnnces by increasing surface area and amplifying stress concentration at the contacting nano/microstructures.^{25,27} For a structural approach, uniquely designed micro/nanoscale structures such as surface micropatterns, micropore, nanoscale assembly, and hierarchical nanoporous and interlocked micro-ridge structures have been suggested, which enables the increases in surface area and stress-induced deformability, thereby producing enhanced power up to a few tens of milliwatts.^{7,28}

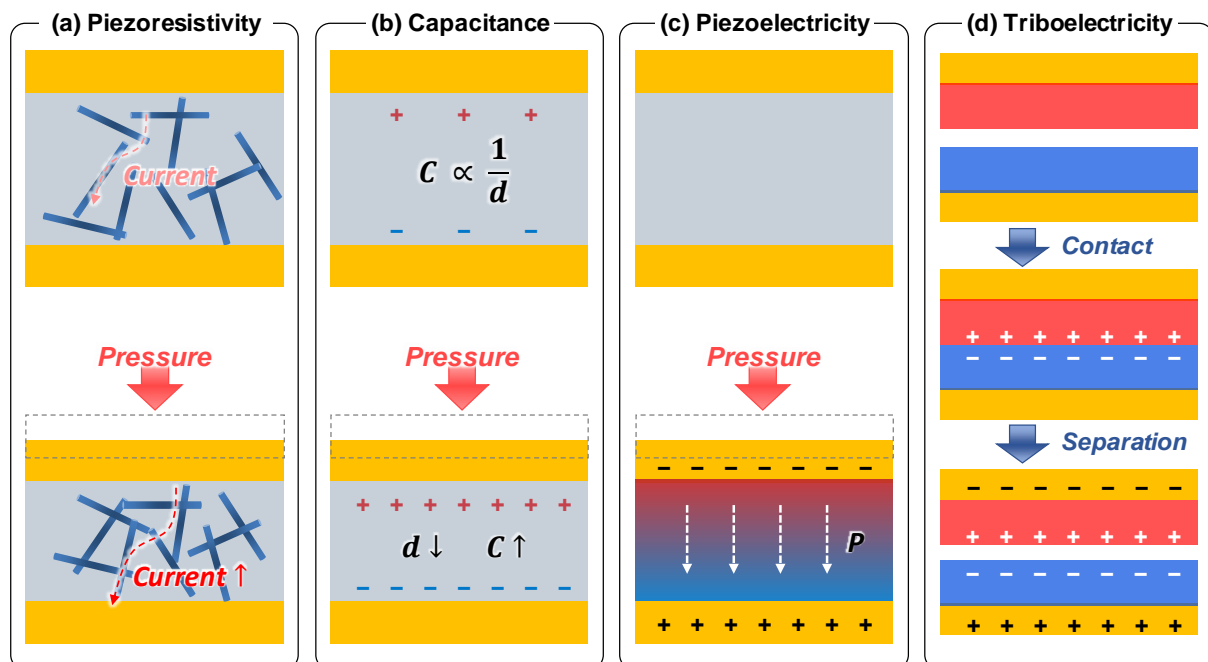


Figure 1.3. Transduction modes for mechanical stimuli-sensitive e-skins. (a) Piezoresistive e-skins based on PSR. (b) Capacitive e-skins of a parallel-plate capacitor. (c) Piezoelectricity generated in single film-based e-skins. (d) Triboelectricity generated in e-skins during contact/separation cycles.

1.2.2 Transduction modes for temperature-sensitive e-skins temperature-dependent behaviors can be determined by the different quantum phenomena, which stem from the variation in interatomic spacing and respective crystal lattices.²⁹ Therefore, it is known that the materials with semiconducting electronic conduction mechanisms (semiconductors, semiconducting CNT, reduced graphene oxide (rGO), conductive polymers, etc.) show NTC behavior and the materials with metallic electronic conduction mechanisms (such as metals, metallic CNT, pure graphene, etc.) show PTC behavior.²⁹ Because the most of the conductive or semiconductive materials with NTC or PTC behavior have rigid characteristics, pyroresistive e-skins based on flexible polymer composite between elastomeric polymer and conductive or semiconductive materials have been studied for the wearable applications.

Pyroelectricity: In addition to mechanical-energy harvesting devices, such as piezoelectric and triboelectric e-skins, ambient-heat variation can be converted into electrical energy by pyroelectric and thermoelectric effects. The pyroelectric effect harvests electrical potential from the thermal energy by spontaneous polarization in certain anisotropic solids as a result of temperature fluctuation.¹ Specifically, when the pyroelectric e-skins are heated, the electric dipole around equilibrium axis of certain materials will randomly oscillate due to larger thermal activity, causing electric dipoles to oscillate with a larger range and decrease in spontaneous polarization. In contrast, when they are cooled, the electric dipoles will oscillate with a smaller range due to the lower thermal activity, resulting in increase in spontaneous polarization.³⁰ For the pyroelectric e-skins, various ferroelectric materials such as P(VDF-TrFE),³¹ ZnO,³² PZT,³³ and BaTiO₃³⁴ have been introduced, but relatively low power density restricts the application for self-powered e-skins. Because pyroelectricity is based on temperature fluctuations, it is mostly utilized in heat-sensing applications such as infra-red imaging, motion detection by body heat, and fire alarms.

Thermoelectricity: The thermoelectric effect induces the diffusion of charge carriers under the thermal gradient in the materials, where the thermoelectricity depends on the Seebeck effect, which can be expressed by $V_{Therm} = S_T \times \Delta T$; V_{Therm} , S_T , and ΔT are the generated voltage, Seebeck coefficient, and temperature gradient in the materials.³⁰ Different with pyroelectricity, if there is temperature gradient in the materials, the thermoelectricity continuously generated in the device. When the thermoelectric e-skins are integrated on the human body, they can generate electrical potential by the temperature gradient between environment and human body, demonstrating their great potential for wearable applications. For thermoelectric e-skins, various materials including conductive polymers such as polyaniline (PANI),³⁵ polypyrrole,³⁶ and poly(3,4-ethylenedioxythiophene):poly(styrenesulfonate) (PEDOT:PSS),³⁷ inorganic materials (such as Bi₂Te₃, Sb₂Te₃, and Bi_{0.5}Sb_{1.5}Te₃),³⁸ and even ionic polymer solution³⁹ have been introduced.

1.2.3 Other working mechanisms

In addition to the e-skins based on electrical transduction modes, colorimetric e-skins were recently have attracted intense research interests, owing to their human-readable output signal and thus instantaneous and intuitive recognition of external stimuli by the user. With the increasing demands of user-interactive devices, a great deal of efforts has been devoted to demonstrate visualized e-skins by integrating with active display components such as polymeric light-emitting devices, organic light-emitting diodes (OLEDs), and various sensing elements such as pressure/strain sensors,⁴⁰ photodetectors,⁴¹ piezo-phototronic devices,⁴² and stretchable conductors.⁴³ Alternatively, electrochromic materials (such as metal oxides, poly(3-hexylthiophene-2,5-diyl) (P3HT) and conductive polymers)⁴⁴ and thermochromic materials (such as liquid crystals, inorganic semiconductor oxides, and organic dyes)⁴⁵ with color-switching properties in response to electrical and thermal inputs exhibit great potential for color-emitting components of visualized e-skins. In addition, luminescence materials, which exhibit light emission in response to mechanical stress,⁴⁶ photo-absorption,⁴⁷ and electrical current,⁴⁸ can also be used in visualized e-skins. For example electroluminescence e-skins that exhibit simultaneous optical and capacitive tactile-sensing capabilities have intensively researched by integrating elastomeric composites (between ZnS and elastomeric polymers) with top and bottom electrodes.⁴⁸ When a tensile strain is applied to the e-skin, the reduced thickness of ZnS-doped dielectric layer induces increased capacitance between the electrodes, resulting in increased electroluminescence intensity.

Visualized e-skins based on mechanochromic polymers or photonic micro/nanostructures provide the advantages of distinct color transition, high compatibility with elastomers, and no requirement of external power.⁴⁹⁻⁵⁰ Furthermore, these devices can maintain a visual appearance during continuous application of mechanical stress or strain, in contrast to the self-powered piezoelectric and triboelectric devices showing dynamic response without persistent visualization. Mechanochromic polymers change their optical properties such as absorption and reflection of light or fluorescence in response to mechanical strain/stress, which have been applied in diverse fields of strain⁵¹ and fracture/damage sensors.⁵² Typically, mechanochromic polymers are synthesized by covalently incorporating mechanophores into the polymer matrix for the effective stress transfer from the macroscopic to the molecular level. The mechanochromic polymers exhibit macroscopic color changes due to the force-induced mechanochemical activation of the mechanophore molecules, such as spiropyran, diarylbibenzofuranone, and rhodamine.⁵³⁻⁵⁵

1.3 Bio-inspired electronic skins

1.3.1 Limitation of conventional electronic skins

In the early stage, the structure of e-skins was mainly based on the planar design (Figure 1.4). The typical example of the conventional e-skins based on planar design is PSR-based e-skins, composed of elastomeric polymer matrix and conductive fillers. Because they can be fabricated by only two components of PSR and electrode, various reseaches about PSR-based e-skins were studied. In addition, the elastomeric properties of PSR provides high flexibility or stretchability to the e-skins, demonstrating compatibility with curvilinear suraces, such as human and robot body. To enhance sensing performances, the PSRs can be integrated with field-effect transistor (FET) for a pressure-sensitive e-skin arrays, which have advantage of signal amplification and mapping of the pressure distribution.^{40,56-58} However, conventional PSR-based e-skins still have limitations of poor sensitivity, single sensing traget, slow response time, and large hysteresis in response to mechanical stimuli, addressing a need of new strategy to fabricate novel e-skins with high sensing performacnes and multifunctionality.

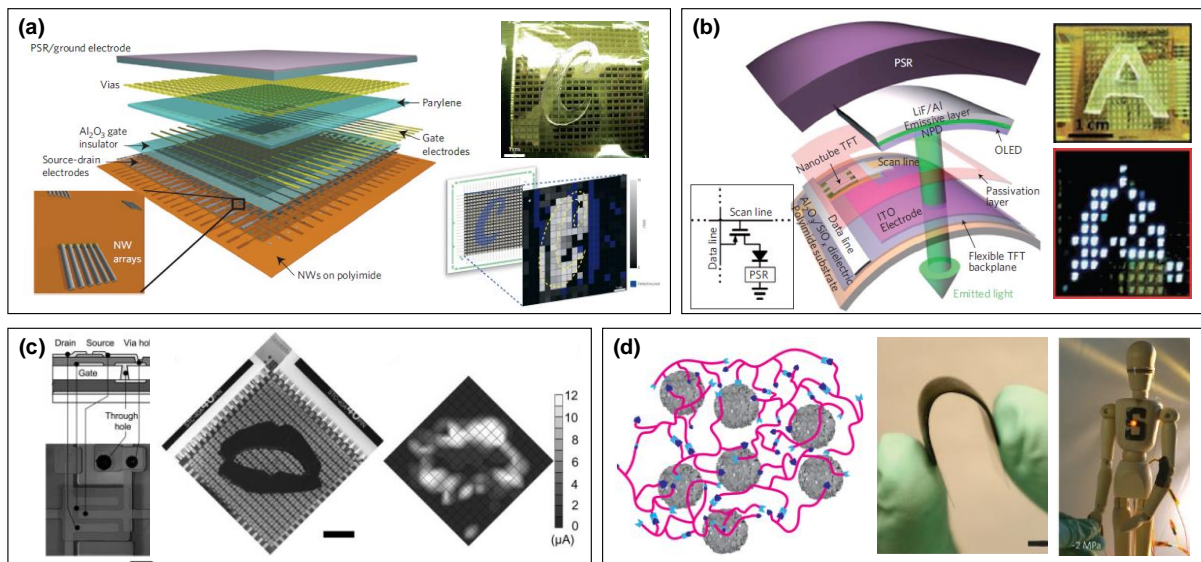


Figure 1.4. Conventional e-skins with planar sensor design. (a-c) E-skins combined with PSR and field-effect transistors. (K. Takei et al. *Nat. Mater.* **2010**, 9, 821, C. Wang et al. *Nat. Mater.* **2013**, 12, 899, T. Someya et al. *Proc. Natl. Acad. Sci. U.S.A.* **2014**, 111, 12998). (d) Piezoresistive e-skin based on planar structure. (B. C.-K. Tee et al. *Nat. Nanotech.* **2012**, 7, 825).

Nature can offer alternative strategies for e-skins to improve the sensing performances and multifunctionality (Figure 1.5). In particular, human skin is an organ elaborately evolved for exquisite sensory functions. With special structures including epidermal–dermal ridge structures, various mechanoreceptors, and afferent nerves, human skin has highly sensitive and multifunctional sensing properties, allowing perception of and discrimination between multidirectional tactile stimuli, such as pressure, bending, stretching, and textures, as well as self-healing ability.⁵⁹ These attributes of human skin have inspired many research groups to develop wearable e-skins with high sensitivity, multidirectional forces, and semipermanent durability through self-healing ability.⁶⁰⁻⁶² In addition to human skin, unique architectures found in certain other living organisms provide them special functions such as visual-stimuli expression, reversible dry/wet adhesion, ultrasensitivity to vibration, and environmental adaptation.⁶³⁻⁶⁶ The technological advancements through biomimicry of those architectures have led to novel e-skin systems with exceptional features such as user-interactive and skin-attachable functions, as well as advanced sensory functions.



Figure 1.5. Bioinspired e-skin systems for wearable devices. Human skin: Dermal-epidermal structure (K. J. Busam, *Dermatopathology E-Book: A Volume in the Series: Foundations in Diagnostic Pathology* **2014**, 1, M. Ha et al. *ACS Nano* **2018**, *12*, 3964) Mechanoreceptor. (M. L. Jin et al. *Adv. Mater.* **2017**, *29*, 1605973) Fingerprint. (J. Park et al. *Sci. Adv.* **2015**, *1*, e1500661). Nerve. (C. Wan et al. *Adv. Mater.* **2018**, *30*, e1801291). Self-healing. (J. Kang et al. *Adv. Mater.* **2018**, *30*, e1706846). **Smart biological skin:** Visualization. (C. Wang et al. *Nat. Mater.* **2013**, *12*, 899). Adhesion. (Y. Park et al. *Adv. Mater.* **2017**, *29*, 1606453). Crack. (D. Kang et al. *Nature* **2014**, *516*, 222). Environmental adaption. (S.A. Morin et al. *Science* **2012**, *337*, 828).

1.3.2 Human skin-inspired electronic skin

Human skin, which covers surfaces of the entire body, provides various functions as a protective and sensitive interface between the outside world and the body's integumentary system. As the outermost layer of skin, the epidermis provides toughness and hardness to skin. The dermis with lower modulus than the epidermis contains mechanoreceptors as well as blood vessels, sweat glands, and free-nerve endings, giving us the tactile sensation of touch.⁶⁷⁻⁶⁸ Various types of mechanoreceptors have their own tactile-sensing mechanisms in response to specific stimuli. For example, while Meissner and Pacinian corpuscles are rapidly adapting receptors, which perceive the onset and offset of applied stimuli, Merkel cells and Ruffini corpuscles are slowly adapting receptors, which experience continuous activation to applied stimuli.⁶⁸⁻⁷⁰ The specific roles and working range of mechanoreceptors are summarized in Table 1.1.^{68,71} When tactile stimuli are applied to skin, relevant mechanoreceptors encode them as an ion-transport-induced action potential at an elevated frequency, where the stronger stimuli induce the higher frequency.⁷²⁻⁷⁴ Through the nerve fibers, the generated action potential is relayed to the synapses, which process the action potentials from multiple presynaptic neurons to multilevel features of tactile perception in the brain (Figure 1.6).

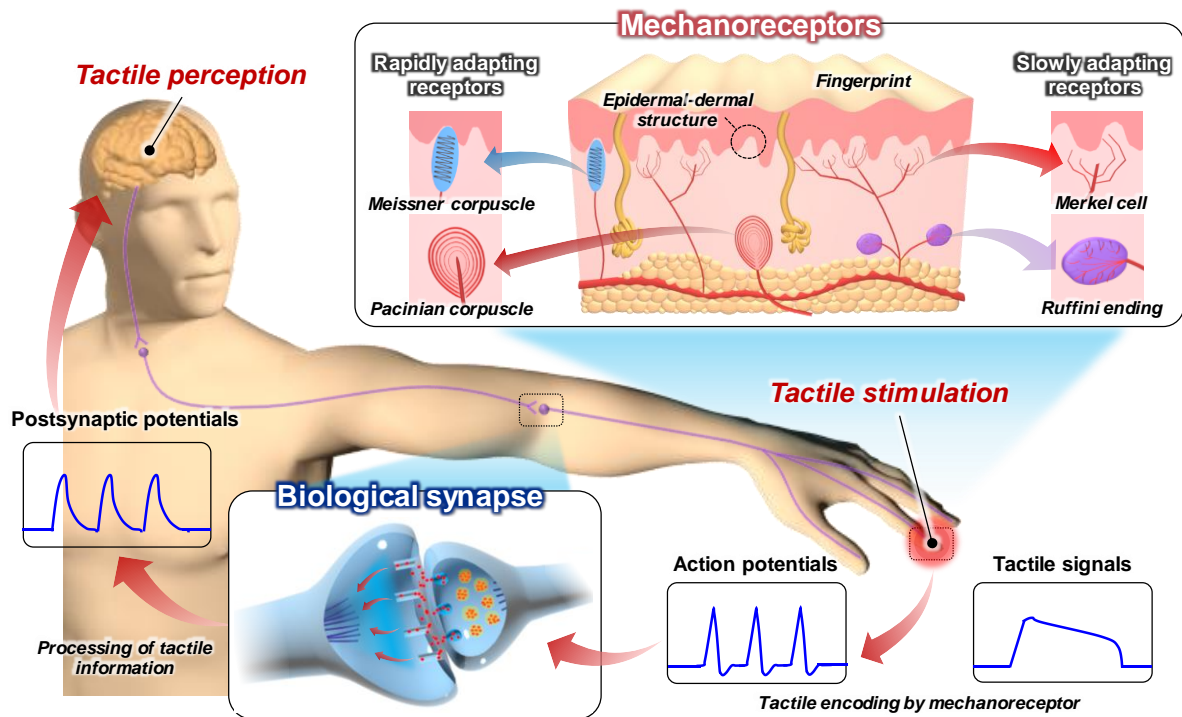


Figure 1.6. Human tactile perception system. The mechanoreceptors in human skin encode the applied tactile stimuli into action potentials, which are sent along the chain of afferent axons to synapse. The action potentials from multiple presynaptic neurons are processed in the biological synapses to obtain multilevel features of tactile perception.

Table 1.1. Summary of specific roles and location of various mechanoreceptors in human skin.

Mechanoreceptors	Class	Location	Receptive Field (mm²)	Frequency range (Hz)	Perceptible stimulus
Meissner corpuscle	Rapidly adapting I	Dermal papillae	1-100	10-60	Dynamic deformation
Pacinian corpuscle	Rapidly adapting II	Deeper dermis	10-1000	50-1000	Vibration
Merkel disk	Slowly adapting I	Basal layer of epidermis	70	0-30	Compressive stress
Ruffini ending	Slowly adapting II	Dermis	49	0-15	Skin stretch direction

Human skin has specialized structures improving the efficiency of tactile sensation by embedded mechanoreceptors.⁷⁵ The epidermis experiences skin deformation and applied stimuli that can be effectively concentrated to the micro-ridge structures at the epidermal–dermal junction. Inspired by the epidermal–dermal microstructures, several types of e-skins were demonstrated using interlocked nano/microstructures, including micropyramid, microdome, micropillar.^{8,15,76-77} Owing to the structural advantages, the interlocked e-skins can accurately differentiate sensing signals from pressure, shear, strain, and torsion stimuli (Figure 1.7a).⁷⁶ Similarly, microstructured elastomers molded from silk-based textiles, mimosa leaves, and sandpaper can be used as highly sensitive piezoresistive pressure sensors after coating with conductive materials and interlocking those two layers. In addition to micro-ridge structures at the epidermal–dermal junction, a gradient of elastic modulus between the epidermis (140–600 kPa) and dermis (2–80 kPa), which enables effective stress concentration and transmission to underlying mechanoreceptors, was modulated by triboelectric e-skins based on interlocked geometry with gradient stiffness (Figure 1.7b).^{28,78}

As other features in human skin, various types of rapidly and slowly adapting mechanoreceptors are distributed throughout the body and function as selective encoding devices. Inspired by various perceptual functions of mechanoreceptors, multifunctional ferroelectric e-skins with both low- and high-frequency signal-detection capabilities have been developed (Figure 1.7c).²² The ferroelectric and conductive properties of e-skins enable both of the piezoelectric dynamic pressure sensing, piezoresistive static pressure sensing, and pyroresistive temperature sensing. Moreover, similar approaches were studied based on the hierarchical ZnO nanowire arrays, integrated sensor arrays, thermosensation-induced sensor, and ionic mechanotransducer to mimic multifunctional sensing properties of mechanoreceptors (Figure 1.7d).^{24,61,79-80}

Epidermal fingerprint patterns enable grasping and delicate manipulation of objects by enhancing friction force and adhesion between hand and objects.⁸¹⁻⁸² In addition, increased friction force reinforces the texture-induced subcutaneous vibrations during tactile exploration, which are perceived and discriminated as fine textures by the rapidly adapting mechanoreceptors.⁸³ To investigate the exact role of fingerprints in texture perception, microelectromechanical system (MEMS)-based texture sensors covered with artificial-fingerprint patterns, which have a geometry similar to human fingerprints, was developed (Figure 1.7e). Furthermore, the interlocked e-skins with high sensitivity can be integrated with artificial fingerprint pattern for highly sensitive texture sensors (Figure 1.7f).^{22,84-85} Recently, the shape-memory polymer-based strain gauge with whisker arrays was successfully visualized surface textures in nanometer-scale (Figure 1.7f).⁸⁶

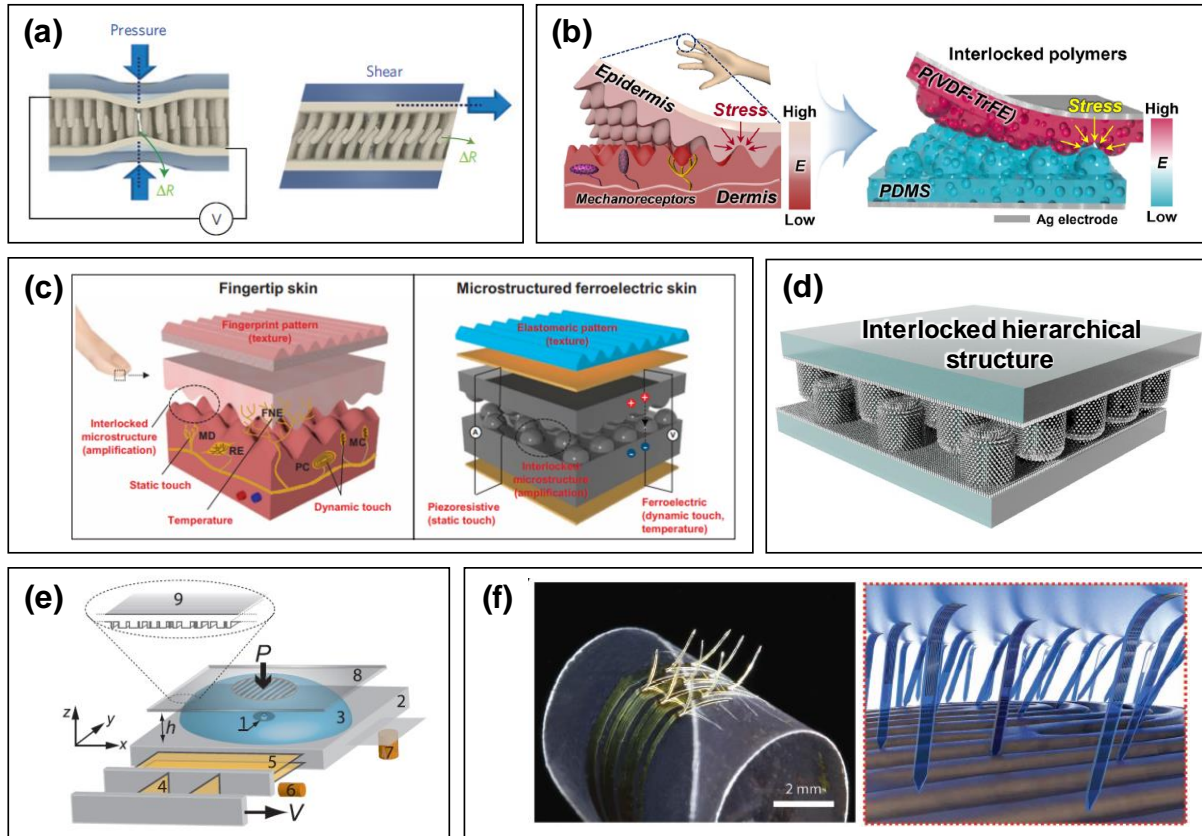


Figure 1.7. Human skin-inspired e-skins. (a) Detection of multiple stimuli with e-skins composed of interlocking nanofibers (C. Pang et al. *Nat. Mater.* **2012**, *11*, 795). (b) Hierarchical and interlocked e-skins with gradient stiffness (M. Ha et al. *ACS Nano* **2018**, *12*, 3964). (c) Skin-inspired multifunctional e-skins based on ferroelectric and conductive composite with interlocked geometry (J. Park et al. *Sci. Adv.* **2015**, *1*, e1500661). (d) Multifunctional e-skins with interlocked and hierarchical geometry (M. Ha et al. *Adv. Funct. Mater.* **2015**, *25*, 2841). (e) Fingerprint-inspired texture sensors with MEMS microforce sensors (J. Scheibert et al. *Science* **2009**, *323*, 1503). (f) 3D, reconfigurable and multimodal e-whiskers for high-fidelity surface mapping (J. T. Reeder et al. *Adv. Mater.* **2018**, *30*, 1706733).

1.3.3 Biological skin-inspired electronic skin

In addition to human skin, the unique structures and functionalities of natural creatures have provided us a great inspiration for new types of e-skin systems. Biological species, such as cephalopods,⁸⁷ chameleons,⁸⁸ and turkeys⁸⁹ possess unique abilities to change the color or fluorescence of their skin via various micro/nanostructure, pigment cell, and muscle-controlled surface structures in response to environmental stimuli for camouflage, display, and communication. Inspired by the responsive color change in biological skins, new types of e-skins that display tactile information by visual outputs such as color, luminescence, and transparency have been recently demonstrated for application in soft robotics,⁹⁰ biometric security services,⁹¹ smart healthcare,⁴¹ and 3D touch screens (Figure 1.8a).⁹² E-skins capable of visualizing intensity, direction and location of physical touches, and even surrounding environmental conditions (such as vibration, roughness, and temperature), provide a human-readable output signal and thus instantaneous and intuitive recognition of external stimuli by the user.⁴⁰

The development of skin-attachable bioelectronic devices with conformal and biocompatible adhesion to skin surfaces is essential for achieving accurate and reliable biological/physical information. In nature, various biosystems, including gecko,⁹³ beetles,⁹⁴ endoparasites,⁹⁵ and cephalopods,⁶⁴ exhibit exceptional wet or dry adhesion functionalities induced by their unique architectures, providing inspiration for development of skin-attachable electronic systems. Mimicking hierarchical nano/microstructures in gecko's foot, dry adhesion pad based on micropillar PDMS arrays, capacitive pressure sensors with microhair interfacial adhesives, and strain sensor with PDMS microfiber-based adhesion pads were fabricated for exact monitoring of electrocardiogram (ECG) and radial artery pulse pressure.⁹⁶⁻⁹⁸ In addition, the unique geometry of the suckers on the skin of cephalopods provides another strategy for the design of biomimetic dry adhesives (Figure 1.8b).^{64,99}

The mechanical sensitivity of e-skins can be extremely enhanced by mimicking sensory organs of arthropods and other insects. Arthropods, including the spider and scorpion, possess crack-shaped special sensory organs (slit organ) that enable ultrasensitive detection of vibrations in their surroundings. Inspired by the mechanosensory systems in spiders, various types of strain-sensitive e-skins with nanoscale crack junctions were developed (Figure 1.8c).⁶⁶ The high-density nanoscale cracks in the thin metal layer, similar to the slit organs in spider legs, induce a sensitive change in resistance in response to the strain, leading to an ultrahigh gauge factor (~2000). Despite the ultrahigh sensitivity, an issue with the nanoscale crack sensors is their narrow sensing ranges (<2%). To address this issue, various researches have been studied by the introduction of stretchable substrates (PDMS, Eco-Flex, or elastic tape) and 2D materials like graphene.¹⁰⁰⁻¹⁰²

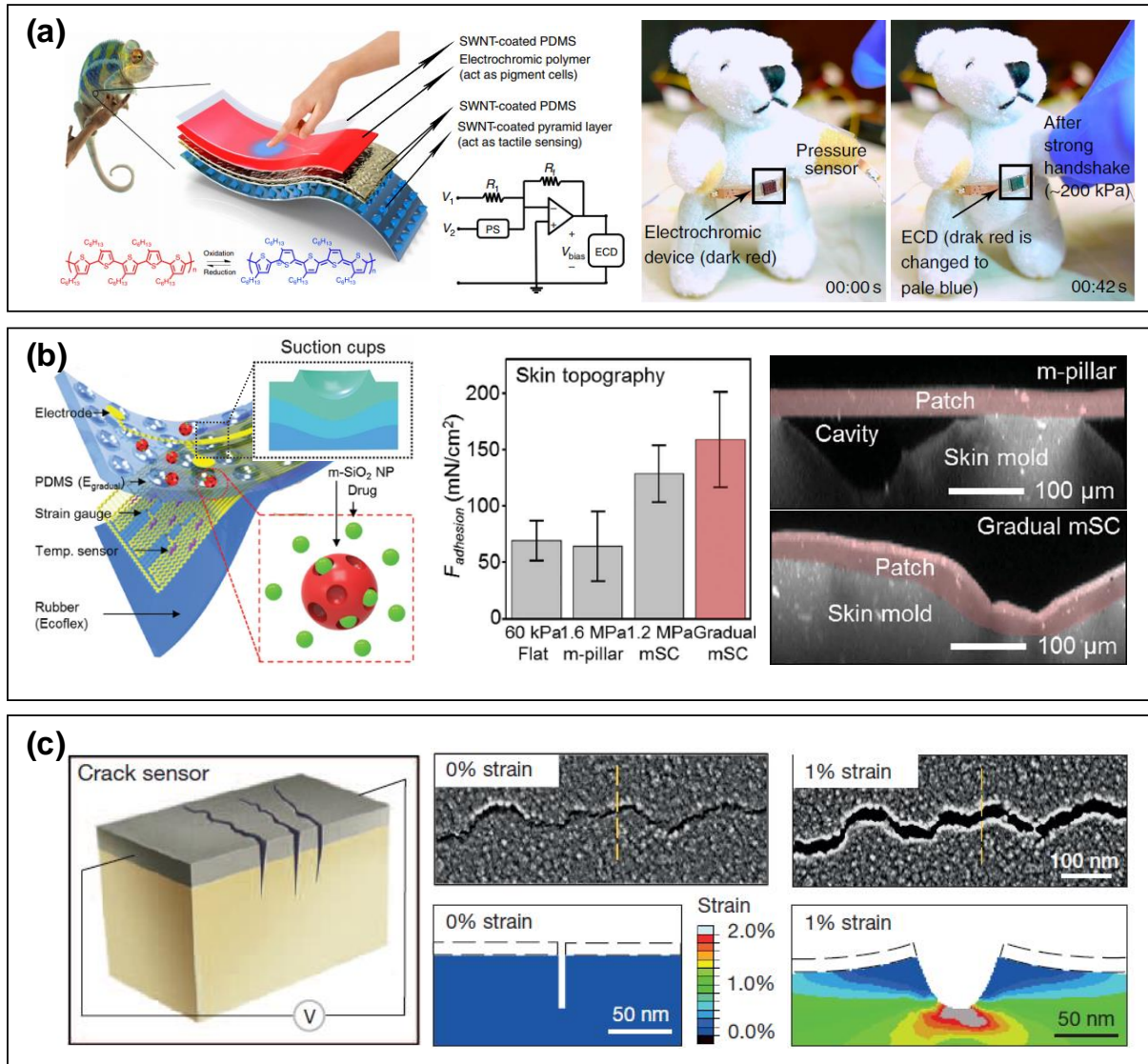


Figure 1.8. Biological skin-inspired e-skins. (a) Visualized e-skin combined with electrochromic materials and piezoresistive sensor (H.-H Chou et al. *Nat. Commun.* **2015**, *6*, 8011). (b) Smart medical patch based on octopus sucker inspired dry adhesive pad (M. K. Choi et al. *Adv. Healthcare Mater.* **2016**, *5*, 80). (c) Spider-inspired strain sensors based on nanoscale crack junction (D. Kang et al. *Nature* **2014**, *516*, 222).

1.4 Applications

The human and biological skin-inspired e-skins have high perceptual functions comparable with or even surpass those of human skin. In addition, introduction of special bioinspired systems enables additional functionalities such as self-healing, visualizing, adhesive, and environment-adaptive functions. Moreover, intrinsically flexible or stretchable e-skins can overcome the critical challenges in traditional rigid sensor devices that could not conformably contact curved surfaces such as the human body. Benefiting from their superior performances, the bioinspired e-skins are considered to be promising candidates for wearable-device applications.

1.4.1 Wearable motion sensors

When e-skins are attached to a person's joints or muscles, they can monitor body motions by electrical or visual signals. Because of their broad range of applications such as sport training, posture correction, and rehabilitation, wearable motion sensors attract intense research interest. As the most active parts in our bodies, movements of hands and limbs create most of our daily activity and are sometimes used for sign language to transfer information. Monitoring different patterns in movements of hands and limbs requires the perception of and differentiation among types and direction of forces. For the wearable motions sensors, various types of e-skins were demonstrated, including interlocked skins, self-healable ionic skins, etc.^{9,103-104} Flexible and piezoresistive e-skins with interlocked geometry can be used as wearable wrist-motion sensors (Figure 1.9a).¹⁰³ Because interlocked microdome structures show different deformation patterns in response to applied forces, the interlocked e-skins can differentiate multidirectional forces, such as normal force, shear force, lateral stretch, and bending. This unique geometric advantage enables successful discrimination of various movements of the human wrist. When colorimetric skins are combined with e-skins, the integrated system enables both instantaneous perception by color change and accurate perception through analysis of electrical signals. Recently, Ha and co-workers demonstrated crack-based resistive-strain sensors integrated with electrochromic devices for dual-mode wearable motion sensors (Figure 1.9b).¹⁰⁵ Because of the prestrain-induced cracks in conductive layers, the strain sensor can sensitively detect tensile stress by change in resistance, which converts to voltage bias for the operation of electrochromic devices, demonstrating dual-mode sensing capabilities for body motion with interactive color display.

Wearable motion sensors, which can convert body motion into electrical signals, allow to control the machines by body motion, realizing the human-machine interfaces technology. Various types of wearable e-skins have been applied to operate robotic arms or hands after integration with a filter module, microcontroller, power supply, and wireless modules.¹⁰⁶⁻¹⁰⁷ Recently, a wireless-controlled interactive electronic system was demonstrated by five crack-inspired wearable strain sensors attached to a glove (Figure 1.9c).¹¹ When the five strain sensors mounted on joints of five fingers perceive a

bending motion, the detected electrical signals from each finger are converted into operating voltage to control the robot hand via the filter module, wireless transmitter, and microcontroller circuit. As a result, the robot hand can replicate various actions of a human hand, demonstrating the feasibility of interactive human–robot systems.

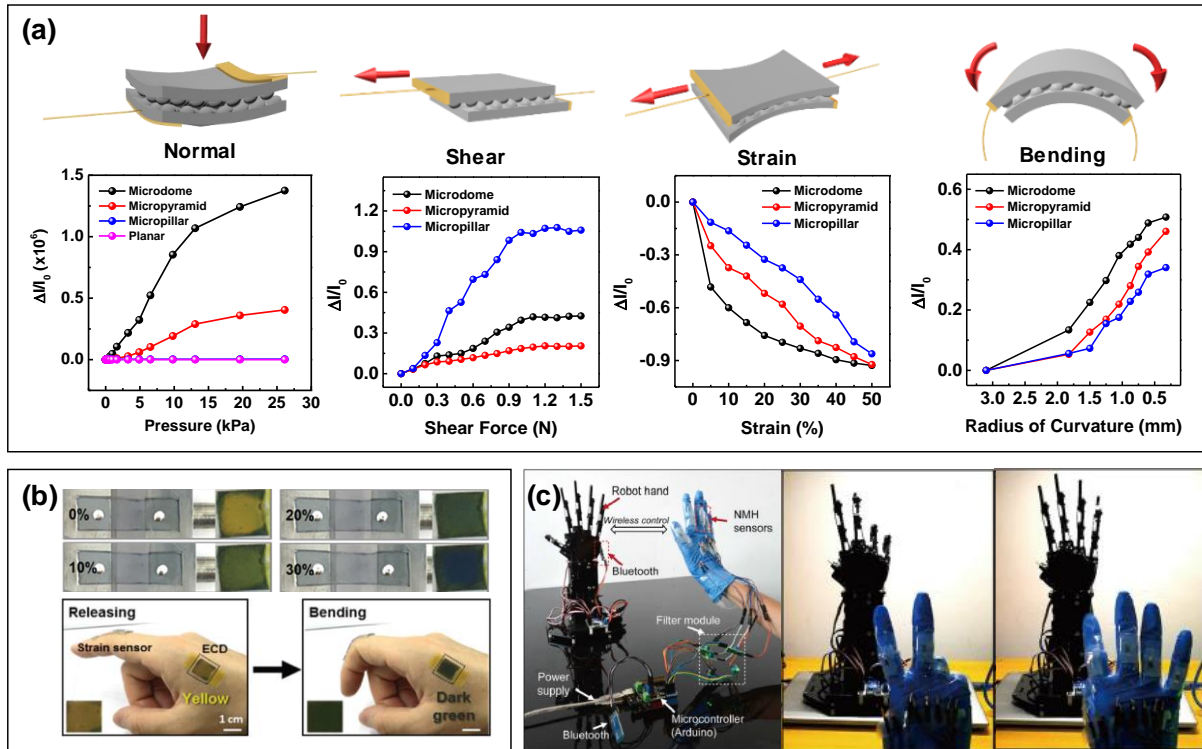


Figure 1.9. Applications for wearable motion sensor. (a) Differentiation of various motions using e-skins with interlocked microdome structure (J. Park et al. *NPG Asia Mater.* **2018**, *10*, 163). (b) Monitoring of finger movement using dual-mode wearable motion sensors (H. Park et al. *Nanoscale* **2017**, *9*, 7631). (c) Wireless-controlled interactive system with crack-inspired e-skins for HMI technology (S. Han et al. *NPJ Flexible Electron.* **2018**, *2*, 16.).

1.4.2. Healthcare devices

With increasing demand for customized home care and individual well-being, remote and personalized health monitoring is currently of great interest for the timely and efficient management of health events and prevention of disease. Because the subtle change in physiological parameters, including pulse wave, blood pressure, and body temperature, may be early signs of abnormal body conditions, it is required to develop the physiological sensors with accurate and reliable sensing capabilities. Wearable e-skins can serve as a noninvasive tool providing physiological information about the users. In particular, conformal contact between sensors and human skin enables exact monitoring of biosignals.

When e-skins monitor wrist pulse, three peaks can be distinguished in pulse waveform—the incident wave (P_1), tidal wave (P_2), and diastolic wave (P_3).¹⁰⁸ These characteristic peaks provide various information about vascular health, such as arterial stiffness. For example, a patient with stiff blood vessels has high blood pressure, causing increased pulse-wave velocity and the early return of reflected waves. Arterial stiffness can be evaluated by the radial augmentation index ($AI_r = P_2/P_1$), diastolic augmentation index ($DAI_r = P_3/P_1$), and digital volume pulse time (ΔT_{DVP} , the time interval between P_1 and P_2). Recently, micropattern-based adhesive skins were developed for the highly sensitive monitoring of pulse pressure (Figure 1.10a).¹⁰⁹ By the introduction of microline patterns with sticky PDMS layers, the graphene-based resistive sensors can conformably adhere to rough skin surfaces and exactly detect a clear pulse waveform of the radial artery. If e-skins can simultaneously perceive both pressure and temperature, evaluation of vascular health becomes more accurate as temperature can affect arterial stiffness (Figure 1.10b).²² Benefiting from multifunctional-sensing capabilities of e-skins to monitor static pressure and temperature, the pulse waveform includes information on both pulse pressure and body temperature, where the low body temperature causes cold vasoconstriction, resulting in increased arterial stiffness. Interlocked e-skins successfully monitored such trends from decrease in AI_r and DAI_r , and increase in ΔT_{DVP} with increasing body temperature. Effects of age on artery stiffness were also studied using graphene-based wearable sensors.¹¹⁰ The sensor outputs show the increase of stiffness with age.

An ECG, which reveals electrical signals from the heart, provides informative parameters about the heart's beating process, which is useful for predicting serious heart attacks.^[9] Inspired by the gecko adhesive, the stretchable and conductive dry adhesive (CDA) was developed for the ECG sensor (Figure 1.10c).^[153] The high conformality of CDA pad to skin allows real-time measurement of ECG signals during extreme human motions, including wrist curl, squat, and writing, facilitating efficient management of vascular health in daily life. Recently the ECG sensors were integrated with a wireless transmitter, filter module, and display unit, the patient, a caretaker or other therapists for easy

monitoring of the vascular health of the user.

Precise and real-time monitoring of body temperature is a critical procedure for accurate diagnosis of human health, indicating abnormal states of health from fever, insomnia, fatigue, infection, or organ dysfunction.¹¹¹⁻¹¹² For accurate diagnosis of health conditions, temperature sensors must be able to detect minute changes that may be as small as 0.1 °C.¹¹¹ In addition, the temperature sensors should be flexible and remain conformably attached on curvilinear surfaces of human body, and they must stably operate under mechanical stimuli. Current wearable devices mainly focus on the metal-based temperature sensors, because metal shows linear response in resistance to temperature differences by PTC effect (Figure 1.10d).⁷⁸ However, their low temperature sensitivity (0.4 Ω/°C) and rigid characteristics prevent them from applying wearable e-skins.¹¹³ Recently, flexible temperature-sensitive e-skins based on thermoresponsive polymer composite have been developed (Figure 1.10e).^{22,114-115} The temperature-sensing performance of thermoresponsive polymer composite between polymer matrix and conductive filler depends on the conductive fillers, where materials with semiconducting electronic conduction mechanisms show NTC behavior and materials with metallic electronic conduction mechanisms show PTC behavior.²⁹ Moreover, designing polymer matrix as temperature-responsive polymer, which shows volumetric change in response to temperature change, can significantly enhance the temperature sensitivity of e-skins.¹¹⁵

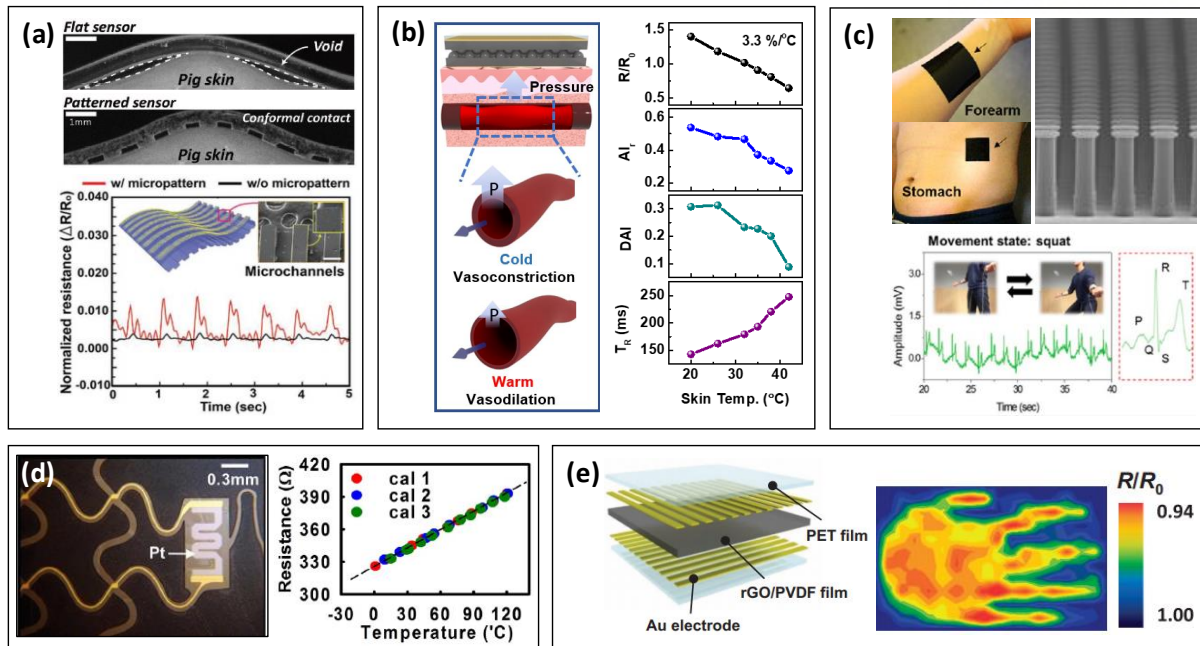


Figure 1.10. Applications for healthcare device. (a) Microtopography-guided conductive e-skins for skin conformal sensors (Y. Park et al. *Adv. Mater.* **2017**, *29*, 1606453). (b) Temperature-dependent evaluation of vascular health based on pulse signals from multifunctional interlocked e-skins (J. Park et al. *Sci. Adv.* **2015**, *1*, e1500661). (c) Gecko-inspired conductive dry adhesives for reliable monitoring of ECG under extreme human motions T. Kim et al. *ACS Nano* **2016**, *10*, 4770). (d) Metal-based temperature sensor (D.-H. Kim et al. *Science* **2011**, *333*, 838). (e) Pyroresistive flexible temperature sensor for wearable e-skins (J. Park et al. *Sci. Adv.* **2015**, *1*, e1500661).

1.4.3. Prosthesis

Human hands can carry out sophisticated manipulation tasks including grasping and locating objects, typing, feeding, and dressing. However, a sensory loss from skin damage or amputation causes loss of sensory functions as well as motor functions of the human body. Robotic prosthetics can restore both sensory and motor functions, giving the user the ability to perceive tactile stimuli and control the prosthesis based on perceived subconscious information. Although various types of prostheses have been developed, most prosthetic limbs focus on the motor element and lack the sensory functions, restricting their use by amputees.¹¹⁶⁻¹¹⁸ Mounting e-skin sensor arrays on the surface of a prosthesis can enable the user to experience the feeling of touch.

Prosthetic hands with sensory functions were developed by integrating robotic hands with wearable pressure, strain, and temperature sensors (Figure 1.11a).¹¹⁹ Stretchable semiconductor composite composed of P3HT nanofibril and PDMS rubber is used as active-sensing materials for pressure and strain sensing via deformation-induced change in resistance. In addition, the intrinsic NTC properties of semiconducting material enable the detection of temperature, as resistance decreases with temperature. Strain-sensor arrays were attached at finger joints to monitor finger movement. To avoid coupled signals from finger movements, pressure and temperature sensor arrays were mounted on the phalanges of the robotic hands. When the smart robotic hands performed sign-language gestures, the integrated sensor arrays enabled gesture interpretation. For the dual-mode smart prosthesis, a stretchable triboelectric–photonic smart skin was developed (Figure 1.11b).¹²⁰ The elastomeric rubber with Ag nanowire electrodes can generate triboelectric voltages in response to applied pressure. In addition, aggregation-induced emission (AIE) compound mixed in the elastomeric rubber was used for the photonic strain sensors, where the photoluminescence intensity increases with strain because of the strain-dependent grating of the crack layer. The smart robotic hands integrated with sensor arrays could perceive various hand motions by the intensity of green light from AIE compound and the applied pressure by the triboelectric outputs.

As human skin can differentiate multidirectional forces such as normal and shear force, multidirectional-sensing capabilities are required for the prosthesis to have human-like somatosensory functions. For this purpose, human skin-inspired multidirectional e-skins based on asymmetric interlocked structures can be integrated on the robotic hands (Figure 1.11c).⁸ The e-skins with highly sensitive multidirectional sensing capabilities allow the robotic hands to perform tactile feedback process, enabling a human-like prosthesis. To realize the ability to process tactile feedback based on perceived information, a sensory-feedback and pain-reflex-feedback control system was developed by integration of multilayered e-dermis sensors with transcutaneous electrical nerve stimulation (TENS) (Figure 1.11d).¹²¹ The piezoresistive e-dermis sensors can perceive and differentiate tactile stimuli from

innocuous pressure and noxious pain, which were converted into the spiky input signals through TENS to quantify the perceived tactile sensation. The sensory stimulation, for which the pulse width and stimulation frequency were varied by perceived tactile stimuli, activated the nerves in the residual limb of an upper-limb amputee and successfully elicited either innocuous or painful sensations in the phantom hand. The ability to sense touch enables sophisticated object manipulation, and the ability to sense pain enhances the sense of self-preservation.

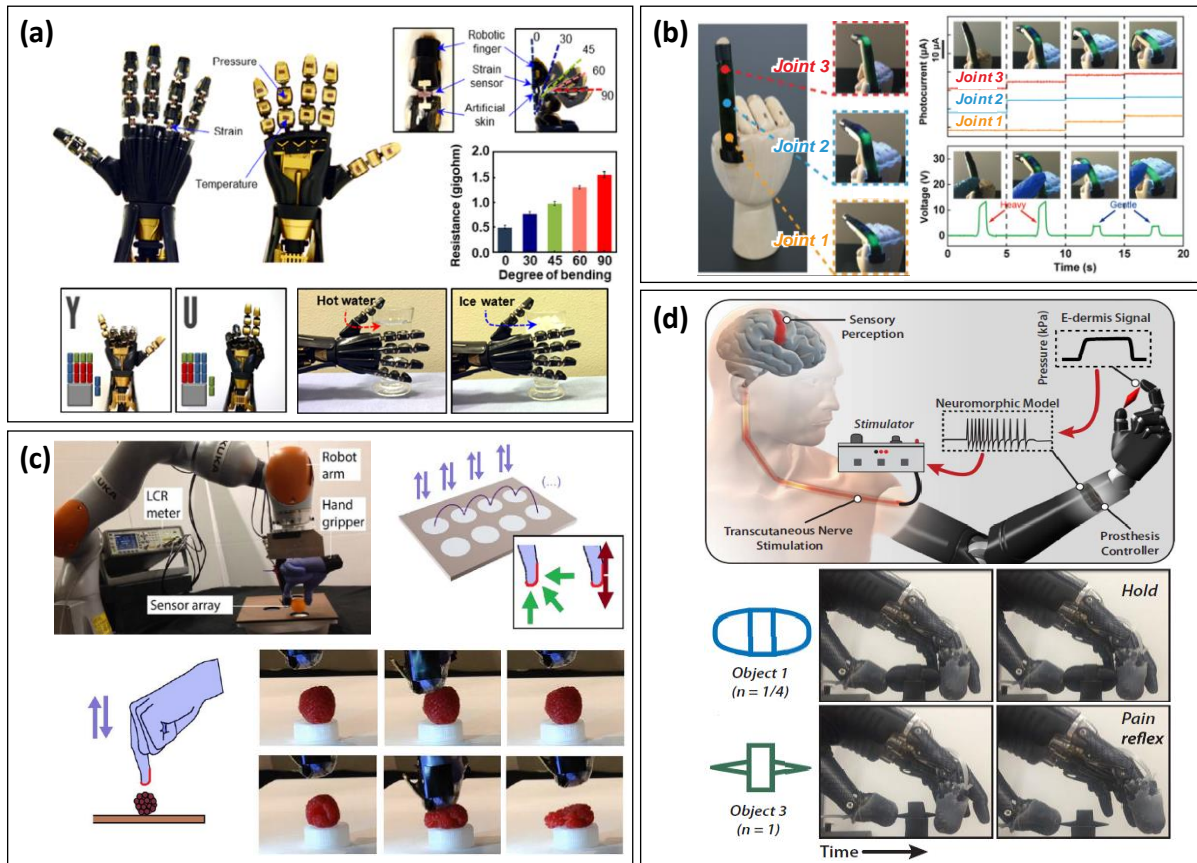


Figure 1.11. E-skins for prosthesis. (a) Robotic hands with pressure, strain, and pressure sensor arrays for perception of hand gestures (H.-J. Kim et al. *Sci. Adv.* **2017**, *3*, e1701114). (b) Dual-mode smart prosthesis based on triboelectric-photonic skins (T. Bu et al. *Adv. Mater.* **2018**, *30*, 1800066). (c) Human skin-like prosthetic hands with multidirectional e-skins (C. M. Boutry et al. *Sci. Robot.* **2018**, *3*, eaau6914). (d) Prosthetics for sensory feedback and a pain reflex feedback control system (L. E. Osborn et al. *Sci. Robot.* **2018**, *3*, eaat3818).

....

1.5 Challenges of current electronic skins

In the introduction, we provided recent progress of wearable e-skins, including basic working mechanisms, bioinspired strategies for novel e-skins, and potential applications. Although various types of wearable e-skins based on novel materials, fabrication techniques, strategies, and sensing mechanisms have been introduced, there are still challenges in their practical application. First, e-skins for smart robots and prostheses should possess the ability to perceive and differentiate multidirectional forces such as normal, tensile, shear, and bending forces without crosstalk.⁸ Although several studies based on microstructured e-skins have demonstrated, they just integrate multiple sensors for multifunctional e-skins^{61,78} or demonstrate multidirectional sensing performances without clear differences in sensor signals.⁷⁶

Second, the medical diagnosis using wearable e-skins should be based on the precise and expeditious analysis of monitored signals from health events, which could be achieved by ultrasensitive and skin-attachable sensor design.⁹ Therefore, it is required to improve the sensitivity of the e-skins in response to mechanical and thermal stimuli. Recent achievement in bioinspired e-skins could meet required sensitivity in a certain degree,^{15,22,77} however there is still unsatisfied issue, which is trade-off between sensitivity and sensing range; highly sensitive e-skins have narrow sensing range and e-skins with broad sensing range show low sensitivity.¹²² In addition, if the e-skins maintain their high sensitivity over broad sensing range, they can possess linear response to target stimuli.¹²³ The realization of e-skins with high sensitivity and linear response over a broad sensing range enables device miniaturization and low power consumption, because they do not require additional signal processing for linear output, high-gain amplifiers, and high-precision analog-to-digital converters.

Third, instantaneous recognition of applied stimuli can be achieved through the immediate change in color or shape, thus enhancing applications in user-interactive devices and human-machine interfaces.^{10,63} To maximize the advantage of colorimetric skins compared to e-skins with electrical transduction modes, the colorimetric skins should be operated without external power source and possess high sensitivity to be intuitively perceived by the naked eyes. In addition, stimuli-induced color change should be maintained under the continuous application of stimuli and fastly recovered after relaxation of stimuli. Furthermore, when the colorimetric skin is integrated with e-skins with electrical transduction modes, they can exactly detect the applied stimuli by the electrical sensing and intuitively perceive the location of stimuli by the colorimetric sensing, complementing each other. However, the colorimetric skin, which combine all of these properties in a single device, is not reported.

To address these issues, this thesis suggest novel types of e-skins mimicking human and biological skins. Inspired by unique structures and functionalities in human skin, we designed nano/microstructured e-skins based on flexible and functional polymer composites, enabling high-

performance e-skins with high sensitivity and multifunctionality in response to tactile stimuli. In chapter 2, we demonstrate highly sensitive e-skins based on human skin-inspired interlocked microdome structures for multidirectional force sensing. Benefitting from structural design, the interlocked microdomes experience different deformation trends in response to multidirectional forces (normal, shear, tensile, and bending forces), enabling clearer differentiation to multidirectional forces with wearable applications. In chapter 3, we introduce the multilayer geometry to further improve the human skin-inspired interlocked microdome structure. Owing to effective stress distribution and stress concentration between stacked layers, the multilayered e-skin shows high pressure sensitivity (47.7 kPa^{-1}) and linear response over an exceptionally broad pressure range (0.0013 – 353 kPa) in dual mode of piezoresistivity and piezoelectricity. In chapter 4, we suggest another strategy for multilayered e-skins based on conductivity-gradient multilayer of conductive and elastomeric polymer composite. The resulting conductivity-gradient multilayer enables ultralarge resistance change in applied pressure, resulting in ultrahigh pressure sensitivity ($3.8 \times 10^5 \text{ kPa}^{-1}$) and linear response to pressure range from 0.8 Pa to 100 kPa. In chapter 5, inspired by responsive color change in biological skins, we developed the mechanochromic skin with hierarchical nanoparticle-in-micropore architecture. Owing to effective stress concentration in modulus-gradient hierarchical structure, the mechanochromic skin shows much higher colorimetric sensitivity, lower detectable range, and larger sensing range, compared to planar sensor. In addition, the mechanochromic skin can be used as triboelectric e-skins by integration of Ag nanowire-based electrode, demonstrating dual-mode stimuli sensing performances of e-skins. In chapter 6, inspired by temperature sensing function of human and snake skins, we develop flexible temperature sensor based on thermoresponsive polymer composite, including semi-crystalline polymer, rGO and polymer matrix. The thermoresponsive volume expansion of semi-crystalline polymer, as well as NTC effect of rGO, enables ultrahigh temperature sensitivity near melting point of semi-crystalline polymer. The temperature sensor was successfully applied to wearable body temperature sensor and dual-mode temperature sensor after integration of thermochromic polymer composite. In this thesis, we suggest five novel designs of bioinspired e-skins with advanced sensory functions and multifunctionalities, which can address aforementioned issues of current e-skins. Through these studies, we believe that our bioinspired e-skins provide a great potential of electronic skins in various application fields of wearable sensors and soft electronics.

Chapter 2. Highly sensitive and multidirectional electronic skins based on human skin-inspired interlocked microdome structure

2.1 Introduction

Artificial electronic skins which mimic the sensing capabilities of biological skins have recently attracted much attention for a broad range of applications in wearable electronics, prosthetic limbs, robotics, remote surgery, and biomedical devices.¹²⁴⁻¹²⁵ As an ideal model system for artificial electronic skins, human skin with various sensory receptors (mechanoreceptor, thermoreceptor, nociceptor, etc.) enables the perception of external stimuli like pressure, shear, strain, vibration, temperature, and pain. In particular, various mechanoreceptors such as the Merkel disk (MD), Meissner corpuscle (MC), Pacinian corpuscle (PC), and Ruffini ending (RE) distributed in the epidermis and dermis layers (see schematic illustration in Figure 2.1a) provide spatiotemporal recognition of the magnitude, location, and direction of contact forces, which is critically essential when a human manipulates an object.⁶⁹ For example, the distribution of normal and shear tangential stresses while making contact with an object provides information on its shape and surface texture, friction between the skin and object, and the accidental slip.¹²⁵ The strain pattern on the skin during finger movements is critical to the brain's perception of the position of finger joints relative to the body.¹²⁶ In addition to the magnitude of stress, the directional sensitivity to force is critical to maintaining the balance between normal and tangential fingertip forces, which enables the handling of irregular-shaped objects.¹²⁷⁻¹³⁰

To fabricate electronic skins which mimic the tactile-sensing capability of human skin, diverse approaches based on various transduction modes, such as those employing resistive,^{40,56,58,131-132} capacitive,^{16,133-135} piezoelectric,¹³⁶⁻¹³⁷ and triboelectric sensors,¹³⁸⁻¹³⁹ have been suggested. In particular, for the detection of various mechanical and environmental stimuli, multi-modal electronic skins have been demonstrated based on the integration of mechanical and physical sensors on flexible substrates,¹⁴⁰⁻¹⁴³ nanostructured conductive composites,¹⁴⁴⁻¹⁴⁵ and organic transistor arrays.¹⁴⁶ However, most of the previous studies either focused on the detection of only one type of mechanical stimuli or developed electronic skins that were not capable of discriminating multiple mechanical stimuli and their directions. There have been several reports on the detection and differentiation of normal and in-plane forces applied to electronic skins.^{76,147-149} Pang *et al.* demonstrated the piezoresistive detection and differentiation of normal, tangential, and torsional forces using Pt-coated micropillar arrays.⁷⁶ Gong *et al.* employed tissue papers impregnated with gold nanowires to enable the perception of pressure, bending, torsional forces, and acoustic vibrations.¹⁴⁹ Stretchable electronic skins with multi-directional sensing capabilities have not yet been demonstrated, however. In addition, the low sensitivities of sensors in previous studies provided only small differences in transduced signals under different

external forces, which reduced the sensors' capabilities to clearly resolve the intensity and direction of the forces.

In human tactile systems, it has been reported that the intermediate ridges present at the epidermal–dermal junction enhance the tactile perception of mechanoreceptors.¹⁵⁰ Intermediate ridges with the geometry of interlocked microstructures (schematic illustration in Figure 2.1a) are known to provide strong adhesion between the epidermis and dermis. They also magnify and transduce the tactile stimuli from the skin surface to the mechanoreceptors by concentrating stress near the ridge tips, where mechanoreceptors like MDs and MCs are located.^{125,150-151} Although there are several recent reports on bio-inspired adhesion systems^{94,152-153} and electronic skins^{15,76} which mimic the interlocked microstructures of beetles and dragonflies, multi-directional, stretchable electronic skins mimicking the interlocked microstructures in human skin have yet to be reported. We have previously reported piezoresistive electronic skins with interlocked microdome arrays for the ultrasensitive detection of normal pressure. In this study, inspired by the interlocked epidermal–dermal ridges in human skin, we further explored the interlocked microdome arrays for stress-direction-sensitive and stretchable electronic skins which can detect directional mechanical stimuli applied along three different axes. resulting from the different deformability of interlocked microdome arrays depending on the direction of applied forces. As proof of concept, the electronic skins attached on human joints or skins are able to distinguish between normal and shear forces and the different bending/stretching movements of arms. We also demonstrate that a fully functional wearable electronic skin with 3×3 sensor arrays can selectively monitor different intensities and directions from air flows and vibrations.

2.2 Experimental Details

Fabrication of elastic composite film with microdome arrays: For the fabrication of composite elastomers, MWNTs (Sigma Aldrich) with diameters of 110–190 nm and lengths of 5–9 μm were first dispersed in chloroform by sonication for 6 h. Using a vortex mixer, the dispersed solution was mixed with a PDMS base (Sylgard 184, Dow Corning) at different ratios (5–8 wt%) of MWNTs to PDMS, followed by heating at 90 °C on a hot plate to remove the chloroform. For the micromoulding process, hexane and a PDMS curing agent (1:10 ratio for the curing agent and PDMS base) were added to each MWNT–PDMS composite mixture (concentration of 500 mg ml⁻¹) and then mixed with a vortex mixer for 5 min. These composite mixtures were cast onto silicon micromoulds with hexagonal hole arrays (diameter: 3.5 μm , pitch size: 6 μm) and stored in a vacuum desiccator for 1 h to remove the residual hexane. Finally, different microdome-patterned MWNT–PDMS composite films (thickness of 500 μm) were prepared by thermal curing at 60–80 °C (strain and curvature sensors: 60 °C, pressure and shear force sensors: 70 °C) for 3 h. For the electronic-skin applications, the interlocked microdome-patterned films were coated with platinum on both sides by a sputter coating system (K575X, Quorum Emitech) to form electrode arrays. To minimize the contact resistance, a silver paste was applied between the composite film and Pt electrode and annealed at 100 °C for 1 h.

Characterization: The surface morphologies of the microdome composite films were characterized by a field-emission SEM (FE-SEM; S-4800, Hitachi) and an optical microscope (PSM-1000, Olympus). The piezoresistive properties of the electronic skins were measured using a two-probe method (4200-SCS, Keithley) at 10 V. To apply mechanical forces on the electronic skins, a pushing tester (JIPT-100, Junil Tech) was used to provide normal forces and a tensile/bending machine (JIBT-200, Junil Tech) was used to provide lateral and bending strain. For the tangential-shear tactile-sensing measurements, a polyethylene terephthalate (PET) film was attached on one side of a composite film and one end of the PET film was connected to a force gauge in the tangential direction. A constant normal force was then applied on the electronic skin using a lab-built microstage system (Micro Motion Technology, Korea), after which a shear force was applied to the electronic skin. For the evaluation of the directional tactile-sensing properties, a flow meter (Ar gas, flow rate of 5.3 m s⁻¹) and a vibrator (2.0 m s⁻²) were used to provide mechanical stimuli in different directions.

Finite-Element Method: For the contact area calculations under stretching and shearing, we conducted structural analyses using finite-element method. Composite films with interlocked microdomes arrays were modeled as linear elastic materials described by experimentally measured elastic constants.¹⁵ We employed more than 2.8 million four-node linear tetragonal elements with adaptive mesh-refinement scheme around the contact area. All calculations were static under proper loading conditions and the mechanical contact between two deformable surfaces was calculated by a

surface-to-surface contact scheme.

2.3 Results and Discussion

Bio-inspired interlocked microdome arrays. The biomimetic design of the interlocked microdome arrays was based on carbon-nanotube (CNT) composite elastomer films with surface microstructures of hexagonal microdome arrays. The interlocked geometry was accomplished by engaging two microdome-patterned CNT composite films with the patterned sides contacting each other. Each elastomeric film with a microdome pattern was fabricated by casting a viscous solution containing multi-walled carbon nanotubes (MWNTs) and poly(dimethylsiloxane) (PDMS) onto a silicon micromould (Figure 2.2). Figure 2.1c shows a representative scanning-electron microscope (SEM) image of a microdome-patterned conductive film with microdomes measuring 3 μm in height and 4 μm in diameter, and an array pitch of 6 μm . The electronic skin was configured by interlocking two microdome composite films, with the microdomed surfaces facing each other (cross-sectional SEM image in Figure 2.1d). When the interlocked microdome arrays were attached on human skin in the arm and wrist areas, it was possible to monitor the magnitude and direction of various mechanical stimuli (pressure, shear, strain, and curvature) applied on the electronic skins (Figure 2.1e).

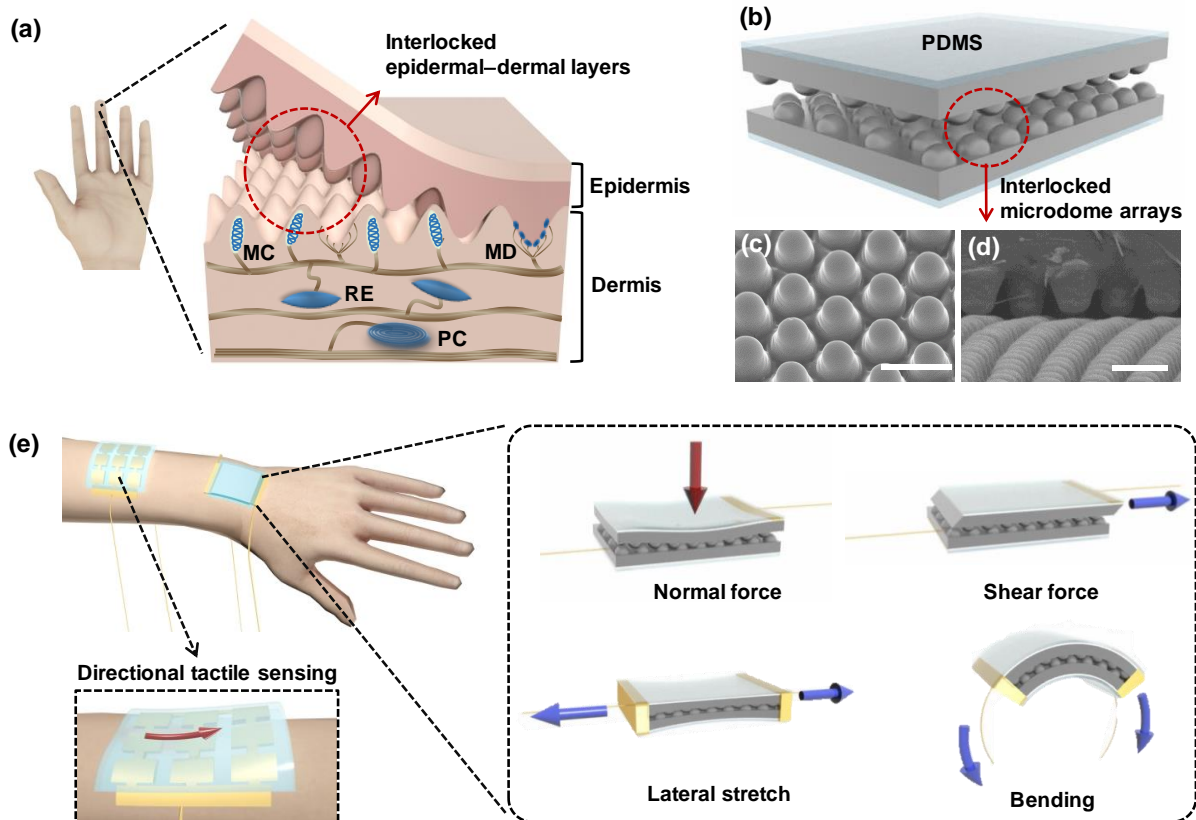


Figure 2.1. Electronic skin based on carbon nanotube–poly(dimethylsiloxane) (CNT–PDMS) composite films with interlocked microdome arrays. (a) Schematic of human skin structure showing interlocked epidermal–dermal layers and mechanoreceptors (MD: Merkel disk; MC: Meissner corpuscle; PC: Pacinian corpuscle; RE: Ruffini ending). (b) Schematic of an interlocked microdome array. (c) Tilted SEM image of a composite film with microdome arrays (diameter: ~3 μm ; height: ~3.5 μm ; pitch: 6 μm). Scale bar: 5 μm . (d) Cross-sectional SEM image of an interlocked composite film. Scale bar: 5 μm . (e) Schematic of a stress-direction-sensitive electronic skin for the detection and differentiation of various mechanical stimuli including normal, shear, stretch, bending, and twisting forces.

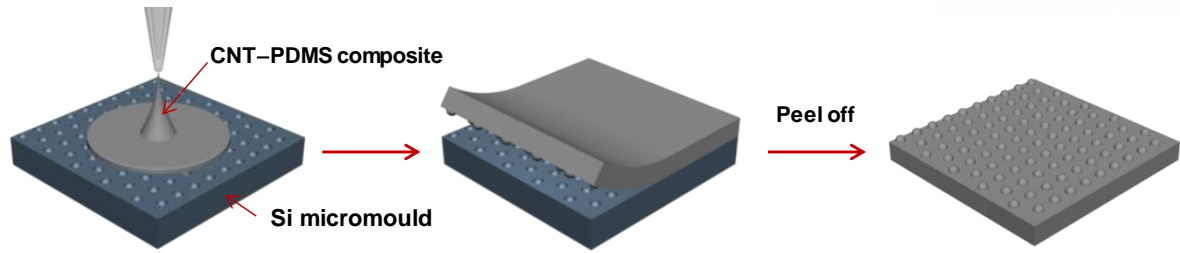


Figure 2.2. Schematic illustration of the micromoulding process for the fabrication of CNT-PDMS composite elastomers with microdome arrays.

Stretchable electronic skins. The perception of stretch in human skin is critical to the sense of position and movement of fingers, elbows, and knees.^{126,154} The stretch-sensing mechanism of the interlocked microdome arrays was based on variations in the contact area between microdomes with changes in the stretch ratio. Figure 2.3a illustrates the variations in the contact (R_c) and film (R_f) resistances when the interlocked microdome arrays were stretched. The contact resistance (R_c) significantly increased with the decrease in contact area between the microdomes when the gaps between them increased under lateral strain. Compared to the large change in R_c , however, the stretching-induced change in R_f had a minimal effect on the change in overall resistance. The strain-induced change of intertube distance within the composite film results in the change of R_f , which is trivial compared to the change of R_c . The small change of R_f is evident from the low gauge factor of planar films in Figure 2.3e. To elucidate the working principle of the interlocked microdome arrays behind their stretch-sensing capability, we investigated the deformation of the microdome array pattern as a function of lateral strain. As can be seen in the SEM images in Figure 2.3b, the microdome arrays changed their geometry from hexagons to elongated hexagons in the stretching direction with increasing lateral strain, resulting in the decrease of contact pressure and increases in gap distances between the microdomes. These increased gap distances decreased the contact area between the interlocked microdomes, thus increasing the contact resistance of the interlocked microdome arrays. In order to verify the variations in contact area with the application of lateral strain, we performed finite-element simulations of the change in contact area in the interlocked microdome arrays. Figure 2.3c shows the changes in contact pressure at various contact points between interlocked microdome arrays with the increase of lateral strain. As the lateral strain increases, both the contact pressure and the number of contact points decrease. Consequently, the decreased contact pressure and the number of contact points results in the decrease of the contact area. The simulation result in Figure 2.3d shows that the inverse contact area increases exponentially with the increase of lateral strain. Since the inverse contact area is directly proportional to tunneling resistance between contact points,¹⁵ the electrical resistance interlocked microdome arrays increases exponentially as a function of lateral strain, as can be seen in Figure 2.3e.

Based on a comparison of sensitivity as functions of CNT concentration and curing temperature (Figure 2.4), we chose a CNT concentration of 7 wt% and a curing temperature of 60 °C as the optimal conditions for the fabrication of stretchable electronic skins. Figure 2.3e shows the change in relative (or normalized) electrical resistance ($\Delta R/R_0$) as a function of applied lateral strain ($\Delta L/L_0$) for the interlocked microdome arrays prepared under these conditions. Here, R_0 and L_0 denote the resistance and length of an electronic skin with and without stretch, respectively. The relative resistance of the interlocked microdome arrays increased significantly with increasing lateral strain, while the planar composite films without interlocked structures showed minimal change in relative electrical resistance.

For a quantitative analysis of the strain sensitivity of the electronic skins, the strain gauge factor (GF) is defined as $GF = (\Delta R/R_0)/\varepsilon$, where ε is the lateral strain and is defined as $\varepsilon = \Delta L/L_0$. The interlocked microdome arrays showed different GF values depending on the lateral strain: 27.8 at a strain of 0–40%, 1084 at a strain of 40–90%, and 9617 at a strain of 90–120%. These GF values are significantly (10–395 times) higher than the values for the planar films (2.7 at a strain of 0–110%), sandwiched Ag-nanowire composites (2–14 at 0–70%),¹⁵⁵ three-dimensional macroporous graphene paper (7.1 at 0–100%),¹⁵⁶ and ZnO–polystyrene nanofibre hybrid films (116 at 0–50%).¹⁵⁷ Although GF values comparable to those of the interlocked microdome arrays have been reported for single-nanotube or single-nanowire sensors (600–1250 at a strain of 0–1.5%)¹⁵⁸⁻¹⁵⁹ and woven graphene films ($\sim 10^3$ at a strain of 0–6%),¹⁶⁰ their sensing ranges are narrow.

In addition to the high GF values, the interlocked microdome arrays exhibited a narrow hysteresis curve for repeated stretch–release cycles (Figure 2.5). One of the additional advantages of our electronic skins with interlocked geometry is the fast response time. Generally, the bulk polymer composite films exhibit slow response owing to the viscoelastic behaviour of bulk polymers.¹⁶¹ On the other hand, the interlocked-microdome strain sensor operated mainly through the change in contact area between interlocking microdome arrays, overcoming the viscoelastic delay of bulk polymers. Figure 2.3f shows the short response (~ 18 ms) and relaxation (~ 10 ms) times of the interlocked microdome arrays under repeated strain cycles at 50% lateral strain and a stretching speed of 3 mm s^{-1} , which are 3–4 times faster than those of planar composite films (response and relaxation times of ~ 58 ms and ~ 46 ms, respectively). The arrays' response and relaxation times are comparable to those of ZnO-nanowire piezotronic strain sensors (~ 10 ms)¹⁵⁸ and much shorter than values obtained for Sb-doped ZnO nanobelt sensors (0.6–3 s)¹⁶² and CNT–silver nanoparticle composite sensors (~ 100 ms).¹⁶³

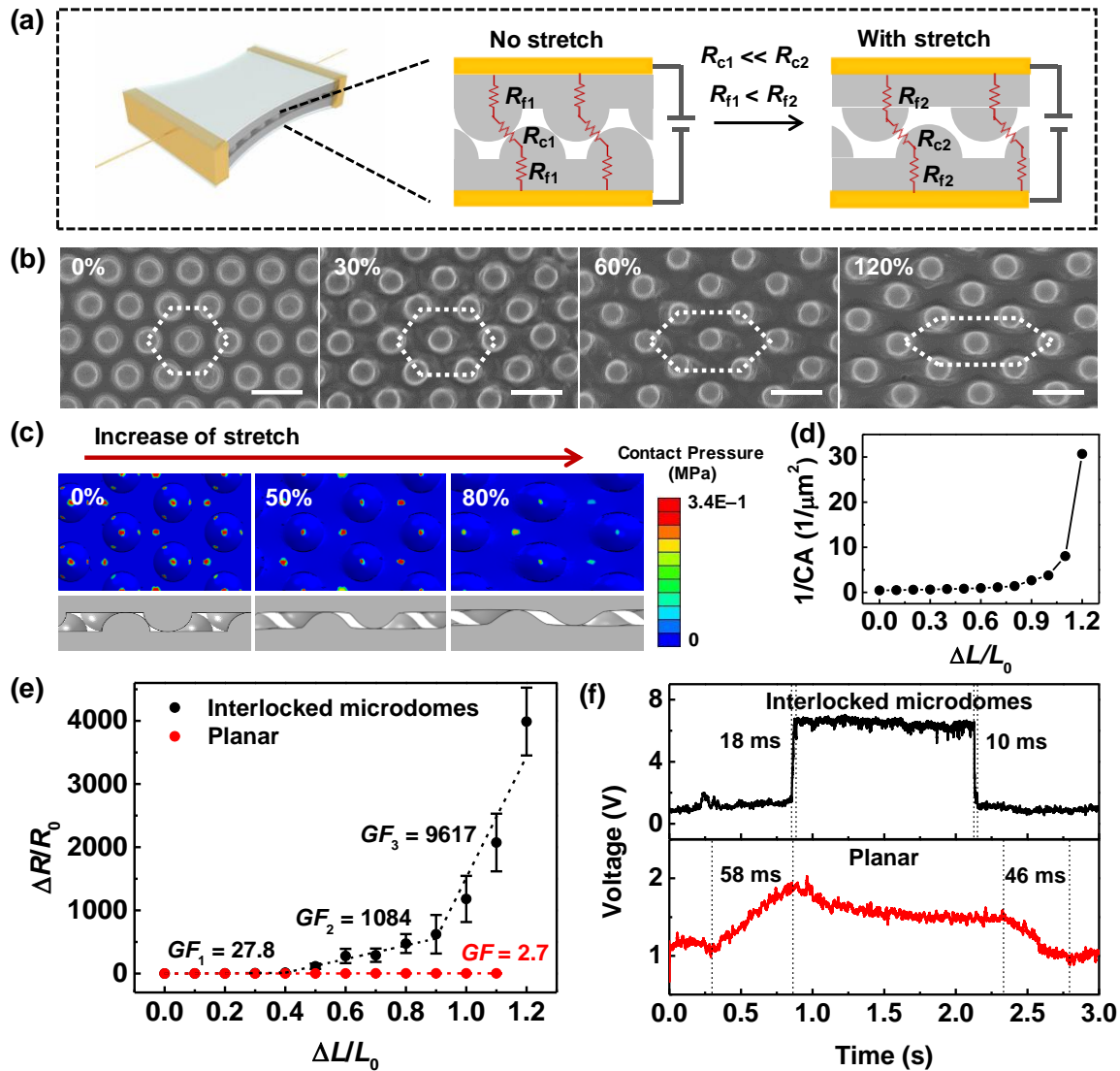


Figure 2.3. Lateral-stretch-sensing capability of electronic skins. (a) Schematic of the stretch-sensing mechanism of interlocked microdome arrays. (b) SEM images of microdome arrays showing the deformation of the array pattern from hexagons to elongated hexagons under different stretch ratios (0, 30, 60, and 120%). Scale bar: 5 μm . (c) Finite-element analysis showing the contact pressure and the contact points between interlocked microdome arrays with the increase of uniaxial stretch. (d) FEA calculated results of the change of contact area between interlocked microdome arrays as a function of stretch. (e) Comparison of stretch-sensing capabilities of interlocked microdome arrays (black) and planar films (red). (f) Comparison of response and relaxation times of interlocked microdome arrays (black) and planar films (red) exposed to a stretching ratio of 50% and stretching speed of 3 mm s^{-1} . The CNT concentration in the composite was 7 wt% and curing temperature was $60 \text{ }^\circ\text{C}$. CNT concentration is 7 wt% for all the results.

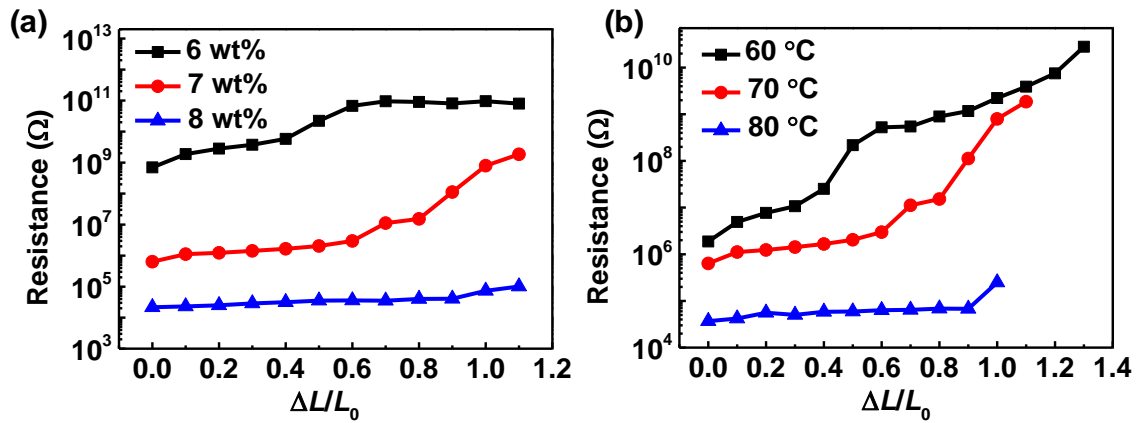


Figure 2.4. Variation in resistance of the interlocked microdome arrays as a function of lateral stretch for (a) different CNT concentrations (6–8 wt%) and (b) different curing temperatures (60, 70, and 80 °C).

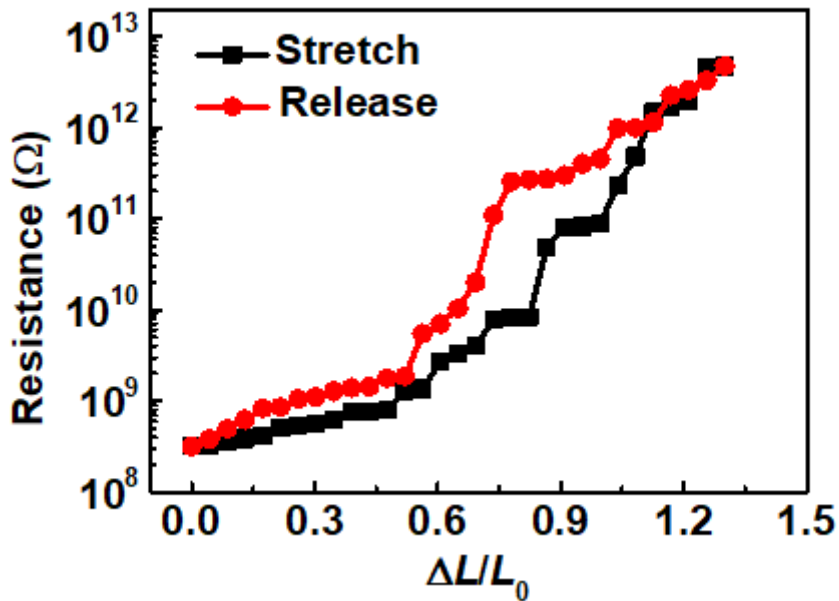


Figure 2.5. Change in piezoresistance of interlocked microdome arrays with lateral stretch for the loading and unloading cycles at 130% lateral strain. The interlocked microdome arrays were prepared with a CNT concentration of 7 wt% and curing temperature of 60 °C.

Shear-force sensitivity. In addition to their stretch-sensing capability with high GF values, the capability of electronic skins to detect and differentiate normal and shear forces is critical in the perception of slip motion, force direction, and strength, as well as the dexterous manipulation of objects for applications in bionic hands, grippers, and tactile displays.¹⁶⁴⁻¹⁶⁷ Our sensor is ideal for the detection of shear stress because the interlocked geometry of microdome arrays provides a strong joint without slip and thus enables the concentration of shear stress at the contact spots. In addition, in our system, the changes in contact resistance were different in response to the normal and shear forces, leading to the differentiation between normal and shear stresses. To test the normal- and shear-force sensitivity, the samples were preloaded with a normal pressure to engage the upper and lower microdome arrays and subsequently subjected to a known value of shear force (Figure 2.6a). The applied normal force immediately induced the surface deformation of microdomes in the interlocked geometry, resulting in an increase in contact area and thus a decrease in contact resistance between the interlocked microdomes. Figure 2.6b shows that the interlocked microdome arrays exhibited a systematic and consistent decrease and increase in relative resistance when the applied normal pressure was reversibly varied from 100 Pa to 25 kPa. As demonstrated in our previous study,¹⁵ the high sensitivity to the normal force can be attributed to the significant change in tunnelling piezoresistance at the contact spots between the interlocked microdome arrays.

The subsequent application of a shear force resulted in the microdome deformation in the lateral direction, which led to a further increase in contact area between the microdomes and decrease in contact resistance. Figure 2.6c shows the change in relative resistance of interlocked microdome arrays as a function of shear force under a normal force (F_N) of 58.8 kPa. For the quantitative analysis, we define a shear-force sensitivity (S) in the linear range for different normal pressure loadings as $S = (\Delta R/R_0) / (\Delta F_s)$, where R and F_s are the resistance and applied shear force, respectively. The interlocked microdome arrays exhibited a shear-force sensitivity of -0.15 N^{-1} , which is approximately four times the sensitivity of a planar film. Because the normal pressure affected the initial contact area between the interlocked microdome arrays, the shear-force sensitivity could be manipulated by controlling the normal pressure to engage the microdome arrays. Figure 2.6d shows the change in relative resistance as a function of shear force for different loadings of normal pressure for electronic skins with 7 wt% CNTs. We observed that the shear-force sensitivity increased with a decrease in normal pressure. The largest sensitivity was -2.21 N^{-1} for a normal pressure of 65 Pa, which is ~ 13 times the sensitivity (-0.15 N^{-1}) at a normal pressure of 58.8 kPa. This behaviour can be explained by the decreased initial contact area between microdome arrays at a lower normal pressure, providing the possibility to further increase the contact area by applying a shear force. Figure 2.7 shows the decrease and increase in the relative resistance of interlocked microdome arrays during pulling and retracting cycles under different shear forces, which also demonstrate their reliability.

In order to verify the variations in contact area with the application of normal and shear forces, we performed finite-element simulations of the change in contact area in the interlocked microdome arrays. The simulation results in Figure 2.6e indicate that the unique structure of interlocked microdome arrays leads to stress concentration and thus deformation of microdomes at the contact spots between spherical microdomes under normal pressure. The subsequent application of shear strain induces further deformation of microdomes at the contact spots, resulting in an increase in contact area. The contact area gradually increases with further increase in shear force, but more importantly, this increase in contact area depends on the normal pressure loadings. As can be seen in Figure 2.6f, the change in the inverse contact area as a function of shear force is greatest for a normal pressure of 0.2 kPa. At higher values of normal pressure, the variation in inverse contact area decreases with increasing shear force. In addition to the normal force, our experiments showed that the shear-force sensitivity could be further manipulated by controlling the CNT concentration. As shown in Figure 2.8, the shear-force sensitivity increased with decreasing CNT concentration, with a sensitivity of -0.44 N^{-1} for 5 wt% CNTs, which is ~ 3 times the sensitivity of the sensor with 7 wt% CNTs (-0.15 N^{-1}) at a normal pressure of 58.8 kPa.

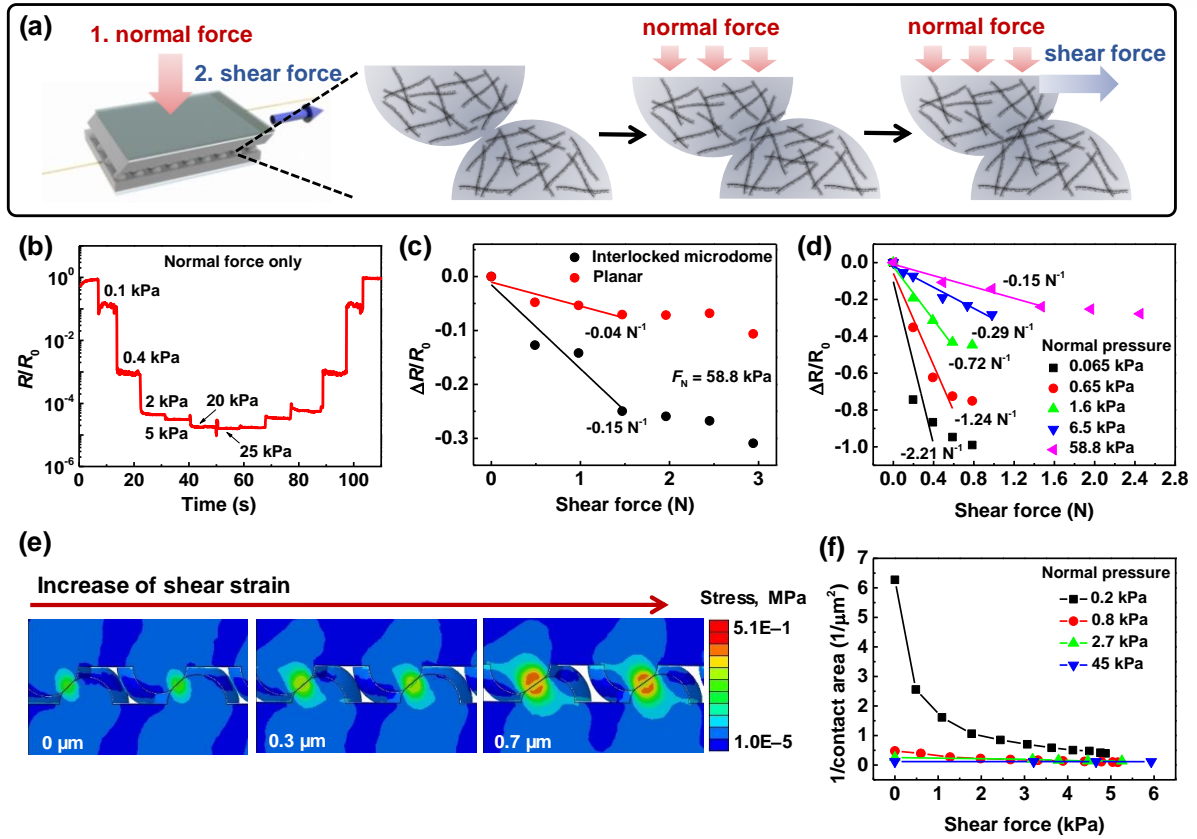


Figure 2.6. Normal- and shear-force-sensing capabilities of electronic skins. (a) Schematic of the deformation of interlocked microdomes during successive applications of normal and shear forces. (b) Relative electrical resistance of electronic skin sample as a function of normal force. (c) Comparison of shear-force sensitivities of interlocked microdomes (black) and planar (red) films under a normal pressure of 58.8 kPa. (d) Comparison of shear-force sensitivities of interlocked microdome arrays under different normal pressures. (e) Finite-element analysis (FEA) showing the deformation and local stress distribution of interlocked microdome arrays with increasing shear force at a normal pressure of 45 kPa. (f) Calculated FEA results of the inverse contact area as a function of shear force under different normal pressures. The CNT concentration was 7 wt% in all electronic skins used for the measurements.

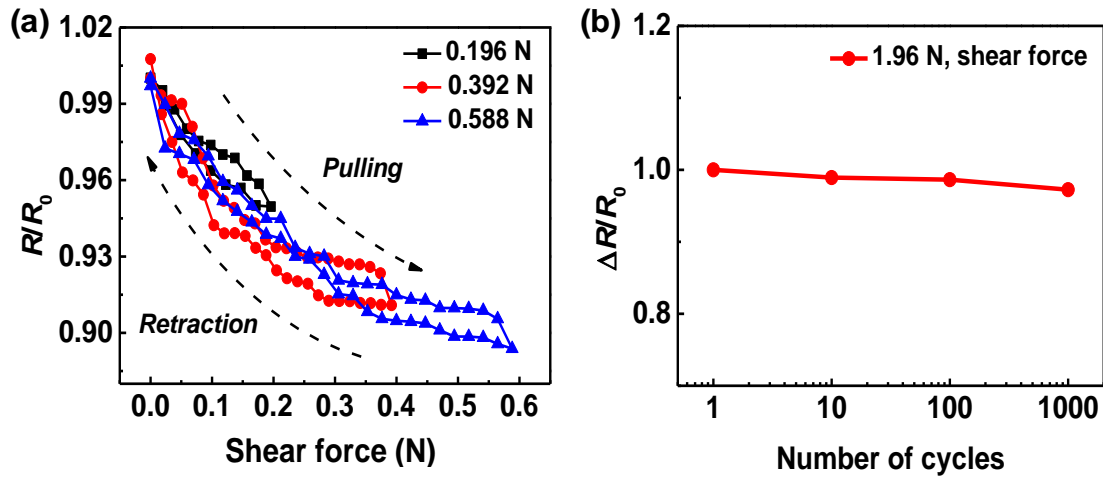


Figure 2.7. (a) Variation in normalized resistance for the pulling and retracting cycles under different shear forces (0.196, 0.392, 0.588 N). (b) Reliability of interlocked microdome composite films through cycles of repeated pulling and retraction under a shear force of 1.96 N.

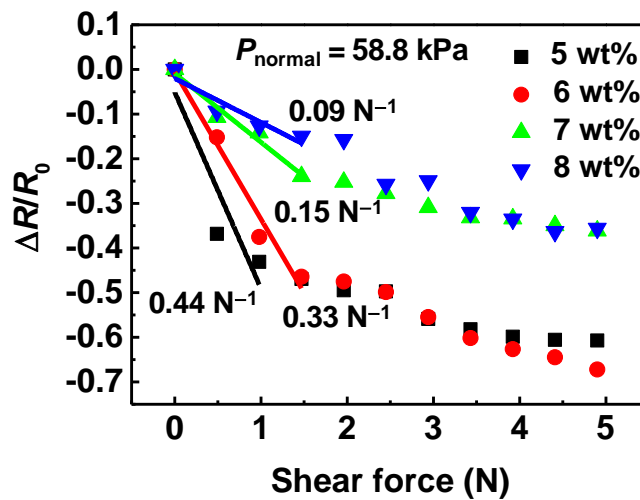


Figure 2.8. Change in relative resistance of interlocked microdome arrays as a function of shear force for electron skins with different CNT concentrations.

Differentiation of multiple mechanical stimuli. Since the interlocked geometry of the microdome arrays provided different deformation patterns specific to the type of mechanical stress, the interlocked microdome arrays were able to detect and differentiate multiple mechanical stimuli. To test their skin-like sensing capabilities, we monitored the normal and shear forces through simple finger contact on the electronic skins attached on human skin. Figure 2.9a shows the change in relative electrical resistance with repeated application of normal forces of 1 kPa and then shear forces. The electronic skin showed different signal intensities and patterns for different types of mechanical stimulus. While a finger touching the electronic skin in the normal direction (F_N) resulted in an immediate decrease in relative resistance, a finger touching the electronic skin in the shear direction, which contained both normal and shear forces ($F_N + F_S$), resulted in additional decreases in the relative electrical resistance. It is worth noting that the patterns of decrease in relative resistance resulting from F_N and F_S were different, therefore allowing the differentiation between normal and shear forces. Figure 2.9b–d show that the electronic skin attached on the front of a human wrist could detect and differentiate different types of wrist movements such as forward bending (F_{FB}), backward bending (F_{BB}), and torsion (F_T). In this experiment, we utilized a curing temperature of 60 °C since we observed that a lower curing temperature resulted in higher bending sensitivity (Figure 2.10). When the electronic skin was bent forward (F_{FB}), the relative electrical resistance increased (Figure 2.9b); a gradual increase in forward bending resulted in the gradual increase in relative resistance. On the other hand, the relative electrical resistance decreased under backward bending (Figure 2.9c), while the twisting of the wrist (F_T) resulted in an increase in electrical resistance. In particular, twisting also generated oscillating signals resulting from the repeated contact-on/contact-off behaviour during the twisting. These different signal patterns in response to different mechanical stimuli are attributed to the unique interlocked geometry of microdome arrays, which, depending on the direction of mechanical stress, could result in distinct variations in contact area. During forward bending, the gap between the neighbouring microdome arrays increased because the upper microdome layer tends to detach from lower microdome layer due to the strain mismatch between the upper (under tension) and lower (under compression) microdome arrays, leading to an increase in relative resistance. Backward bending decreased the electrical resistance because the lower microdome layer is sandwiched between the human skin and the upper microdome layer, resulting in the decreased gaps between neighboring microdome arrays. As shown in Figure 2.9d–j, the individual shapes of generated electrical signal pattern under different input forces could provide the exact information for differentiation to multiple mechanical stimuli beyond simply detection to intensity of applied forces. This tendency is related to their flexibility and unique structural advantages enabling different alternation to contact area in accordance with varied motions, which results in precise perception to directions, locations and intensity of various stimulations. In case of pressure, shear force, backward bending, the number of contact points between conductive elements increases under

deformation of films, in contrast with those decrease in detecting stretch, forward bending. Differ from live human skin that enables diverse spatiotemporal perceptions by deformation and distortion in exclusive mechanoreceptors, in our electronic skins, variation on relative distances between conductive fillers under deformation serves as a main factor for detection of various mechanical forces. Over to inspire interlocked epidermal–dermal ridges in human skin, imitating the mechanoreceptors in dermis still remains to be solved for comprehensive human skin inspired electronic skins

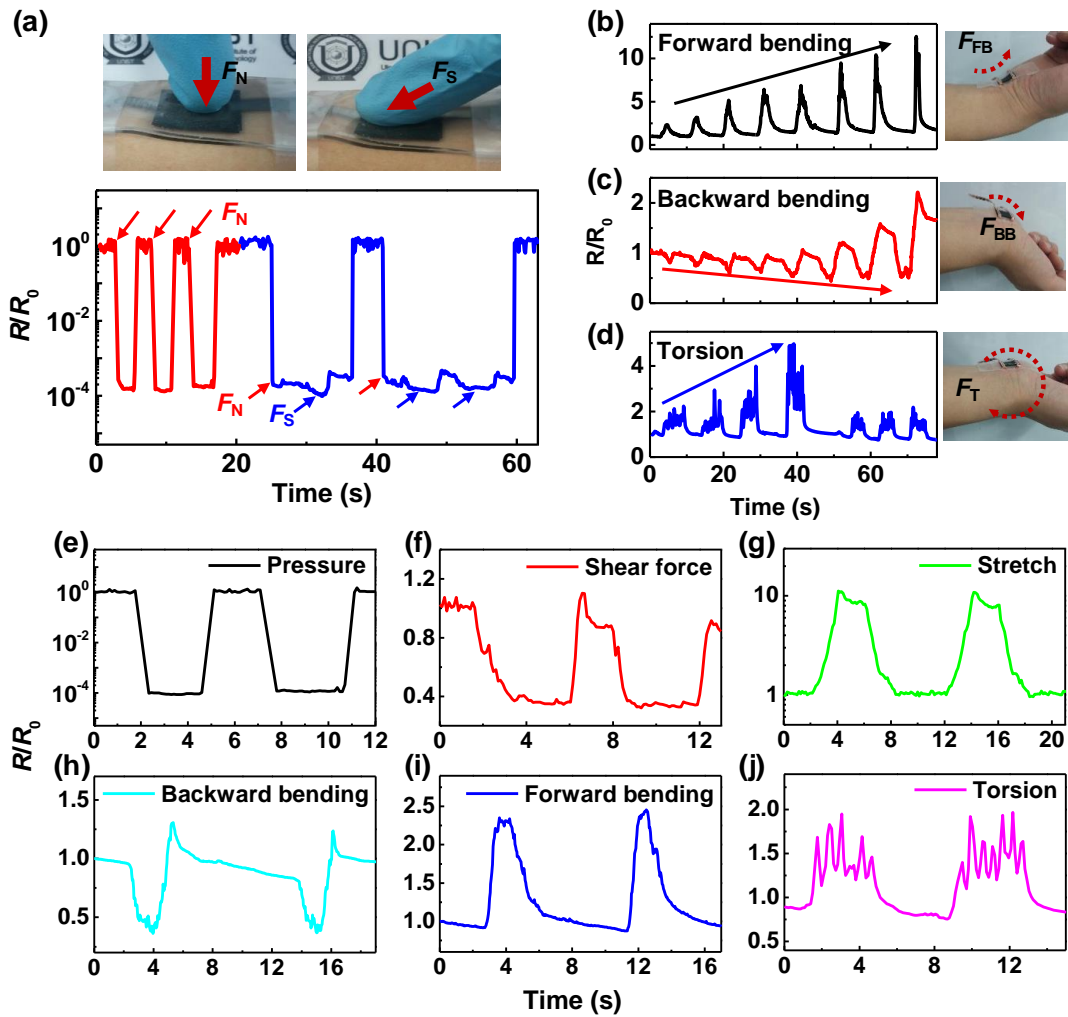


Figure 2.9. Stress-direction-sensitive electronic skins for the detection and differentiation of multiple mechanical stimuli. (a) Real-time monitoring of changes in the relative resistance of interlocked microdome arrays subjected to different normal and shear forces. (b–d) Change in relative electrical resistance of an electronic skin attached on the front of a human wrist under different types of wrist movements: (b) forward bending; (c) backward bending; (d) torsion. The electronic skin showed different signal patterns in response to different wrist movements. (e–j) Change in relative electrical resistance of electronic skins in response to different mechanical stimuli: (e) normal force; (f) shear force; (g) lateral stretch; (h) forward bending; (i) backward bending; (j) torsion.

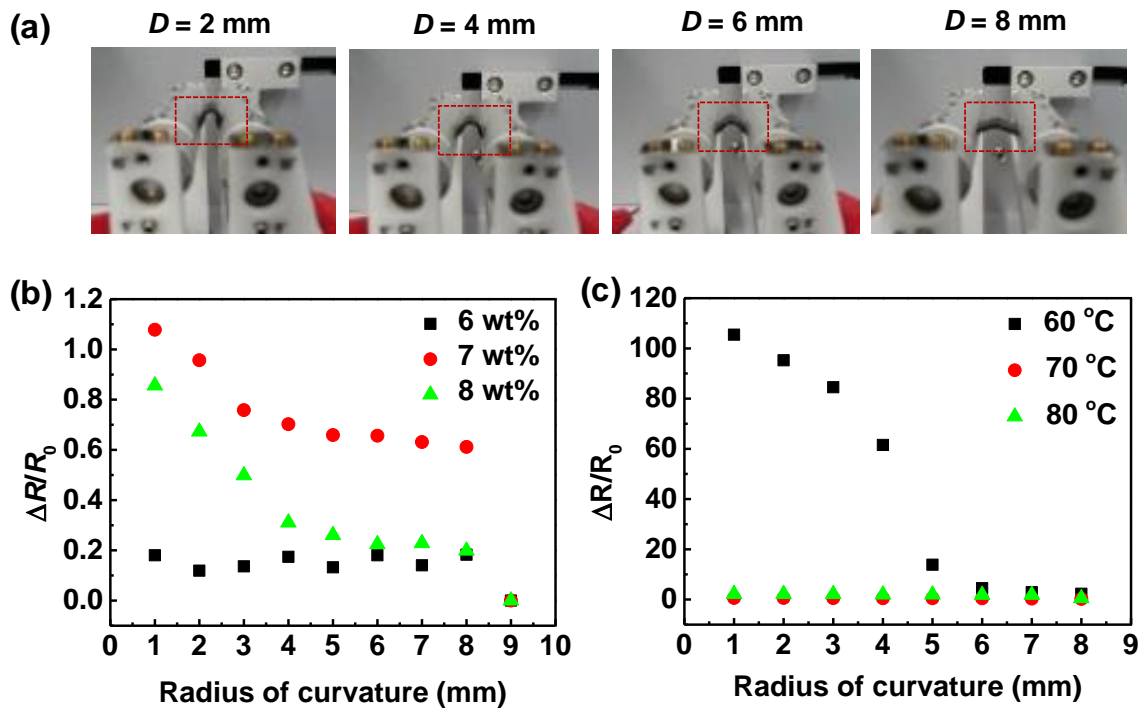


Figure 2.10. (a) Photographic images of bending tests of electronic skins with interlocked microdome arrays. (b) Variation in relative resistance of interlocked microdome arrays as a function of radius of curvature for electronic skins with different CNT concentrations (6–8 wt%) and cured at 80 °C. (c) Variation in relative resistance of interlocked microdome arrays as a function of radius of curvature for electronic skins prepared with 7 wt% CNTs at different curing temperature (60, 70, 80 °C). The decrease of curing temperature results in the decrease of elastic modulus and thus the increased deformability in response to mechanical stress, resulting in the increased sensitivity.

Wearable electronic skins with stress-direction sensitivity. For the proof-of-concept wearable electronic skins to resolve the spatial distribution and the directions of applied external stimuli such as touch, flow, and vibration, we fabricated 3×3 pixel arrays of electronic skin sandwiched between cross arrays of platinum electrodes (Figure 2.11a). When we touched two different pixels (R1-C3 and R3-C1 in Figure 2.11b) on the electronic skin, it could provide spatially resolved mapping of the touch positions. The high sensitivity of each pixel on the electronic skin could also provide the ability to resolve gradual changes in mechanical stimuli, therefore enabling the detection of the direction of mechanical stress. Figure 2.11c shows that depending on the finger-pushing directions (left, right, up, and down), the electronic skin exhibited different spatially resolvable patterns, indicating the perception of the intensity and direction of tactile stimuli. Figure 2.11d also demonstrates the directional sensing capability of the electronic skin, where fluid flows in different directions (left, right, and diagonal) could be clearly resolved by the signal patterns. The sensitivity to gradual changes and directions of external stimuli was also verified by applying a vibrational stimulus on the electronic skin. Figure 5e shows the application of radial vibration on one pixel located at the corner (R1-C1) of the electronic skin and the resulting spatial mapping of the vibrational stimulus. Owing to vibrational damping, the change in relative resistance gradually decreased as the pixel location was farther away from the original pixel at which vibration was applied, which led to gradually decreasing changes in the relative resistance.

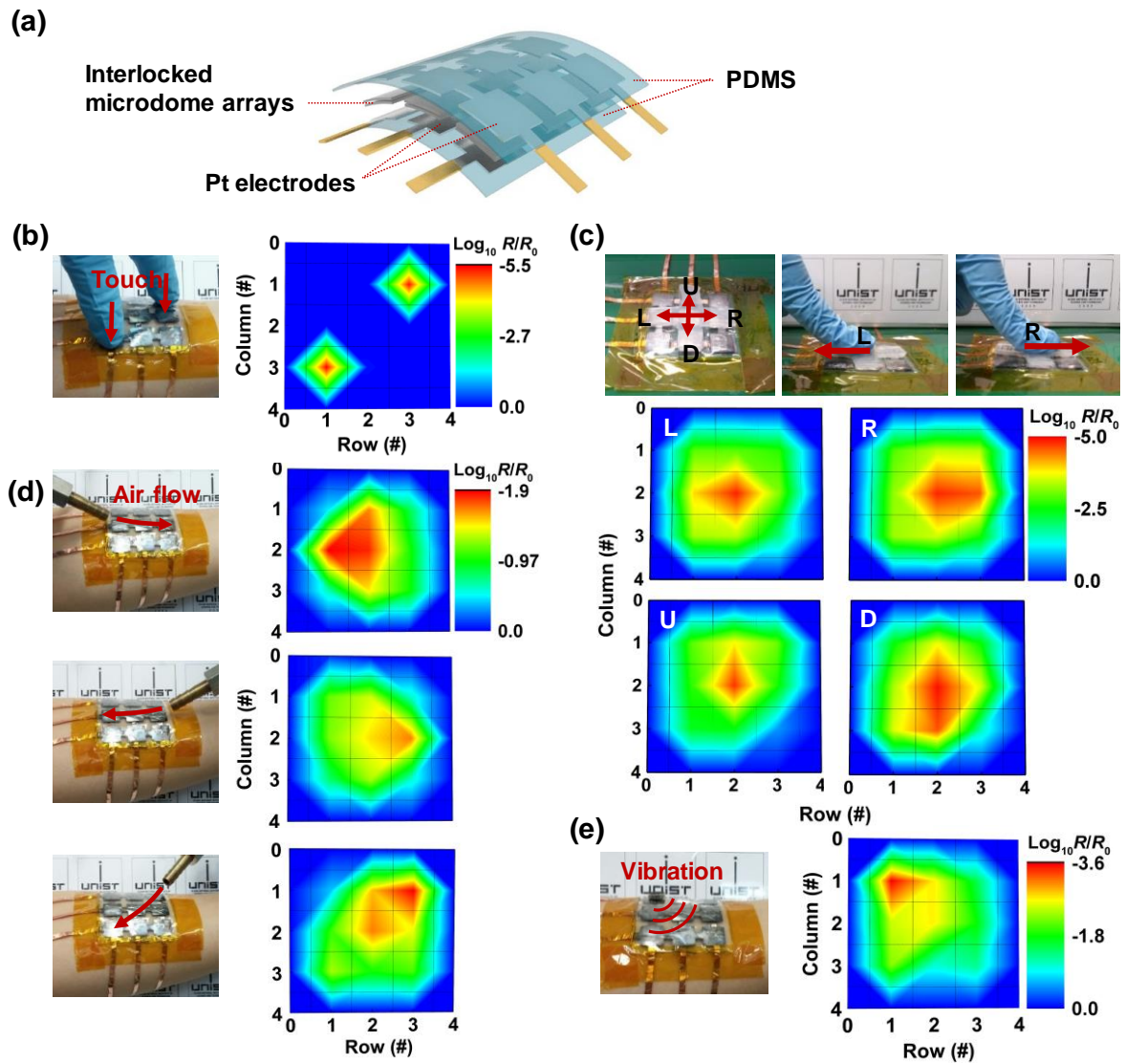


Figure 2.11. Stress-direction-sensitive electronic skins for directional sensing of mechanical stimuli applied in three axial directions. (a) Schematic of sensor arrays, where interlocked microdome arrays are sandwiched between the electrodes and PDMS protection layers. (b) Spatial pressure mapping capability of electronic skin for the detection of finger touch on two different pixels (R1-C3, R3-C1). (c) Detection of different finger-pushing directions: left (L), right (R), up (U), down (D). (d) Detection of different directions of fluid flow (left, right, diagonal). (e) Detection of the location of applied vibration and the gradual damping of vibration.

2.4 Conclusion

In summary, we have demonstrated stress-direction-sensitive and stretchable electronic skins with three-axial stress-sensing capabilities. We employed piezoresistive, interlocked microdome arrays which were inspired by the interlocked epidermal–dermal layers in human skin. Similar to the stress concentrating function of interlocked epidermal-dermal ridges which magnify the tactile stimuli, the arrays could induce exclusive stress concentration at the contact spot and thus deformation of the microdomes, resulting in enhanced sensitivity of the piezoresistive response to stress. In particular, the unique geometry of the interlocked microdome arrays led to different deformation patterns which depend on the type and direction of mechanical stress, enabling detection and differentiation of various mechanical stimuli including normal, shear, stretch, bending, and twisting forces. Owing to the direction-sensitive tactile-sensing properties, various electronic skins attached on human skin were successfully employed to monitor different intensities and directions of finger touches, air flows, and vibrations. Because our design is the simplified version of complicated human skin, where papillary ridges, location of mechanoreceptors, the elastic moduli of layers, and the shape and size of intermediate ridges are all closely related to each other to efficiently transduce and magnify tactile stimuli, we expect that the interlocked geometry can be further explored to develop bio-inspired electronic skins with human-skin-like tactile-sensing capabilities. Finally, we anticipate that our stretchable electronic skins with multi-directional stress-sensing capabilities can find applications in robotic skins, prosthetic limbs, and rehabilitation devices to monitor motion and stress distribution.

Chapter 3. Human skin-inspired multilayered ferroelectric skins with ultrahigh pressure sensitivity and linear response over exceptionally broad pressure range

3.1 Introduction

Rapid advances in physical/chemical sensors, wireless communication, and energy storage systems are driving the interest in wearable electronic devices, such as smartwatches, smartbands, and smartglasses, which enable the monitoring and diagnosis of the personal health status in real-time.⁷ Flexible electronic skins (e-skins), which mimic perceptive functions of human skin, have attracted strong research interest as essential components of potential applications in robotics, prostheses, and wearable healthcare monitoring devices. High sensitivity, fast response time, mechanical flexibility, and durability are major requirements for e-skins used for these practical applications and various approaches focused on the improvement of these attributes.^{16,134,168-169} Another significant requirement for e-skins with human skin-like tactile sensing properties is the discrimination of spatiotemporal tactile stimuli, including static and dynamic pressure, which allows dexterous manipulation of objects and the perception of vibration and surface textures.^{22,170} In addition, to use e-skins for various applications as a single device, they should have a large dynamic sensing range and linear pressure-sensing capability to constantly maintain their high sensitivity, even in the high-pressure region.^{123,171} E-skins with a high sensitivity over a broad sensing range can perceive, for example, subtle pressure of light breeze and respiration (<1 kPa), medium pressure of pulse pressure and gentle touch (1–10 kPa), and large pressure of plantar foot pressure (>10 kPa). Furthermore, e-skins with linear sensing ability over a large dynamic range do not require additional complex signal processing, which meets the increasing demand for device miniaturization and low power consumption. Although several approaches have been adopted to improve some of the aforementioned requirements of e-skins, the combination of all of these properties in a single e-skin remains a challenge.^{24,123,172}

As an ideal sensory system, human skin can perceive and differentiate various tactile sensation under different mechanical stimuli.⁶⁸ In particular, various sensory receptors are embedded in the human skin, which transduce information from applied stimuli, such as magnitude, distribution, and frequency, into tactile sensation.⁶⁹ In addition, the special intermediate ridge structure between dermal and epidermal layers efficiently transmits tactile signals from the skin surface to sensory receptors located in interlocked ridge structures due to the effective stress concentration between dermal and epidermal layers with different moduli.^{125,150,173} To mimic tactile sensing functions and structures of human skin, various types of e-skins based on different signal transduction modes, including piezoresistivity, capacitance, piezoelectricity, and triboelectricity, have been developed.^{56,58,135-138,149} In particular,

various types of microstructures (e.g., micropyramid, microdome, and micropillar) have attracted much attention with respect to the improvement of sensing characteristics of e-skins such as sensitivity, response time, sensing range, and durability.⁷ Recently, Pan et al.¹⁶⁹ demonstrated hollow sphere microstructure-based pressure sensors with a high sensitivity of 133 kPa^{-1} and Su et al.⁷⁷ designed an irregular microstructure for a mimosa-inspired pressure sensor with a high sensitivity of 50.17 kPa^{-1} . However, the high sensitivity is only valid in subtle pressure regions ($<100 \text{ Pa}$) and they can only detect static pressure using the piezoresistive sensing of e-skins. To differentiate spatiotemporal tactile stimuli, interlocked microdome-based e-skins have been suggested.²² This work showed highly sensitive and multifunctional tactile sensing performance with various transduction modes, but the dynamic pressure-sensing range was still under 50 kPa and a linear sensing capability could not be achieved. Therefore, a significant challenge remains in the development of e-skins with new device designs to realize a large dynamic pressure range and linear tactile sensing performances.

In this paper, we demonstrate a flexible ferroelectric sensor with ultrahigh pressure sensitivity and linear response over an exceptionally broad pressure range based on the ferroelectric composites with a multilayer interlocked microdome geometry. Due to the conductive and ferroelectric nature of polymer composites comprising poly(vinylidene fluoride) (PVDF) and reduced graphene oxide (rGO), our e-skins can perceive and differentiate static and dynamic pressures using piezoresistive and piezoelectric modes. Each layer of e-skins comprises interlocked microdome arrays inspired by interlocked ridge structures between the dermal–epidermal layers, and three interlocked layers are stacked for the fabrication of multilayer e-skins. While previous pressure sensors exhibit nonlinear or narrow range linear sensing, our e-skins can maintain their high sensitivity and linear response over a broad pressure range due to the increased contact area change and efficient stress distribution between stacked layers compared with single-layered e-skins (Figure 3.1a). The multilayer e-skins can constantly maintain an ultrahigh sensitivity of 47.7 kPa^{-1} over an exceptionally broad pressure range of $0.0013 - 353 \text{ kPa}$. Furthermore, our sensor displayed a fast response time (20 ms) and high reliability over $5,000$ repetitive cycles even at extremely high pressure of 272 kPa . For proof of concept, our e-skins were used for the monitoring of diverse stimuli from low to high pressure range (Figure 3.1b). For example, our e-skins were used for precise detection of weak gas flow and acoustic sound in a low pressure regime and for monitoring respiration and pulse pressure in a medium pressure regime. In addition, the large dynamic range pressure-sensing capability of e-skins was employed for plantar pressure monitoring in a high pressure regime.

3.2 Experimental Details

Preparation of ferroelectric and conductive composite films: GO was prepared based on a modified Hummers method.¹⁷⁴⁻¹⁷⁵ Briefly, graphite powder (SP-1, Bay Carbon), $K_2S_2O_8$ (Sigma Aldrich), and P_2O_5 (Sigma Aldrich) were dispersed in concentrated H_2SO_4 solution (Sigma Aldrich). The mixture was stirred at $80\text{ }^\circ\text{C}$ for 4.5 hours. This solution was then diluted with deionized (DI) water, followed by filtration and DI washing to achieve a neutral pH. The resulting filtrate was dried under $30\text{ }^\circ\text{C}$ vacuum conditions overnight. The preoxidized graphite was dispersed in concentrated H_2SO_4 . Subsequently, $KMnO_4$ (Sigma Aldrich) was slowly added to the solution under vigorous stirring, followed by stirring at $36\text{ }^\circ\text{C}$ for 2 hours. The mixture was gradually diluted with DI water, followed by stirring at $36\text{ }^\circ\text{C}$ for 2 hours. Subsequently, 30% H_2O_2 (Sigma Aldrich) was added to this mixture, which resulted in a color change to bright yellow with violent bubbling. This mixture was then stirred for 1 hour and centrifuged several times in 10% HCl to remove residual salts. The resulting mixture was subjected to dialysis to adjust the acidity. Finally, the solution was concentrated by drying under $30\text{ }^\circ\text{C}$ vacuum conditions and dispersed in dimethylformamide (DMF) solvent by sonication to obtain GO–DMF solution. Prior to blending graphene and PVDF (Sigma Aldrich; molecular weight $\approx 534,000$), PVDF was first dispersed in DMF solvent and the dispersed PVDF–DMF solution (20 wt%) was mixed with GO–DMF solution (10 mg/mL) in the desired mixing ratio. The prepared GO/PVDF was poured on the glass substrate for planar composite films and a microdome-patterned mold (diameter $\approx 10\text{ }\mu\text{m}$; pitch $\approx 12\text{ }\mu\text{m}$; height $\approx 4\text{ }\mu\text{m}$) for microdome composite films. The casted solution was first dried on a heating plate at $50\text{ }^\circ\text{C}$ for 12 hours and then annealed in a vacuum oven at $160\text{ }^\circ\text{C}$ for 2 hours to reduce GO to rGO and remove residual DMF solvent.

Multilayer e-skin fabrication: For the interlocked microdome structure, two microdome-patterned rGO/PVDF composite films with patterned sides face each other. The multilayer structure was fabricated by stacking several layers of interlocked microdome structures with adhesive layers, which had a similar thickness with a single rGO/PVDF composite film. Finally, two copper electrodes were attached to the top and bottom side of the multilayer interlocked microdome composite films using silver paste. To fabricate 3×3 and 4×8 pixel arrays, the PET supporting layers were coated with a platinum electrode with a mask using sputter coating system (Hitachi, E-1045) and multilayer interlocked microdome rGO/PVDF composite films were sandwiched by patterned electrodes.

Characterization: The microstructures and interlocked geometry of rGO/PVDF composites were analyzed by field-emission SEM (S-4800, Hitachi). To check ferroelectric properties, the crystal structures of pure PVDF and PVDF of composite films were measured by XRD spectroscopy (Bruker AXS, D8 ADVANCE) with $CuK\alpha$ radiation. The pressure-responsive electric properties of e-skins were measured using a semiconductor parameter analyzer (4200-SCS, Keithley) for piezoresistive signals

and a sourcemeter (S-2400, Keithley) and oscilloscope (DPO 2022B, Tektronix) for piezoelectric signals. The static/dynamic normal pressure was applied to e-skins with the pushing tester (JIPT, JUNIL TECH) at different frequencies. For the application of multilayer e-skins, the 3×3 and 4×8 pixel arrays were measured with a multichannel biosensor test system (OT15-3010D, ONTEST).

Finite element calculation: The structural analysis of the interlocked microdome multilayers (single, double, and triple layer) was performed by finite element simulations (ABAQUS software). The contact area and stress between different numbers of interlocked layers were numerically calculated as a function of the applied pressure. All the simulated top and bottom layers comprised rGO/PVDF composite films with interlocked microdome structures (10 μm in diameter and 12 μm in pitch) and PET-based adhesive layers. The occupied areal ratio of adhesive layer, partly located at the edges of film, is $\sim 14\%$ in simulated condition, which is almost equal with experimental values ($\sim 12\%$). The elastic modulus of the rGO/PVDF and PET materials was 2.5 GPa and 1.0 GPa, respectively, which is consistent with experimental values. We implemented general surface-to-surface contact interaction with linear elastic deformable materials to consider the mechanical contact interaction between the stacked multilayers under the applied pressure.

3.3 Results and Discussion

A schematic of interlocked microdome multilayer e-skins for highly sensitive, linear, and large dynamic range pressure sensors is shown in Figure 3.1c. To fabricate conductive and ferroelectric rGO/PVDF composite films, mixtures of graphene oxide (GO) sheets with a PVDF matrix in dimethylformamide (DMF) were cast onto a microdome patterned mold and dried at 50 °C for 12 hours. Subsequently, GO/PVDF films were annealed at 160 °C for 2 hours to completely remove residual DMF and reduce GO to rGO. Figure 3.1d shows the cross-sectional scanning electron microscopy (SEM) image of an rGO/PVDF composite film with interlocked microdome multilayer structures. Figure 3.1e shows a layer with interlocked microdome structures, where the microdome is 10 μm in diameter, 4 μm in height, and 12 μm in pitch size (Figure 3.1f). To check the ferroelectric properties of rGO/PVDF composite films, we performed X-ray diffraction (XRD) spectroscopy analysis on pure PVDF films, GO/PVDF, and rGO/PVDF composite films (Figure 3.2a). Pure PVDF film shows 2θ diffraction peaks at 18.0 °, 18.7 °, 20.2 °, and 26.9 ° which correspond to the (100), (020), (110), and (021) reflection planes of the nonpolar α -phase of PVDF.¹⁷⁶ In contrast, PVDF of GO/PVDF composite films has a strong polar β -phase based on the 2θ diffraction peak at 20.7 ° and a weak γ -phase based on the 2θ diffraction peaks at 19.0 ° and 20.4 °.¹⁷⁶ The polar β -phase crystal structure can be maintained even after the reduction of GO to rGO under high-temperature annealing. To further investigate the phase transition of PVDF, the crystal structure of PVDF in rGO/PVDF composite films was investigated under different rGO loading concentrations (Figure 3.2b). With an rGO loading over 0.5 wt% of the composite film, all characteristic peaks of the nonpolar α -phase disappeared and new diffraction peaks due to the polar β -phase of 2θ at 20.7 °, corresponding to (200/110), and due to the polar γ -phase of 2θ at 19.0 ° and 20.4 ° occurred. The formation of a polar crystal structure of PVDF in composite films, even without additional electric poling process, can be attributed to the steric effect between rGO sheets and PVDF molecules.^{20,177} In addition to ferroelectric properties, the conductivity of rGO/PVDF composites increased with increasing rGO loading concentration after the reduction of GO to rGO (Figure 3.3). To mimic the interlocked ridge structures between dermal–epidermal layers, rGO/PVDF composite films with interlocked microdome arrays were used in each layer of the multilayer e-skins (Figure 3.1e). Finally, three interlocked layers were stacked for the fabrication of multilayer e-skins with an effective stress concentration (Figure 3.1d).

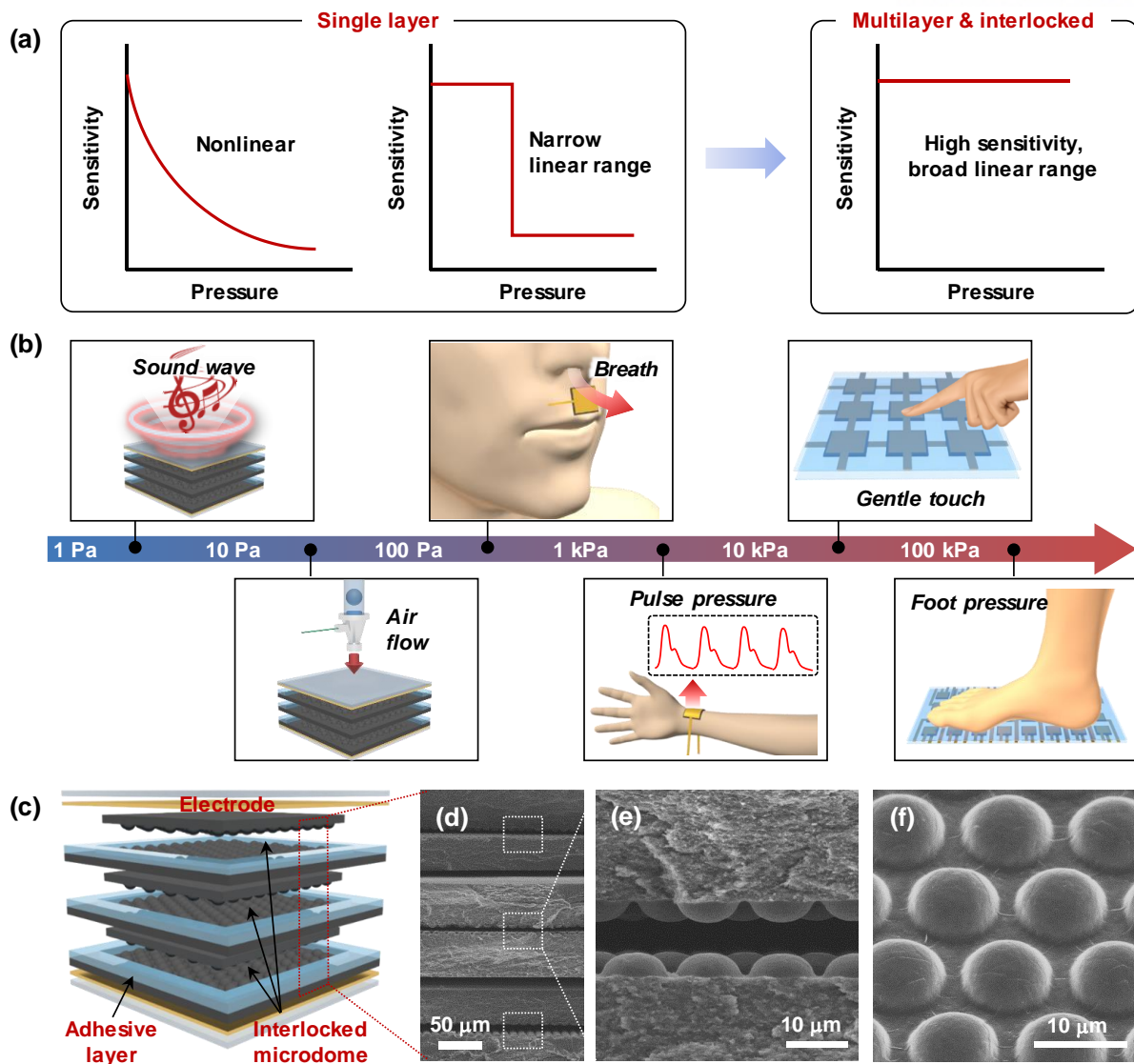


Figure 3.1. Various applications to show highly sensitive and large range pressure sensing of multilayered e-skins. (b) Schematic illustration of multilayered e-skins. (c) Cross-sectional scanning electron microscopy (SEM) image of microdome-patterned rGO/PVDF composite film with multilayer stacked structures. (d) Cross-sectional SEM image of interlocked microdome geometry of rGO/PVDF composite film. (e) Tilted SEM image of microdome array of rGO/PVDF composite film.

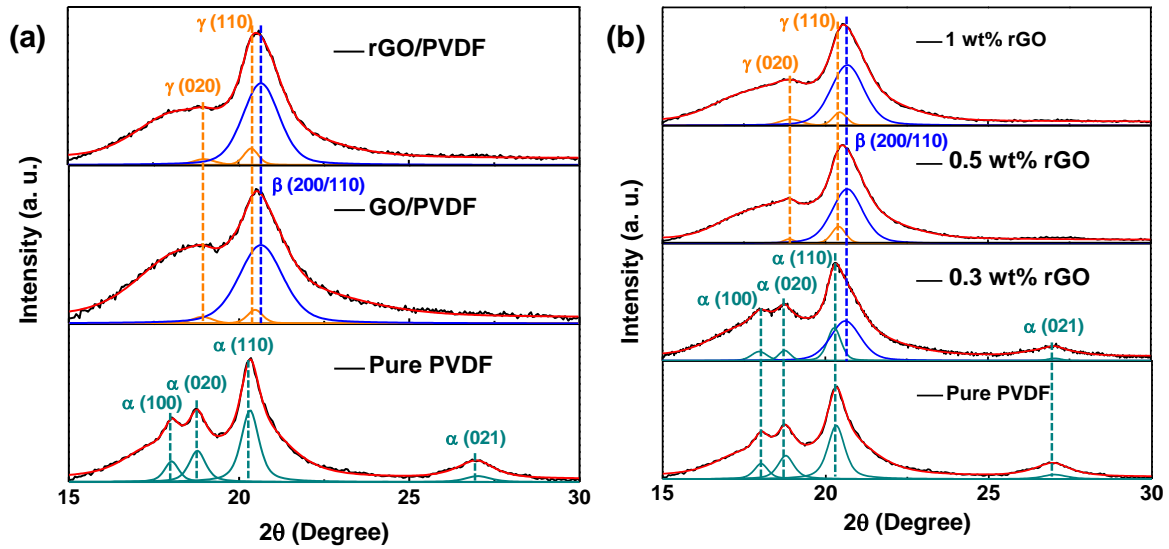


Figure 3.2. X-ray diffraction (XRD) spectroscopy of (a) a pure PVDF film, 2 wt% GO/PVDF, and 2 wt% rGO/PVDF composite films; and (b) pure PVDF and 0.3, 0.5, and 1 wt% rGO/PVDF composite films.

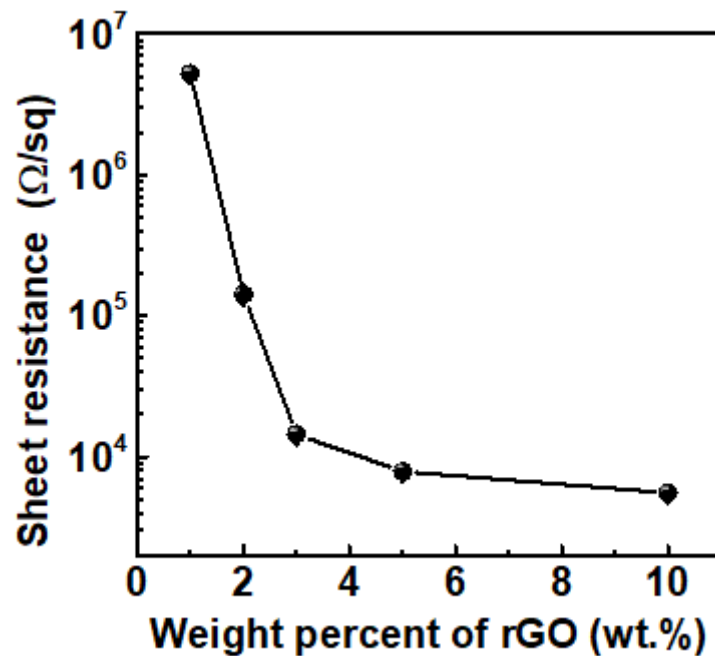


Figure 3.3. Sheet resistance of rGO/PVDF composite films as a function of the loading concentration of rGO.

The multilayer structure of interlocked microdome arrays enables e-skins with highly sensitive and linear pressure-sensing capabilities over an exceptionally broad pressure range. The multilayer e-skins are based on conductive composites of interlocked microdome arrays, which can detect static pressure using a piezoresistive sensing mode. Figure 3.4 shows the piezoresistive pressure sensing of multilayer e-skins based on the bulk film resistance (R_f) and contact resistance (R_c), where large amount of differences in contact resistance is dominant in e-skins with interlocked microstructures.¹⁵ As previously reported, although the small contact area between interlocked microdomes sharply increases due to the stress concentration effects and the subsequent deformation of microdomes, resulting in an extremely high pressure sensitivity, the linear pressure-sensing over a large pressure range is quite limited and the sensitivity significantly decreases when the pressure is over 1 kPa.^{15,60} These issues can be addressed with multilayer structures, which significantly increase the linearity of pressure sensing and maintain the high pressure sensitivity over a range of several hundred kPa. Figure 3.5a shows that interlocked microdome structures can enhance the pressure sensitivity compared with planar structures. Of particular importance, the linearity increases with the increase of interlocked microdome layers, indicating the important role of multilayer structures in enhancing the pressure linearity over large pressure ranges. Figure 3.5b shows the pressure sensitivity of e-skins with different numbers of stacked layers and planar structures. The pressure sensitivity (S) can be defined as $S = (\Delta I/I_0)/\Delta P$, where I is the current of the e-skins and P is the applied pressure. The interlocked microdome e-skins with different stacked layers have a sensitivity of at least four orders higher than that of planar e-skins. Importantly, e-skins with triple-stacked multilayers maintain their high sensitivity of 47 kPa^{-1} over an exceptionally broad pressure range (0.0013–353 kPa), demonstrating the linear pressure-sensing capability. In contrast, single- and double-layered e-skins can linearly detect the pressure with a pressure sensitivity of 20 kPa^{-1} up to 54 kPa and 27 kPa^{-1} up to 190 kPa, respectively. Their high sensitivity gradually decreases beyond the linear detection pressure region. Further increase of the interlocked layers over three layers results in a rather small increase of the sensitivity; i.e., the pressure sensitivity increased from 47 kPa^{-1} for three interlocked layers to 52 and 54 kPa^{-1} for four and five interlocked layers, respectively (Figure 3.6). In comparison with previous literature, the e-skins with triple multilayer e-skins exhibit a very high sensitivity over an exceptionally broad pressure range (0.0013–353 kPa) with a linear response to pressure (Figure 3.5c and Table 3.1).^{61,123,149,172,178-184} Most of sensors exhibited a linear range below 60 kPa. Only a few sensors (Refs. 11 and 35 in Figure 3.5c) showed a linear range over 60 kPa, but the sensitivities were below 0.026 kPa^{-1} . Although some of previous pressure sensors reported a higher sensitivity than our sensor, they exhibited a nonlinear response¹⁶⁹ or only have been achieved at low pressure range ($< 100 \text{ Pa}$).⁷⁷ The simultaneous achievement of linear sensing capability with a high sensitivity of 47 kPa^{-1} over a large pressure-sensing range from 1.3 Pa to 353 kPa has not been made in previous works.

To elucidate the structural effect of stacked multilayers on pressure sensitivity and linearity, we performed finite element calculations based on the model system with different numbers of interlocked layers (Figure 3.7a). Figure 3.5d shows the calculated contact area change of three different multilayer e-skins as a function of the applied pressure. The contact area of the interlocked microdome structures rapidly increases from almost zero in the initial unloading state to an extremely high value in the high-pressure loading state, which is attributed to the concentrated and amplified stress at a small spot between interlocked microdomes that greatly deforms the interlocked microdomes, resulting in the significant increase of the contact area (Figure 3.7b). With increasing number of stacked layers, the contact area dramatically increases due to the increased number of contacted microdomes. The contact area change in Figure 3.5d also indicates that the linearly increasing contact area starts to decrease at a pressure over ≈ 244 and 148 kPa for double- and single-interlocked layers, respectively, which matches the trend in Figure 3.5a well. The multilayer geometry can enhance the linearity of pressure sensing because the multilayer interlocked microdomes can distribute the applied stress to each stacked layer (Figure 3.5e). As a result, pressure sensitivity and linearity increase with an increase in the number of layers in multilayer e-skins. We also investigated the effect of the rGO loading concentration on the pressure-sensing performances of multilayer e-skins. Figure 3.8 shows the pressure-sensing performances of single- and multilayer e-skins with different rGO loading concentrations, which indicate that a 2 wt% rGO loading concentration is the best condition for multilayer e-skins (Section S3.1). In addition, the size of microdomes affects to the pressure sensing performances of multilayer e-skins. Figure 3.9 shows the pressure response of multilayer e-skins with different size of microdomes (Section S3.2).

To investigate the real-time pressure-sensing performances of multilayer e-skins, the relative current change of e-skins was measured under incremental pressure (Figure 3.5f). Under a step-by-step increase of pressure from 54 to 326 kPa, e-skins show a fast and linearly increasing current change. In the real-time pressure detection, multilayer e-skins show slight increase of sensor signals under high pressure over 200 kPa, due to the slow response of the bulk film. Although there are some delayed pressure reading at high pressure, those delayed pressure calculated by sensitivity of multilayer e-skins (47 kPa^{-1}) was only 2-4 % of the applied pressure, which does not affect much on the detected pressure. In addition, the interlocked geometry can provide a fast response and relaxation time due to the immediate deformation and recovery of surface microstructures in response to the applied pressure.¹⁵ At a low pressure of 10 kPa, which corresponds to the pressure of gentle finger touch, multilayer e-skins show a fast response and relaxation time of 40 and 20 ms, respectively (Figure 3.5g), which are comparable to the response time of human skin (30–50 ms).¹⁸⁵ Even at a high pressure of 200 kPa, which can induce significant microdome deformation, e-skins show a fast response/relaxation time of 150/30 ms. Furthermore, during repetitive cycles of high pressure loads of 272 kPa at a frequency of

0.5 Hz, e-skins show a reliable and uniform pressure-sensing performance up to 5,000 cycles (Figure 3.5h).

S3.1 Pressure sensing performances of multilayered e-skins depending on the loading concentration of rGO

The static pressure sensing performance of multilayer e-skins was highly affected by the loading concentration of rGO in rGO/PVDF composite films. Figure S6a plots pressure-sensing performances of single interlocked microdome e-skins with different loading rGO concentration. In single interlocked structures, e-skins with lower rGO concentration show higher pressure sensitivity, because the modulus of rGO/PVDF composite films increases with increasing rGO concentration, leading to reduced amount of deformation in interlocked microdomes.¹ On the other hand, triple interlocked microdome e-skins show different trends, as e-skins with 2 weight percent (wt%) rGO loading concentration provide higher pressure sensitivity than e-skins with 1 and 3 wt% rGO loading concentrations (Figure S6b). This behavior can be attributed to the fact that the initial resistance of multilayer interlocked microdome e-skins is much higher than that of single interlocked microdome e-skins due to the increased contact resistance between multilayer interlocked microdomes (Figure S6c). In triple interlocked geometry, the high initial resistance of e-skins with 1 wt% rGO/PVDF composites imposes a too high barrier for the pressure-induced variation of piezoresistive current. On the other hand, e-skins with 3 wt% rGO/PVDF composites are relatively stiff compared to 2 wt% rGO/PVDF composites, resulting in a lower pressure sensitivity.

S3.2 Effect of size of microdomes on pressure sensing performances

To investigate the effect of size of microdomes on pressure sensing performances, we fabricated triple multilayer e-skins based on various size of microdome-patterned films (Figure S7a-c). Figure S7d shows the pressure responses of multilayer e-skins based on microdomes with different pitch size. The microdome arrays with larger pitch size provide smaller surface area and decreased number of contact spots between interlocked microdomes, resulting in lower sensitivity in multilayer e-skins. In addition, due to the diminished stress distribution between decreased number of contacted spots, multilayer e-skins based on microdomes with larger pitch size show linear pressure sensing performances up to lower pressure range (217 kPa) than that of smaller pitch size, resulting in the sensitivity change from 22.8 kPa⁻¹ to 15.8 kPa⁻¹ when the pressure is over 217 kPa. We also investigated the effect of different dome diameter on the performances of multilayer e-skins at the fixed dome diameter to pitch size ratio of 0.833 (Figure S7e). We confirmed that the multilayer e-skins based on microdomes with various diameter sizes (10, 25, 50 μm) show similar pressure sensing performances, which can be attributed to the same ratio between dome diameter and pitch size, resulting in the same total contact area between

interlocked microdome arrays and contact area change in response to applied pressure. However, microdome patterned films with larger diameter will have larger thickness due to increased height of microdomes, which will cause decreased flexibility of e-skins.

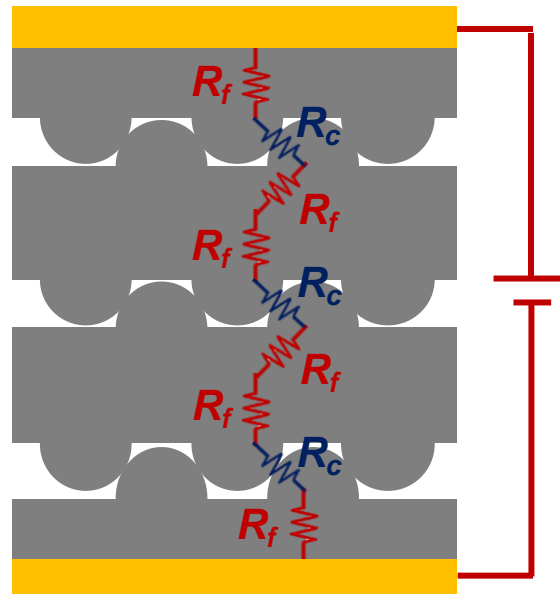


Figure 3.4. Circuit diagram of triple multilayer e-skins. piezoresistive properties of multilayer e-skins mainly depend on the bulk film resistance (R_f) and contact resistance between neighboring interlocked microdomes (R_c), which are connected in series.

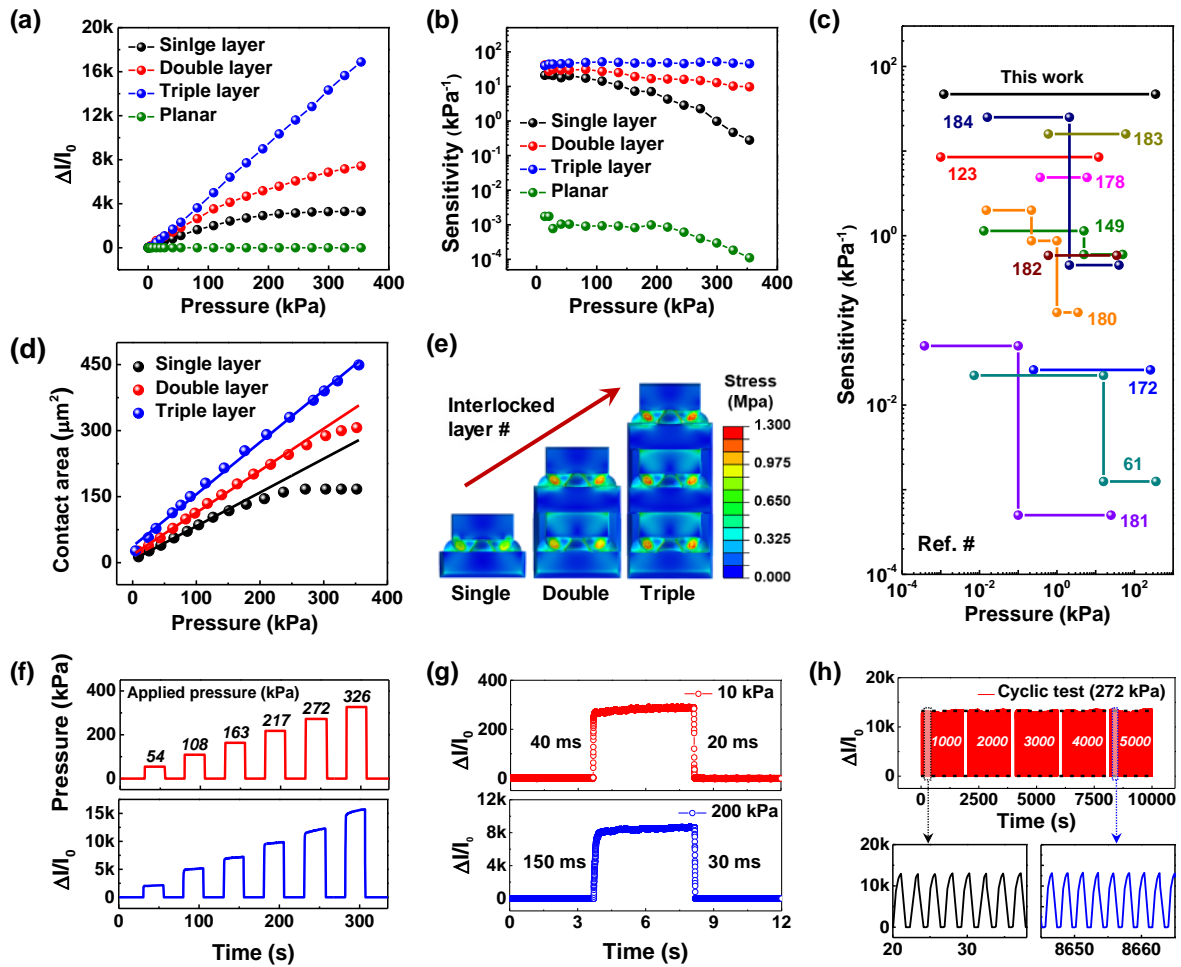


Figure 3.5. Piezoresistive static pressure-sensing performances of multilayer interlocked microdome e-skins. (a) Relative current of e-skins with multilayer geometry with different numbers of stacked layers and planar geometry in response to the applied pressure. (b) Pressure sensitivity of e-skins converted from Figure 2a. (c) Comparison of the sensitivity and linear sensing performances based on this work and previous reports. (d) Finite element calculation of the contact area change as a function of pressure for different numbers of stacked layers. (e) Finite element calculations of the local stress distribution for different numbers of interlocked layers showing the concentrated and amplified stress at the small spot between interlocked microdomes under a pressure of 355 kPa. (f) Real-time pressure monitoring of e-skins at an applied pressure of 54, 108, 163, 217, 272, and 326 kPa. (g) Response and relaxation times for multilayer e-skins under different pressures of 10 and 200 kPa. (h) Cyclic stability test of multilayer e-skins under repetitive high-pressure loading of 272 kPa at a frequency of 0.5 Hz.

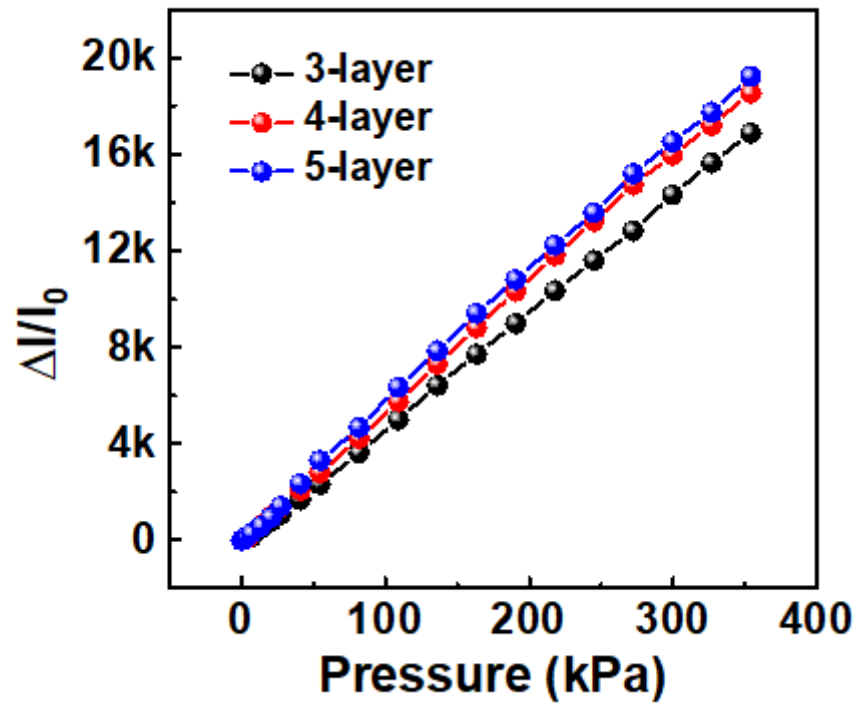


Figure 3.6. Static pressure-sensing performances of multilayer e-skins over three layers.

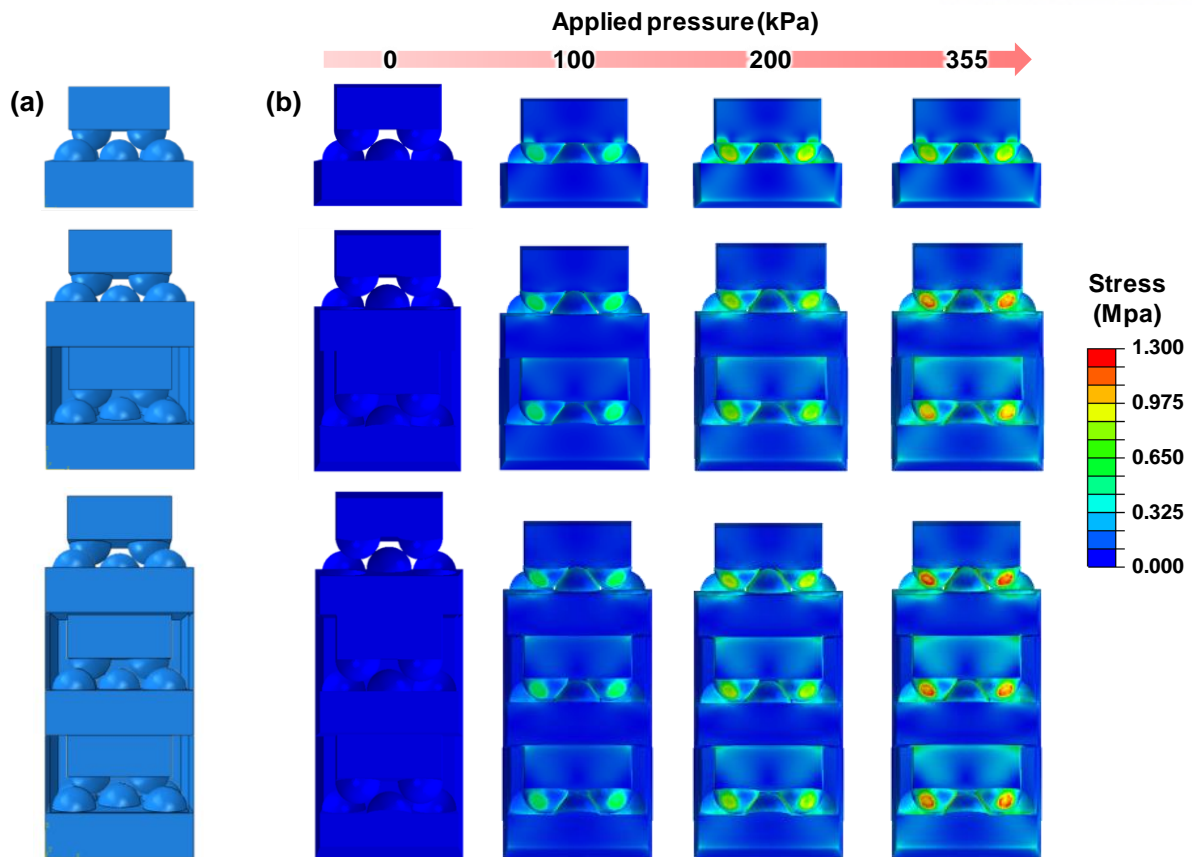


Figure 3.7. Finite-element calculation showing the stress distribution in multilayer e-skins with single, double, and triple layers. (a) Model systems with different number of interlocked layers. (b) Stress distribution of multilayer e-skins with single, double, and triple layers under different applied pressure.

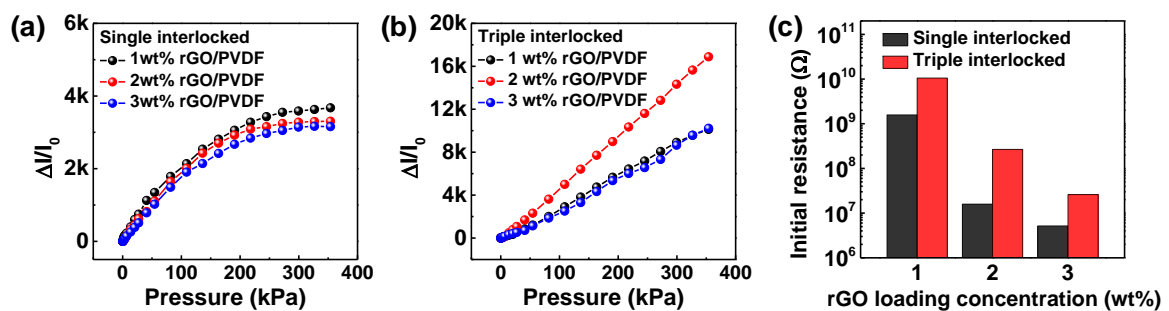


Figure 3.8. (a) Static pressure-sensing performances of single-interlocked e-skins with different rGO loading concentrations. (b) Static pressure-sensing performances of triple-interlocked e-skins with different rGO loading concentrations. (c) Initial resistance of single- and triple-interlocked e-skins using 1 and 2 wt% rGO/PVDF composite films.

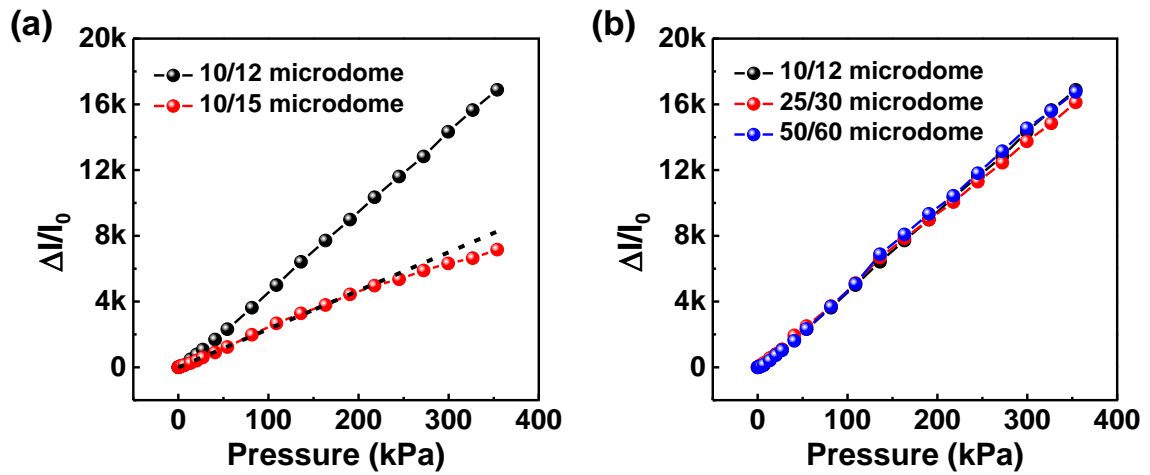


Figure 3.9. Pressure-sensing performances of multilayer e-skins based on different size of microdomes. Cross-sectional SEM images of microdome arrays with (a) 10, 15, and 4 μm , (b) 25, 30, and 10 μm , (c) 50, 60, 20 μm in diameter, pitch, and height, respectively. Relative current of multilayer e-skins based on microdomes with (d) different pitch size and (e) different diameter.

Table 3.1. Summary of pressure sensors with linear pressure responses and their performances.

NO.	Materials	Type	Range [kPa]	Sensitivity [kPa ⁻¹]	Linear range [kPa]	Ref.
1	PEDOT:PSS/PUD micropyramid	Resistive	0.37 – 5.9	4.88	0.37 – 5.9	178
2	Porous CNT/PDMS	Resistive	0.25 – 260	0.026	0.25 – 100	172
3	Au NWs	Resistive	0.013 – 50	1.14 (<5 kPa) 0.6 (<50 kPa)	0.013 – 5	149
4	Single crystal silicon	Resistive	– 200	0.0041	– 200	179
5	Polyaniline/Au micropillar	Resistive	0.015 – 3.5	2.0 (< 0.22 kPa) 0.87 (< 1 kPa) 0.12 (< 3.5 kPa)	0.015 – 0.22	180
6	CNT microyarn	Capacitive	0.00038 – 25	0.05 (< 0.1 kPa) 0.0005 (> 10 kPa)	0.00038 – 0.1	181
7	Graphene/PDMS hierarchical microdome	Resistive	0.001 – 12	8.5	0.001 – 12	123
8	Carbon black- coated fabric	Resistive	0.6 – 35	0.585	0.6 – 35	182
9	Hollow structured graphene-silicon composite	Resistive	0.6 – 60	15.9	0.6 – 60	183
10	Ecoflex dielectric layer with Ag electrode	Capacitive	0.0073 – 360	0.0224 (< 16 kPa) 0.00125 (< 360 kPa)	0.0073 – 16	61
11	rGO/PDMS microstructures	Resistive	0.016 – 40	25.1 (<2.6 kPa) 0.45 (<40 kPa)	0.016 – 2.6	184
12	rGO/PVDF multilayer interlocked microdome	Resistive	0.0013 – 353	47.7	0.0013 – 353	This work

Multilayer e-skins with high sensitivity, large dynamic pressure-sensing range, and linear detection capabilities can be used in diverse applications requiring a large dynamic pressure range from low to high pressure regimes. To demonstrate the low pressure detection capability of our e-skins, we applied weak gas flow to the surface of multilayer e-skins (Figure 3.10a). Figure 3.10b shows the piezoresistive response of multilayer e-skins under weak gas flow with flow rates ranging from 3 to 15 L/min. The gas flow rate of 3 L/min corresponds to an extremely low static pressure of ≈ 1.3 Pa, demonstrating the ultra-low minimum detection limit of our e-skins (Figure 3.11). Even in a very low pressure region, the real-time monitoring of weak gas flow exhibits no significant noise signals, indicating a stable operation of multilayer e-skins. (Figure 3.10c).

In addition to piezoresistive static pressure sensing, multilayer e-skins can be used under dynamic pressure with high frequency due to the piezoelectric properties of rGO/PVDF composites. In this composite, conductive rGO fillers can transform the PVDF phase from the nonpolar α -phase to the polar β -phase, which can induce high piezoelectric properties.^{20,177} Similar to the piezoresistive sensing mode, interlocked e-skins have higher piezoelectric performances due to the effective stress concentration at the small contact area between microdomes compared with planar structures (Figure 3.10d). The introduction of multilayer geometry in e-skins provides a much higher piezopotential compared with single-interlocked e-skins due to the increased contact area between multilayer-interlocked microdomes. The rGO loading concentration also affects the piezoelectric pressure-sensing performances of multilayer e-skins. Multilayer e-skins with a 2 wt% rGO loading concentration show slightly lower piezoelectric performances than those with a 1 wt% rGO loading concentration (Figure 3.12). This behavior is attributed to the increasing film conductivity with higher rGO loading, which can decrease the piezoelectric polarization of composite films due to the leakage current.^{22,186}

The fast response time of piezoelectric e-skins enables the detection of acoustic sound waves with a wide range of frequencies of up to several tens of kHz (Figure 3.10e). To demonstrate the sound detection performances of e-skins, sound waves were applied to multilayer e-skins using a commercially available microphone. The e-skins with triple-interlocked multilayers show the best sound wave detection performance due to the immediate contact/release of interlocked microdomes in response to vibrations and an increased overall contact area change (Figure 3.10f). The piezoelectric voltage output increases with increasing sound frequency of up to 20 kHz and then slowly decreases. In contrast, single-interlocked microdome e-skins have a slightly decreased piezoelectric voltage due to the reduced contact area and planar e-skins provide a tiny piezoelectric voltage. Figure 3.13 shows the fast Fourier transform (FFT) spectra of the piezoelectric signals of multilayer and planar e-skins after applying a sound wave with a single frequency of 1, 5, 10, and 20 kHz. The multilayer e-skins exhibit a single distinguishable peak according to each sound wave, where the amplitude is 0.006 at 1 kHz and increases with the frequency of the sound wave (Figure 3.13a). On the other hand, the planar

e-skins reveal weak signals with the amplitudes below 0.0005 (Figure 3.13b), indicating a low piezoelectric sensitivity of planar e-skins compared with multilayer e-skins.

The multilayer e-skins can precisely detect time-dependent variation of acoustic sound when the well-known piece “Piano Sonata K.545, 1st movement (W.A. Mozart)” was played. Here we chose electric guitar music, which covers a large range of frequencies. Figure 3g shows the time-dependent sound waveforms and corresponding spectrograms, which were converted using a short-time Fourier transform (STFT) of the original sound source (black) and recorded piezoelectric signals from multilayer e-skins (red) and planar e-skins (blue). The time-dependent sound waveform and corresponding spectrogram of music recorded by multilayer e-skins accurately match with those of the original sound source covering a large range of frequencies of up to 6 kHz. The enlarged plot of the frequency spectrogram further demonstrates the superior sound wave detection performance of multilayer e-skins (Figure 3.10h). Conversely, planar e-skins with low piezoelectric outputs could not precisely record the waveforms and spectrogram of the original music (Figure 3.10g, blue). The multilayer e-skins also precisely detected the variation of the sound waveform when the same music was played by different musical instruments. Figure 3.14a shows that the waveforms and corresponding spectrograms of the same music differ depending on the musical instruments (piano, guitar, electric guitar). The waveforms and frequency spectrograms recorded from multilayer e-skins in Figure 3.14b indicate that the information from music played by different musical instruments matches well with those of the original sound source.

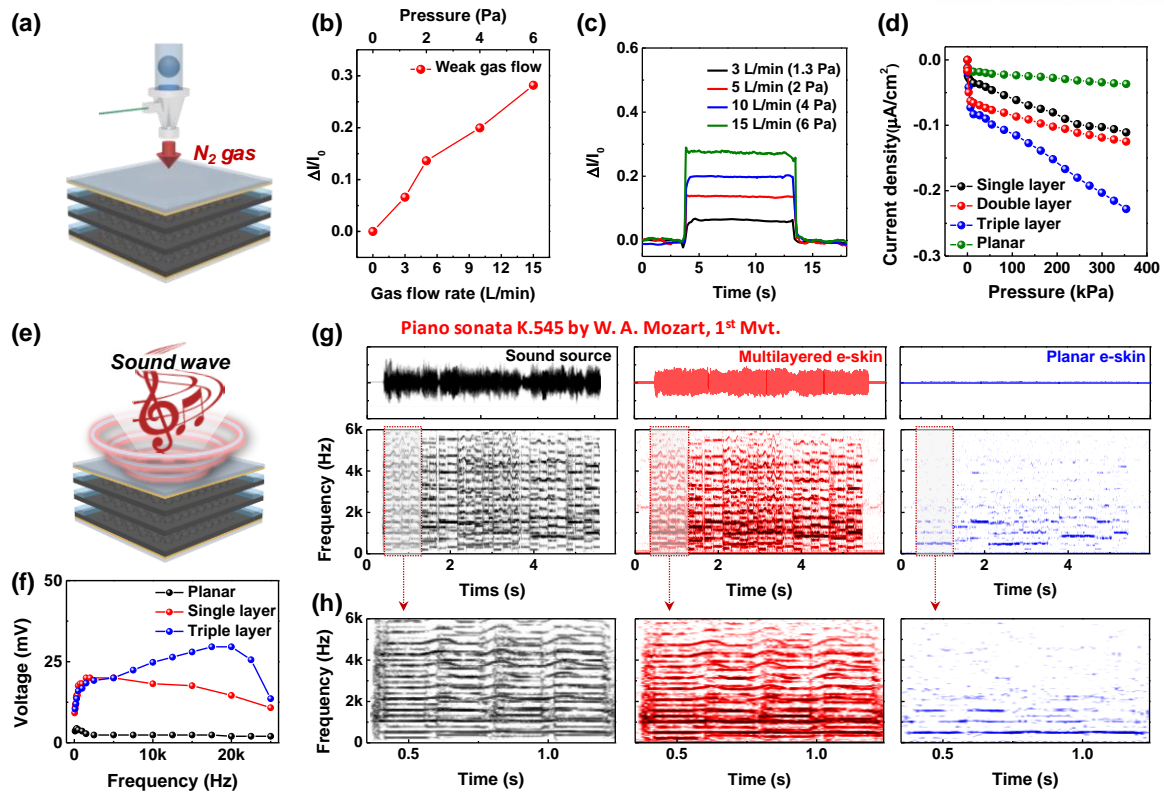


Figure 3.10. Application of weak pressure on multilayer e-skins. (a) Schematic illustration showing the detection of weak air flow by multilayer e-skins. (b) Relative current change of multilayer e-skins as a function of gas flow rate. (c) Real-time monitoring of gas flow by multilayer e-skins. (d) Piezoelectric dynamic pressure-sensing performances of e-skins with different multilayer structure geometries with different stacked layers and planar structures. (e) Schematic of sound wave detection by multilayer e-skins. (f) Detection of the sound wave with single frequency for planar, single-interlocked, and multilayer interlocked microdome e-skins. (g) Sound waveforms and corresponding spectrograms converted by STFT from the original sound source (black), signals recorded from multilayer e-skins (red), and planar e-skins (blue). (h) Expanded frequency spectrograms in Figure 3g.

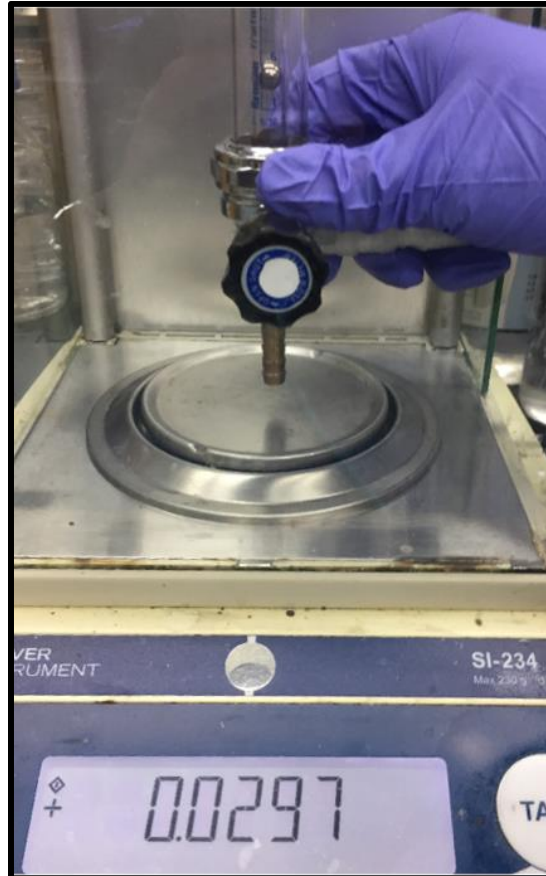


Figure 3.11. Applied pressure due to weak gas flow with a flow rate of 3 L/min. Considering the size of the multilayer e-skins, the applied pressure due to gas flow with a flow rate of 3 L/min is ≈ 1.3 Pa.

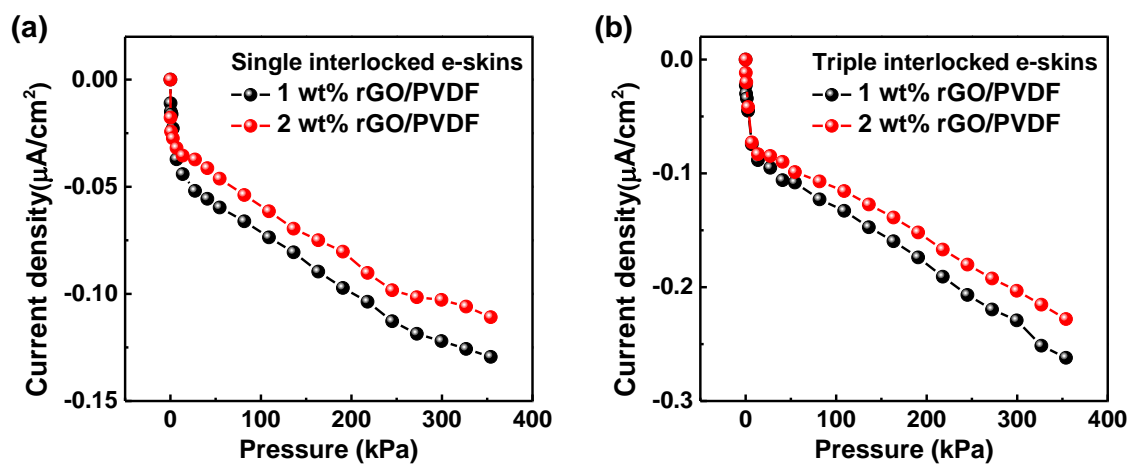


Figure 3.12. (a) Dynamic pressure-sensing performances of single-interlocked e-skins with 1 and 2 wt% rGO/PVDF composite films. (b) Dynamic pressure-sensing performances of triple-interlocked e-skins with 1 and 2 wt% rGO/PVDF composite films.

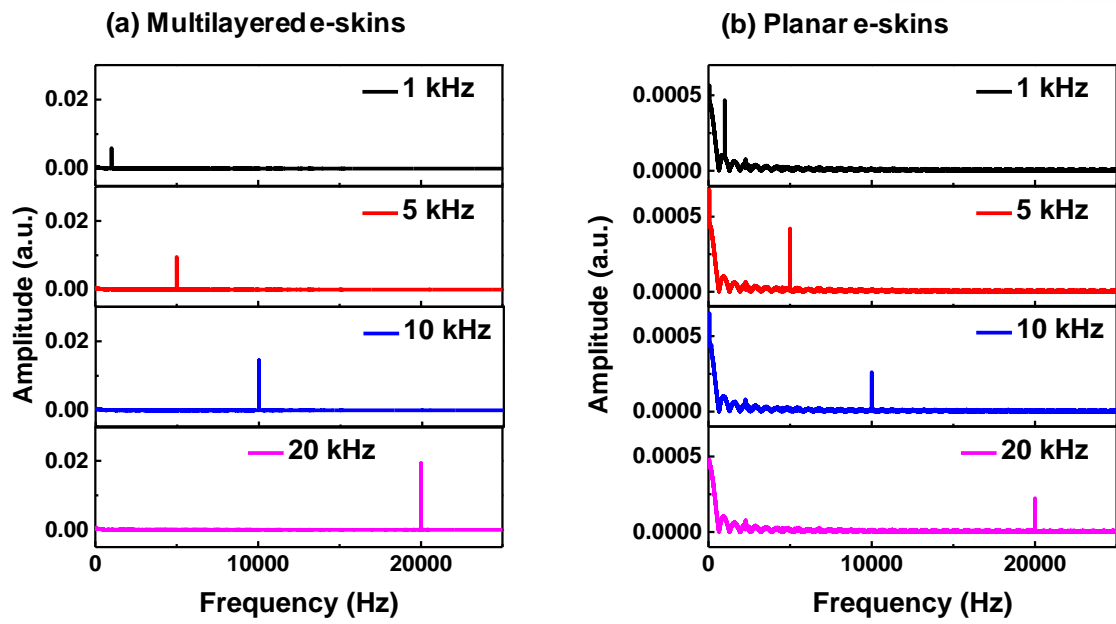


Figure 3.13. Piezoelectric single sound frequency detection performances of (a) multilayer e-skins and (b) planar e-skins.

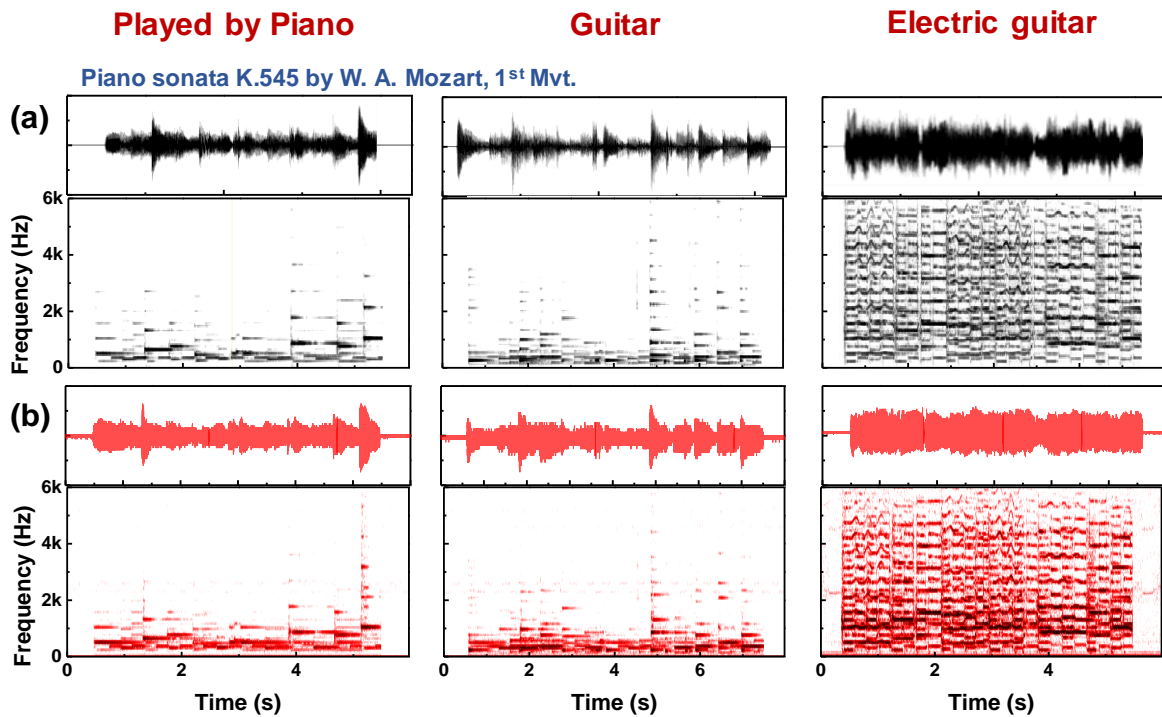


Figure 3.14. (a) Sound waveforms and corresponding spectrograms converted by STFT of the original sound from a piano, guitar, and electric guitar (black). (b) Recorded piezoelectric waveforms and corresponding spectrograms from multilayer e-skins, converted by STFT of sound from a piano, guitar, and electric guitar (red).

In addition to low pressure-sensing performances, multilayer e-skins with high sensitivity and large pressure-sensing range with a linear sensing performance can be used for applications requiring the detection of medium pressure (1–20 kPa). For medium pressure sensing applications, highly flexible multilayer e-skins were used as wearable healthcare devices for the monitoring of human breathing and wrist pulses that are considered the four primary vital signs of human life (pulse rate, blood pressure, respiration rate, and temperature).¹⁸⁷ For this purpose, multilayer e-skins were attached to the nostrils (Figure 3.15a). The multilayer e-skins clearly differentiate between weak and deep breathing signals of a volunteer (Figure 3.15b). The monitored weak breathing signals provide a breathing rate of 18 breaths/min, which corresponds to that of healthy adults (12–20 breaths/min).¹⁸⁸ In contrast, intentional deep breathing results in the increase of the signal intensity and decrease of the respiration rate to 12 breaths/min. This capability of breathing detection allows the use of e-skins for applications such as diagnosing the sudden infant death syndrome and monitoring body health state during exercise. As other primary vital signs of human life, the monitoring of pulse signals provides medical information to diagnose and prevent cardiovascular diseases.^{108,189} Figure 3.15c shows multilayer e-skins attached on wrist skin, which provide real-time monitoring of the wrist pulse pressure period and waveform (Figure 3.15d). A pulse frequency of 72 beats/min was recorded, which corresponds to the value of healthy adults.¹⁹⁰ In addition, the pulse waveform contains three distinguishable peaks P_1 , P_2 , and P_3 , which correspond to incident, tidal, and diastolic waves, respectively.¹⁰⁸ Based on these three peaks, the arterial stiffness of a volunteer can be diagnosed by analyzing the radial augmentation index ($AI_r = P_2/P_1$), diastolic augmentation index ($DAI_r = P_3/P_1$), and digital volume pulse time ($\Delta T_{DVP} = t_{P_2} - t_{P_1}$), where t_{P_1} and t_{P_2} are the time of the first (P_1) and second peak (P_2), respectively. The calculated AI_r , DAI_r , and ΔT_{DVP} values under relaxed conditions are 0.472, 0.264, and 0.196, respectively, which match the expected values for healthy adults in their mid-twenties.¹⁰⁸

The multilayer e-skins with pixel array possess the ability to perceive the magnitude and spatial distribution of various tactile stimuli. Figure 3.15e shows the schematic illustration of 3×3 pixel arrays of e-skins sandwiched by patterned electrodes. When different shapes of loads in the medium pressure region (≈ 2 –20 kPa) are applied on e-skin arrays (Figures 3.15f–h), the sensor array can differentiate the compressed local regions from other regions, demonstrating the ability of e-skins to perceive the spatial pressure distribution (Figure 3.15f). The linear pressure-sensing capability of multilayer e-skins enables the precise perception of the magnitude and location of the applied pressure. When two different loads, with one load weighing twice than that of the other, are applied to the sensor array, the magnitude and difference of the applied pressure can be visualized by a color map (Figure 3.15g). In addition, for the large load size, the sensor array can differentiate between the center and corner areas of the object based on the color mapping image (Figure 3.15h).

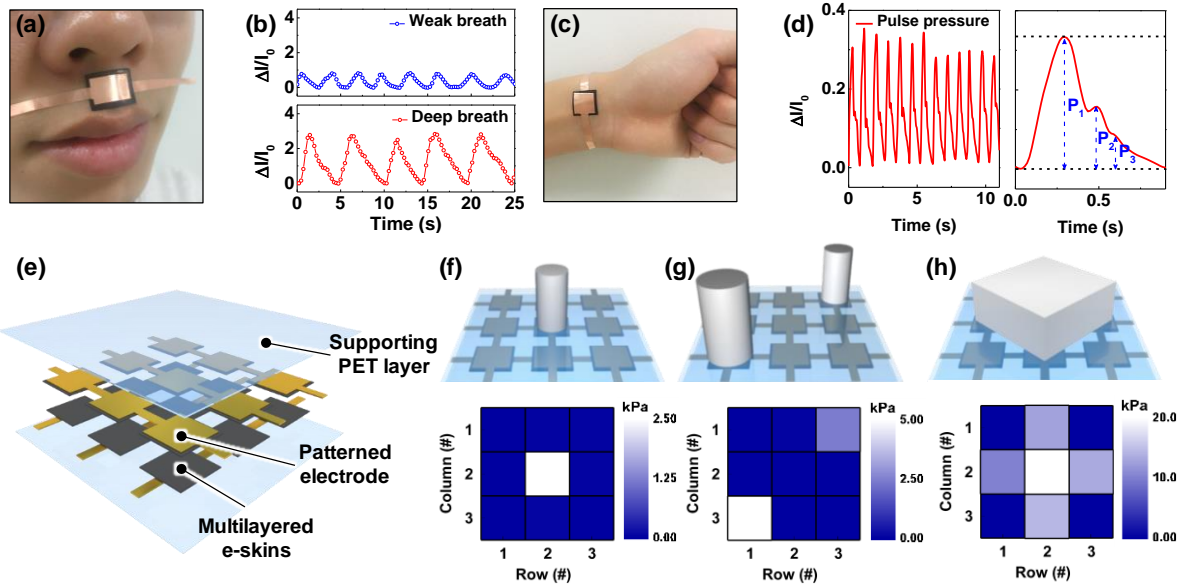


Figure 3.15. Application of medium pressure on multilayer e-skins. (a) Photograph showing the detection of human breath by attaching multilayer e-skins to the nostril of a volunteer. (b) Monitored real-time signals of weak and deep breathing detected by multilayer e-skins. (c) Photograph showing the pulse pressure detection after attaching multilayer e-skins to wrist skin. (d) Real-time monitoring of the pulse signals and expanded pulse wave containing three peaks, *i.e.*, P_1 (incident wave), P_2 (tidal wave), and P_3 (diastolic wave), recorded by multilayer e-skins. (e) Schematic of the 3×3 sensor array for the multilayer e-skins with an ability to perceive the magnitude and spatial distribution of the applied pressure. (f–h) Schematics of the detection of applied pressure from different shapes and weights of loads and their corresponding pressure maps.

Monitoring of the foot pressure distribution is considered to be a useful tool in the fields of footwear design, sport biomechanics, and wearable healthcare systems.¹⁹¹ In particular, abnormal gait patterns and excessive foot pressure in certain areas may cause several diseases such as diabetic foot ulcer.¹⁹² In addition, representative symptom of patients with Parkinson's disease was known as characteristic gait patterns, which are noticeably different with normal gait patterns.¹⁹³ Therefore, monitoring of the walker's gait patterns and posture enables the early diagnosis and progress monitoring of those diseases. Pressure sensors with highly sensitive and ultra large range pressure sensing capabilities up to several hundred kPa are required for the precise detection of the foot pressure distribution. In addition, linear pressure sensing is critical for directly comparing the foot pressure distribution of different areas using the contour color maps. Our multilayer e-skins have excellent potential for this purpose due to their high sensitivity (47 kPa^{-1}) and linear pressure sensing over an exceptionally broad pressure range (0.0013–353 kPa). To fabricate a smart insole for the monitoring of the foot pressure distribution, we designed a sensor array consisting of 4×8 pixel e-skin arrays and supporting polyethylene terephthalate (PET) layers (Figure 3.16a). Firstly, to investigate the distribution of the low-pressure detection capability, a petri dish was placed upside down on the sensor array for the application of circular-distributed low pressure below 300 Pa (Figure 3.16b). The corresponding map of the sensor array clearly shows the circular pressure distribution with different colors (Figure 3.16c). Our sensor array was used as a smart insole for the monitoring of the high foot pressure distribution experienced during walking. Figure 3.16d shows the schematics of five different walking motions and the corresponding color maps monitored by a smart insole based on multilayer e-skins. The smart insole precisely detects the foot pressure distribution, where red areas indicate concentrated high stress and blue areas reflect low stress, demonstrating potential applications in wearable medical devices and the sports industry.

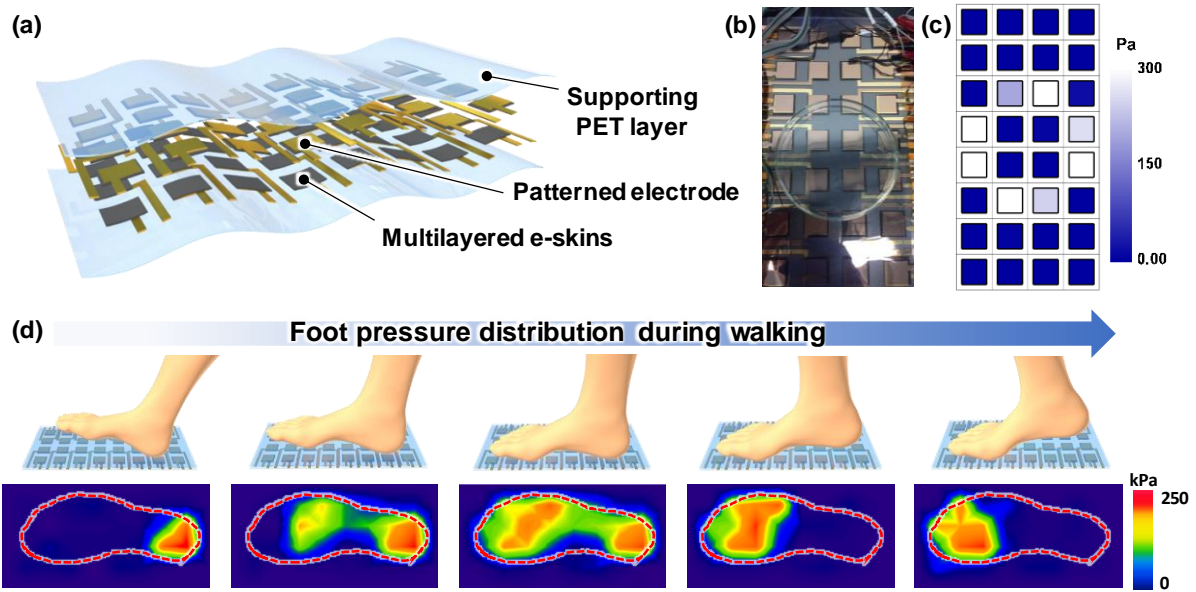


Figure 3.16. Application of high pressure to multilayer e-skins. (a) Schematic of the smart insole consisting of 4×8 pixel arrays of multilayer e-skins, patterned electrodes, and supporting PET layers. (b) Photograph of 4×8 pixel arrays of multilayer e-skins with pressure applied by an upside-down petri dish. (c) Corresponding pressure map. (d) Schematics of five walking motions on the smart insole to monitor the foot pressure distribution and their corresponding pressure maps.

3.4 Conclusion

In conclusion, we demonstrated a flexible ferroelectric sensor with high pressure sensitivity and linear response over an exceptionally broad pressure range. The suggested ferroelectric sensor is based on the rGO/PVDF ferroelectric composites with a multilayer interlocked microdome geometry. Our multilayer e-skins showed a simultaneous achievement of linear sensing capability with an ultrahigh sensitivity of 47 kPa^{-1} over an exceptionally large pressure-sensing range from 1.3 Pa to 353 kPa. The ultrahigh pressure sensitivity and linear response over an exceptionally broad pressure range can be achieved by the effective stress concentration, increased contact area, and stress distribution between multilayer interlocked microdome arrays, which has been also verified by the theoretical calculations. These sensing capabilities enabled our e-skins to monitor diverse stimuli from low to high pressure range. For example, our e-skins can precisely monitor the weak gas flow and acoustic sound in a low pressure regime, respiration and pulse pressure in a medium pressure regime, and plantar pressure monitoring in a high pressure regime. The suggested e-skins may be useful for diverse sensor applications requiring precise detection of pressure from extremely low to high pressure range such as robotics, prostheses, and wearable healthcare devices.

Chapter 4. Human skin-inspired multilayered flexible electronic sensors with tunable sensitivity and linearity

4.1 Introduction

Electronic skin (e-skin), which emulates the capabilities of human skin and confer various functionalities, has emerged as one of the promising technology of wearable devices.^{7,61} Recently, e-skins integrated with different functionalities have been developed to mimic sensory capabilities of human skin, which can perceive different external stimuli including magnitude and distribution of mechanical stimuli, temperature, and subtle textural differences.^{22,61,179,181,194-197} Light-weight, flexible, and biocompatible e-skins with multifunctionalities have wide potential applications in soft robotics, designing artificial prostheses, and real-time healthcare monitoring.¹⁹⁸⁻²⁰³ In particular, high-performance pressure sensing capability of e-skins based on various mechano-transduction mechanisms is a key component to realize wearable devices that provide real-time monitoring of vital signals such as blood pressure, pulse rate, and respiration rate.^{141,149,168,204} For the application of e-skin as the wearable devices in real life, the combined pressure sensing capabilities of linearity, high sensitivity, and wide detection range are critical, however, rarely have been demonstrated.

Pressure-sensing e-skins have been developed using various mechano-transduction mechanisms (e.g., piezoresistivity, capacitance, piezoelectricity, and triboelectricity) for precise conversion of mechanical stimuli (e.g., dynamic/static pressure, strain, and shear force) into electrical signals.^{60,205-208} Especially, piezoresistive-type sensors, which perceive mechanical stimuli by resistance change, have attracted considerable research interest due to their simple fabrication process, low cost, and easy readout mechanism.¹⁷¹ Conventional piezoresistive sensors utilize the pressure-induced deformation of elastic composites to decrease the distance between conductive fillers, resulting in the decrease in the bulk film resistance (R_f).⁷ Although conventional planar composites exhibit low sensitivity, introduction of micro/nanostructures (e.g., micro-domes/pillars/pyramids,^{15,103} microporous structures,^{172,209} and sea-urchin nanoparticles²¹⁰) to conductive polymer composites can improve sensitivity *via* significant changes in contact area and contact resistance. Park et al. reported a microdome-patterned carbon nanotube (CNT)/polydimethylsiloxane (PDMS) composite which exhibited interlocked geometry and a sensitivity of 15.1 kPa⁻¹.¹⁵ Further, Jung et al. developed an multi-walled carbon nanotubes (MWCNTs)-mixed porous pressure sensor using a reverse micellar solution.¹⁷² Although microstructured e-skins indicated enhanced sensing performance in contrast to planar e-skins, they exhibited both limited sensitivity and pressure detection range due to insufficient deformation of the piezoresistive materials. It should be noted that previous e-skins primarily utilized a sandwiched

electrode structure with piezoresistive materials sandwiched between top and bottom electrodes.^{15,103,172,209-211} In this structure, besides the contact between active layer and electrodes, the pressure-induced bulk film resistance change is a primary factor in determining the pressure sensitivity, resulting in the limited pressure sensitivity. Alternatively, introduction of a coplanar electrode structure (characterized by an active layer and two electrodes on the same side of the active layer) can ensure high pressure sensitivity.^{107,178,212-214} This could be attributed to sensor resistance being dominantly affected by deformation of surface microstructures rather than bulk film, resulting in the significant change of the contact resistance rather than bulk film resistance in contrast to sensors with sandwiched electrode structures for the same applied pressure (Figure 4.1). In addition, employing slit²⁰⁰ or interdigitated¹⁴⁹ patterns on the electrode can induce high initial resistance, thus resulting in enhanced pressure sensitivity. For example, a pressure sensor with the coplanar electrode facing a micro-pyramid patterned polypyrrole (PPy) layer indicated a very high sensitivity of 1907 kPa⁻¹; however, it was limited by a narrow pressure detection range (less than 100 Pa).²¹⁵ Further, pressure sensors with carbon foam integrated on the interdigitated electrode exhibited high sensitivity of 100.29 kPa⁻¹ at pressure values less than 2 kPa.²¹⁶ Although pressure sensors with coplanar electrodes have been shown to exhibit high sensitivity, they indicate a non-linear pressure response or a narrow linear range because piezoresistance is mainly governed by variation in contact resistance which causes faster resistance saturation in contrast to pressure sensors with sandwiched electrodes.²¹⁷

In order to simultaneously obtain a linear response over a large pressure range as well as high pressure sensitivity, various approaches have been suggested to further increase the contact area change and control the deformation patterns of active materials under pressure. Bae et al. fabricated a pressure sensor characterized by hierarchical microstructure with graphene monolayer, resulting in a pressure sensitivity of 8.5 kPa⁻¹ with a high linearity in pressure range up to 12 kPa.¹²³ Luo et al. suggested the piezoresistive sensor based on the hollow structure of graphene and PDMS composite which indicated linear detection and a sensitivity of 15.9 kPa⁻¹ until 60 kPa.¹⁸³ Recently, Lee et al. utilized the multi-layered interlocked polyvinylidene fluoride (PVDF)/reduced graphene oxide (rGO) composite to design a pressure sensor with a sensitivity of 47.7 kPa⁻¹ up to a pressure of 353 kPa.¹²² However, most previous sensors exhibited sensitivities less than 50 kPa⁻¹ which are insufficient to detect subtle differences in bio-signals such as pulse pressure variation and intracranial pressure. Thus, e-skins exhibiting high pressure sensitivities at high applied pressures are essential for applications requiring high sensitivities.

This study proposed a novel design comprising coplanar electrodes interlocked with microdomes coated with conductivity-gradient multi-layers to fabricate e-skins characterized by high linearity, ultrahigh pressure sensitivity, and a wide pressure detection range. For the enhanced sensitivity, we designed a coplanar electrode based on interlocked microdome structure, where the top microdome-patterned layer is used as an active layer for the pressure sensing and the bottom microdome-patterned

layer acts as an electrode for the coplanar electrode design. In particular, we employed the multi-layered structure with gradient conductivity based on the conductive polymer composite (PEDOT:PSS/PUD) on the top microdome-patterned layer, which enables ultrahigh variation in piezoresistance and wide range pressure detection. Furthermore, the interlocked layers were characterized by modulus-gradient geometry to ensure effective stress concentration effect and reliable working of the e-skin. The e-skin designed in this study indicated an ultrahigh pressure sensitivity of $3.8 \times 10^5 \text{ kPa}^{-1}$, which was constantly maintained at pressure values ranging from 0.8 Pa to 100 kPa. For a proof of concept application, the e-skin was utilized as a wearable sensor for detection of pulse pressure and hand motion during manipulation of objects. Finally, a 3×3 pixel array of e-skins was fabricated to differentiate gases with different flow rates or densities.

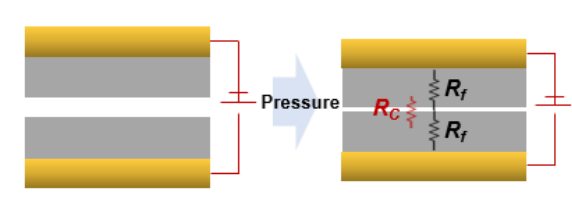
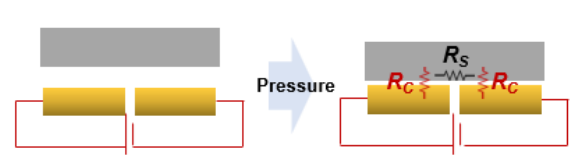
	Scheme of working mechanism	Related resistances
Sandwiched electrode		<p>Bulk film resistance (R_f) + Contact resistance (R_c) ↓ Total resistance</p>
Coplanar electrode		<p>Sheet resistance (R_s) + Contact resistance (R_c) ↓ Total resistance</p>

Figure 4.1. Comparison of the electrode with sandwiched structure and coplanar structure (Upper) A scheme of the sandwiched electrode which experiences both of contact resistance and bulk film resistance and affects change of total resistance (Bottom) A scheme of the coplanar electrode which only is affected by the contact resistance.

4.2 Experimental Details

Conductivity Control of PEDOT:PSS: Fabrication of the multi-layered pressure sensor comprised addition of EG (Sigma Aldrich) to PEDOT:PSS (CLEVIOS PH1000). EG, which is biocompatible and readily soluble, was utilized as the conductivity enhancer. Further, surfactants, including 4-dodecylbenzene sulfonic acid (Sigma Aldrich) and 3-methacryloxypropyltrimethoxysilane (Sigma Aldrich), were added and stirred for 6 h to increase wettability and develop a fine film on the PDMS substrate. Subsequently, the amount of EG was varied and the lowest resistance of the solution was set as 170 Ω (for an EG to PEDOT:PSS ratio of 1:20). Finally, PUD (Alberdingk U3251) was added to the PEDOT:PSS solution to rendered elastic properties.

Fabrication of Substrates with Interlocked Structures: The microdome-patterned top layer (5:1 mixture of PDMS (Sylgard 184, Dow Corning) and a curing agent) was cast onto a microdome patterned silicon mold and cured at 80 °C for 2 h. The prepared PEDOT:PSS/PUD solution with different conductivity was coated on the cured PDMS substrate with multiple spin-coating for the multi-layered composite. In this regard, the PEDOT:PSS/PUD solution was filtered using a 0.45 μm PVDF syringe filter and spin-coated on the prepared PDMS substrate. Subsequently, it was treated with O₂ plasma for 5 min and annealed at 100 °C for 10 mins. The fabricated PDMS layer was integrated onto the electrode layer of the TPU film. The TPU film was also replicated from the microdome-patterned silicon mold and sputtered with Pt (EMITECH, K575X) under the mask of the interdigitated pattern for 3 min. Subsequently, AgNWs were spray-coated on the Pt layer. Thereafter, the TPU layer with Pt and AgNWs was treated with O₂ plasma for 1 min to remove the polyvinylpyrrolidone (PVP) layers on AgNWs and enhance the contact between AgNWs.

Characterization of the PEDOT:PSS/PUD Film: A clear cross-sectional image of the PEDOT:PSS/PUD composite was obtained by field-emission SEM (S-4800, Hitachi). The varied sheet resistance of the PEDOT:PSS/PUD composite and pressure-responsive electric properties of sensors were verified by a semiconductor parameter analyzer (4200-SCS, Keithley). In this regard, the normal pressure was applied to the sensors with a pushing tester (JIBT-200, Junil Tech.).

4.3 Results and Discussion

Figure 4.2a-c presents a schematic of the multi-layered e-skin. The PEDOT:PSS/PUD composite was coated as multi-layers on the microdome-patterned PDMS substrate as the top layer (Figure 4.2b). It should be noted that conductivity of each layer gradually decreased from the inner to outer layers of the multi-layered composite (Figure 4.2c). The multi-layered structure was fabricated by spin-coating three different PEDOT:PSS/PUD solutions, in which their conductivity can be easily controlled by the addition of polar solvent (Figure 4.3a).²¹⁸⁻²¹⁹ In this study, ethylene glycol (EG) was utilized to control the sheet resistance ($\sim 200 \text{ } \Omega/\text{sq}$ to $\sim 300 \text{ k}\Omega/\text{sq}$) of the thin composite film (Figure 4.4). Moreover, the addition of PUD rendered elastic properties to the originally brittle PEDOT:PSS layers, thus enabling effective compression of the multi-layered film on the microdomes and stable working of the e-skin under high mechanical stress without incurring damage on the multi-layered film (Figure 4.5).¹⁷⁸ The PEDOT:PSS/PUD solutions with different conductivities controlled saturation resistance in single layered sensors (Figure 4.6). The cross-sectional scanning electron microscope (SEM) images indicated uniform coverage of the PEDOT:PSS/PUD layers which were arranged between thin metal layers on the microdome-patterned PDMS (Figure 4.7). For the highly durable coplanar electrode as the bottom layer, the microdome-patterned thermoplastic polyurethane (TPU) substrate was coated with Pt/silver nanowires (AgNWs) using the interdigitated mask (Figure 4.3b). The mixture of Pt and AgNWs enables the electrodes with low and stable resistance under the repeated pressure application due to the robust connection of AgNW networks on the Pt film. The multi-layered e-skin with coplanar electrodes was fabricated by interlocking the top and bottom layers with the microdome-patterned surfaces facing each other (Figure 4.2d).

Figure 4.2d indicates the pressure-sensing mechanism of the multi-layered microdomes with gradient conductivity. The geometrical effect of the interlocked microdome structure enabled effective concentration of the applied pressure at small contact spots between the microdomes. Therefore, the contact area significantly increased with increasing pressure. In addition, the concentrated stress decreased the thickness of the elastic multi-layers on microdomes, which consequently decreases the film resistance of the multi-layered film, thereby enabling dramatic increase of current flow. The most important feature in this study is the multi-layered PEDOT:PSS/PUD structures with gradient conductivity on the top microdome-patterned PDMS substrate. While previous pressure sensors based on coplanar electrodes without conductivity-gradient multi-layers have been shown to exhibit high pressure sensitivities only within limited pressure ranges under few kPa due to fast saturation of piezoresistance variation (Figure 4.2e), our design of coplanar electrodes interlocked with conductivity-gradient multi-layers ensures high sensitivities over ultra-large pressure ranges. In particular, the second and third outer layers with higher resistance than that of the first inner layer acted as buffer layers to prevent direct contact between conductive composite film with low resistance and the coplanar

electrodes. Therefore, the conductivity-gradient structure prevented rapid decrease and saturation of piezoresistance, enabling highly sensitive and linear pressure detection over a large pressure range. Since the top microdomes with conductivity-gradient multilayers were in contact with the bottom microdomes coated with Pt/AgNW in the coplanar electrodes, the low resistance of inner layer and the high resistance of outer layer enabled the low saturation resistance and high initial resistance, respectively, allowing the ultrahigh variation in piezoresistance over the wide pressure range (Figure 4.2f).

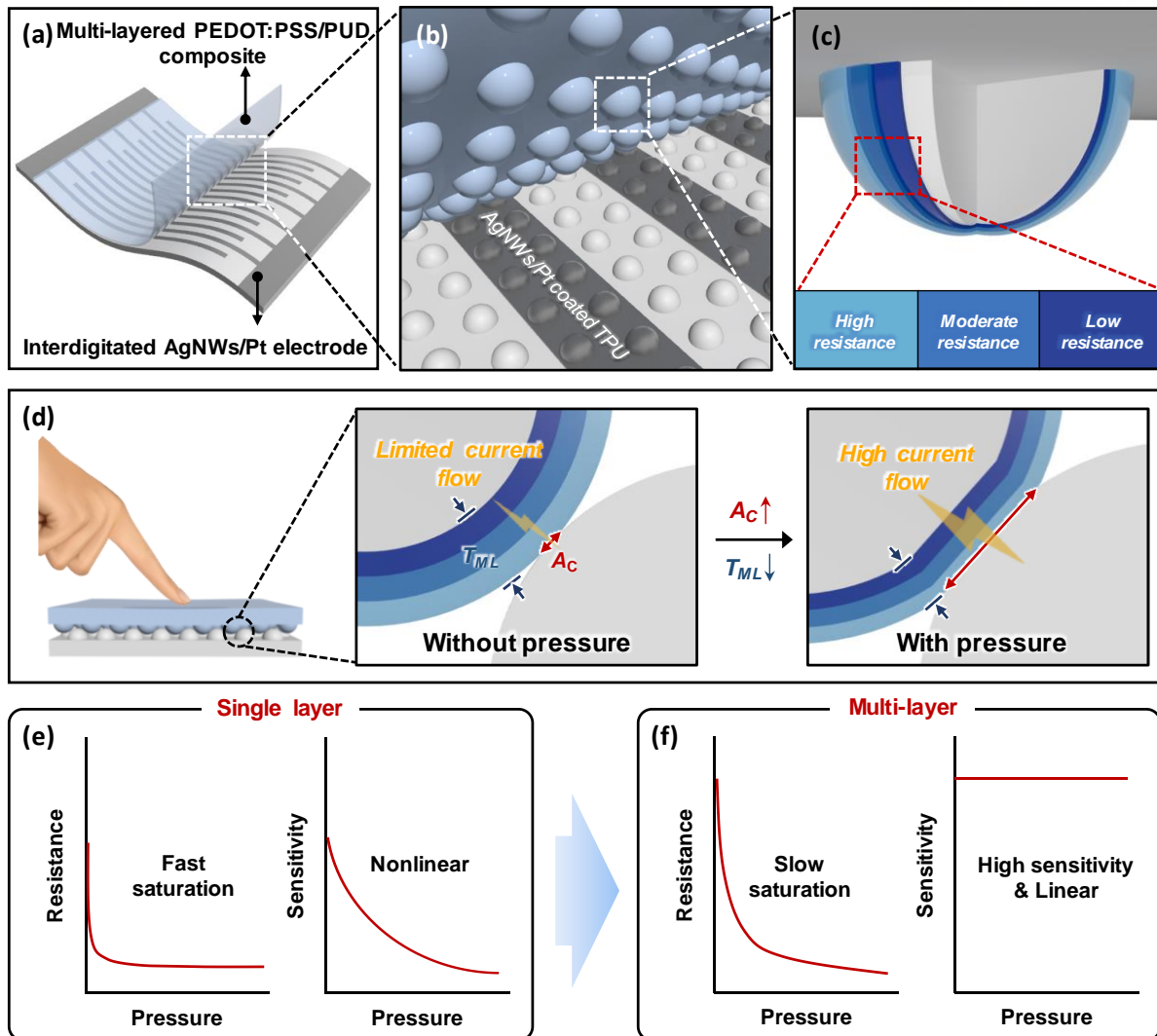


Figure 4.2. Design and functional mechanism of the flexible multi-layered e-skin. (a,b) Scheme of sensor with multi-layered poly(3,4-ethylenedioxythiophene):poly(styrene sulfonate)/ polyurethane dispersion (PEDOT:PSS/PUD) composite and an interdigitated electrode. (c) Multi-layered PEDOT:PSS/PUD composite with different conductivities on the microdome-patterned polydimethylsiloxane (PDMS) layer. (d) Pressure-sensing mechanism of the multi-layered sensor. (e) Limitations of single-layered sensors with co-planar electrodes. (f) Sensing profiles of the multi-layered e-skin.

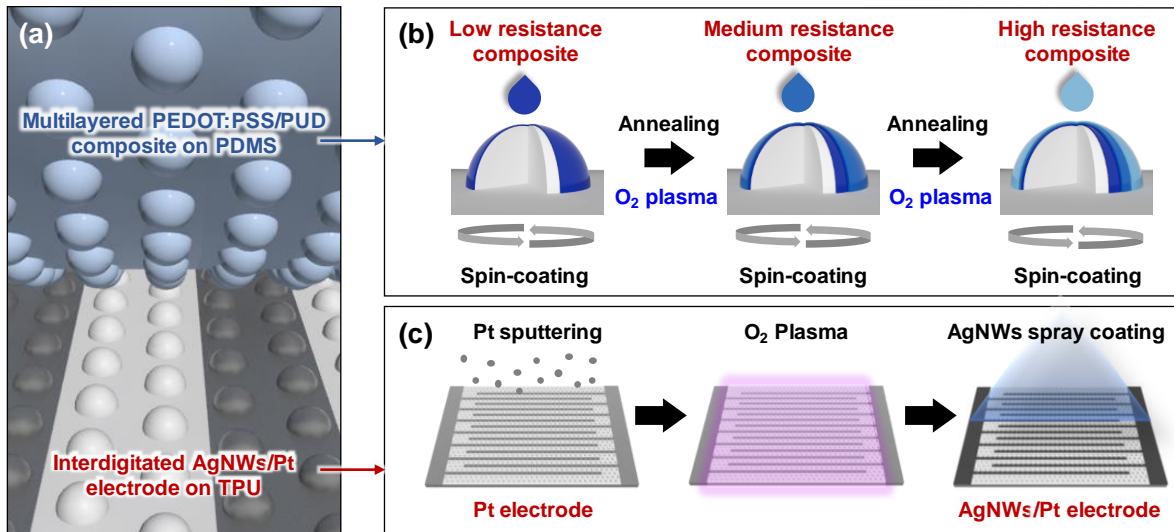


Figure 4.3. Fabrication process of the e-skins. (a) Schematic of multi-layered pressure sensor. (b) Fabrication process of the upper active layer; on the microdome patterned PDMS, PEDOT:PSS/PUD composite with different conductivity is coated successively. (c) Fabrication process of the bottom electrode layer; on the microdome patterned TPU, Pt is sputtered and AgNWs are spray-coated under the interdigitated mask.

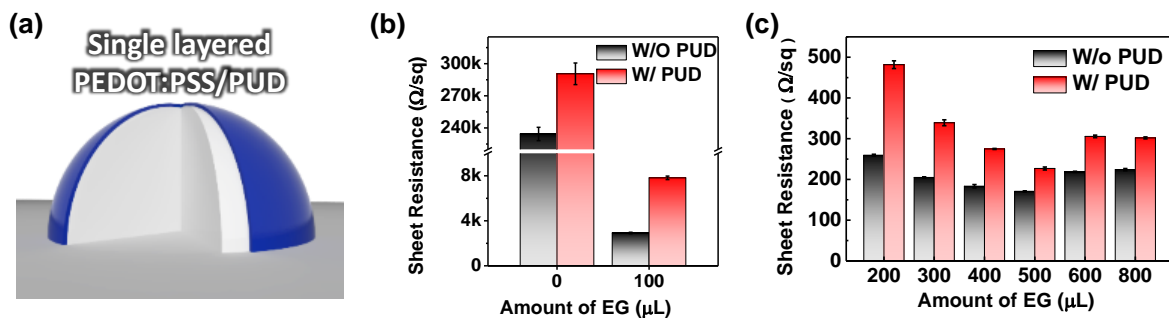


Figure 4.4. Control of the sheet resistance of PEDOT:PSS depending on the amount of ethylene glycol and PUD addition (50 wt%) (a) Scheme indicating single layered PEDOT:PSS/PUD film on the microdome PDMS. (b) The sheet resistance of the PEDOT:PSS with addition of 0 and 100 μL of ethylene glycol in 10 mL of PEDOT:PSS solution. (c) The sheet resistance of the PEDOT:PSS with addition from 200 to 800 μL of ethylene glycol in 10 mL of PEDOT:PSS solution.

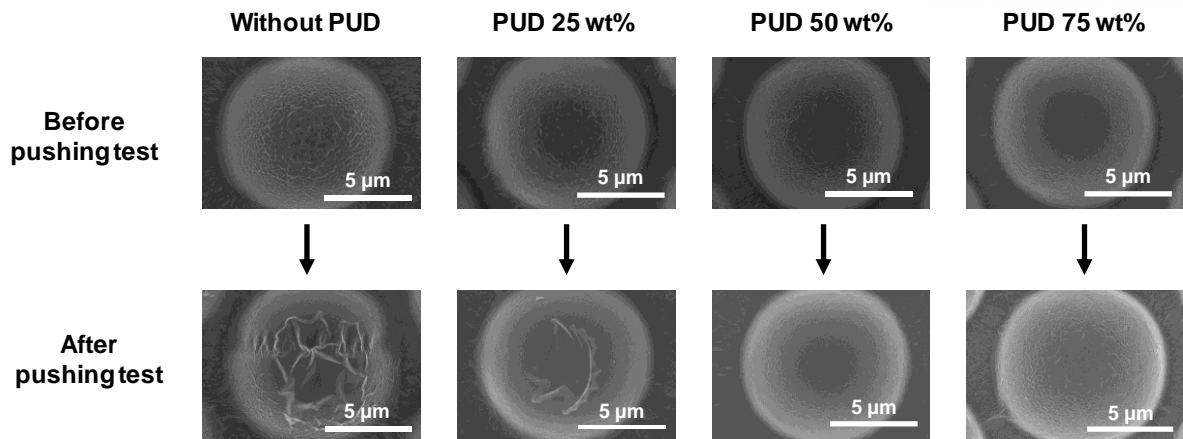


Figure 4.5. SEM image of the surface of PEDOT:PSS/PUD coated microdome depending on the amount of the Polyurethane Dispersion (PUD). (upper) The SEM image showing microdome surface before pushing test. (Below) The SEM image showing microdome surface after pushing test with 10 kPa of the pressure.

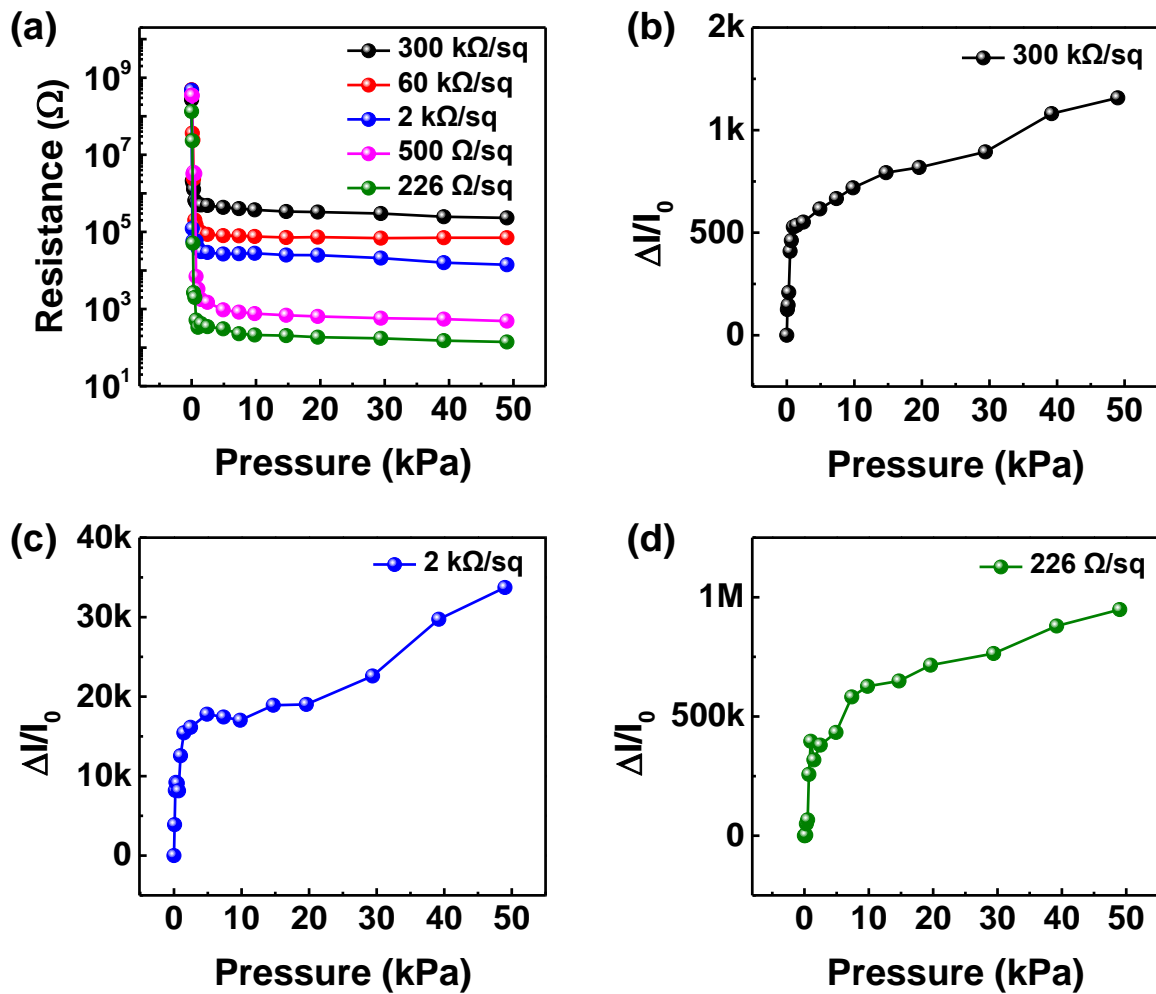


Figure 4.6. The sensing performance in resistance with single layered sensor with 30 nm of thickness. (a) Resistance change in single layered sensor with different resistance. (b-d) Relative current change of single layered sensor with different sheet resistance 300 k Ω /sq, 2 k Ω /sq and 226 Ω /sq in response to applied pressure.

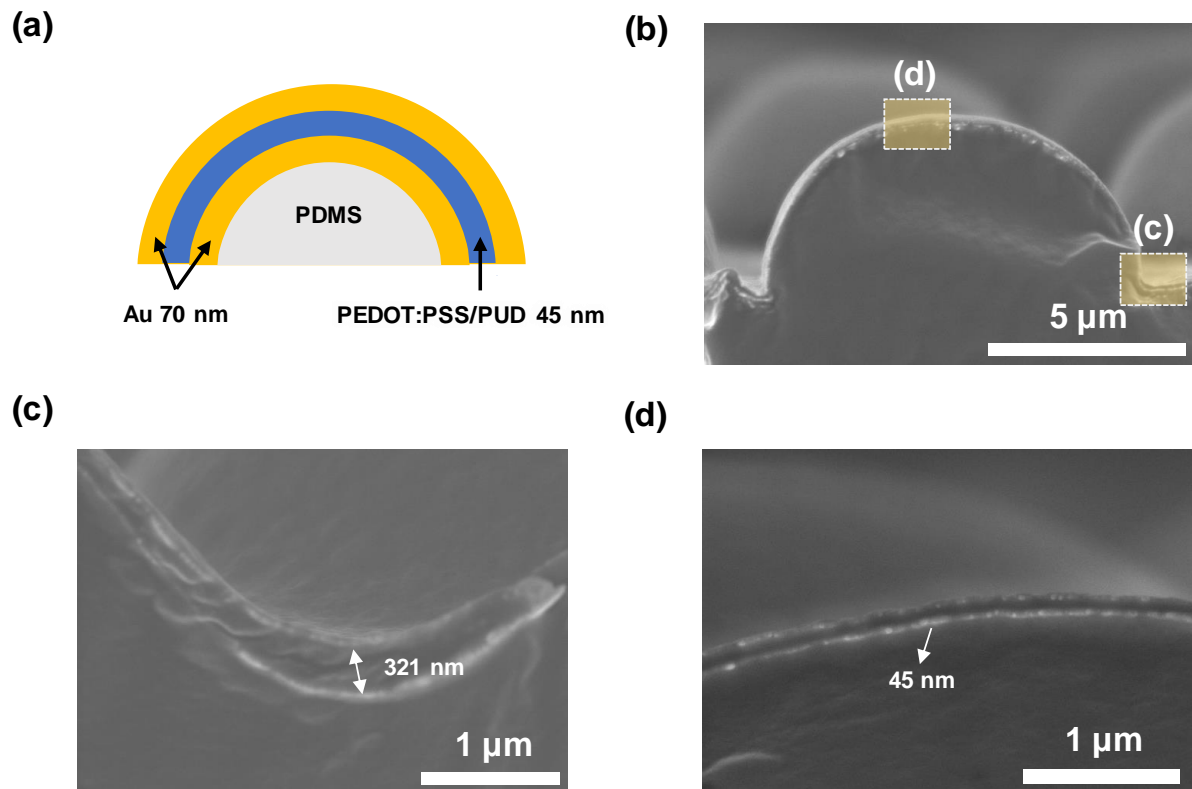


Figure 4.7. (a) The scheme of the single layered PEDOT:PSS/PUD on the microdome PDMS with 45 nm of thickness (b) SEM image showing whole microdome's cross section. (c) Enlarged SEM image showing valley between microdomes with thickness of the 320 nm. (d) Enlarged SEM image showing upper section of the microdome with thickness of the 45 nm.

To demonstrate the effect of multi-layered structure with gradient conductivity on the pressure sensitivity, we compared the pressure sensing performances of e-skins with different numbers of PEDOT:PSS/PUD multi-layers. Pressure sensitivity was defined as $S = (\Delta I/I_0)/\Delta P$, where I is the current of the pressure sensor and P is applied pressure. Pressure sensor with a single PEDOT:PSS/PUD layer with a sheet resistance of $226 \Omega/\text{sq}$ indicated lower sensitivity compared to double- and triple-layered sensors (Figures 4.8a and b) due to the low initial resistance of $1.3 \times 10^8 \Omega$ (Figure 4.9), causing a narrow resistance variation. Similar to previously designed pressure sensors with coplanar electrodes, the single-layered sensor exhibited a significant decrease in sensitivity from 146000 kPa^{-1} to 6800 kPa^{-1} in an initial pressure range of 5 kPa, because direct contact between the conductive film and the electrode significantly decreased the resistance from the initial state ($1.3 \times 10^8 \Omega$) to the saturation state ($\sim 228 \Omega$) within a low pressure of 5 kPa (Figure 4.9). Therefore, the single-layered sensor exhibited high non-linearity and a narrow working range. For different sheet resistances of PEDOT:PSS/PUD films, all of the single-layered pressure sensors show similar nonlinear pressure response while the variation of the resistance and relative current increase with the decrease of film resistance due to the lower saturation resistance (Figure 4.6).

Linearity and sensitivity of e-skins can be improved by multi-layering the PEDOT:PSS/PUD film with gradient conductivity. For the fabrication of multi-layered e-skins, the PEDOT:PSS/PUD layers with higher resistance than that of single layer were coated on top of the single-layered film, resulting in the gradient sheet resistivities of $225 \Omega/\text{sq}$, $60 \text{ k}\Omega/\text{sq}$, and $300 \text{ k}\Omega/\text{sq}$ for the first, second, and third layers, respectively (Figure 4.9). Because the initial contact resistance is determined by the resistance of the outermost layer, an increase in the sheet resistance of the outmost layer led to an increase in the initial resistance at zero pressure. Therefore, the difference between the initial and saturation resistances of the sensor increased with the number of layers to consequently improve pressure sensitivity. Furthermore, the multi-layers with gradient resistance increased the linearity of pressure detection, thereby enabling highly sensitive pressure sensing at pressure values of up to 100 kPa. Figure 4.8b presents pressure sensitivities of e-skins with different layer numbers for pressure values ranging up to 100 kPa. Multi-layered e-skins exhibited significantly improved pressure sensitivity than the single-layered e-skin. In multi-layered e-skins, the second and third layer with high sheet resistance acted as buffer layers, which mitigate rapid saturation of resistance change and rapid decrease in pressure sensitivity at low-pressure ranges (Figure 4.9). Especially, the triple-layered e-skin maintained an ultrahigh pressure sensitivity of $\sim 3.8 \times 10^5 \text{ kPa}^{-1}$ at pressure values ranging from 0.8 Pa to 100 kPa, thus indicating highly sensitive and linear pressure sensing capabilities over a broad pressure range. In contrast, the single- and double-layered e-skins indicated pressure sensitivities of $\sim 1.5 \times 10^5$ and $\sim 7.0 \times 10^5 \text{ kPa}^{-1}$ (respectively), which rapidly decreased within ~ 5 and ~ 10 kPa, respectively. Here, the double-layered e-skin shows higher pressure sensitivity at low pressure range (< 10 kPa) than the triple-

layered e-skin. This could be attributed to an increase in the saturation resistance of the triple-layered e-skin due to presence of a high-resistance third layer (Figure 4.9). However, high pressure sensitivity of the double-layered e-skin continuously decreased with increasing pressure due to an insufficient buffer layer. Figure 4.10 presents the effects of the conductivity-gradient on the pressure sensing performance of the sensors. The multi-layered PEDOT:PSS/PUD with gradient conductivity showed a continuous and linear increase in current flow, due to high initial resistance by the third layer and prevention of fast saturation of resistance change by the conductivity-gradient multi-layers. However, pressure sensors with multiple coatings (three times) of PEDOT:PDSS/PUD layer with the same resistance ($225 \Omega/\text{sq}$) showed low pressure sensitivity and poor linearity. These results indicate that the conductivity-gradient design was critical in enhancing the pressure sensing performances of the multi-layered e-skins.

The effects of the interlocked microdome structure on the pressure-sensing performance were investigated by comparing the pressure sensing performances of sensors with planar-planar, microdome-planar, and interlocked microdome structures (Figure 4.8c and 4.11). Because of the multi-layering effect, sensors with planar-planar and microdome-planar structures also have a high initial resistance values of 7×10^7 and $4 \times 10^9 \Omega$ (Figure 4.11b) respectively, enabling high initial pressure sensitivities of 2.6×10^5 and $2.7 \times 10^6 \text{ kPa}^{-1}$, respectively (Figure 4.11c). However, these sensors indicated a significant decrease in sensitivity to 2.3×10^4 and $5.4 \times 10^5 \text{ kPa}^{-1}$, respectively, at pressures less than 5 kPa, which could be attributed to limited deformation of the active materials and small changes in the contact area between the top and bottom layers (Figure 4.11c). Contrarily, the sensor with interlocked microdome structure exhibited a highly linear detection profile owing to large deformability and substantial change in the contact area between the interlocked microdomes. As previously reported, the unique spherical geometry of a microdome enables effective stress concentration at small contact spots between the interlocked microdomes; further, the area of contact spots gradually widens with applied pressure.¹⁵ Therefore, the interlocked microdomes and the multi-layered structure enabled a gradual increase in the contact area between the microdomes with increasing applied pressure, thus preventing rapid saturation of pressure sensitivity.

In accordance with the results of pressure-sensing performance with multi-layered sensor, the additional experiments were conducted with optimized condition of three-layered sensor, which is stacked with PEDOT:PSS/PUD composite layers ($225 \Omega/\text{sq}$, $60 \text{ k}\Omega/\text{sq}$, and $300 \text{ k}\Omega/\text{sq}$ for the first, second, and third layers, respectively). Under optimized conditions, the multi-layered pressure sensor showed a linear and highly sensitive pressure detection during sequential application of pressure ranging from 0.5 kPa to 100 kPa (Figure 4.8d). Despite the significantly large difference in resistance ($R/R_0 = \sim 10^7$) between the application and release of pressure, the multi-layered pressure sensor

indicated fast response (< 170 ms) and relaxation (< 16 ms) times (Figure 4.8e). This could be attributed to the interlocked microdome structure which contributed to immediate deformation and recovery of the microdomes.¹⁵ In addition, the pressure sensor designed in this study could maintain a uniform pressure sensing performance even after 5000 applications of 20 kPa pressure (Figure 4.8f). Furthermore, the e-skins exhibited a reliable sensing performance at voltage values ranging from 0.1 to 5 V (Figure 4.8g), thus demonstrating low-power operation of the e-skins.

One of most notable features of multi-layered e-skin is the tunable sensitivity and linearity through control of conductivity and the number of layers, which leads to the simultaneous achievement of high sensitivity and linearity. Compared to previously reported pressure sensors, the triple-layered sensor with gradient conductivity exhibited the highest sensitivity (3.8×10^5 kPa⁻¹) with linear detection over a broad pressure sensing range (0.8 Pa to 100 kPa) (Figure 4.8h and Table 4.1).^{61,107,122-123,149,172,178-179,181,183-184,215,217} Previous studies have indicated limitations in attaining both high sensitivity and linearity due to trade-off characteristics between sensitivity and linearity, caused by limited deformability and direct contact between the sensing materials and the electrodes. Most sensors with high sensitivity (> 100 kPa⁻¹) either showed limited detectable pressure ranges or exhibited non-linear sensing profiles. For example, pressure sensors with high sensitivities of 9.8×10^4 kPa⁻¹ and 1907 kPa⁻¹ could maintain the sensitivities only up to 0.2 and 0.1 kPa, respectively.^{215,217} In another study, the pressure sensor indicated excellent linearity at pressure range up to 30 kPa but exhibited poor sensitivity (1.2 kPa⁻¹).²²⁰ Although a pressure sensor with multi-layered interlocked structure was recently reported with linear pressure sensing over a broad detection range (1.3 Pa–353 kPa), its pressure sensitivity (47.7 kPa⁻¹) was still low.¹²² This study incorporated three strategies to improve sensor performances, i.e., utilizing a multi-layered thin film of PEDOT:PSS/PUD with gradient-resistance, interlocked microdomes, and a coplanar electrode structure. Compared to previous single-layered sensors, the multi-layered sensor with conductivity-gradient exhibited sequential variation in sensor resistance in response to applied pressure. This enabled successful control of both saturation behavior of resistance change and the initial and saturation resistances, thus ensuring superior linearity and ultrahigh pressure sensitivity across wide pressure ranges. In addition, the interlocked microdome structure with coplanar electrode design enabled ultrahigh pressure sensitivity owing to direct contact between the conductive composite and the electrode, where the contact area significantly varied in response to the applied pressure based on the high deformability between the interlocked microdomes. Therefore, the multi-layered e-skin performed enhanced pressure sensitivity (3.8×10^5 kPa⁻¹) and linear detection over a broad pressure range (0.8 Pa–100 kPa).

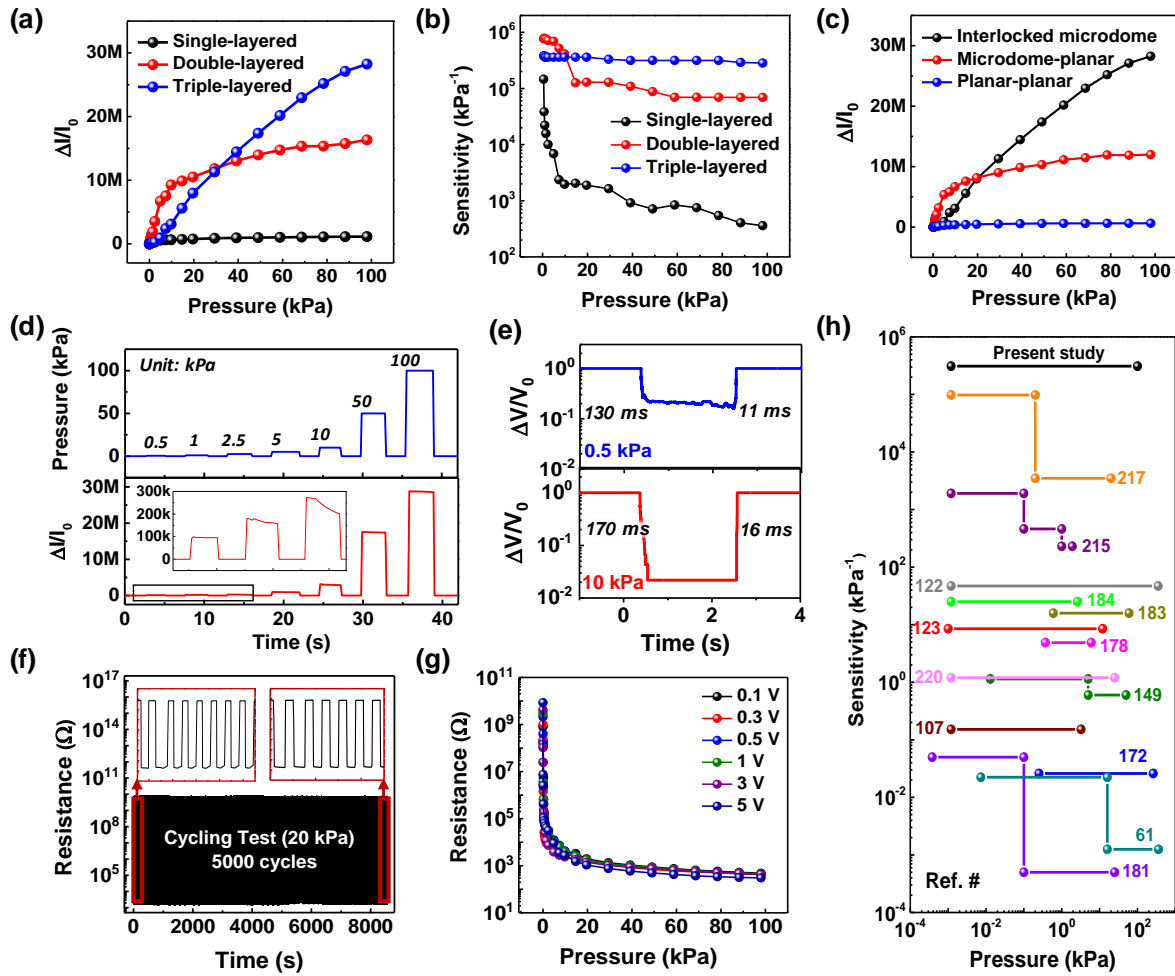


Figure 4.8. Sensing performance and sensitivity of pressure sensors. (a,b) Resistive pressure-sensing performance and sensitivity of multi-layered pressure sensors with different number of layers. (c) Resistive pressure-sensing performance of multi-layered pressure sensors with different structures. (d) Real-time monitoring of pressure sensor at pressure loads of 0.5, 1, 2.5, 5, 10, 50, and 100 kPa. (e) Response and relaxation times of pressure sensor at 0.5 and 10 kPa. (f) Cyclic stability test of e-skin under repetitive pressure loading of 20 kPa at a frequency of 0.25 Hz. (g) Resistance change in multi-layered pressure sensor at different applied voltage biases (0.1 to 5 V). (h) Sensitivity and linear sensing performance obtained in present study and previous reports.

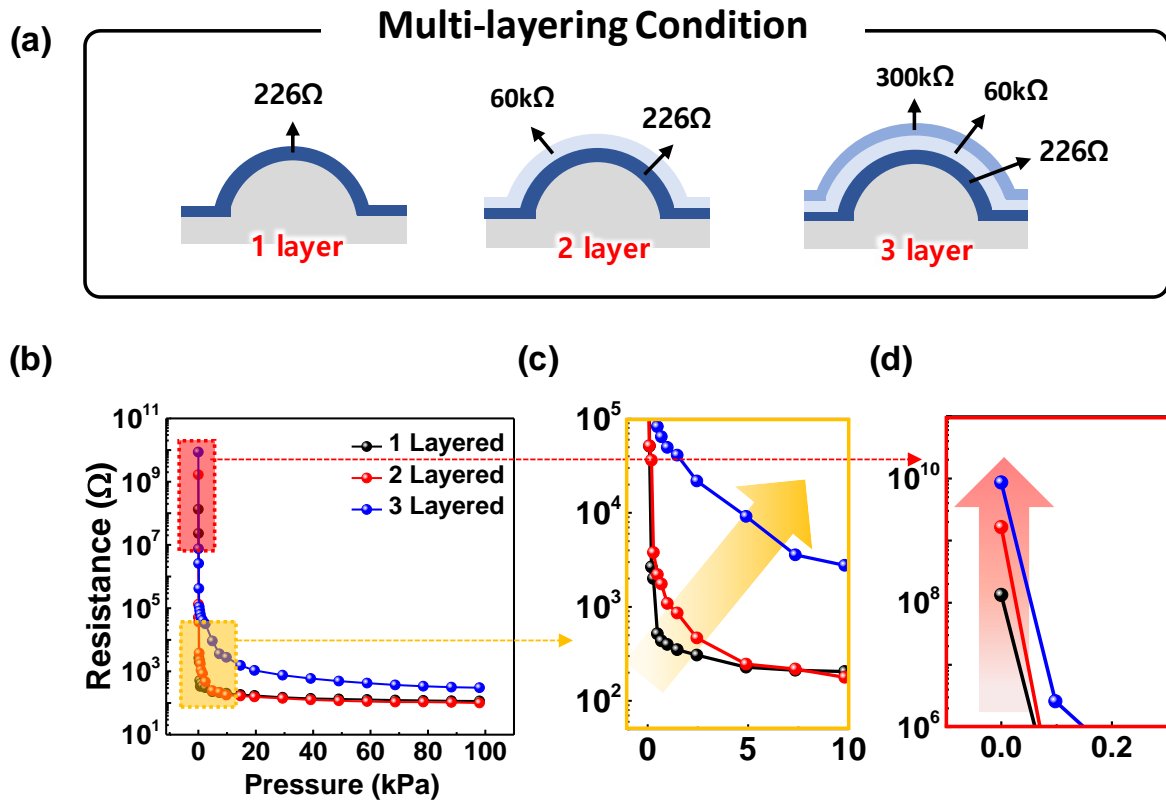


Figure 4.9. Resistance change depending on the number of layers (a) Multi-layering condition with different resistance in each layer. (b) Resistance change under the pressure from 0 to 100 kPa. (c) Enlarged graph in the pressure range from 0 to 10 kPa showing released saturation trends of resistance as the number of layers increase. (d) Enlarged graph in the pressure range from 0 to 0.2 kPa showing Increase of the initial resistance as the resistance of the outermost layer increases.

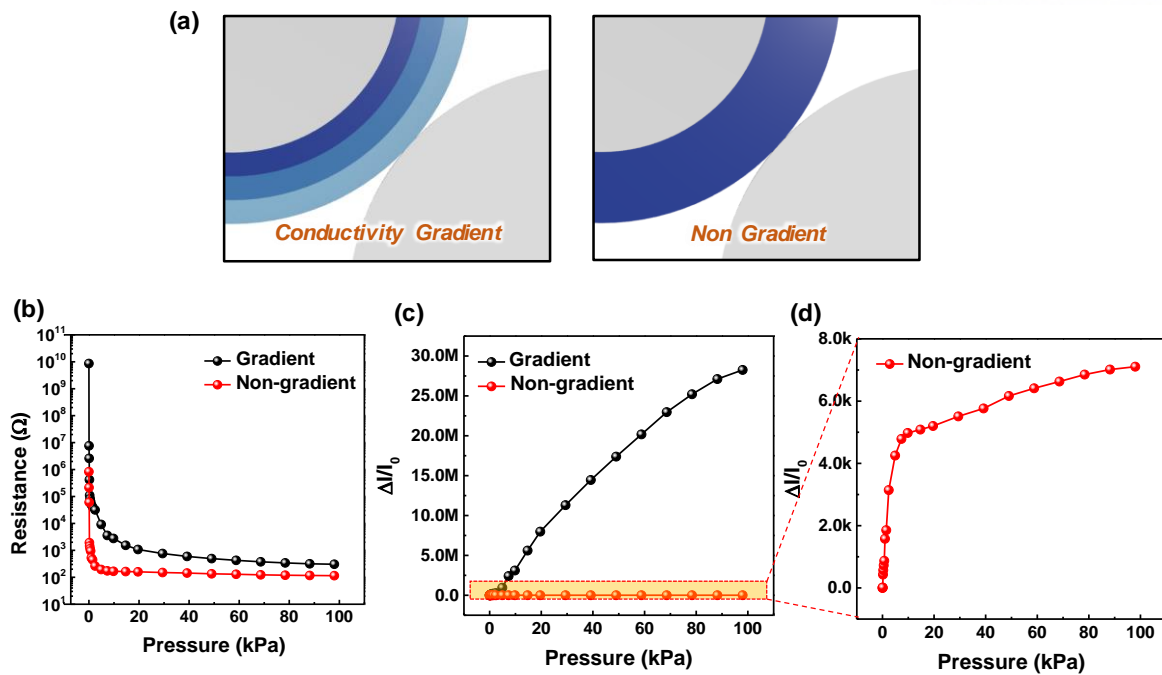


Figure 4.10. Scheme and sensing performance in resistance and current change indicating the effect of multi-layering. (a) Scheme of the conductive gradient PEDOT:PSS/PUD film by multi-layered structure and uniformly conductive film. (b) Resistance change of the sensors with conductive gradient and non-gradient composite. (c-d) Current change of the sensors with conductive gradient and non-gradient composite.

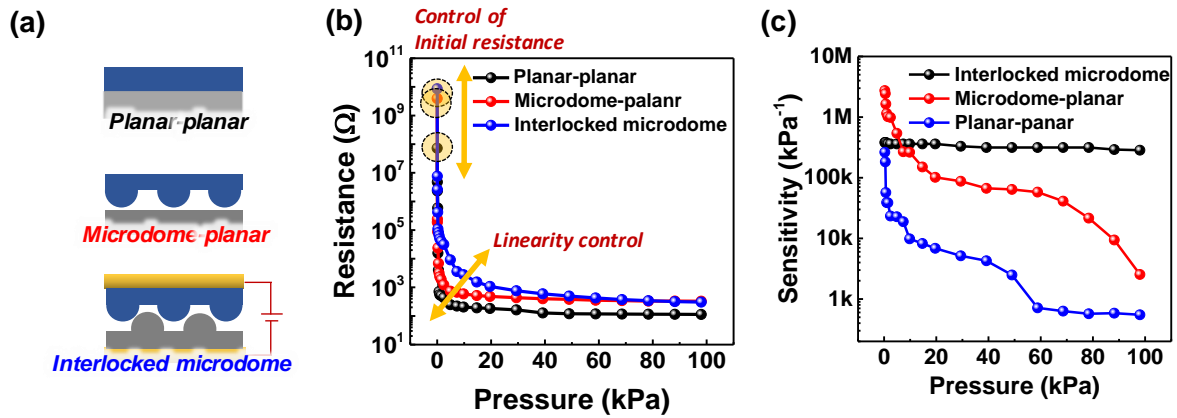


Figure 4.11. Sensing performance depending on the structure of the sensors. (a) Scheme of the sensor with different structures; Planar, single dome, and interlocked structure (b) Resistance change depending on the structure of the multi-layered sensor (c) Sensitivity depending on the structure of the multi-layered sensor.

Table 4.1. Summary of recent pressure sensors with linear pressure responses and their key parameters.

NO.	Materials	Range (kPa)	Sensitivity (kPa ⁻¹)	Linear range (kPa)	Type	Ref.
1	CNT microyarn	0.0038 – 25	0.05 (<0.1 kPa) 0.0005 (>10 kPa)	0.00038	Capacitive	181
2	Ecoflex dielectric layer with Ag electrode	0.0073 – 360	0.0224 (< 16 kPa) 0.00125 (< 360 kPa)	0.0073 – 16	Capacitive	61
3	Porous CNT/PDMS	0.25 – 260	0.026	0.25 – 100	Resistive	172
4	rGO/Polyaniline Sponge	0 – 27	0.152 (< 3.24 kPa) 0.0049 (<27.39 kPa)	0 – 3.24	Resistive	107
5	Au NWs	0.013 – 50	1.14 (< 5 kPa) 0.6 (< 50 kPa)	0.013 – 5	Resistive	149
6	Hierarchical graphene/PDMS	0.2 – 25	1.2	0.2 – 25	Resistive	220
7	PEDOT:PSS/PUD micro pyramid	0.37 – 5.9	4.88	0.37 – 5.9	Resistive	178
8	Graphene/PDMS hierarchical microdome	0.001 – 12	8.5	0.001 – 12	Resistive	123
9	Hollow structured graphene-silicone composite	0.6 – 60	15.9	0.6 – 60	Resistive	183
10	rGO/PDMS microstructures	0.016 – 40	25.1 (< 2.6 kPa) 0.45 (< 40 kPa)	0.016 – 2.6	Resistive	184
11	rGO/PVDF multilayer interlocked microdome	0.0013 – 353	47.7	0.0013 – 353	Resistive	122
12	Micro pyramid Ppy/PDMS and coplanar electrode	0 – 1.9	1907.2 (< 0.1 kPa) 461.5 (< 1 kPa) 230.1 (< 1.9 kPa)	0 - 0.1	Resistive	215
13	AgNWs/PDMS	0 – 20	9.8×10^4 (< 0.2 kPa) 3.5×10^3 (< 20 kPa)	0 - 0.2	Resistive	217

This work	rGO/PVDF multilayer interlocked microdome	0 – 100	3.8×10^5	0 – 100	Resistive	-
------------------	--	----------------	-------------------------------------	----------------	------------------	----------

The other important feature of the multi-layered pressure sensor is modulus-gradient interlocked structures, which can be observed in interlocked microridge structures on the human skin.⁴⁹ In the human skin, owing to the modulus difference between the epidermal and dermal layers, applied tactile stimuli are highly concentrated at the interface of the modulus-gradient interlocked ridge structure and efficiently transferred to the underlying mechanoreceptors, allowing highly sensitive tactile sensing functions.^{2, 50-52} The design of the present e-skins was inspired by the modulus-gradient structure. Specifically, it comprised interlocked structures with different moduli for the top and bottom layers, i.e., the top layer was the microdome-patterned PDMS with low modulus (~ 3 MPa)² and the bottom layer was the microdome-patterned TPU with high modulus (~ 25 MPa).⁵³ The stress concentration effect between the interlocked layers was theoretically assessed by performing finite-element calculations based on model systems with different materials. Figure 4.12a presents the calculated stress distribution for the interlocked microdome structure with PDMS-PDMS layer by finite-element calculation (ABAQUS software). The structural effect of the interlocked microdome structure resulted in significant concentration of applied stress at contact spots between the microdomes, which increased with increasing pressure. Introduction of TPU as the bottom layer of the interlocked structure not only offered a structural advantage but also amplified the stress concentration effect due to modulus difference between the PDMS and TPU layers (Figure 4.12b). Figures 4.12c and d indicate variation in both average contact stress and contact area at the interface between the interlocked microdomes for three combinations of top and bottom materials with different moduli (PDMS-PDMS, PDMS-TPU, and TPU-TPU). TPU-TPU indicated the largest change in contact stress but the smallest variation in contact area due to high modulus. Meanwhile, PDMS-PDMS exhibited the largest change in contact area but the smallest variation in contact stress owing to low modulus and large deformation of the interlocked microdomes, resulting in severe damage to the metal electrode, specifically disconnection of the AgNW network and cracks in the Pt film (Figure 4.12e). The damage significantly increased the resistance of the electrode to consequently increase saturation resistance and decrease pressure sensitivity (Figure 4.12g and 4.13). When the high modulus TPU layer is employed as an electrode substrate, it exhibited smaller deformation than the PDMS layer. Consequently, the Pt/AgNWs electrode maintained a conductive network characterized by a robust AgNW network and crack-free Pt-coated microdome surface (Figure 4.12f). Therefore, sensors with TPU-based electrodes (TPU-PDMS, TPU-TPU) indicated relatively low saturation resistance, high sensitivity, and linear response to pressure compared to sensors with PDMS-based electrode (PDMS-PDMS) (Figure 4.12g and 4.13). Especially, the sensor with the PDMS active layer (TPU-PDMS) experienced a large change in resistance and stable pressure sensing over a broad pressure range, which could be attributed to the modulus-gradient geometry of the interlocked layers. In addition to large deformation of the PDMS active layer, effective stress concentration between the TPU-PDMS layers enabled further compression of the multi-layered

PEDOT:PSS/PUD composite., resulting in exceptionally large decrease in sensor resistance upon application of pressure with the stable electrode on the bottom TPU layer.

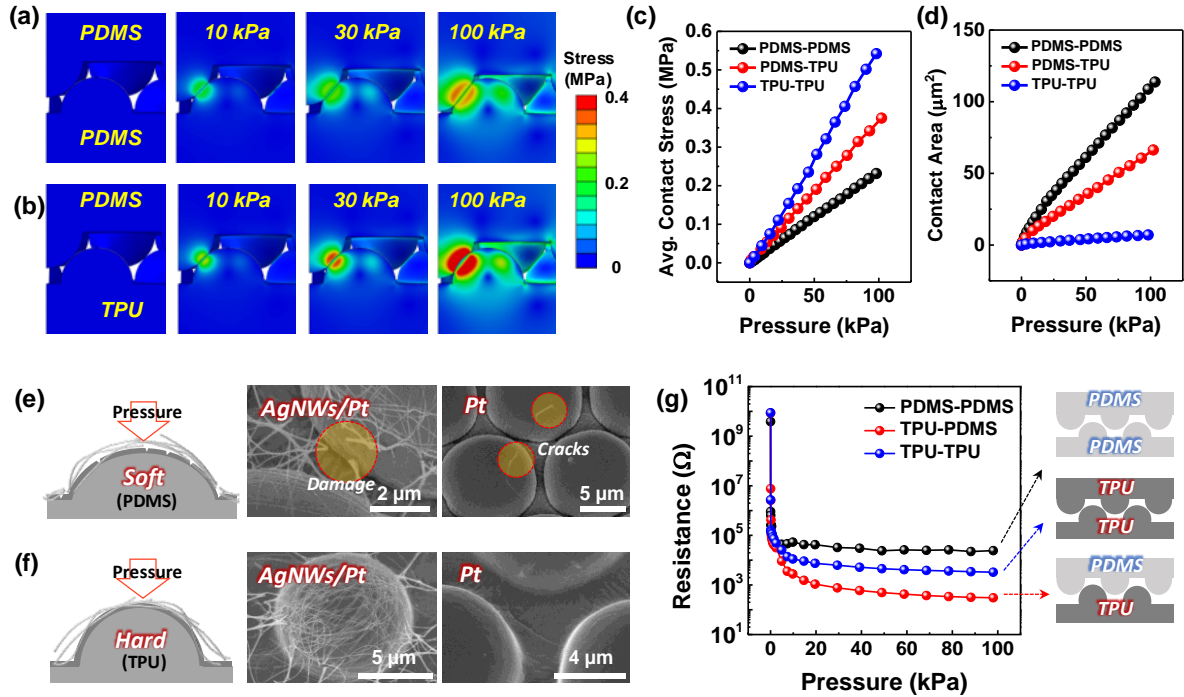


Figure 4.12. Structural contribution to the sensing performance. (a) Local stress distribution in the interlocked microdome structure with PDMS-PDMS layers at different pressures. (b) Local stress distribution in the interlocked microdome structure with PDMS-TPU layers at different pressures. (c,d) Contact stress and contact area as a function of pressure for top and bottom substrates with different moduli. (e,f) Deformation degrees of different moduli and SEM images of (upper) microdome-patterned PDMS layer with Pt and AgNWs, microdome-patterned PDMS layer with Pt and (bottom) microdome-patterned TPU layer with Pt and AgNWs, microdome-patterned TPU layer with Pt. (g) Resistance change in multi-layered pressure sensor with top and bottom layers characterized by different moduli.

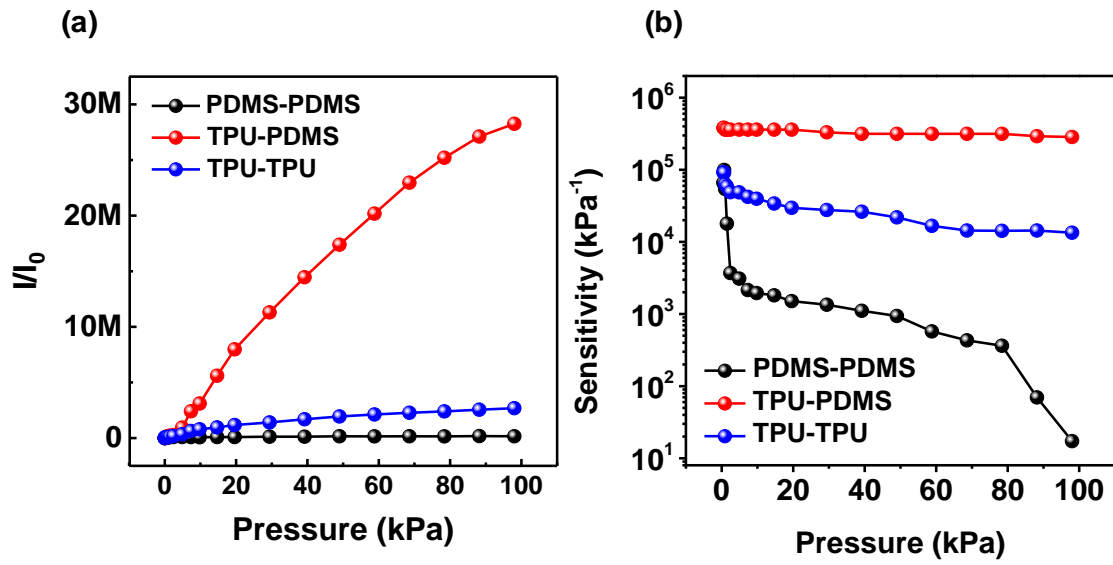


Figure 4.13. The electrical sensing performance with different modulus of active and electrode layer. (a) The current change. (b) Sensitivity.

Multi-layered pressure sensor with ultrahigh pressure sensitivity and linear sensing performance over wide pressure range can be utilized in various applications that require detection of subtle pressure (~few Pa) or wide range pressure sensing capabilities (~100 kPa). Designed pressure sensor could clearly distinguish different pressures of gases characterized by different flow rates. Figure 4.14a and b present the piezoresistive response to a weak gas flow ranging from 3 to 10 L min⁻¹, which corresponded to a pressure ranging from 0.8 to 2.7 Pa, respectively.⁴⁷ Notably, the gas flow of 3 L min⁻¹ corresponded to an extremely low pressure of ~0.8 Pa (Figure 4.15). Flexible multi-layered e-skins can be utilized in wearable applications for real-time pressure detection during human hand's manipulation of objects. As indicated in Figure 4.14c, a smart glove was fabricated by integrating the e-skins on the finger-side of the glove. When a volunteer wearing the smart glove was instructed to hold and lift a cup with different quantities of water (25–250 g), the pressure applied to lift the cup would depend on the weight of water. Therefore, an increase in the quantity of water would correspondingly increase the signal from the pressure sensor.

The carotid artery and internal jugular vein in the neck supply the head and neck with oxygenated blood and collect deoxygenated blood from the brain, respectively. As shown in Figure 4.14d, certain blood vessel was located on the surface of the skin, when the volunteer exhibited different neck motions. Therefore, when the e-skin was attached to the neck, it could detect two distinct pulse pressures with different characteristic peaks according to the postures of wearer. It should be noted that previous pressure sensors only focused on detection of artery pulse signals which are the dominant signals on the neck.^{7, 54} The e-skin designed in this study exhibited ultrahigh sensitivity and could detect two different pulse signals depending on the posture of volunteer, i.e., the carotid artery signal and the internal jugular vein signal. When the volunteer looks ahead, the multi-layered pressure sensor could distinguish the characteristic peaks of the arterial pulse signal, i.e., P₁, P₂, and P₃, which represents incident, tidal, and diastolic waves, respectively (Figure 4.14e). The pulse frequency of the volunteer estimated from the recorded pulse signal was 85 beats/min which corresponded to the value for healthy adults.⁵⁵ In addition, the characteristic peaks of the pulse signal can be utilized to estimate health indices such as radial augmentation index ($AI_r = P_2/P_1$), diastolic augmentation index ($DAI_r = P_3/P_1$), and digital volume pulse time ($T_{DVP} = t_{p2} - t_{p1}$), where t_{p1} and t_{p2} indicate occurrence times of the first (P₁) and second (P₂) peaks, respectively. In this study, the AI_r , DAI_r , and T_{DVP} values estimated from the monitored carotid artery signal were calculated as 0.73, 0.52, and 0.187 s, respectively. These results show that the volunteer exhibited good health conditions for the corresponding age range (mid 20s).⁵⁶ Moreover, the multi-layered sensor on the neck could monitor the internal jugular vein signal when the volunteer bent the head to the left by 45° (Figure 4.14f).⁵⁷ The results indicated three characteristic peaks, i.e., A (atrial contraction), C (tricuspid bulging and ventricular contraction), and V (systolic filling of the atrium), and two descents, i.e., X (atrial relaxation) and Y (early ventricular filling), which

were clearly discriminated in the detected signal.⁵⁸ In particular, A and V corresponded to heart tones S1 and S2 which were produced by closing of the atrioventricular and semilunar valves, respectively. The time interval between S1 and S2 was ~170 ms for the volunteer which corroborates with clinical statistics.⁵⁹ The internal jugular vein is a reliable indicator for diagnosing diseases such as right ventricular failure, pericardial compression, and tricuspid stenosis because it is anatomically closer and has a direct course to the right atrium in contrast to the external jugular vein.

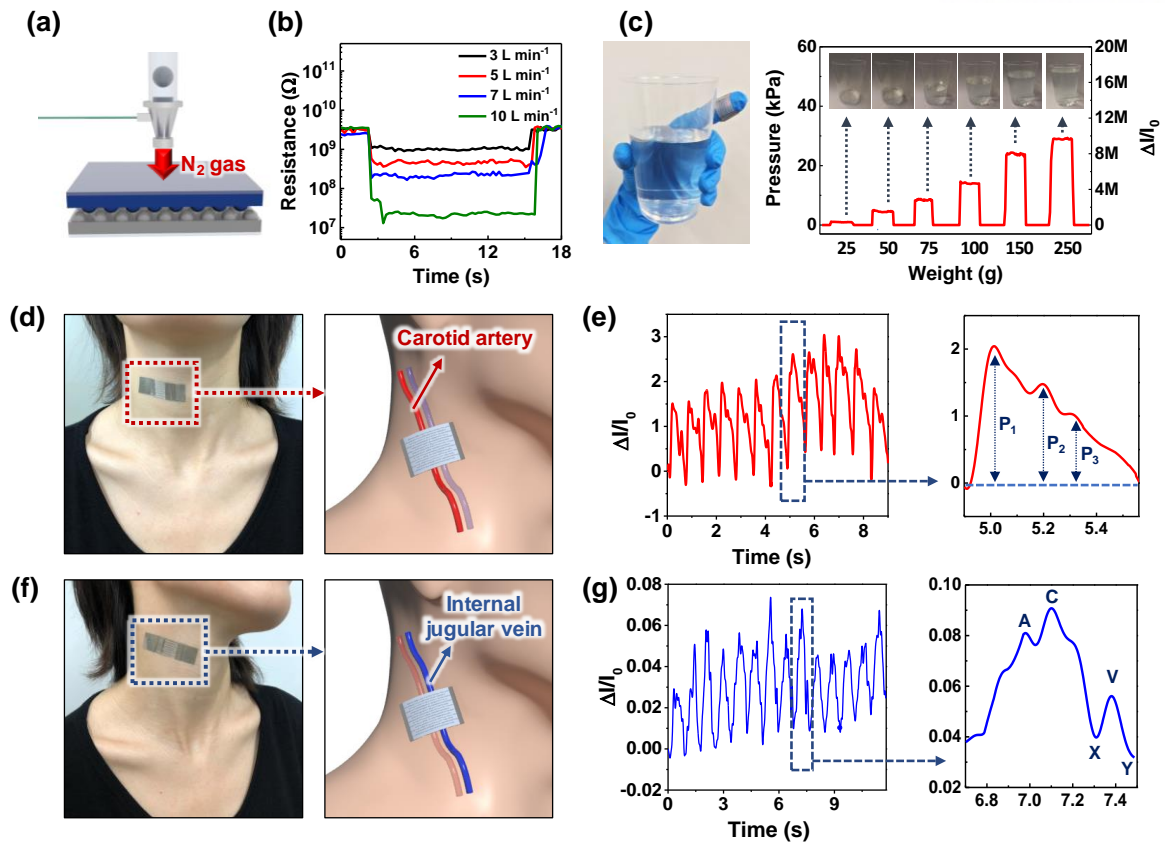


Figure 4.14. Applications of multi-layered pressure sensor characterized by high sensitivity and linearity (a) Scheme of sensing weak gas flow by multi-layered e-skin. (b) Real-time monitoring of resistance variation for different gas flow rates. (c) Glove with multi-layered sensor on the fingertip and real-time pressure sensing for varying weights of water (25, 50, 100, 150, 200, and 250 g). (d) Photograph and illustration of multi-layered sensor on human neck for detection of carotid artery signal. (e) Monitored real-time pulse signals for carotid artery with characteristic peaks, i.e., P_1 (incident wave), P_2 (tidal wave), and P_3 (diastolic wave). (f) Photograph and illustration of multi-layered sensor on volunteer facing slightly left for detection of internal jugular vein signal. (g) Monitored real-time pulse signals for internal jugular vein with characteristic peaks, i.e., A (atrial contraction), C (tricuspid bulging, ventricular contraction), and V (systolic filling of atrium), and two descents, i.e., X (atrial relaxation) and Y (early ventricular filling).

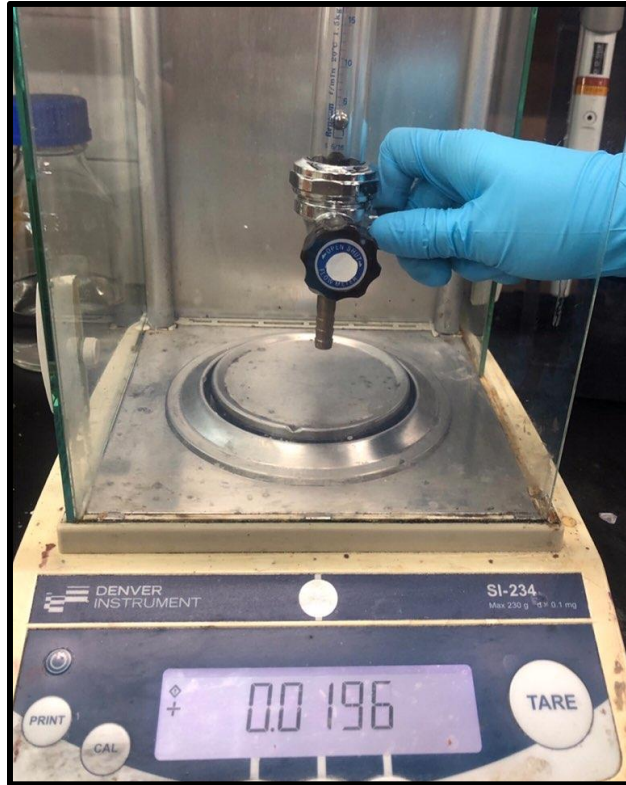


Figure 4.15. Photograph of the weighing of weak gas flow (~ 3 L/min)

A highly sensitive multi-layered pressure sensor array can detect spatial distributions as well as magnitudes of external stimuli. In this regard, a 3×3 sensor array was fabricated with polyethylene naphthalate (PEN) as the substrate for top and bottom layers (**Figure 4.16a and b**). The sensor characterized by high sensitivity and linearity could distinguish varying pressures (in the medium pressure region (~ 2.5 kPa)) resulting from different weights of the object (Figure 4.16c and d). Furthermore, the magnitude and spatial distribution of the applied pressure could be utilized for obtaining an image of the pressed shape on the sensor array, when loading the objects with the shape of alphabet U (Figure 4.16e). In particular, the ultrahigh pressure sensitivity of the multi-layered sensor allowed discrimination of subtle pressure differences in gas flows with different densities (Figure 4.16f and g). In this regard, nitrogen and argon gases (exhibiting densities of 1.25 and 1.78 g/L, respectively) were tested. When each gas was blown on the 3×3 sensor array at a flow rate of 15 L/min and a distance of 20 mm, argon, which has a higher density than nitrogen, induced a larger variation in resistance. In addition, spreading argon gas around the blowing point induced slight variation in the neighboring sensor arrays. Contrarily, nitrogen gas induced a small resistance variation only in the center pixel and no changes were observed in the resistance values of the neighboring sensor arrays. Although the density difference of these gases is very small and undetectable by human skin, artificial e-skins exhibited excellent discrimination capabilities beyond the sensing capabilities of human skin.

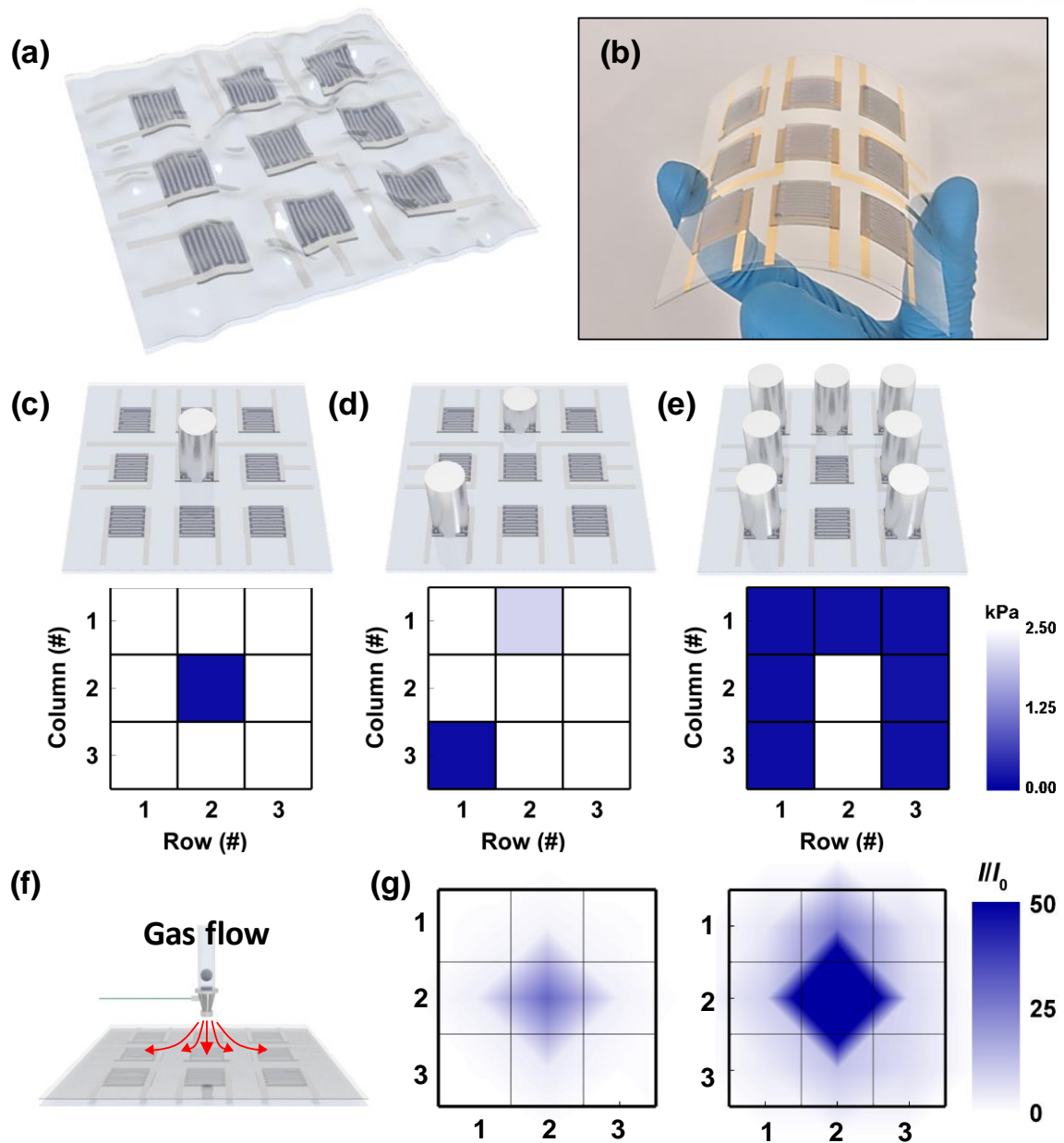


Figure 4.16. Application of multi-layered pressure sensor for detection of spatial distribution on a 3×3 sensor array. (a,b) Scheme and photograph of the fabricated 3×3 sensor array. (c–e) Detection of spatial distribution for different locations and weights on the multi-layered 3×3 sensor array. (f,g) Ar and N_2 gases on the multi-layered sensor and detected spatial distributions for different air densities.

4.4 Conclusion

In conclusion, we demonstrated a multi-layered flexible pressure sensor with high sensitivity and linearity over a wide pressure range. The suggested pressure sensor based on the interlocked microdome structure was characterized by the multi-layered PEDOT:PSS/PUD composite with gradient conductivity as top layer and coplanar electrode (Pt/AgNW) as bottom layer. The multi-layered composite with gradient conductivity was utilized to control saturation behavior of resistance change and the initial and saturation resistances, thus ensuring superior linearity and ultrahigh sensitivity at a pressure range up to 100 kPa. Especially, the pressure sensor indicated the highest sensitivity ($3.8 \times 10^5 \text{ kPa}^{-1}$) observed to date. In addition, human skin-inspired modulus-gradient interlocked structure exhibited effective stress concentration between the TPU-PDMS layers and enabled stable working of coplanar electrode up to 100 kPa. Further, the pressure sensor indicated a rapid response time of 170 ms and a relaxation time of 16 ms despite the significantly large difference in resistance ($R/R_0 = \sim 10^7$), thus indicating highly sensitive, fast, and durable sensing performance in real time. The designed pressure sensors were utilized to various application fields, including weak gas pressure, pulse rate in humans, and pressure when holding a cup of water. Moreover, fabrication of a 3×3 sensor array allowed detection of spatial distribution of objects on the sensor array depending on the weight. Finally, the sensor could discriminate between different gas densities, i.e., 1.25 and 1.78 g/L for nitrogen and argon, respectively. The exceptionally superior performances of multi-layered e-skins can be utilized in various fields including design of wearable devices, prostheses, and personalized healthcare monitoring.

Chapter 5. Biological skin-inspired mechanochromic electronic skin for visualization of mechanical stimuli

5.1 Introduction

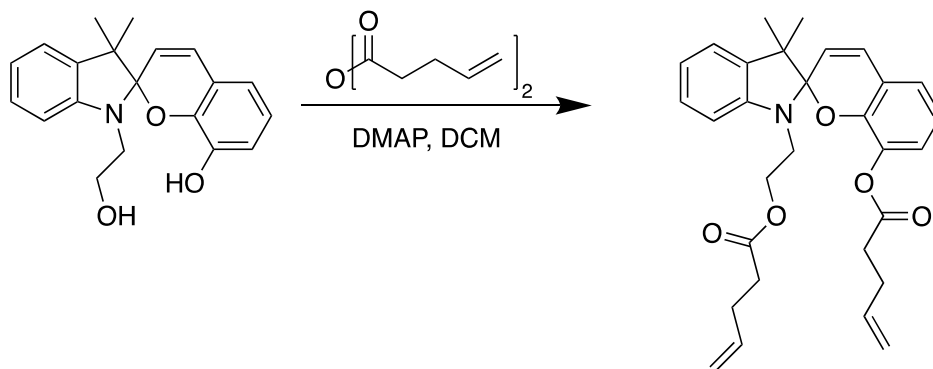
The multi-functional mechanical sensitivity of biological tissues,^{69,221} such as skin, is difficult to reproduce. In polymers that incorporate force-responsive molecules (i.e. mechanophores), mechanical force induces chemical transformations of mechanophores,²²²⁻²²⁴ enabling controlled colour/luminescence changes,^{50,225} mechanocatalysis,²²⁶⁻²²⁷ isomerisation,²²⁸ release of small molecules²²⁹ and self-healing behaviours.²³⁰ Mechanochromic polymers that undergo colour changes in response to mechanical stress can be used to directly visualise the stress distribution and mechanochemical activations within polymers, which is advantageous for application in stress/strain sensing^{51,54,231} and damage monitoring in polymeric materials.²³²⁻²³³ To induce stress-driven mechanochemical transformations, efficient transmission of mechanical stress through the polymer matrix and coupling to the mechanophore is critical. Various factors affect the efficiency of mechanochemical activation, including the mechanophore position in the polymer chain,⁵⁰ polymer molecular weight,²³⁴ polymer chain alignment²³⁵ and temperature.²³⁶ Mechanochemical activation can also be enhanced by controlling the hard and soft blocks within the polymer. In this approach, soft polymer chains can be aligned parallel to the tensile direction via localised stress at the hard polymer blocks²³⁷⁻²³⁸ or soft mechanophores and hard ligands enable mechanochemistry even under isotropic compressive force.²³⁹ However, most previously reported mechanochromic polymers exhibit mechanophore activation after irreversible plastic deformation²³³ or provide reversible stretchability at the expense of mechanosensitivity.^{49,51,235,240} For use in sensing applications, e.g. electronic skins, mechanochromic polymers with high stress sensitivity and reversible stretchability under large strain are needed. Furthermore, although several mechanophores based on fluorescent and phosphorescent properties have exhibited fast response/relaxation times to track force-induced luminescence changes in real-time,²⁴¹⁻²⁴² mechanochromic polymers with sensing capability of high-frequency dynamic forces over a few hundreds of Hz are still required for multifunctional e-skins.^{22,28,122} However, multifunctional mechanochromic materials with all these properties are yet to be demonstrated.

Stress concentration is a phenomenon that is well demonstrated in composite materials wherein stress concentrates at the interface between mechanically dissimilar materials, inducing localised crack and failure.²⁴³ In artificial and biological materials, hierarchical structures can dissipate stress from macroscale to smaller nanoscale structures, thereby enhancing mechanical strength and toughness.²⁴⁴⁻²⁴⁵ Thus, controlling stress concentration in hierarchical structures may enable mechanochromic

polymers with high mechanosensitivity and stretchability. Herein, we introduce a hierarchical nanoparticle-in-micropore (NP-MP) architecture in porous mechanochromic composites comprising spiropyran (SP), polydimethylsiloxane (PDMS) and silica nanoparticles (SNPs; **Figure 5.1a**) to enhance force sensitivity and stretchability. In this design, the SP mechanophore undergoes a force-induced reversible ring-opening process from colourless SP to coloured merocyanine (MC).⁴⁹ Upon the application of external stress to the mechanochromic composites, the hierarchical NP-MP architecture induces stress concentration near the pore regions decorated with SNPs, significantly enhancing the mechanochromic sensitivity. Our porous mechanochromic composites undergo mechanochromic colour change at lower strain/stress values (tensile strain: 50%; normal force: 1 N) in comparison with composites without the NP-MP architecture (tensile strain: 150%; normal force: 6 N). Furthermore, the failure strain of the hierarchical NP-MP structure (~400%) is larger than that of the nonporous structure (240%), enabling reversible mechanochromic behaviour at 250% tensile strain in the hierarchical NP-MP composite. In addition, our mechanochromic e-skins are capable of the dual-mode detection of static and dynamic forces without any external power. This property allows the instantaneous visualisation of writing intensity based on colour change, the monitoring of writing speed and the detection of vibrations and acoustic sounds based on changes in triboelectric signal. Based on the structural design of hierarchical nanoparticle-in-micropore architectures of previously reported SP/PDMS mechanochromic composites,^{49,87,246} significant enhancement of mechanochromic performances and dual mode mechanochromic and triboelectric sensing capabilities could be achieved, which was not possible in previous works.

5.2 Experimental Details

Fabrication of porous mechanochromic composites: The mechanophore (SP) was prepared via the chemical reaction shown below. The synthetic procedure and characterisation are detailed in a previously published report.^{49,247} This alkene-functionalized spiropyran can be covalently incorporated into PDMS matrix via platinum-catalyzed hydrosilylation reaction of a PDMS curing agent.⁴⁹



The fabrication of the porous PDMS/SP composites was initiated by adding SP (2 wt%) into a 10:1 mixture of PDMS (Sylgard 184, Dow Corning) and curing agent. Subsequently, hydrophilic solvents (DI water and ethanol) were added into the PDMS/SP precursor, affording PDMS: DI water: ethanol weight ratios of 3:2:0, 3:1.5:0.5 and 3:1:1. The resulting mixtures were mechanically stirred. SNPs (Polysciences) of different sizes (20, 100 and 300 nm) dispersed in DI water (1.07 wt% SNPs) were added to the mixtures of PDMS/SP precursor and solvents. The gel-type mixtures were poured into polyethylene terephthalate (PET) substrates and stored in a desiccator for 1 h to eliminate air bubbles from the PDMS. Subsequently, the prepared mixtures were annealed at 70°C for 2 h to cure the PDMS and eliminate the hydrophilic solvents, generating porous mechanochromic composites. The as-prepared composites were freeze-dried (TFD5503, ilShinBioBase) for 24 h to completely eliminate residual solvent.

Characterisation of porous mechanochromic composites: The structures and morphologies of the porous mechanochromic composites were observed using field-emission scanning electron microscopy (S-4800, Hitachi). Mechanical property was measured using a dynamic mechanical analyser (RSA III, TA Instruments) under a stretching velocity of 1 mm/s.

Evaluation of the colourimetric sensing capability of the e-skins: The mechanochromic properties of the e-skin were quantitatively evaluated as a function of pressure and strain by analysing the colour gradients ('R', 'G' and 'B') extracted from photographs using both a colour picker program (Color cop) and a spectroradiometer (PR-655, Photo Research, Inc.). Normal pressure was applied using a laboratory-built pushing tester comprised of a push-pull gauge (DFG-10, OPTECH) and a microstage system. Strain was applied using a tensile strain tester (TXA-TM, Yeonjin Corp.). A triboelectric sensor

was constructed by attaching silver nanowire flexible electrodes onto a PET substrate (thickness: ~ 1.3 μm) on the top of the porous mechanochromic composite. The generated current and voltage outputs were collected using a source meter (S-2450, Keithley) and an oscilloscope (DPO 2022B, Tektronix), respectively. To confirm the dynamic acoustic pressure, a speaker was placed 1 cm from the e-skin and the generated voltage output induced by a sound wave with an intensity of 96.5 dB was recorded.

5.3 Results and Discussion

Porous mechanochromic composites with hierarchical NP-MP architectures were fabricated by mixing SP, PDMS and SNPs in hydrophilic co-solvents (water and ethanol), followed by the evaporation of solvents during the hydrosilylation curing process (Figure 5.2). During this process, spherical pores were formed within the composites as a result of phase separation between the hydrophobic PDMS matrix and hydrophilic solvents following the elimination of trapped solvents.²⁴⁸ The porous PDMS/SP/SNP composite films were then subjected to a freeze-drying process to eliminate residual solvent (Figure 5.3). The porous PDMS/SP/SNP composite films were light yellow in colour (Figure 5.1b). The scanning electron microscopy (SEM) images in Figure 5.1b show that the porous PDMS/SP/SNP composites contained uniformly distributed pores with SNP-decorated inner pore surfaces, resulting in a hierarchical NP-MP architecture. The pore size was controllable to 5, 10 and 25 μm (referred to as pore-5, pore-10 and pore-25, respectively) by controlling the ratio of water to ethanol (Figure 5.4, Section 1 in the Supplementary materials). The porosity remained constant ($\sim 36\%$) at the different pore sizes, whereas the surface area increased with decreasing pore size (Figure 5.5, Section 5.1). In this study, the SNPs dispersed in hydrophilic water/ethanol droplets within the hydrophobic PDMS matrix were uniformly decorated on the inner pore surfaces during solvent evaporation (Figure 5.6a). SNPs with diameters of 20, 100 and 300 nm (referred to as SNP-20, SNP-100 and SNP-300, respectively) were uniformly decorated on the inner surfaces of the PDMS pores (Figure 5.6b, c).

The hierarchical NP-MP architecture significantly affects the mechanical properties of the mechanochromic composite. Compared to the nonporous structure, the porous structure enhances the maximum strain and decreases the maximum stress (Figure 5.1c). The decoration of the porous composite with SNPs further increases the stretchability and maximum stress; this effect is attributed to the increase in energy dissipation induced by localised stress in the hierarchical NP-MP architecture.^{244-245,249} The maximum strain of the porous composite increases with decreasing pore size (Figure 5.7a), which can be attributed to the large number of sites that dissipate mechanical energy via pore–stress interaction.²⁵⁰ The maximum strain of the porous composite increases with increasing SNP size (Figure 5.7b), which is attributed to the enhanced load-bearing ability with increasing SNP size in hierarchical structures.^{244,251}

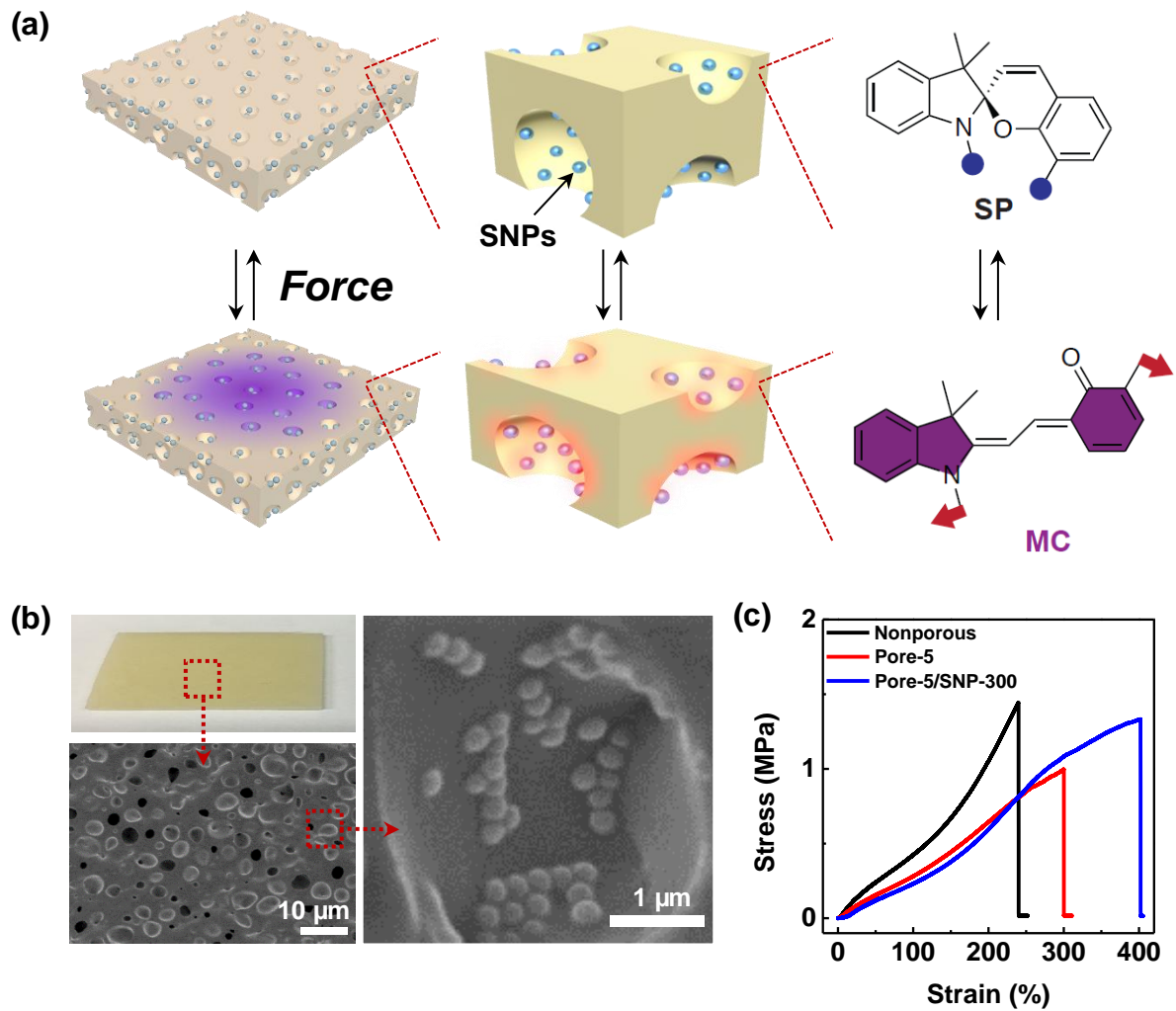


Figure 5.1. Hierarchical NP-MP architecture in porous mechanochromic composites. (a) Schematic of the working mechanism of porous mechanochromic composites with hierarchical NP-MP architecture. (b) Photograph and SEM images of porous (pore-5) mechanochromic composites comprising PDMS, SP and 300-nm SNPs (SNP-300). The SEM images show uniform spherical pores and SNPs decorated on the inner pore surfaces. (c) Stress–strain behaviours of the stretchable mechanochromic polymers with planar, porous and SNP-decorated porous structures.

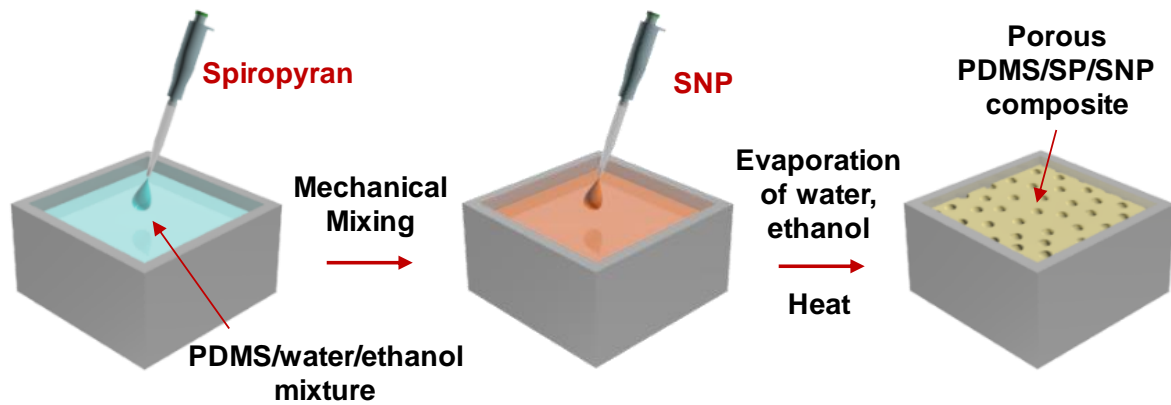


Figure 5.2. Schematic of the fabrication procedure for porous mechanochromic composites with PDMS/SP/SNPs. SP, PDMS and SNPs are mixed in hydrophilic co-solvents (water and ethanol) and solvents are evaporated during the hydrosilylation curing process.

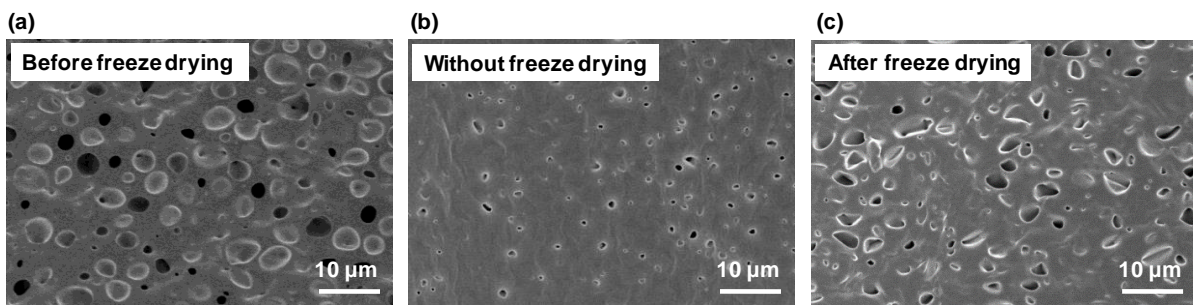


Figure 5.3. (a) Scanning electron microscope (SEM) image of a porous mechanochromic composite with an average pore size of 5 μm before freeze-drying. SEM images of a fabricated porous mechanochromic composite after three days before (b) and after (c) freeze-drying. Due to the capillary force-induced pore closure during solvent evaporation, freeze-drying is required to completely evaporate the solvent and obtain uniform pores.

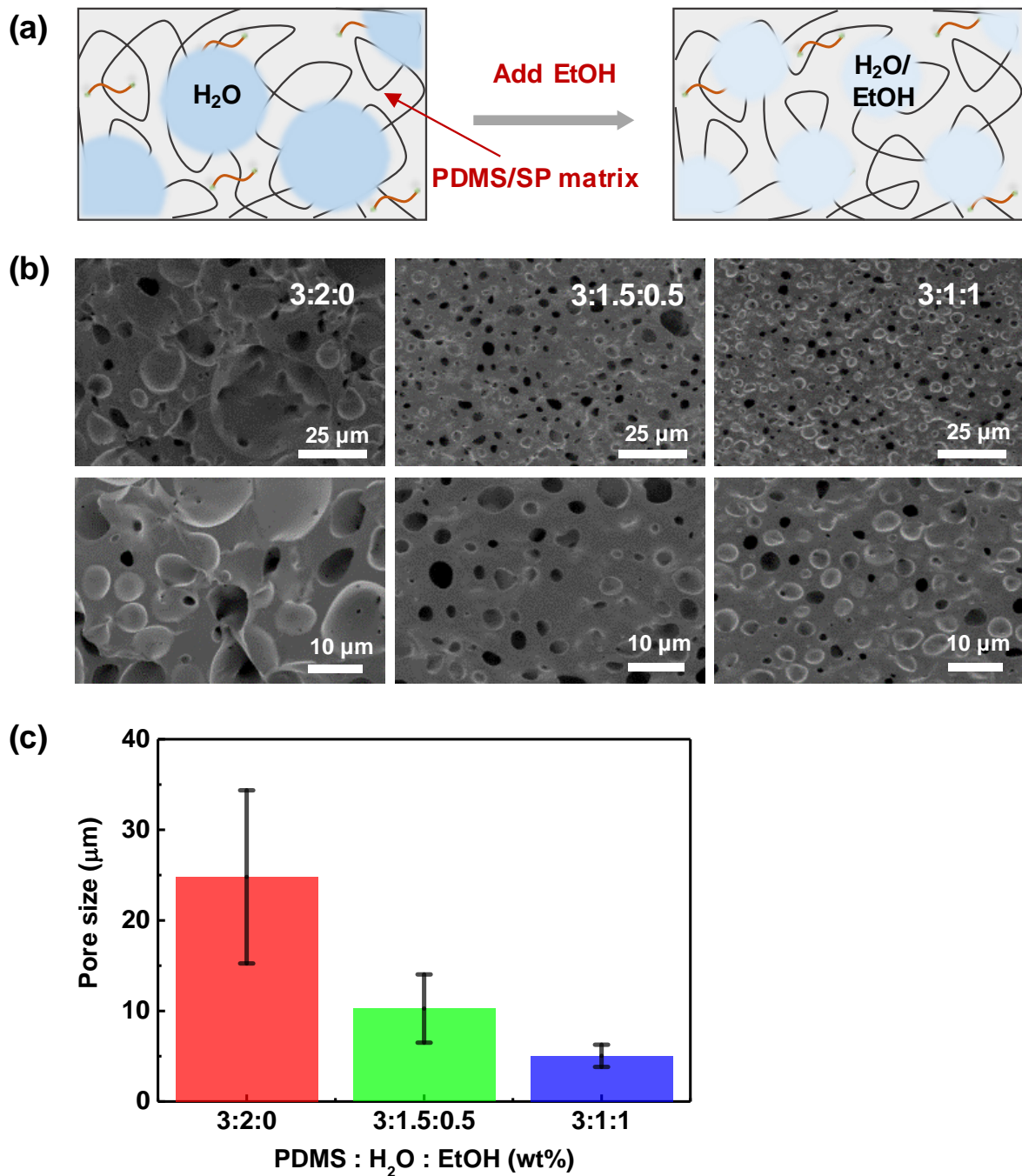


Figure 5.4. (a) Schematic of the mechanism of pore formation in composites based on the addition of hydrophilic solvents. (b) Cross-sectional SEM images of porous PDMS/SP composites with different mixed solvent ratios (PDMS:water:ethanol = 3:2:0, 3:1.5:0.5 and 3:1:1). The lower row shows magnified SEM images. (c) Pore size distributions of porous PDMS/SP composites with different mixed solvent ratios.

(a)

	No pore	Pore (25 μm)	Pore (10 μm)	Pore (5 μm)
Volume (mm^3)	0.001	0.000738	0.000738	0.000738
Area (mm^2)	0.06	0.0993	0.194	0.351

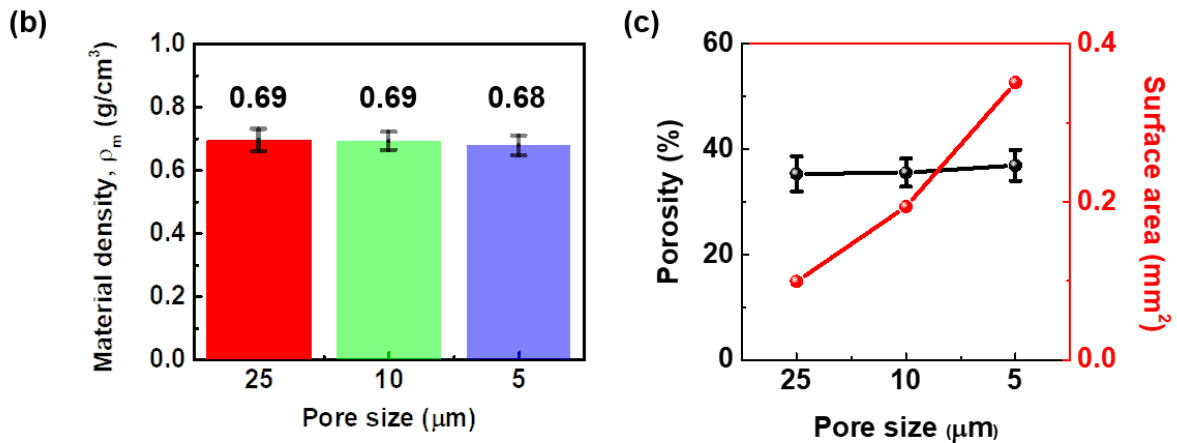


Figure 5.5. (a) Simulated surface areas of porous mechanochromic composites with different pore sizes based on face-centered cubic (FCC) unit cell arrays. The porous structures are modelled according to average pore sizes of 25, 10 and 5 μm with the same porosity (26%) based on FCC unit cell arrays. Volume is determined as the total material volume, excluding the pore volume. Area is the total surface area of the porous structure. (b) Material densities of the fabricated porous mechanochromic composites with different pore sizes. (c) Porosity and surface area of porous mechanochromic composites as functions of pore size.

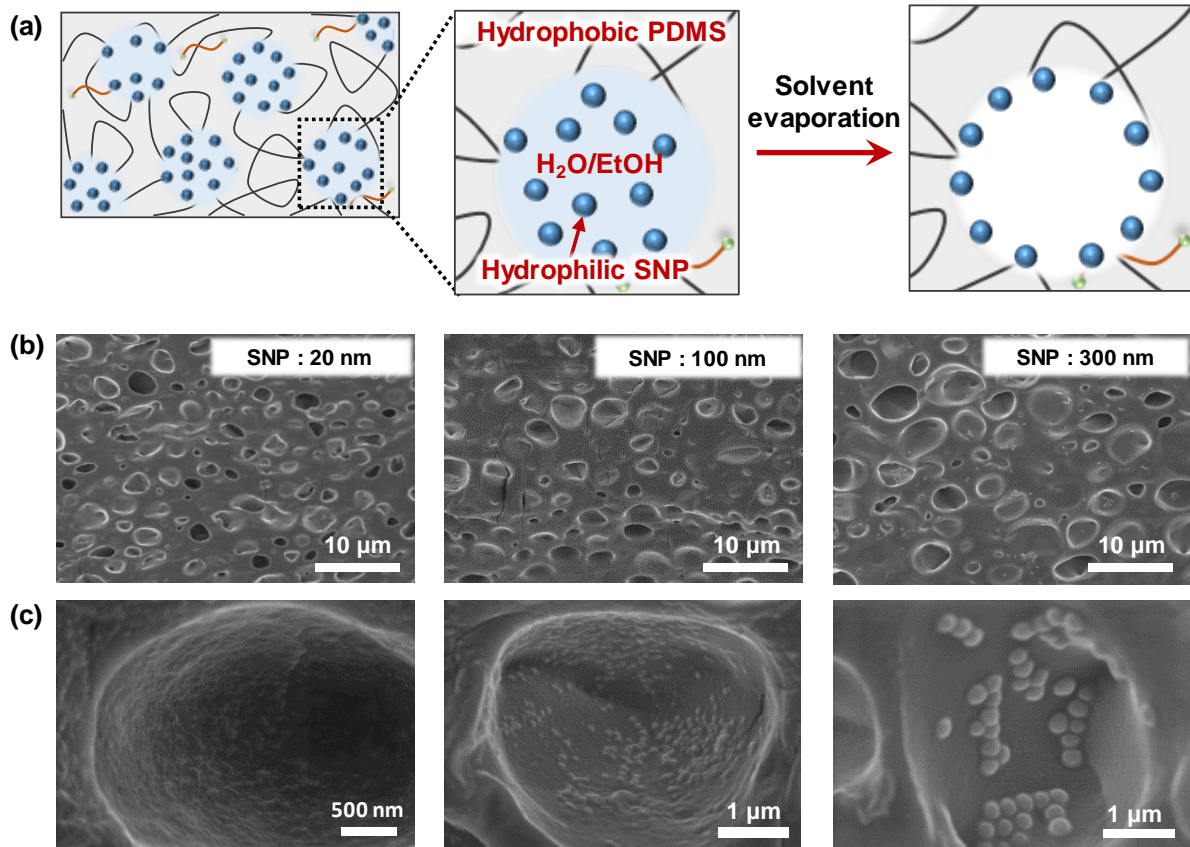


Figure 5.6. (a) Schematic of SNP decoration on the inner pore surfaces of a mechanochromic composite during heat-induced solvent evaporation. (b) Cross-sectional SEM images of porous PDMS/SP composites (pore size = 5 μm) with different SNP sizes (20, 100 and 300 nm). (c) Magnified SEM images showing that the SNPs are uniformly decorated on the inner pore surfaces.

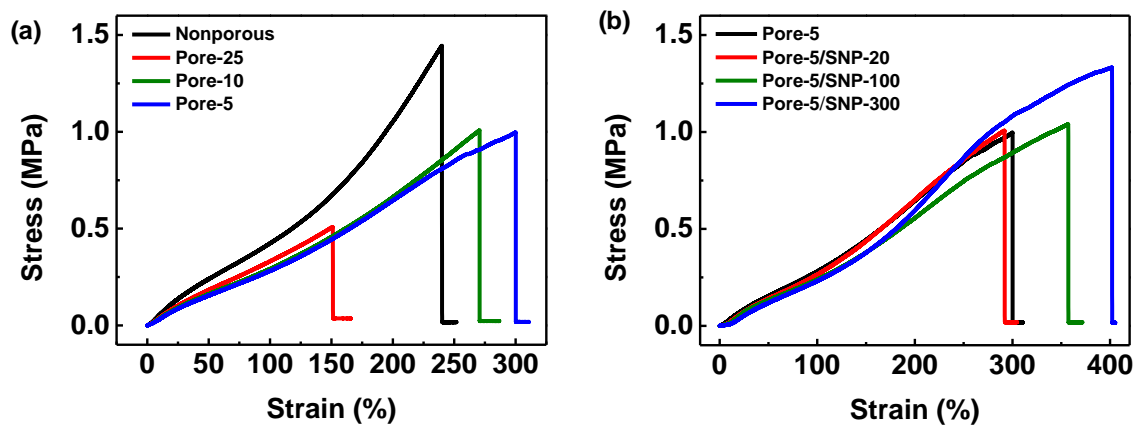


Figure 5.7. (a) Strain–stress curves of porous PDMS/SP composites with different pore sizes. (b) S–S curves of porous PDMS/SP composites (pore size = 5 μm) with different SNP sizes.

We monitored the changes in the colour of mechanochromic polymers under tensile strain using a spectroradiometer (Figure 5.8). Compared to nonporous PDMS/SP polymers, the porous PDMS/SP/SNP composites undergo a distinct colour change from pale yellow to blue at 200% tensile strain, indicating the mechanochemical ring-opening reaction of SP into MC (Figure 5.9a). As the pore size decreases, the critical strain needed to observe the colour change decreases, while the intensity of the blue colour and stretchability increases (Figure 5.10). For pores decorated with SNPs, a further colour change to a vivid blue colour is observed (Figure 5.11). Amongst the tested composites, the composite with small pores (5 μm) and large SNPs (300 nm) exhibits the greatest colour change in response to a large range of strain ($\sim 400\%$; Figure 5.9a). The pore-5/SNP-300 composite displays a reversible and highly stable mechanochromic response for up to 100 cycles under a tensile strain of 250% (Figure 5.9b and Figure 5.12).

The detailed colour changes of the mechanochromic polymers were further investigated by analysing the changes in the average colour coordinates based on the CIE 1931 colour space diagram (Figure 5.9c). Compared to nonporous PDMS/SP polymers, porous PDMS/SP polymers exhibit a larger colour transition range, and this range is further increased by decoration with SNPs. This behaviour is ascribed to the effective stress concentration near the hierarchical NP-MP region in the composite by the support of nanoscale hard SNPs at the inner pore surface against the local stress around the microscale pore region. In addition, the improved stretchability increases the colour transition range of the porous composite. The colour transition range increases gradually with decreasing pore size and increasing SNP size (Figure 5.13). For different tensile strains, the porous composites with pore-5/SNP-300 clearly exhibit distinct luminescence spectra in the visible wavelength range in which the peaks in 420–480 nm (blue) significantly increase, whereas those in 500–600 nm are dissipated (Figure 5.9d), supporting the blue colour transition with the tensile strain. The time required for recovery from MC to SP depends on the strain. Figure 5.14a shows that the intensity of the green colour decreases with increasing strain and becomes saturated under fixed strain. Upon releasing the strain, the saturated colour returns to the original colour after a delay of ~ 2 , 14, and 35 s for the strains of 125%, 150%, and 175%, respectively. Thus, the recovery time increases with increasing tensile strain. The recovery times of our porous mechanochromic composites compare favourably with those of previous mechanochromic polymers (2–60 min; Table 5.1).^{49,51,53,252} This fast recovery time can be ascribed to the much larger deformable surfaces due to the inner pores, which induces rapid storage and release of the elastic energy, and thus easier stress relaxation.²⁵³ It is also possible that the polarity of the interface might differ (due to the hydrophilic silica particles), and polar environments are expected to stabilize the merocyanine form of the mechanophore.²⁵⁴ It is worth noting that exposing the sample to white light can shorten the recovery time (Figure 5.14b). The ring-closing reaction from MC back to SP can be accelerated by heating or visible-light irradiation.²⁵⁵

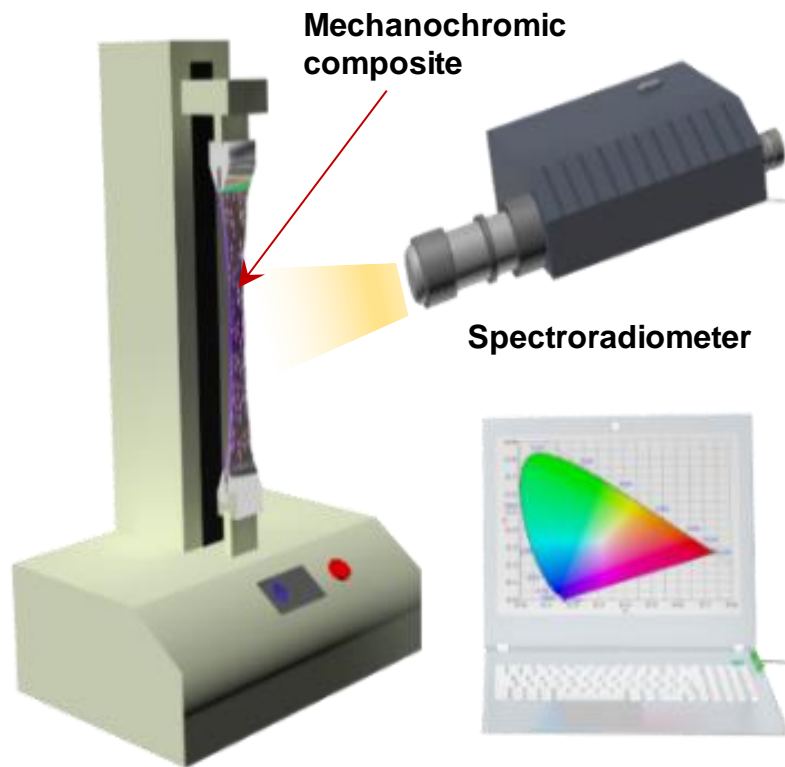


Figure 5.8. Schematic of a measurement system using a spectroradiometer for investigating the colour transition properties of porous mechanochromic composites in response to tensile strain.

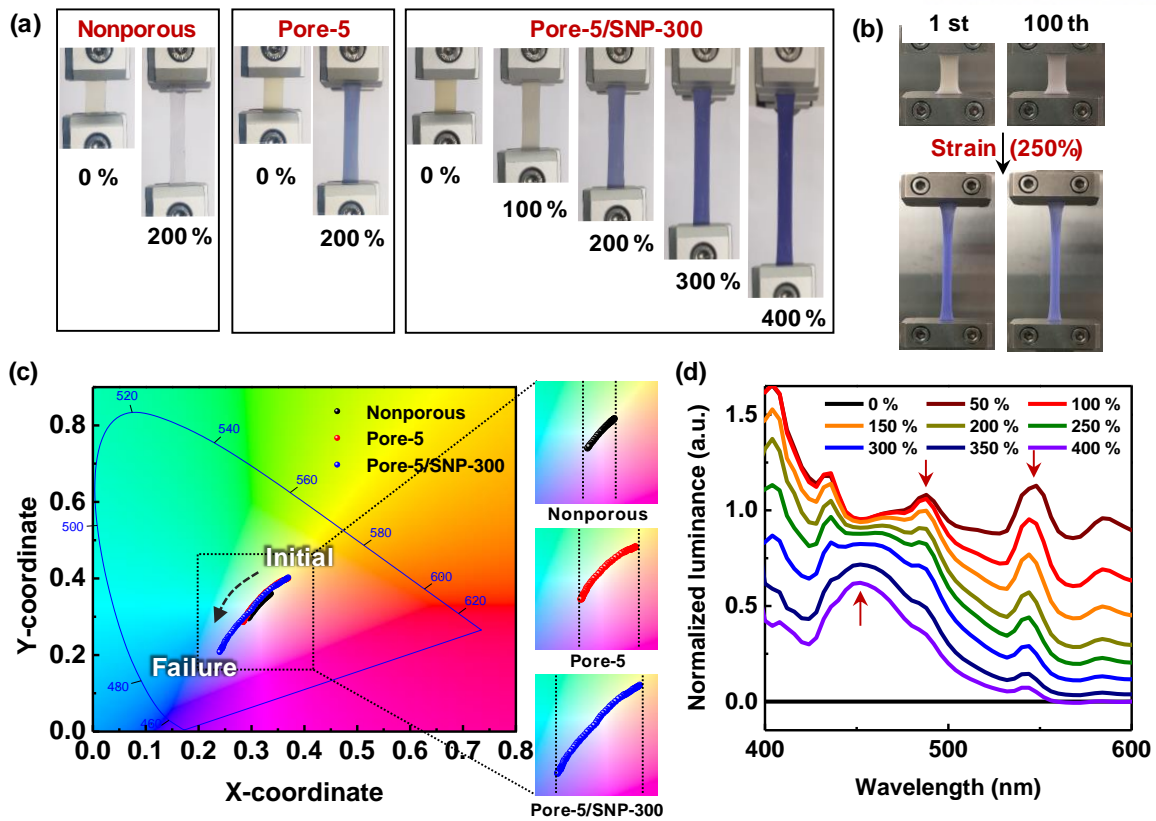


Figure 5.9. Properties of porous mechanochromic composites under tensile strain. (a) Photographs of mechanochromic polymers with different structures exhibiting colour changes in response to tensile strain. (b) Colour change of the pore-5/SNP-300 mechanochromic composite at the first and 100th stretching and releasing cycles. (c) Changes in the average colour coordinates of the mechanochromic polymers with different structures under applied tensile strain. (d) Normalised luminance as a function of wavelength for the pore-5/SNP-300 mechanochromic composite under tensile strains up to 400%.


















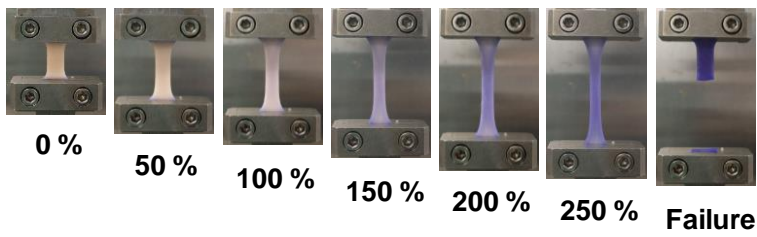
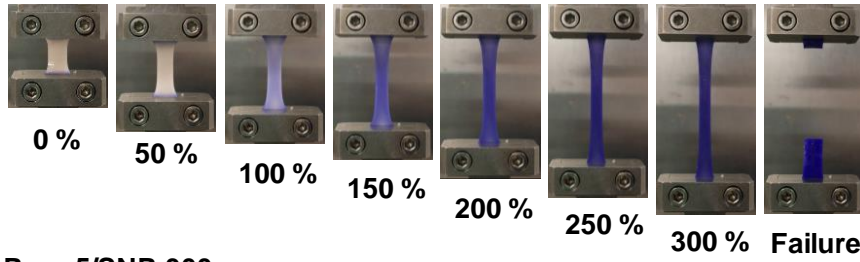
Tensile strain	0 %	50 %	100 %	150 %	200 %	Failure
Porous (25 μm)						
Porous (10 μm)						
Porous (5 μm)						

Figure 5.10. Photographs showing the colourimetric strain sensing properties of porous mechanochromic composites with different pore sizes.

(a) Pore-5/SNP-20



(b) Pore-5/SNP-100



(c) Pore-5/SNP-300

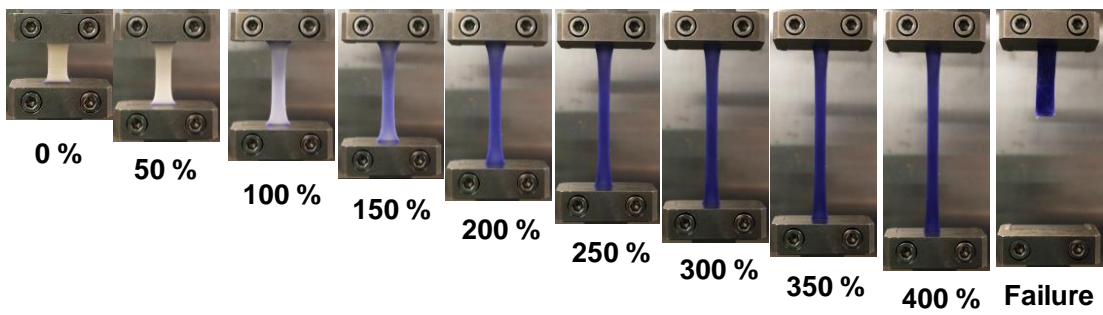


Figure 5.11. Photographs showing the colourimetric strain sensing of porous PDMS/SP composites (pore size = 5 μm) decorated with SNPs with different sizes: (a) 20 nm. (b) 100 nm. and (c) 300 nm.

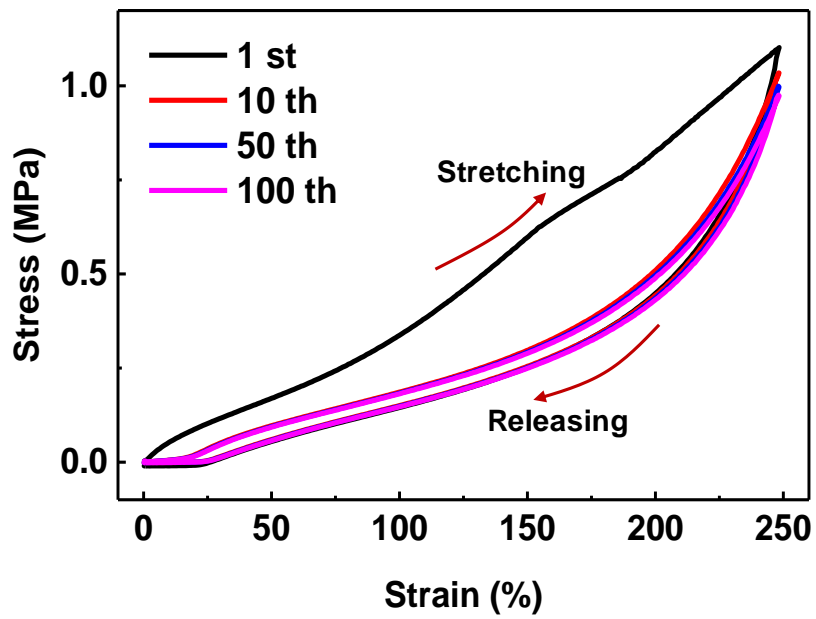


Figure 5.12. Strain–stress curves of a porous mechanochromic composite (pore size = 5 μm ; SNP size = 300 nm) under repeated loading/unloading strain of up to 250%.

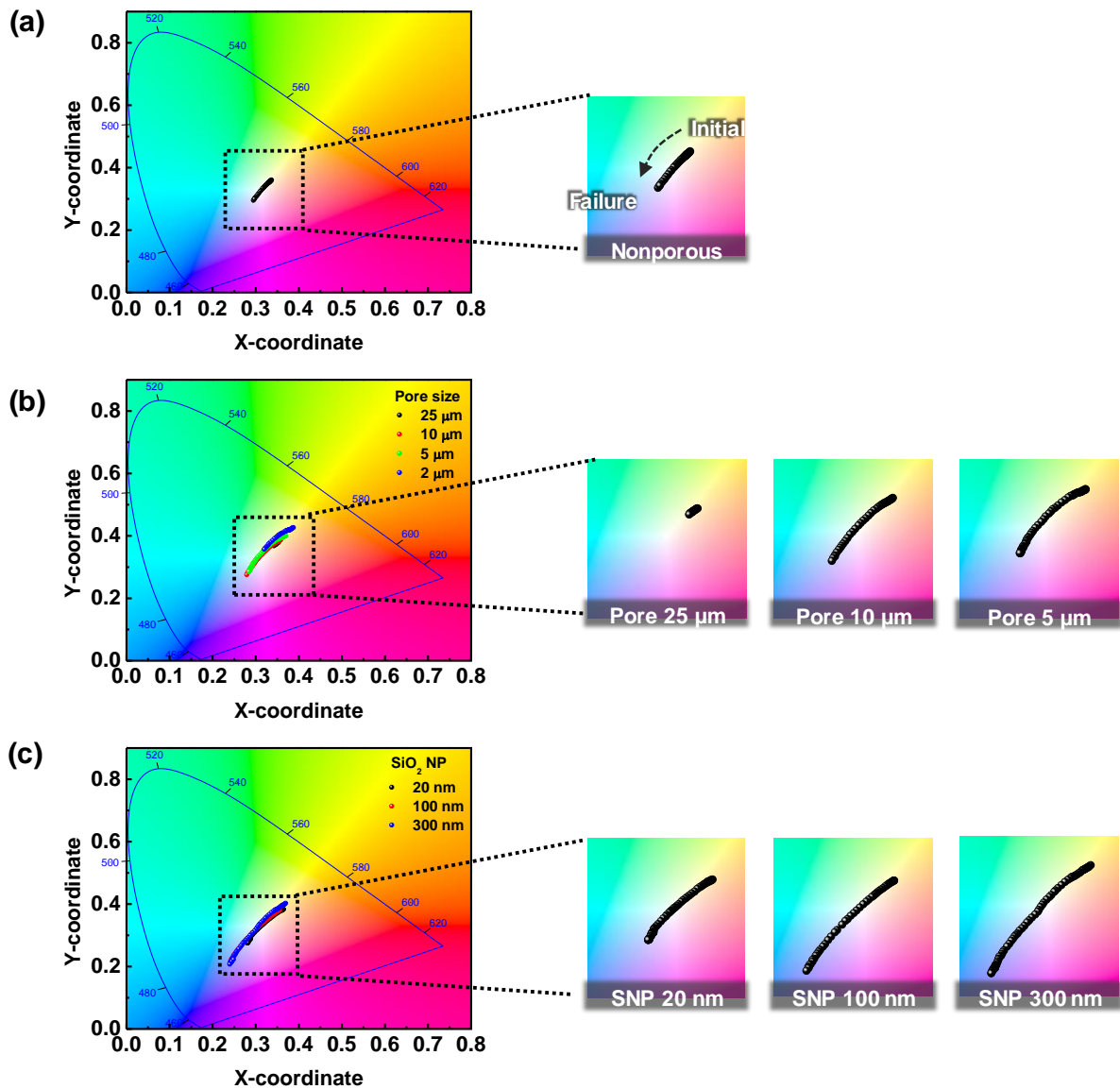


Figure 5.13 (a) Average colour coordinates of planar mechanochromic composites under loading tensile strain. (b) Average colour coordinates of porous mechanochromic composites with different pore sizes under loading tensile strain. (c) Average colour coordinates of mechanochromic composites with different SNP sizes under loading tensile strain.

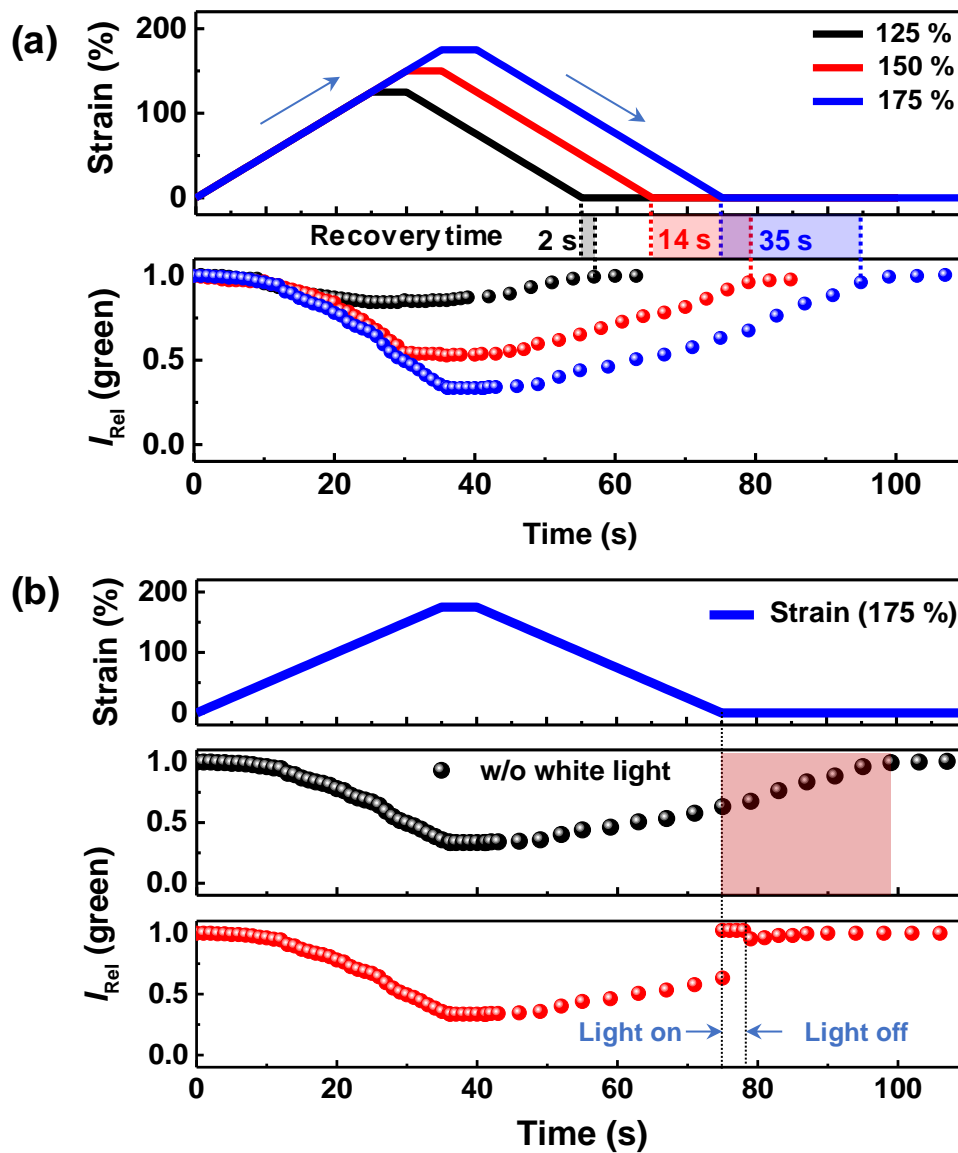


Fig. 5.14. Recovery time of a porous mechanochromic composite (pore size = 5 μm , SNP size = 300 nm) under different tensile strains. (a) Time-dependent tensile strains of 125%, 150% and 175% (top) and the corresponding change in relative intensity (I_{Rel}) of green colour in response to loading strain (bottom). (b) Relaxation under a loading/unloading strain of 175% depending on exposure to white light.

Table 5.1. Summary of recently reported mechanophore systems.

Journal	Materials	Critical strain	Critical pressure	Maximum strain	Recovery time	Ref.
Nature (2009)	SP/PMMA	200%	<50 MPa	1000% (reversible)	-	50
ACS Macro Lett. (2014)	SP/PDMS	75%–100%		200% (reversible)	1 h (w/o light); 10 s (with light)	49
ACS Macro Lett. (2015)	Diarylbibenzofuranone/ PU	50%		>300% (reversible)	-	54
Polymer (2016)	SP/PMA	259%		350% (reversible)	12 min	252
ACS Macro Lett. (2013)	SP mechanophore linked triblock copolymers	>600%		>1000% (irreversible)	-	238
Macromolecules (2013)	SP-linked segmented PU	200%		>550% (reversible)		231
Macromolecules (2014)	Dual crosslinked SP/PU composite	500%		900% (reversible)	-	240
ACS Macro Lett. (2014)	SP/ureidopyrimidinone (Supramolecular interaction)	500%		1000% (reversible)	-	237
Adv. Mater. (2017)	SP-crosslinked poly(AM-co-MA/SP) hydrogel	>100%		570% (reversible)	30 min (with light)	51
Adv. Mater. (2015)	Rhodamine/PU		375 MPa	- (reversible)	-	55
Adv. Mater. (2016)	Mechanochromic molecule-epoxy composite	14%		49% (irreversible)		233
Adv. Mater. (2018)	P(SP- <i>alt</i> -C ₁₀) nanofiber/PDMS	~10%		70% (irreversible)	120 s	53
This work	Porous SP/PDMS/SNPs	50%	1 MPa	400% (reversible)	35 s (w/o light); 3 s (with light)	

Hydrophilic SNPs are important in the formation of hierarchical NP-MP structures. Hydrophobic SNPs result in a different morphology of porous mechanochromic composites and colour transition properties (Figure 5.15). For hydrophobic SNPs, SNPs are embedded into the polymer matrix without decoration on the inner wall of pores due to the similar hydrophobic property with the PDMS matrix (Figure 5.15b). The resulting porous composites with hydrophobic SNPs exhibit a different mechanochromic property with a smaller colour transition range compared to those with hydrophilic SNPs (Figure 5.15d). This different mechanochromic behaviour is ascribed to the effective stress concentration near the hierarchical NP-MP region in the composite for hydrophilic SNPs, which cannot be observed for hydrophobic SNPs due to the aggregated SNPs in the bulk polymer matrix without the formation of hierarchical NP-MP region. Consequently, we found that the hydrophilic SNPs plays a critical role in the formation of hierarchical NP-MP architectures, resulting in the significant improvement of both mechanochromic sensitivity and stretchability.

To quantitatively analyse the strain sensitivity of mechanochromic composites, we monitored the changes in the intensity of red–green–blue (RGB) colour parameters under tensile strain (Figure 5.16). For the accurate investigation of colour change, the relative B/G intensity ratios ($\Delta C/C_0$, where C is the B/G colour intensity ratio) were analysed for mechanochromic polymers with different structures under tensile strain (Figure 5.17a). Compared to the nonporous structure, the porous structures exhibit larger colour intensity ratio, indicating a more vivid colour change in the porous structures. The pore-5 structure exhibits the maximum colour intensity ratio of 1.5, which is five times higher than that of the nonporous structure (0.3). Decorating the pore-5 composite with SNPs further improves the colour intensity ratio to 3.0, which is 10 times higher than that of the nonporous structure. In addition to the large colour change, the porous structure displays an initial variation in the colour intensity ratio at a critical strain of 75–80%, which is ~ 2 times lower than that of the nonporous structure (150%; Figure 5.17b). Decorating the pore walls with SNPs further decreases the threshold strain to 50–55%. The critical strain of 50% for the pore-5/SNP-300 composite is significantly lower than those of previous stretchable (stretchability > 200%) mechanochromic polymers based on SP mechanophores (critical strains of 75–500%; Table 5.1).^{49-51,240,252,256} Only the hard mechanochromic polymer with the irreversible stretchability of 70% exhibits a lower critical strain (10%).⁵³ To quantitatively analyse mechanochromic sensitivity, strain sensitivity (S) was calculated as $S = (\Delta C/C_0)/\Delta\varepsilon$, where ε is the applied strain (Figure 5.17c). For strain of 50–80%, all porous composites with SNPs show higher sensitivities (0.53–0.58) compared to the porous polymers without SNPs (0.08–0.14) and the nonporous structure (0). In the strain regime of 80%–240%, the pore-5/SNP-300 composite exhibits the highest sensitivity of 1.51, which is ~ 4.1 and ~ 5.6 times higher than those of porous composites without SNPs (0.37–0.8) and the nonporous composites (0.27), respectively.

To evaluate the stress concentration near the hierarchical NP-MP architecture, which significantly enhances the mechanochromic sensitivity, we further examined the strain–stress relationships by numerical finite-element analysis (FEA). Unlike the nonporous structure in which stress is homogeneously distributed throughout the matrix, the porous structure has a high stress concentration in the pore region (Figure 5.17d, left). Compared to the nonporous structure, the porous structures all exhibit higher maximum localised stress at strains up to 100% (Figure 5.17e and Figure 5.18). Furthermore, the porous structure with the smallest pore size amongst the samples possesses the highest PDMS/air surface area, resulting in a greater number of mechanochromic activation sites of concentrated stress near the interface (Figure 5.18). This produced a considerable enhancement in colour change and strain sensitivity, as shown in Figure 5.17a–c. For the porous composites decorated with SNPs, additional stress concentration occurs in the pore region near the SNPs because of the load-bearing support provided by the hard SNPs at the inner surfaces of the soft pores (Figure 5.17d, right). Furthermore, the maximum localised stress near the SNPs gradually increases with SNP size (Figure 5.17f and Figure 5.19), thereby enhancing mechanochromic sensitivity (Figure 5.17a–c). Based on the FEA results, we can conclude that both the amount of activation sites and the maximum stress localised around the pores and SNPs determine the overall mechanochromic sensing properties (relative colour intensity and strain sensitivity).

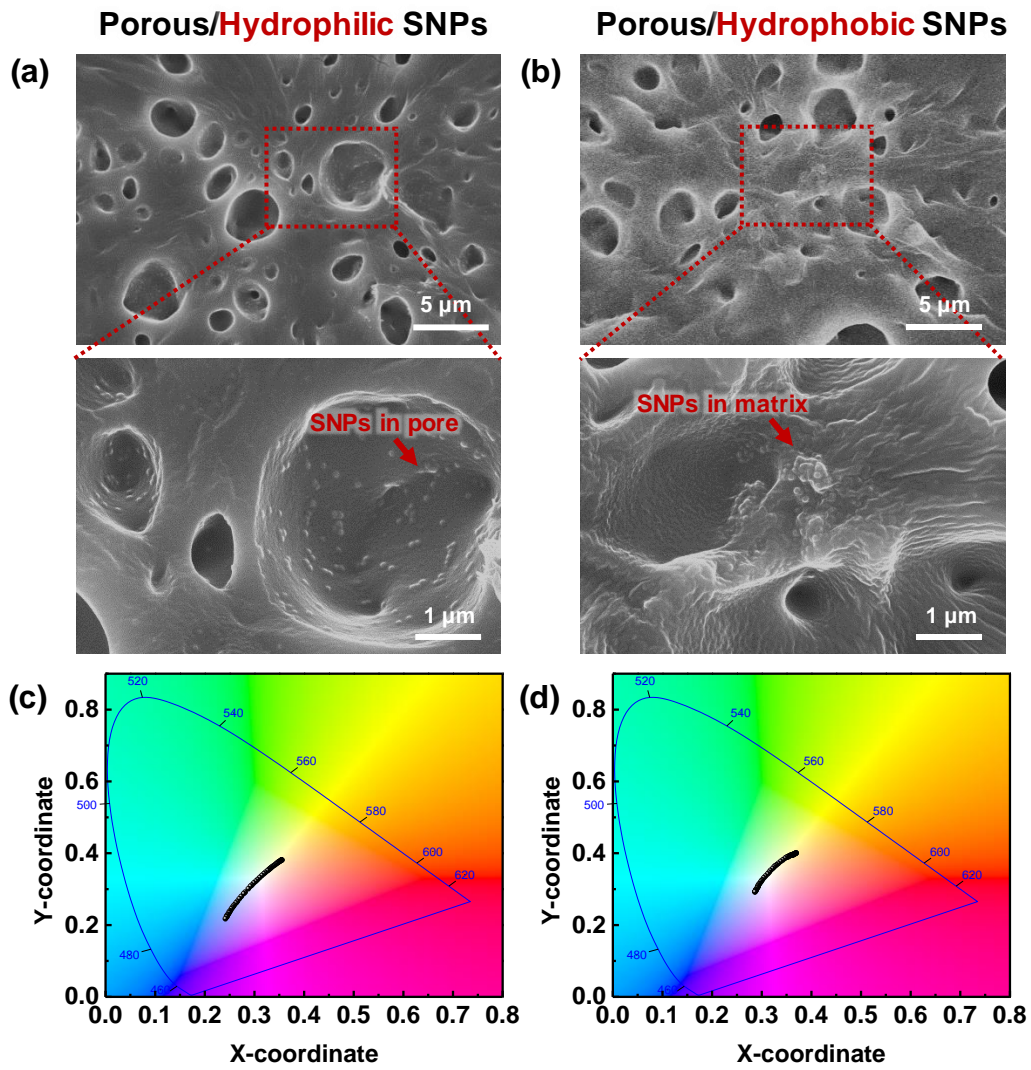


Figure 5.15. Effect of SNPs with different polarity on the mechanochromic property of polymer composites (pore size = 5 μm, SNP size = 100 nm). SEM images of porous PDMS/SP composites with (a) hydrophilic SNPs and (b) hydrophobic SNPs. Average colour coordinates of porous PDMS/SP composites with (c) hydrophilic SNPs and (d) hydrophobic SNPs.

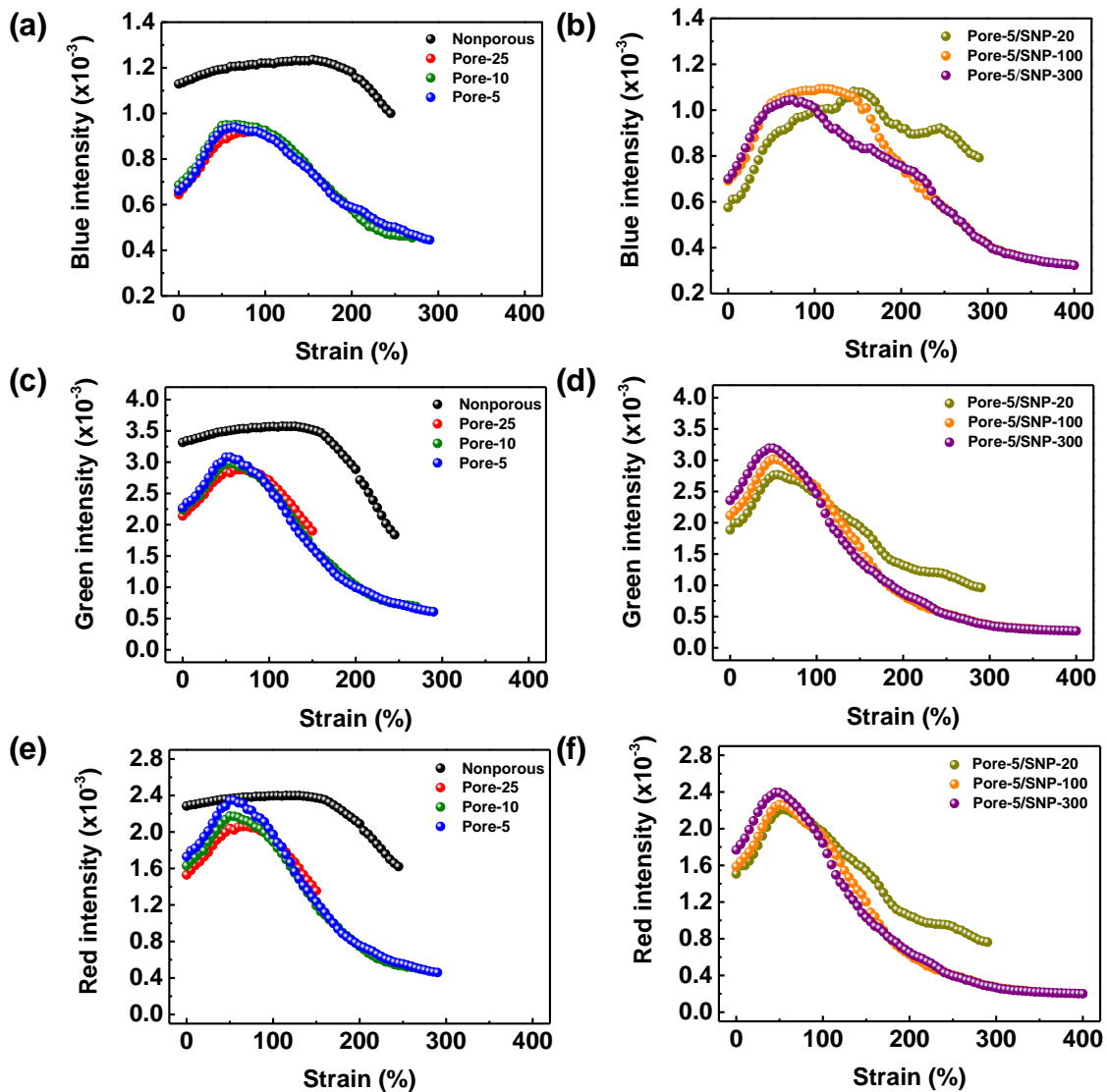


Figure 5.16 Variation in colour component intensities (R, G and B) of porous mechanochromic composites under loading strain at different wavelengths: (a,b) 488 nm. (c,d) 544 nm. and (e,f) 612 nm. The intensity of each colour component initially increases because of the decrease in light absorption caused by the concurrent decrease in film thickness. The intensity subsequently decreases because of the colouration of SP.

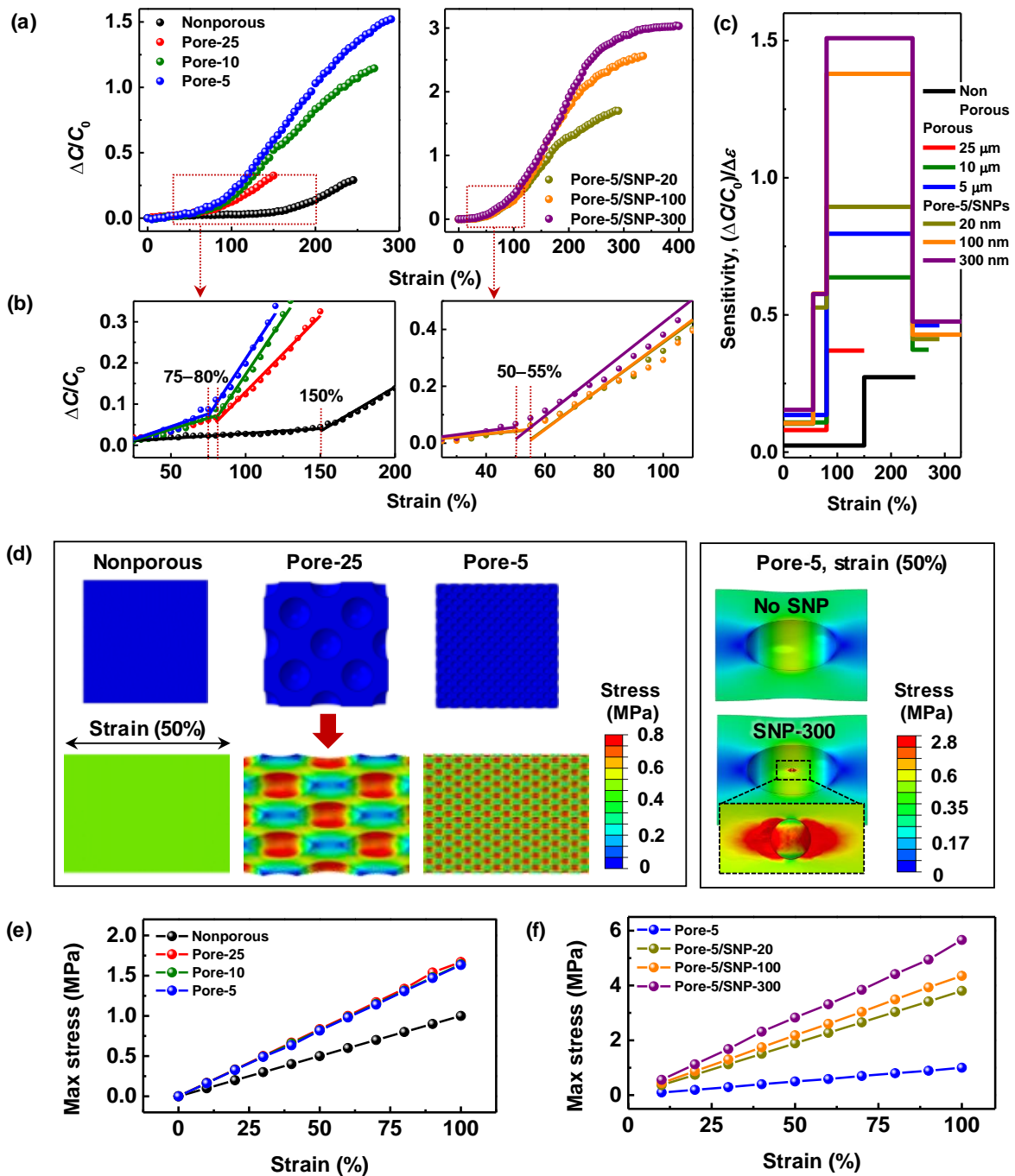


Figure 5.17 Structure-dependent strain sensitivity of porous mechanochromic composites. (a) Normalised colour intensity ratio as a function of strain for mechanochromic polymers with different pore sizes (left) and with different SNP sizes at a pore size of 5 μm (right). The colour intensity in response to strain is measured by spectroradiometer. (b) Enlarged plot from a in the strain range 20%–100%. (c) Strain sensitivity [$S = (\Delta C/C_0)/(\Delta \epsilon)$, where C is the colour intensity ratio and ϵ is the applied strain] of mechanochromic polymers with different structures. Sensitivity is estimated from the plot in a for the linear regimes of mechanochromic response. (d) Finite-element analysis (FEA)-determined

stress distributions of mechanochromic polymers with different pore sizes (left) and with 300-nm SNPs and a 5- μm pore size (right) under a tensile strain of 50%. (e,f) FEA-determined maximum localised stress near the pore surface in porous mechanochromic polymers with e different pore sizes and f different SNP sizes and a pore size of 5 μm as a function of strain.

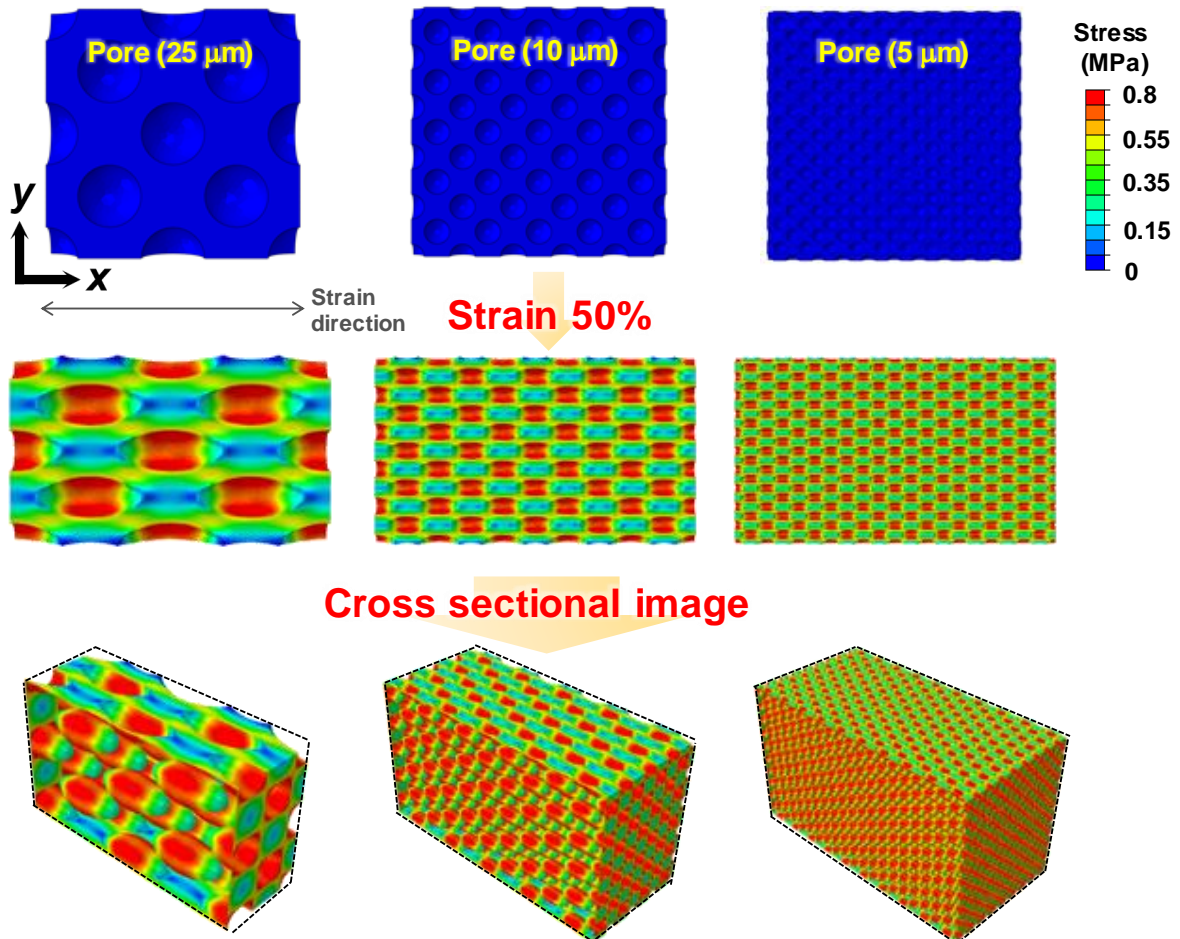


Figure 5.18. Stress distributions of porous PDMS/SP composites with different pore sizes (25, 10 and 5 μm) placed under 50% tensile strain calculated numerically using ABAQUS software. For simplicity, the elastic modulus is set to 1 MPa with the same porosity (26%) for all porous composites.

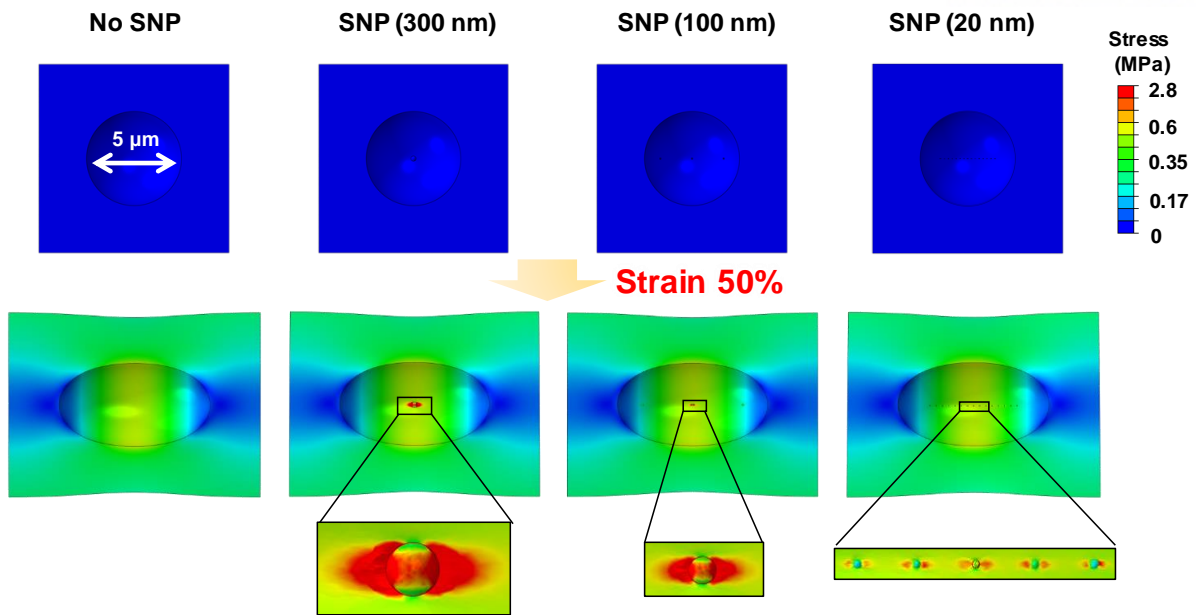


Fig. 5.19 Stress distribution of porous PDMS/SP composites (pore size = 5 μm) decorated with SNPs with different sizes (300, 100 and 20 nm) placed under 50% tensile strain calculated numerically using ABAQUS software. For simplicity, to understand the role of the SNPs at the pore walls, the elastic modulus of the porous matrix is set to 0.24 MPa. The elastic modulus of the SNPs is set to a general value of 180 GPa for all sizes.

The hierarchical NP-MP architecture of the mechanochromic composites also enhances the mechanochromic sensitivity in response to normal force in addition to tensile strain. This property allows the composites to be applied in touch-sensitive mechanochromic e-skins.⁹² We evaluated the changes in the RGB colour parameters of the composites in response to normal forces applied using a force gauge (Figure 5.20a). Under a normal force of 6 N, the porous PDMS/SP/SNP composites exhibit more vivid mechanochromic colour than the nonporous and porous structures (Figure 5.20b). Compared to the nonporous and porous structures, the changes in the relative red intensities were larger for the hierarchical NP-MP structures, indicating a more vivid colour change (Figure 5.21a). The relative red intensity decreased from 0.42 to 0.24 in conjunction with decreasing pore size (Figure 5.22a). This phenomenon is attributed to the increase in the area of stress concentration with decreasing pore size (Figure 5.22b). Meanwhile, decorating the porous structures with SNPs further increases the dynamic colour transition range to 85% (relative red intensity of 0.15 in Figure 5.21a) over a wide range of force (1–12 N). Amongst the composites with different SNP sizes, the composite with the largest SNPs (300 nm) exhibits the largest colour variation (85%) without saturation (Figure 5.23a).

Figure 5.21b shows the relative changes in the intensity of the green colour under different normal forces in increments of 0.1 N. With decreasing pore size, the critical stress required for the initial colour transition is reduced from 2.5 N (pore-25) to 1.8 N (pore-5). Decorating the pores with 300-nm SNPs further improves the pressure sensitivity, thus enabling detection at a minimum force of 1 N, six times lower than the minimum detection force of nonporous polymers (6 N). The improvement in mechanochromic sensitivity achieved by the addition of SNPs is attributed to the drastic increase in localised stress near the hard SNPs. The FEA calculations indicate that amongst the tested SNPs, the 300-nm SNPs exhibit the strongest localised stress in response to normal force (Figure 5.23b). The low detection limit (1 N or 1 MPa) represents a significant enhancement (~50 times increase) over previously reported mechanochromic polymers (50 and 375 MPa; Table 5.1).^{50,55} The porous mechanochromic composites reported herein also provide a high lateral resolution for force sensing, enabling the mapping of local pressure distribution without the need for complex sensor array patterns. Figure 5.21c shows the optical mechanochromic pressure maps after contact with various microscale objects. The pressure-induced local colour distribution patterns match the shape and wall thickness of the round microtips. The mechanochromic e-skins exhibit a minimum line width of 80 μm for contact with a needle tip.

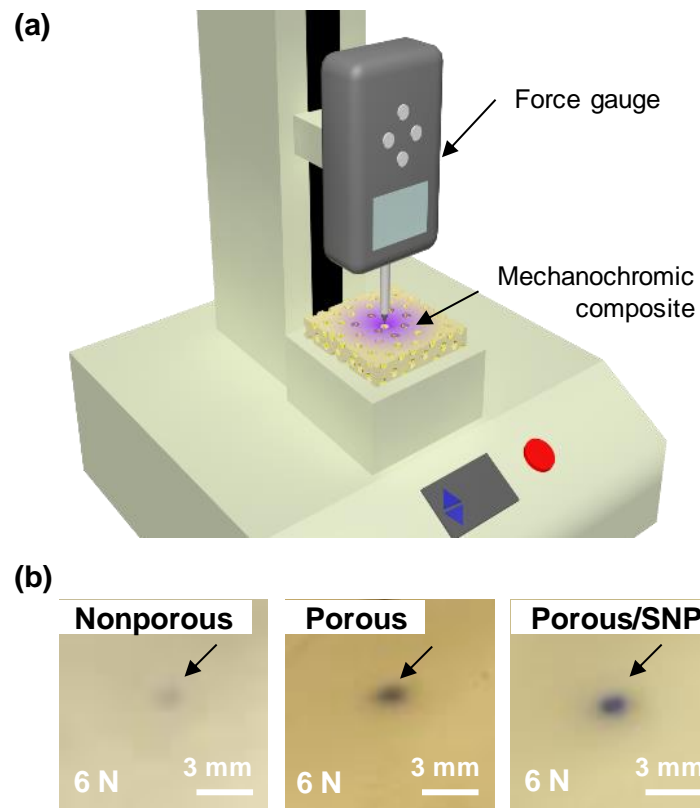


Figure 5.20. (a) Measurement system used to evaluate the colour transition properties of porous mechanochromic composites in response to normal stress. (b) Photographs of the mechanochromic composites with different porous structures under a loading normal stress of 6 N.

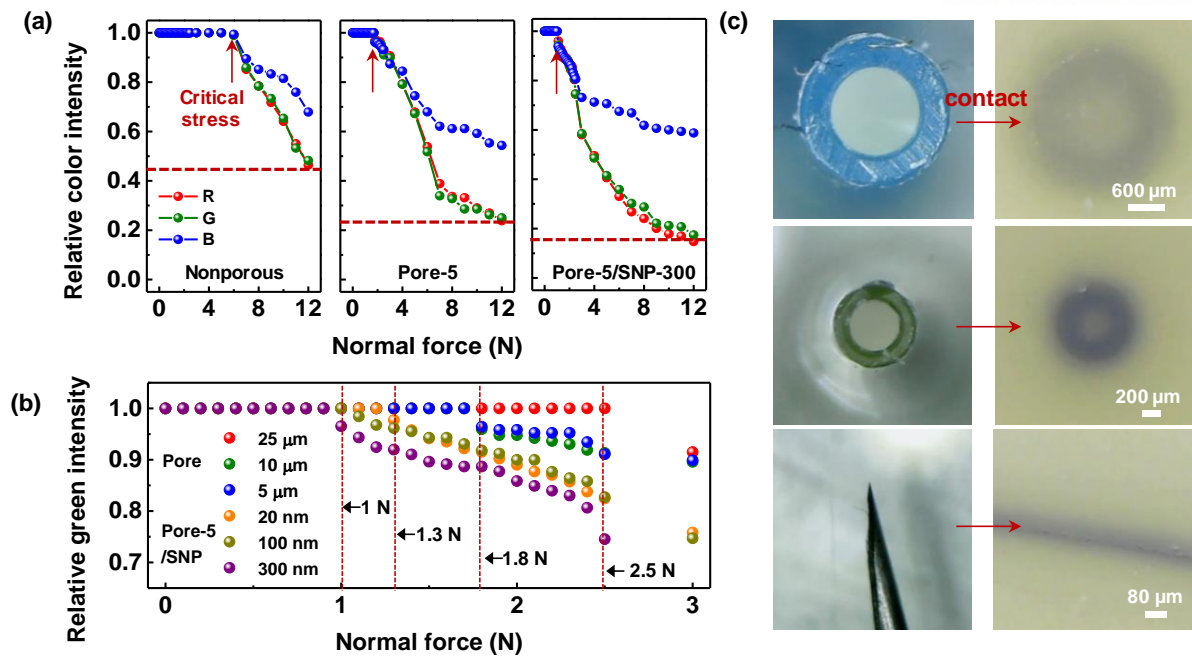


Figure 5.21. Normal force detection capabilities of porous mechanochromic composites. (a) Relative intensities of the colour components (red, green and blue) of mechanochromic polymers with different structures as functions of normal force. The colour intensity in response to normal force is measured by I-phone camera and colour picker program. (b) Relative green intensity as a function of normal force for mechanochromic polymers with different pore sizes and different SNP sizes with 5- μm pores. (c) Optical images showing the local colour distributions of the porous mechanochromic composites after contact with various objects (microtips and needle).

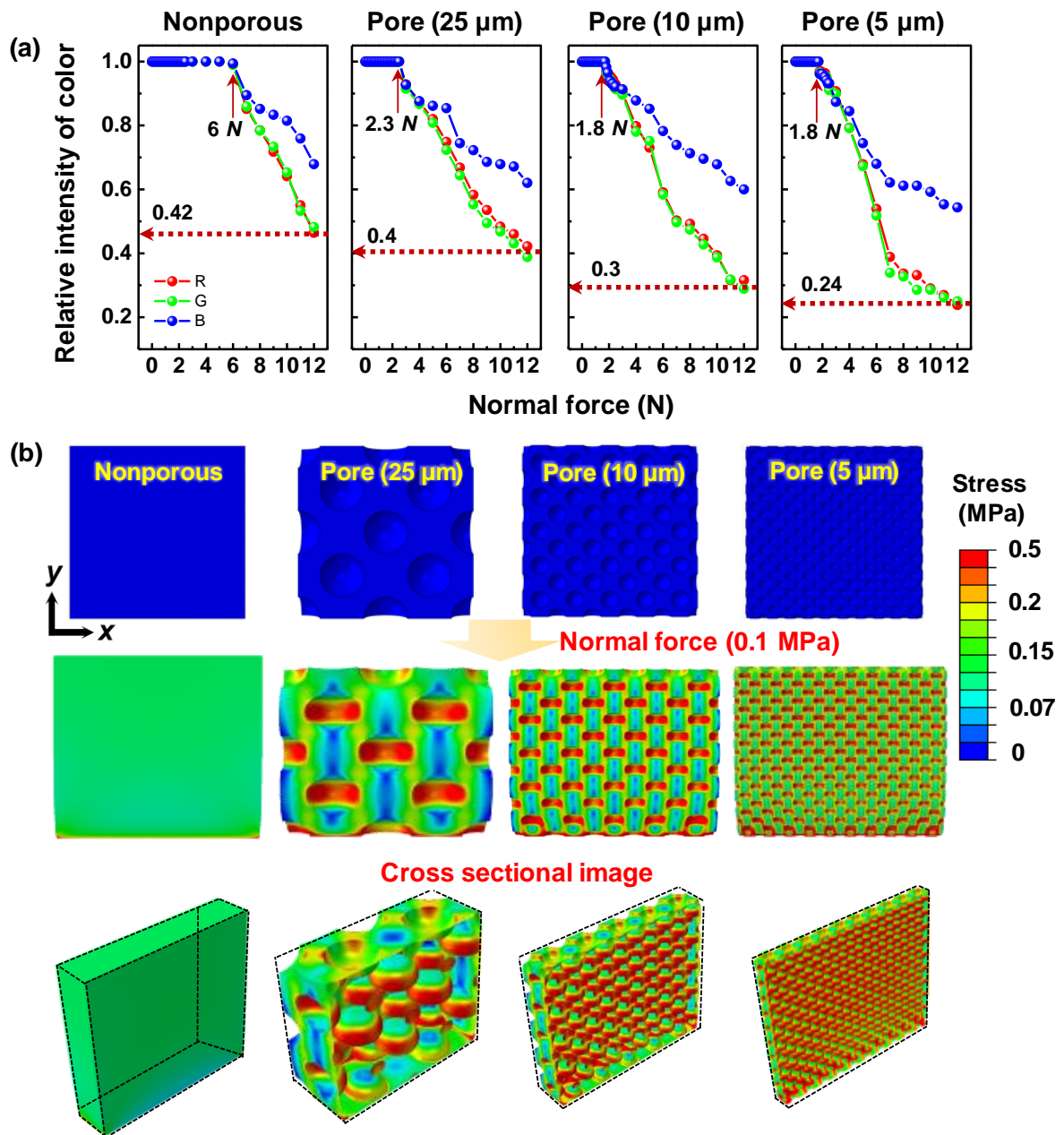


Figure 5.22 (a) Relative colour changes of porous PDMS/SP composites with different pore sizes in response to applied normal pressure. (b) Finite-element analysis-determined stress distributions in porous PDMS/SP composites with different pore sizes under applied normal pressure.

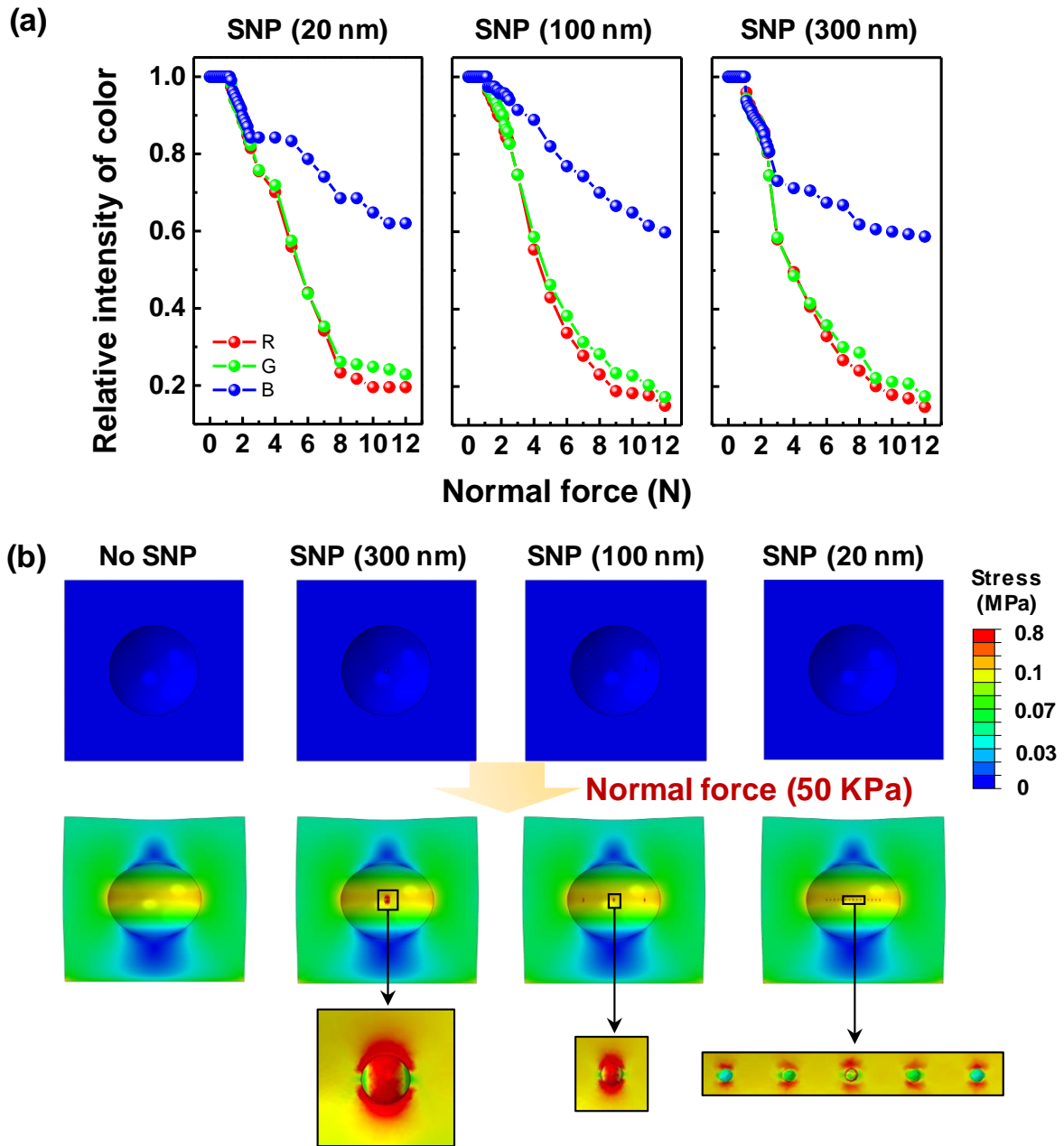


Figure 5.23 (a) Relative colour intensities of porous PDMS/SP composites (pore size = 5 μm) decorated with SNPs of different sizes (20, 100, 300 nm) as functions of pressure. (b) Finite-element analysis-determined stress distributions at the surfaces of pores in porous PDMS/SP composites with SNPs under applied pressure.

As a proof of concept, we have demonstrated the application of porous mechanochromic composites with hierarchical NP-MP architecture in mechanochromic e-skins. Figure 5.24a shows the colour changes of the mechanochromic e-skins attached to human fingers undergoing different hand motions, including folding/unfolding, rock, scissors and grasping objects. The colour changes enable the real-time detection of the spatial distribution of forces without any complicated monitoring instrument. Thus, the e-skins provide an intuitive perception of local forces according to various hand gestures. While the colour transition of the mechanochromic e-skin is typically limited to static force sensing applications,⁹² the present mechanochromic e-skins can be combined with flexible and transparent silver nanowire electrodes for use as triboelectric force sensors. These sensors can be applied in the spatiotemporal detection of both static and high-frequency dynamic forces (Figure 5.24b, left). In this triboelectric force sensor, triboelectrification and electrostatic induction between the porous PDMS (negatively charged) and plastic pen (positively charged) results in spontaneously generated triboelectric current in response to high-frequency dynamic forces (Figure 5.25, Section 5.2).^{26,257-258} This generated current can be utilised in self-powered dynamic force sensors. In particular, porous structures with large surface areas and high compressibility provide enhanced triboelectric force sensitivity.²⁸ Figure 5.24b (right) shows a dual-mode mechanochromic e-skin that can simultaneously detect the location and intensity of the writing force based on the mechanochromic colour and the writing speed based on the triboelectric output signals in real time. The triboelectric current and voltage of the mechanochromic e-skin depends on the intensity of the applied normal pressure (Figure 5.26a–b) and the power density also increased up to a maximum of $4.2 \mu\text{W}/\text{cm}^2$ (Figure 5.26c). Furthermore, the triboelectric output current of the mechanochromic e-skin gradually increases as the frequency of the dynamic impact force increases (Figure 5.26d). This phenomenon can be attributed to the increase in dynamic modulus resulting from the elasticity of the porous mechanochromic composites.^{22,28} To evaluate the ability of our mechanochromic e-skins to detect sound, we monitored the output voltage induced by the acoustic pressure of a speaker (Figure 5.27). When the e-skin is exposed to the sound waves of the words ‘electronic’ and ‘skin’, the generated triboelectric output voltage closely matches the waveform of the sound source (Figure 5.24c, left). The time-dependent frequency obtained by short-time Fourier transformation corresponds to the location and intensity of the recorded frequency, in accordance with the spectrogram of the sound source (Figure 5.24c, right).

This study demonstrates that a hierarchical NP-MP architecture in porous mechanochromic composites can enhance both mechanochromic strain/stress sensitivity and stretchability. The experimentally determined structure–activity relationships and computational modelling results suggest the following general design principle: reducing pore size while increasing SNP size should enhance the mechanochromic sensitivity. Most material modifications that enhance the onset of mechanochromism also reduce extensibility, because mechanochromism is triggered by polymer chains

approaching their maximum extension. In contrast, the hierarchical NP-MP architecture of the porous composite structure in this study simultaneously reduces the onset of mechanochromism and enhances the extensibility. This advance will allow us to introduce mechanochromism to devices which operate under a range of strain conditions, from very small to large amounts of deformation. As a proof of concept, we fabricated an e-skin based on the composite material and used it as a wearable motion sensor and dual-mode touch audio sensor. The e-skin enabled the detection of static/dynamic force without any external power source.

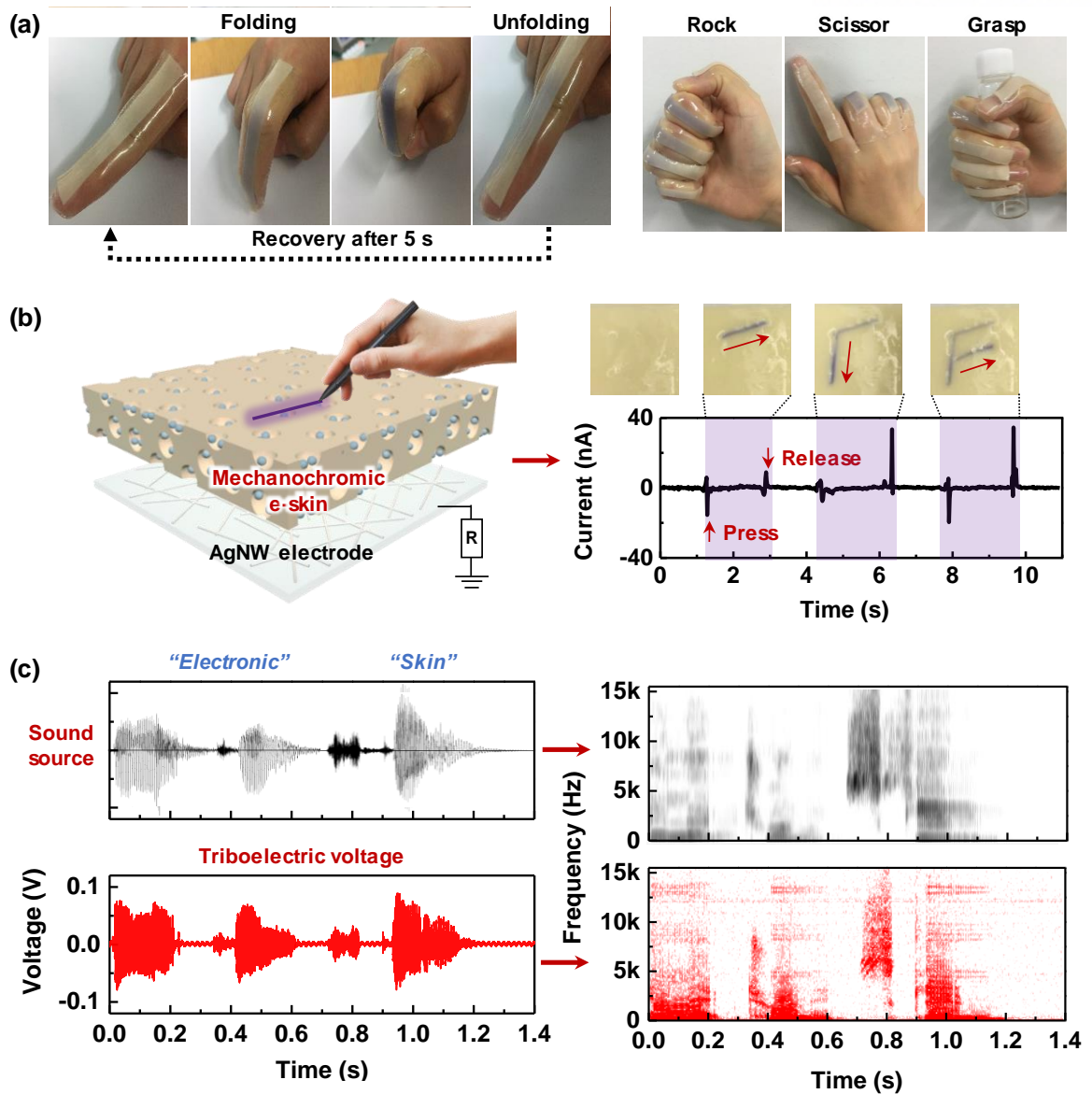


Figure 5.24. Applications of porous mechanochromic composites in wearable e-skins and dual-mode static/dynamic touch and audio sensors. **a**, Images of wearable mechanochromic e-skins for the detection of various hand gestures (folding/unfolding, rock, scissor and grasp). **b**, Schematic of a dual-mode mechanochromic and triboelectric force sensor that enables the spatiotemporal detection of both writing force and speed. **c**, Waveforms of the sound sources of the words ‘electronic’ and ‘skin’: waveforms of the detected read-out signals (left) and short-time Fourier transform of the sound source along with the read-out signals from the dynamic force sensor (right). These applications are based on the pore-5/SNP-300 porous mechanochromic composite.

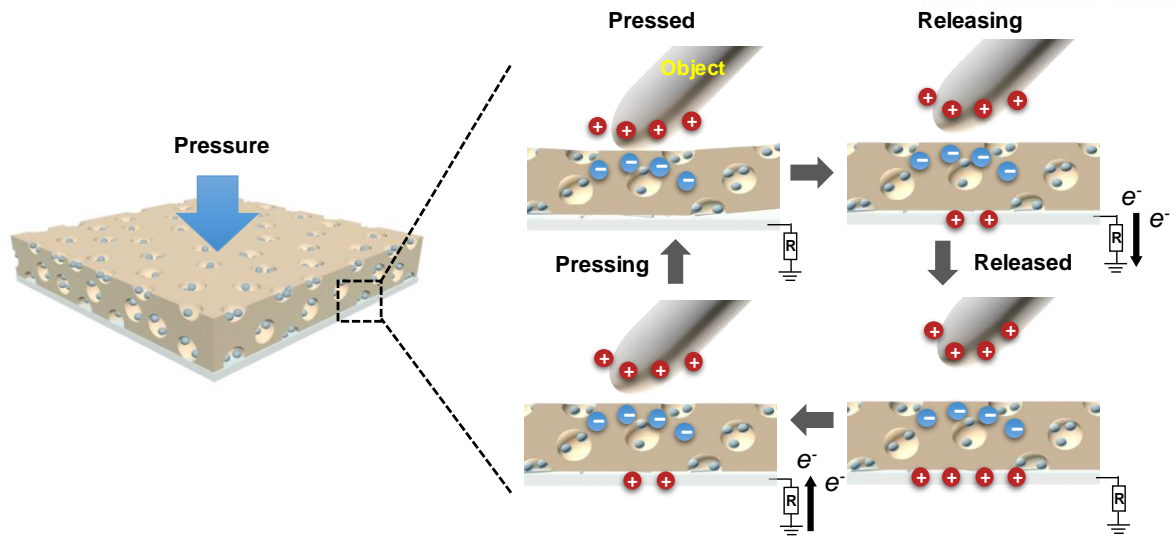


Figure 5.25. Schematic of the working mechanism of the single-electrode triboelectric sensor, which comprises a porous mechanochromic composite and silver nanowire-based electrode. Object is the plastic pen in this work.

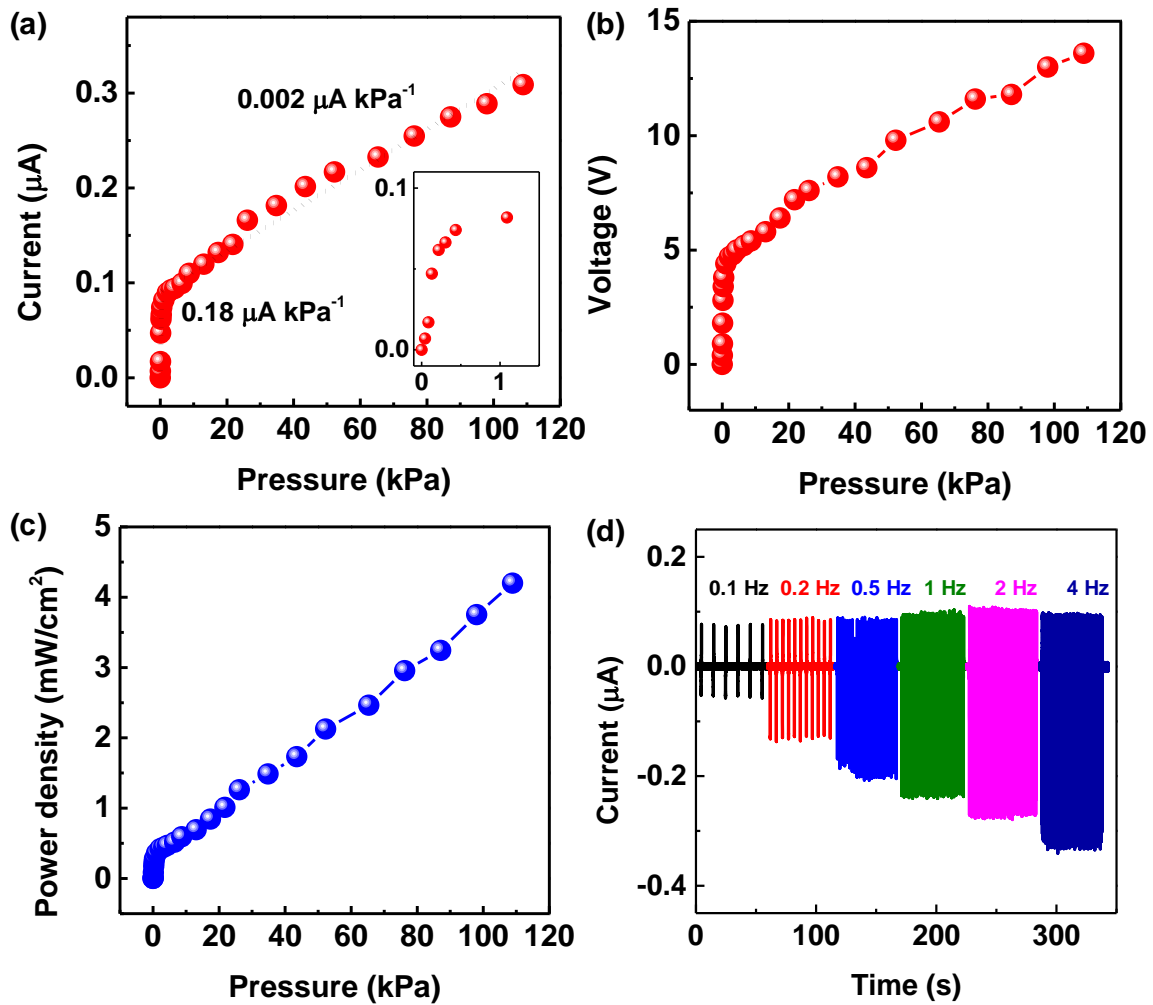


Figure 5.26. (a) Output triboelectric current of a mechano-chromic composite in response to normal pressure. The sensitivity is $0.18 \mu\text{A kPa}^{-1}$ below 0.4 kPa and $0.002 \mu\text{A kPa}^{-1}$ in the range 1–108 kPa. (b) Triboelectric output voltage and (c) power density of porous PDMS/SP composites with 5- μm pores and 300-nm SNPs as functions of applied pressure. (d) Output current of the porous mechano-chromic composite in response to dynamic normal pressure with different loading frequencies (0.1–4 Hz).

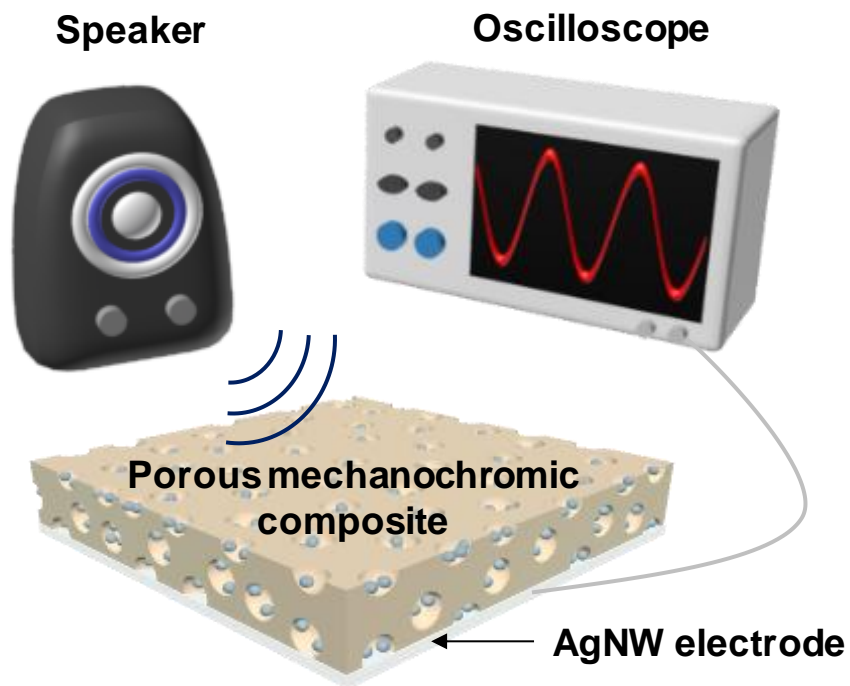


Figure 5.27. Schematic showing the setup used to detect dynamic acoustic waves.

5.4 Conclusion

In the future, this strategy could be extended to improve the stress-reporting capabilities of other mechanophores.^{225,242,259-262} Previous work has indicated that (a) the extent of mechanophore activation can be directly related to the first invariant of the local strain,⁸⁷ independently of whether the strain is applied in a uniaxial or biaxial manner, and (b) while the absolute magnitude of mechanophore activation depends on the mechanophore, the relative amount of mechanophore activation as a function of strain is constant across a range of strains in filled PDMS elastomers.²⁴⁶ The strain-focusing approach described here should therefore carry over to other mechanophores, and we anticipate that further work in this and similar composite materials will provide additional insight into the design of more active mechanochromic materials. Our hierarchical NP-MP framework is expected to allow the development of multifunctional and multiresponsive mechanochemical materials for user-interactive devices, smart robotics and wearable healthcare/diagnosis applications in future.

Chapter 6. Human and biological skin-inspired electronic skin for deformation-insensitive flexible and highly sensitive dual-mode temperature sensor

6.1 Introduction

With increasing attention paid to healthcare and growing demand to improving the quality and longevity of human lives, there has been much interest in the development of wearable devices that can sense the users' motions and biosignals, thus allowing fitness tracking, as well as remote and real-time healthcare monitoring.¹ To accurately detect and analyze the physical signals generated by the human body, flexible physical sensors are required to measure parameters such as temperature, pressure, and strain.^{22,122,135,195} In particular, body temperature, one of the main vital signs, is a critical indicator of human health conditions.²⁶³ Real-time monitoring of deviations from normal body temperature indicates abnormal states of health resulting from fever, insomnia, fatigue, infection, or organ dysfunction.¹¹¹⁻¹¹² For accurate diagnosis of health conditions, temperature sensors must be able to detect minute changes that may be as small as 0.1 °C.¹¹¹ In addition, the temperature sensors should be flexible and remain conformably attached on curved skin surfaces, and they must stably operate under bending or applied pressure, and rapidly respond to temperature variations.¹¹⁵

Various types of flexible temperature sensors with high sensitivity have been reported, including thermocouples, resistive temperature sensors, pyroelectric sensors, thermoelectric sensors, organic transistors, and thermochromic sensors.^{10,146,264-267} Among them, resistive temperature sensors have attracted intense research interest because of their high sensitivity, flexibility, and simple fabrication process.²⁶⁸ In particular, most studies focused on metal-based resistive temperature sensors because of their advantages of high conductivity, linear temperature sensing in a wide temperature range, and flexibility with thin or narrow serpentine geometry.²⁶⁹⁻²⁷⁰ Owing to the low temperature sensitivity of commercial metal-based sensors (0.4 Ω °C⁻¹), however, additional equipment, such as high-gain amplifiers and high-precision analog-to-digital converters, is required for precise temperature measurement.¹¹³ On the other hand, resistive temperature sensors based on conductive polymer composites are attractive because of their high sensitivity when compared to that of metal-based sensors, mechanical stability, and flexibility.²⁶⁸ Because their temperature-sensing performances are mainly affected by the temperature coefficients of resistance (TCR) of conductive fillers such as nanocarbon materials, metallic nanostructures, or conductive polymers, the sensitivity of most previously studied resistive temperature sensors was not high enough to monitor small temperature variations of the order of 0.1 °C.^{144,195,271} Jeon et al. demonstrated resistive temperature sensors based on conductive polymer

composites composed of Ni microparticles, poly(ethylene oxide) (PEO), and polyethylene (PE).¹¹³ Although the volume expansion of semi-crystalline PEO induces large changes (several orders of magnitude) in resistance near the melting temperature of PEO, its accuracy in temperature sensing is only ~ 2.7 °C and the sensing range is narrow (35–42 °C).²⁶⁸ Therefore, for accurate and real-time monitoring of health conditions, new materials that meet all of the aforementioned requirements must be developed for resistive temperature sensors.

In the study reported here, we developed a flexible and highly-sensitive temperature sensor based on a thermoresponsive polymer nanocomposite consisting of reduced graphene oxide (rGO), PEO microdomains, and a polyvinylidene fluoride (PVDF) matrix. The resistance of the sensor was designed to decrease with increasing temperature owing to the negative temperature coefficient (NTC) of rGO. In addition, melt-induced volume expansion of PEO microdomains induced compressive stress in the neighboring polymer matrix, resulting in further decreases in resistance with increasing temperature. Our flexible resistive temperature sensor showed an ultrahigh TCR value of $-6.94\% \text{ } ^\circ\text{C}^{-1}$ and high temperature-sensing accuracy of 0.1 °C. The ultralow thickness (~ 30 μm) of our sensor also enabled highly stable deformation-insensitive operation under external mechanical stimuli such as bending and applied pressure, facilitating wearable application for skin temperature monitoring with high accuracy (< 0.1 °C). Finally, we encapsulated the temperature sensor with a thin thermochromic composite to form a dual-mode temperature sensor with simultaneous electrical and colorimetric sensing capabilities. The 8×8 dual-mode sensor arrays enabled exact monitoring of temperature and the location of applied temperature.

6.2 Experimental Details

Fabrication of rGO–PEO–PVDF composite film and dual-mode temperature sensors: First, PVDF (molecular weight: ~534,000, Sigma-Aldrich, USA) was dispersed in DMF (20 wt%), which served as the solvent, and mixed with a certain amount of melted PEO at 70 °C. Next, a GO–DMF solution, synthesized by Hummers method,^{174,272} was added to the PEO–PVDF–DMF solution in the desired mixing ratio. For the fabrication of the conductive and thermoresponsive rGO–PEO–PVDF composite film, the prepared GO–PEO–PVDF–DMF solution was poured onto a glass substrate and annealed at 160 °C for 1 h in a vacuum oven; GO was reduced to rGO and the residual DMF was completely removed. Using a sputter-coating system (E-1045, Hitachi, Japan) and a mask, a interdigitated Pt electrode was sputtered onto the fabricated rGO–PEO–PVDF composite film. To form the dual-mode temperature sensors, three thermochromic dyes of different colors (Nano I&C, Korea) and different response temperatures were mixed with the PDMS prepolymer and curing agent. The rGO–PEO–PVDF composite film with the electrode on the PDMS substrate was encapsulated by the thermochromic-dye–PDMS composite and annealed at 80 °C to cure the thermochromic composite film.

Fabrication of 8 × 8 temperature-sensor arrays: A PEN or PDMS supporting layer was first coated with a Cr/Au electrode by using a horizontal electrode mask and spray coated with Ag nanowire for further conductive and stable electrode using Ag nanowire solution in ethanol (Nanopysis Corp., Korea). To avoid direct contact between the horizontal and vertical electrode lines, we used a parylene coater (Alpha Plus Corp., Korea) to cover the overlapping area between two electrodes with parylene. The vertical electrode was coated using the same method as that for the horizontal electrode. To form a patterned rGO–PEO–PVDF composite film, the GO–PEO–PVDF–DMS solution was poured on the substrate with an electrode using the mask; the composite-covered substrate was annealed at 160 °C for 1 h in the vacuum oven. Finally, it was encapsulated by the parylene layer or thermochromic composite film.

Characterization: The surface morphology of rGO–PEO–PVDF composite films was analyzed by field-emission SEM (S-4800, Hitachi, Japan). To investigate the temperature-dependent changes in the morphology or phase, the rGO–PEO–PVDF composite films were measured by AFM (DI-3100, Veeco, Japan) and Raman spectroscopy (alpha300R, WITec, Germany) with a 532 nm excitation laser (laser power: 1.5 mW; integration time: 1 s; accumulations: 10). The thermal characteristics of the composite films were analyzed by DSC (Q200, TA Instruments, USA). The temperature measurements of the temperature sensors were carried out on a heating–cooling thermal plate (PT-CHS-C, Tokai Hit, Japan). The temperature-responsive electrical properties of the temperature sensors were measured by using a semiconductor parameter analyzer (4200-SCS, Keithley, USA) to obtain the pyroresistive signals. The color shift of the thermochromic composite films was measured with a spectroradiometer

(PR-655, Photo Research, USA). The 8×8 temperature-sensor arrays were measured using a multichannel biosensor test system (OT15-3010D, ONTEST, Korea).

6.3 Results and Discussion

The thermoresponsive polymer composite films were fabricated by rod-casting of a mixture of graphene oxide (GO), PEO, and PVDF dissolved in dimethylformamide (DMF); the GO–PEO–PVDF–DMF mixture was dried at 160 °C for 1 h in a vacuum oven. The high-temperature annealing process completely removed the residual DMF and yielded pyroresistive composite films by reducing GO to rGO. The simple and scalable fabrication process allowed large-area ($15 \times 15 \text{ cm}^2$) composite films to be easily fabricated (Figure 6.1a). Cross-sectional scanning electron microscope (SEM) images of the thermoresponsive rGO–PEO–PVDF composite films indicate the formation of PEO microdomains in the polymer matrix, which resulted from phase separation between PEO and the PVDF domains (Figure 6.1b,c). In addition, spherical micropores were formed inside the composite films during film formation, followed by evaporation of DMF after the composite film was formed. The PEO microdomains were mainly located near the micropores, which can be attributed to the higher solubility of PEO in DMF solvent compared to that of PVDF in DMF solvent, as estimated by the Hansen solubility parameter.²⁷³⁻

274

Similar to conventional temperature sensors based on conductive-polymer composites that detect temperature changes through the TCR effect of conductive fillers, the resistance of our thermoresponsive composites with rGO sheets decreased with increasing temperature owing to the NTC effect of the rGO sheets.²² To further enhance the temperature-sensing performance of the composites, we introduced semi-crystalline PEO microdomains in the composite films. Semi-crystalline polymers such as PEO, polyethylene, and polyethylene adipate show a large volume expansion near their respective melting points, caused by the phase transition from the crystalline phase to the amorphous phase.²⁷⁵ Previously, these semi-crystalline polymers were introduced for the fabrication of ultrasensitive temperature sensors because of their tendencies for large thermal expansion.^{113,265} Owing to the high thermal expansion properties of semi-crystalline polymers, the conductive networks between conductive fillers in the resulting sensors can be easily broken near the melting temperatures of semi-crystalline polymers. Although the temperature sensitivity of this type of sensor is significantly higher than that of conventional temperature sensors, the temperature sensing accuracy is too low ($\sim 2.7 \text{ }^\circ\text{C}$) and the sensing range is very narrow ($35\text{--}42 \text{ }^\circ\text{C}$), limiting their use to other areas of switching devices for preventing overheating and short-circuiting of electronic devices.^{268,276} The temperature-sensing mechanism of a rGO–PEO–PVDF composite is illustrated in Figure 6.1d. Among various semi-crystalline polymers, we chose PEO for the study because its melting point can be easily tuned from -45 to $65 \text{ }^\circ\text{C}$ by adjusting its molecular weight. We utilized PEO with a molecular weight of 1000, which has a melting point near the human body temperature ($\sim 35 \text{ }^\circ\text{C}$). In addition to the NTC effect of rGO, the volume of semi-crystalline PEO microdomains increased as a result of the phase transition when the temperature increased toward the melting temperature of PEO. Because the PVDF matrix

prevented the movement of the PEO microdomains, the volume expansion of PEO induced compressive stress in the neighboring polymer matrix, resulting in further decreases in the sensor resistance with increasing temperature.

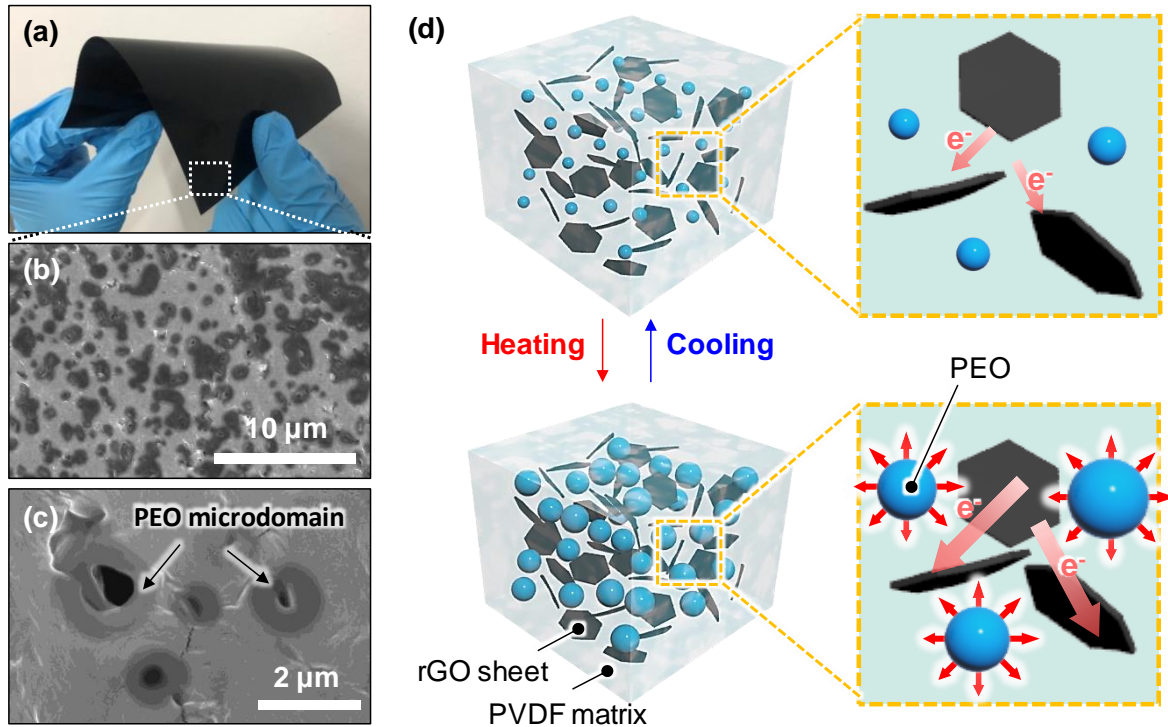


Figure 6.1. Thermoresponsive composite film based on a semi-crystalline polymer. (a) Photograph of a flexible rGO-PEO-PVDF composite film with large area ($15 \times 15 \text{ cm}^2$). (b) SEM image of rGO-PEO-PVDF composite film. (c) High-magnification SEM image of rGO-PEO-PVDF composite film with PEO microdomains. (d) Schematic showing the temperature-sensing mechanism of rGO-PEO-PVDF composite film based on the melt-induced volume expansion of PEO microdomains. The hexagons represent rGO sheets; the blue spheres represent PEO microdomains.

The device structure of flexible temperature sensors based on a thermoresponsive composite film is schematically shown in Figure 6.2a. The thin rGO–PEO–PVDF composite film (~20 μm) with an interdigitated electrode was encapsulated by bottom polydimethylsiloxane (PDMS) layer and top parylene layer, enabling conformal contact between the sensors and curved objects. The temperature-sensing performances of the sensors based on thermoresponsive rGO–PEO–PVDF composite films with different PEO concentrations were evaluated by varying the temperature of the heating–cooling plate from 20 to 60 °C (Figure 6.2b). The temperature sensitivity continuously increased as the PEO concentration in the rGO–PEO–PVDF composite film increased, which can be explained by the effect of enhanced volume expansion of the PEO microdomains. The temperature sensitivity reached a saturated value when the PEO concentration of the composite film was 15 wt%. Sensors with PEO concentrations below 15 wt% showed no noticeable hysteresis, whereas sensors with PEO concentrations above 15 wt% showed a small hysteresis loop (Figure 6.3). Therefore, we chose a PEO concentration of 15 wt% as the optimal value. When the temperature was varied from 20 to 60 °C, the temperature sensor with 15 wt% PEO showed a relative resistance (R/R_0) of 0.04, which is 1/14th of that ($R/R_0 = 0.56$) of the temperature sensor without PEO. The temperature sensitivity can be quantified by the TCR value, which is defined as $TCR = (\Delta R/R)/\Delta T$, where R is the resistance of the temperature sensor and T is the applied temperature. The TCR of the temperature sensor with PEO microdomains was 6.94% °C⁻¹ at room temperature, which is 6.5 times higher than that of the sensor without PEO (Figure 6.4), indicating the critical role of semi-crystalline PEO microdomains in enhancing the sensitivity of our temperature sensors. We further optimized the temperature sensors by controlling the rGO concentration (Figure 6.5a). As the rGO concentration of the composite film increased, the temperature sensitivity increased owing to the enhanced NTC effect of rGO. However, when the rGO concentration of the composite film exceeded 2 wt%, the temperature sensitivity decreased again because the high rGO content resulted in a well mixed polymer blend between PEO and PVDF, without forming PEO microdomains (Figure 6.5b,c). When the temperature of the heating–cooling plate was increased from 32 °C in steps of 0.1 and 0.2 °C, the optimized temperature sensors precisely exhibited stepwise decreases in resistance and returned to the original resistance value (Figure 6.2c and 6.6). The high TCR of 6.94% °C⁻¹ and the high temperature-sensing accuracy of 0.1 °C for our flexible temperature sensors can be favorably compared with previously reported flexible temperature sensors (Table 6.1), which exhibited much lower TCR values and sensing accuracy.^{22,115,195,271,277-282} One study demonstrated organic transistor-based temperature sensors with high TCR values, which are still lower than 6.94% °C⁻¹; moreover, the fabrication process was complex.²⁸⁰ Although several papers cited temperature accuracies of 0.1 or 0.2 °C, the TCR values of the reported sensors were still low (<1.5% °C⁻¹).^{195,282}

To verify the effect of PEO microdomains on the ultrahigh sensitivity of our temperature sensors, we used atomic force microscopy (AFM) to investigate the phase changes of rGO–PEO–PVDF composite films at different temperatures. The phase mode of an AFM is a useful tool to visualize the crystallization and melting process of semi-crystalline polymers.²⁸³ Figure 6.2d and 6.2e show the AFM phase images of rGO–PEO–PVDF composite films at 25 and 40 °C, respectively. At the low temperature of 25 °C, the differences between the two phases, crystalline PEO microdomains and crystalline PVDF matrix, were very small. When the temperature was increased to 45 °C, the PEO microdomains transitioned from the crystalline to amorphous phase. As a result, mixed phases between amorphous PEO microdomains and the crystalline PVDF matrix could be clearly observed, confirming that melt-induced volume expansion of the PEO microdomains induced compressive stress in the neighboring polymer matrix, thereby resulting in further decreases in resistance with increasing temperature. The topographic images of rGO–PEO–PVDF composites at different temperatures were analyzed by the confocal laser scanning microscopy (Figure 6.7). At the low temperature of 20 °C, the surface image and 3D profile show the roughness of the thermoresponsive composite, caused by well-dispersed PEO microdomains near the micropores (Figure 6.7a,b). When the temperature was increased to 40 °C, the depth of the depressions decreased owing to the phase transition-induced volume expansion of PEO (Figure 6.7c,d). These results indicate that the volume expansion of PEO microdomains on the film surface with increasing temperature.

We also used Raman spectroscopy to check the temperature-induced phase transition of PEO microdomains in the composite film. We began by analyzing the temperature-dependent Raman spectra of pure PEO (Figure 6.8). At Raman spectra obtained at low temperature clearly show characteristic Raman peaks of PEO at 840, 1085, 1239, and 1484 cm^{-1} , as well as a broad band between 2800 and 3000 cm^{-1} , which correspond to the C–O stretching mode, CH_2 rocking mode, out-of-phase C–H twisting mode, in-phase CH_2 bending mode, and C–H stretching mode, respectively (Figure 6.8a).²⁸⁴⁻²⁸⁵ The intensity of the characteristic peaks decreased with increasing temperature (Figure 6.8b). When the temperature was over 35 °C, the characteristic peaks significantly decreased and broadened with increasing temperature, indicating the formation of an amorphous phase (Figure 6.8c).²⁸⁶ In the spectra of the rGO–PEO–PVDF composite films, most of the characteristic peaks of PEO overlap the characteristic peaks of rGO and PVDF (Figure 6.9).²⁸⁷⁻²⁸⁸ Thus, we investigated the phase transition of PEO in the composite films using the Raman peak at 2871 cm^{-1} instead, and this peak corresponds to the C–H stretching mode of PEO (Figure 6.2f). The intensity of the Raman peak at 2871 cm^{-1} decreased with increasing temperature, confirming the phase-transition-induced volume expansion of PEO in the rGO–PEO–PVDF composite.

Because the melt-induced volume expansion of PEO microdomains and the NTC effect of rGO fillers were the two main factors of the ultrahigh sensitivity of our temperature sensors, we could tune

the critical temperature range of high sensitivity by adjusting the molecular weight of PEO. According to our analysis of the endothermic peaks in differential scanning calorimetry (DSC) thermo-diagrams (Figure 6.10a), the melting points of PEO with molecular weights of 1000, 1500, and 4000 were 35, 45, and 57 °C. The DSC thermo-diagrams of the corresponding rGO–PEO–PVDF composites show two distinct peaks for the melting points of PEO and PVDF (Figure 6.10b). Depending on the molecular weight of PEO, a different critical temperature range was obtained for the composite (Figure 6.11a), and the temperature sensors showed different critical temperature ranges of 20–40 °C, 30–50 °C, and 40–60 °C, which correspond to the melting point of each PEO (Figure 6.11b–d).

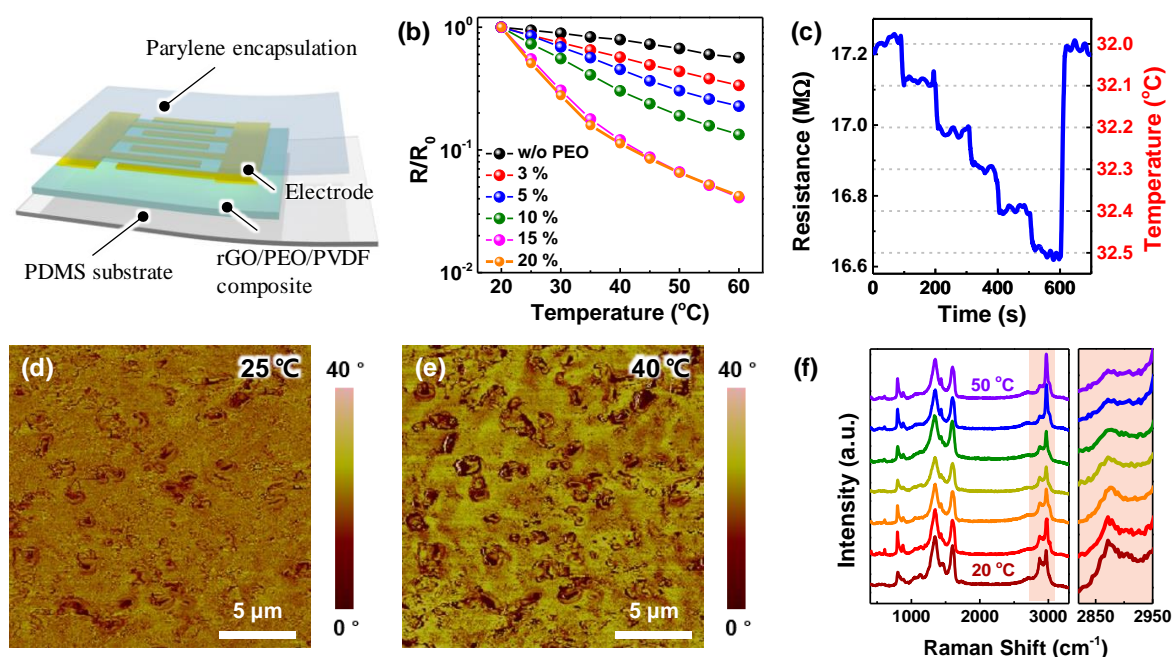


Figure 6.2. Temperature-sensing properties of flexible and highly sensitive temperature sensors based on a rGO/–PEO–PVDF composite film. (a) Schematic illustration of flexible temperature sensor. (b) Relative resistance as a function of temperature (20–60 °C) of temperature sensors with different loadings of PEO (0 to 20 wt%). (c) Real-time temperature monitoring of temperature sensors as the temperature was increased from 32 °C in steps of 0.1 °C. (d) AFM phase image of a rGO–PEO–PVDF composite film at a temperature of 25 °C. (e) AFM phase image of a rGO–PEO–PVDF composite film at a temperature of 40 °C. (f) Temperature-dependent Raman spectra of rGO–PEO–PVDF composite films; a magnified view of the Raman spectra is shown on the right.

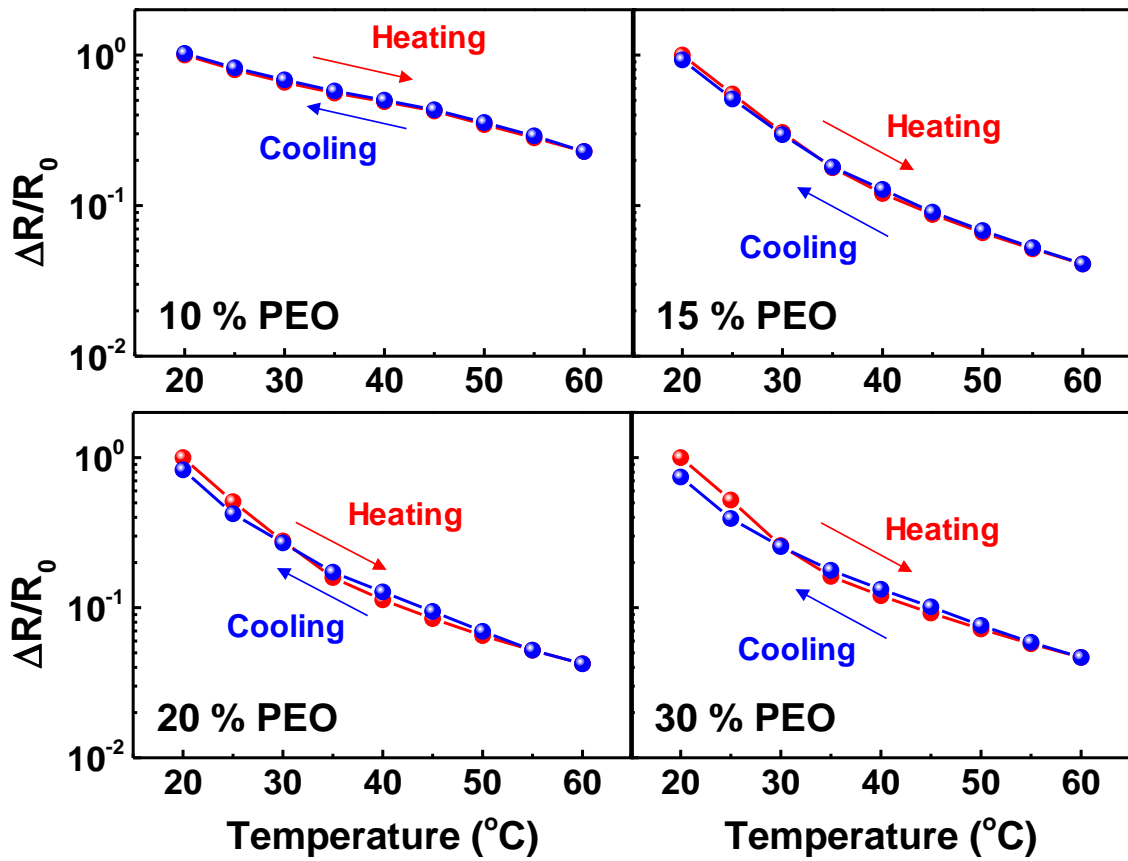


Figure 6.3. Hysteresis curve of temperature sensors with different PEO concentration.

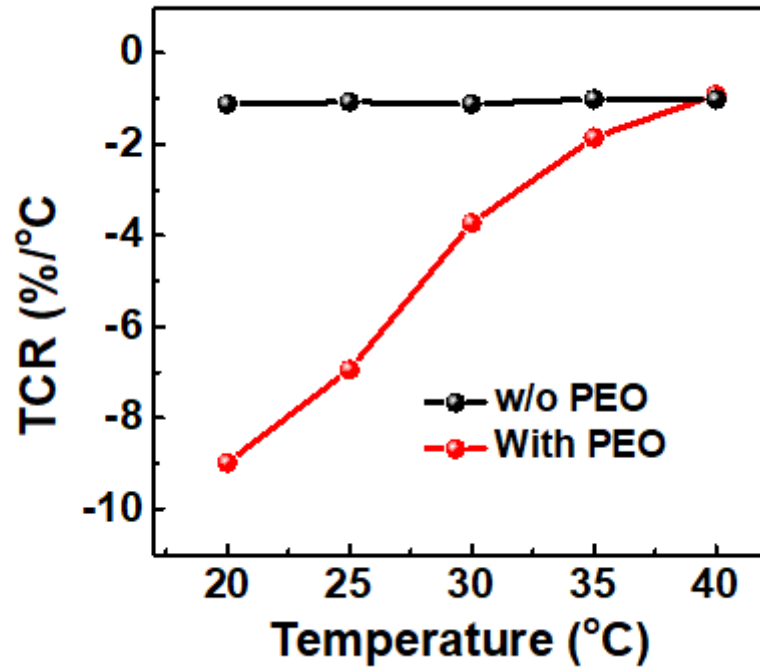


Figure 6.4. TCR values of temperature sensors with and without PEO microdomains

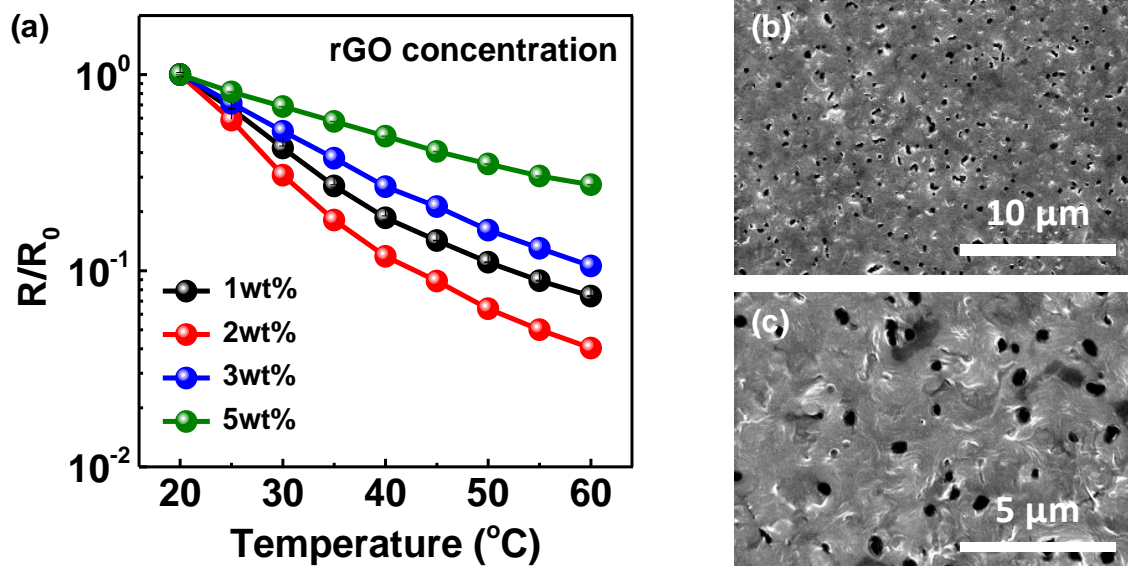


Figure 6.5. (a) Relative resistance of temperature sensors with different loadings of rGO as a function of temperature. (b,c) SEM images of rGO-PEO-PVDF composite films with 5 wt% rGO.

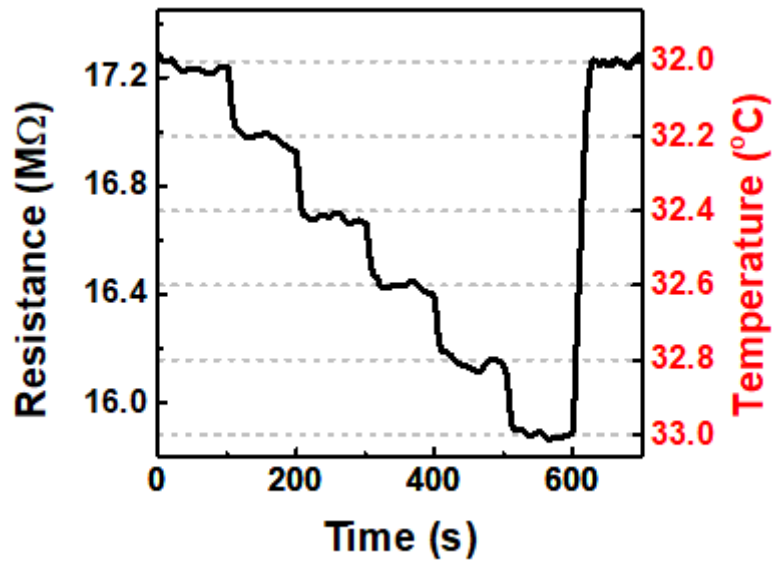


Figure 6.6. Decrease in resistance of temperature sensor as the applied temperature was increased in steps of 0.2 °C.

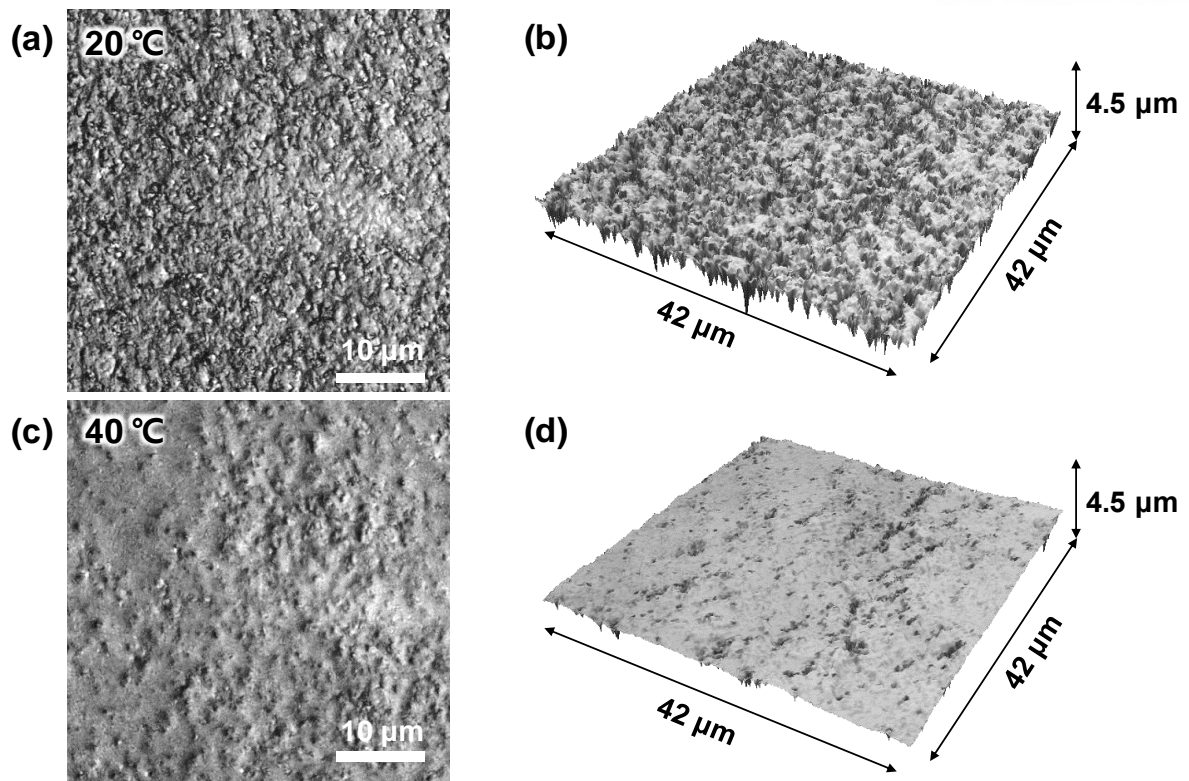


Figure 6.7. (a,b) Confocal laser microscopy image and 3D profile for surface morphology of rGO-PEO-PVDF composite at 20 °C. (c,d) Confocal laser microscopy image and 3D profile for surface morphology of rGO-PEO-PVDF composite at 40 °C.

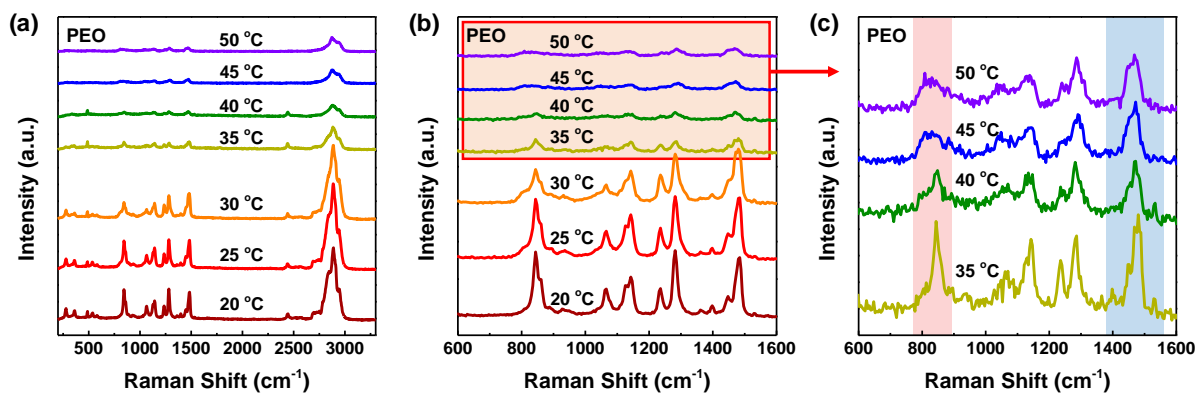


Figure 6.8. (a) Temperature-dependent Raman spectra of pure PEO. (b, c) Magnified view of the Raman spectra in (a).

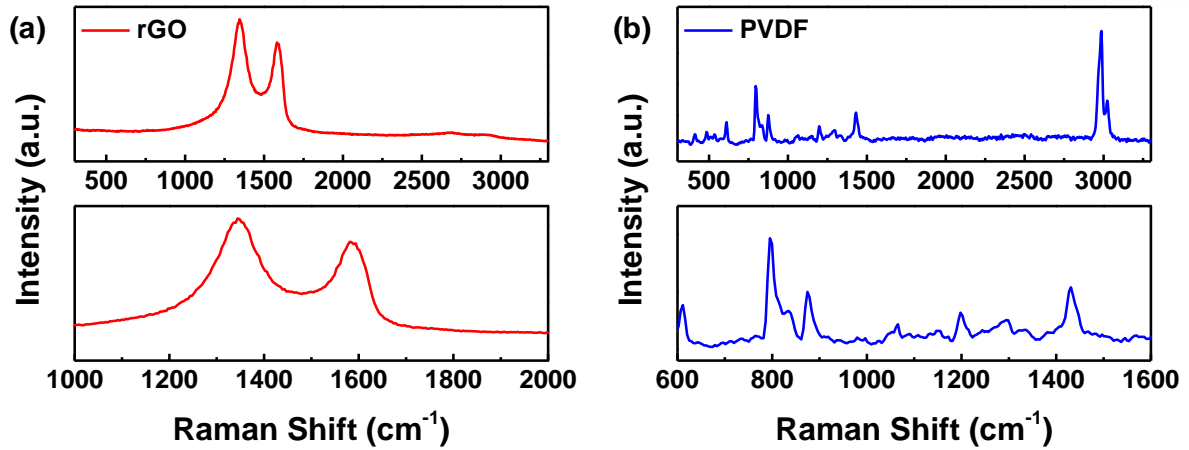


Figure 6.9. Raman spectra of (a) rGO and (b) PVDF.

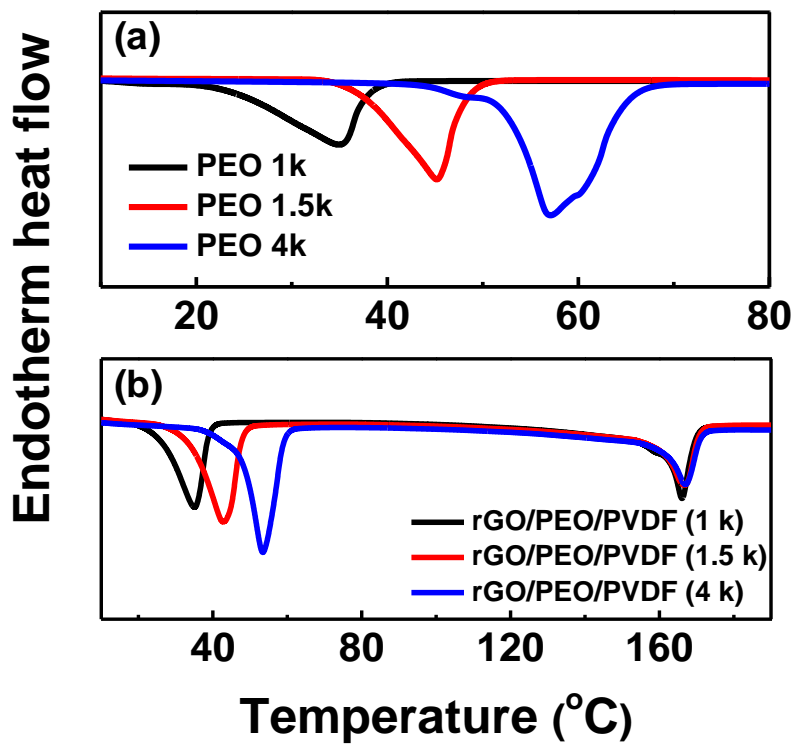


Figure 6.10. (a) DSC thermo-diagrams of PEO with molecular weight (M_w) of 1000, 1500, and 4000. (b) DSC thermo-diagrams of rGO-PEO-PVDF composites with PEO molecular weights of 1000, 1500, and 4000.

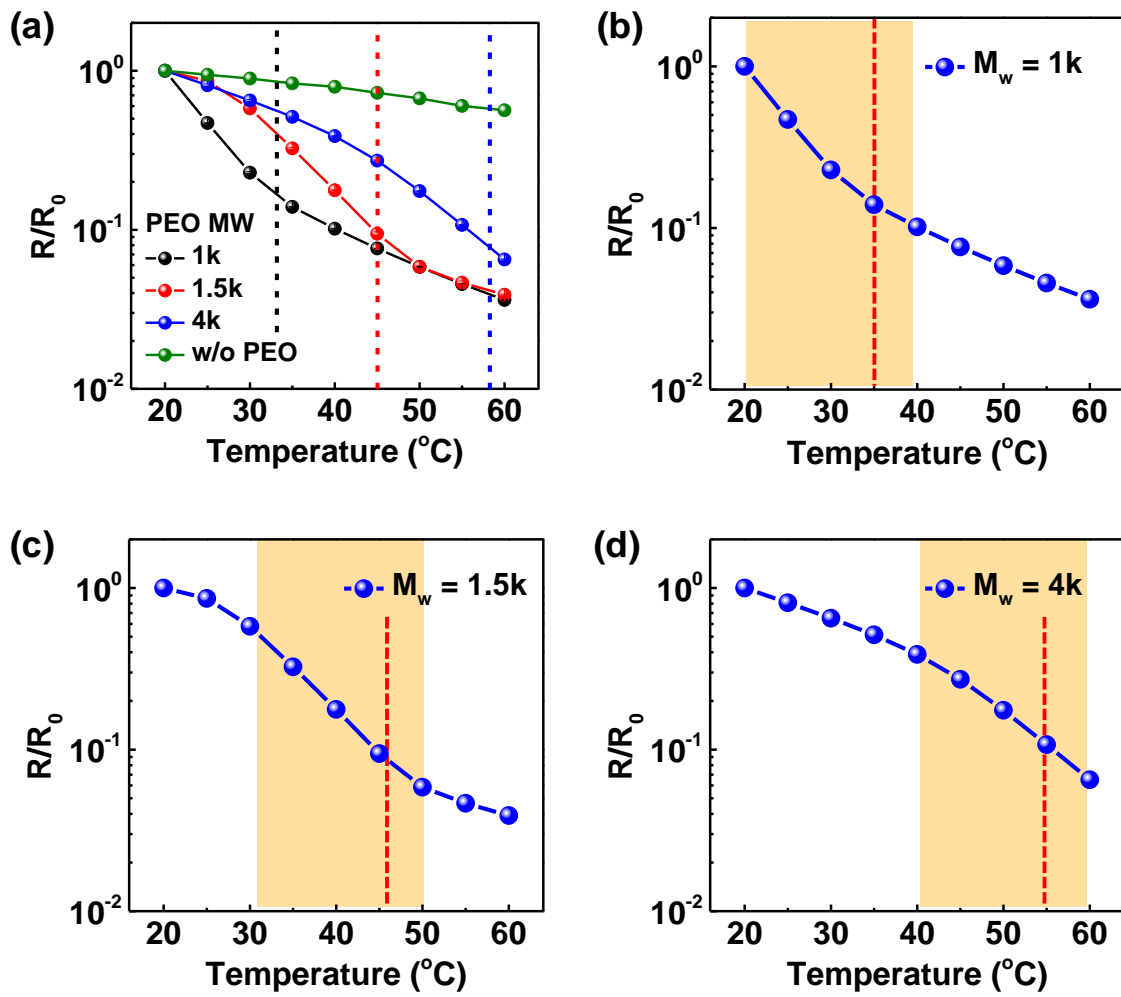


Figure 6.11. (a) Relative resistance as a function of temperature of temperature sensors with different PEO molecular weights (1000, 1500, or 4000). Relative resistance as a function of temperature of temperature sensors with PEO molecular weights of (b) 1000, (c) 1500, and (d) 4000.

Table 6.1. Summary of resistive temperature sensors and their performances.

Journal	Materials	Range (°C)	TCR (%/°C)	Accuracy (°C)	Reference
Sci. Adv. (2015)	rGO/PVDF	20 – 40	3.15	–	22
Adv. Mater (2015)	Polyaniline	15 – 45	1.0	–	271
Adv. Mater. (2015)	CNT/PEDOT:PSS	20 – 45	0.68	0.3	277
ACS Nano (2015)	Graphene/PDMS	30 – 100	1.05	–	278
RSC Adv. (2015)	MWCNT/parylene	24 – 40	2.0	–	279
Adv. Mater (2016)	rGO/PU	30 – 80	1.34	0.2	195
Adv. Mater. (2016)	Ag NPs/Pentacene	20 – 100	4.4	0.4	280
ACS Appl. Mater. Interfaces (2018)	pNiPAM/PEDOT:PSS/CNT	25 – 40	2.6	–	115
ACS Appl. Mater. Interfaces (2018)	Polyacrylamide/carrageenan hydrogel	25 – 70	1.99	0.77	281
Adv. Mater. (2018)	rGO/parylene	20 – 70	0.83	0.1	282
Our study	rGO/PEO/PVDF	20 – 60	6.46	0.1	–

Snakes, which have a unique temperature-sensing system of pit membranes, can perceive minute temperature variations from infrared (IR) radiation of a mammalian prey at a distance.²⁸⁹ Similarly, ultrasensitive temperature sensors could perceive tiny temperature changes of warm objects at a distance (Figure 6.12a). Figure 6.12b shows the changes in relative resistance of our temperature sensors when a warm object with temperature of 30 °C was located at a certain distance and then removed. The measurements were repeated for five cycles with the distance varying from 3 to 30 cm. The temperature sensors exactly detect the positioning of the warm object, demonstrating fast and highly sensitive temperature-sensing performances of the temperature sensors based on rGO–PEO–PVDF composites. We also tested these procedures with warm objects at 40 and 50 °C and obtained enhanced sensor signals (Figure 6.12c and 6.13).

For temperature sensors to be useable in wearable devices, mechanical flexibility and mechanical-deformation-independent perception of temperature variations are critical requirements for exact temperature sensing under conformal contact with curved objects. The pressure-independent sensitivity of our temperature sensor was evaluated under different values of normal pressure and at different temperatures (Figure 6.12d). The temperature sensor did not respond to the applied pressure, but they exhibited significant changes in resistance at different temperatures, which can be attributed to the coplanar electrode design. When the thermoresponsive composite film was vertically sandwiched between two electrodes, the sensor showed a noticeable change in resistance in response to normal pressure (Figure 6.14). On the other hand, the temperature sensor with a coplanar electrode structure did not respond to the applied pressure. In addition, our temperature sensor was insensitive to bending deformation with different bending radii (Figure 6.12e). Owing to the ultrathin design of our temperature sensor, the resistance variations induced by bending deformation were negligible compared to the resistance variations from temperature change. Under deformation at a bending radius of 3.2 to 13.3 mm, the temperature sensor could exactly perceive a temperature change (Figure 6.15a). The small variation at the increased temperature was caused by the rough contact between the bent temperature sensors and the flat heating plate. After 1000 cycles of the bending test, the temperature sensor still exhibited ultrahigh temperature sensitivity (Figure 6.15b). Furthermore, during repetitive cycles of heating from 20 to 60 °C, the temperature sensors showed reliable and uniform temperature-sensing performance for up to 10 cycles (Figure 6.12f).

The deformation-insensitive temperature sensor was successfully applied to wearable sensor for the monitoring of the skin temperature change. Benefitting from ultrathin thickness (~30 μm), the temperature sensor was conformally mounted on the back of hand (Figure 6.12g). Figure 3h shows the change in skin temperature detected by our temperature sensor and surface thermometer. In this time, skin temperature detected by temperature sensor was obtained from the non-linear power fitting of resistance change of temperature sensor (Figure 6.16). Because normal human always keep their the

skin temperature in certain boundaries through thermoregulation, we applied IR irradiation and cooling with fan to the skin for the dramatic shift in skin temperature during monitoring of skin temperature. The wearable temperature sensor exactly read the sharp increase and decrease of skin temperature by applied events and the skin temperature detected by our temperature sensor was well matched with that detected by surface thermometer. Moreover, enlarged plot in Figure 6.12h shows that the accuracy of temperature sensor was much higher than that of surface thermometer ($0.1\text{ }^{\circ}\text{C}$), indicating superior accuracy ($<0.1\text{ }^{\circ}\text{C}$) of our temperature sensor (Figure 6.12i).

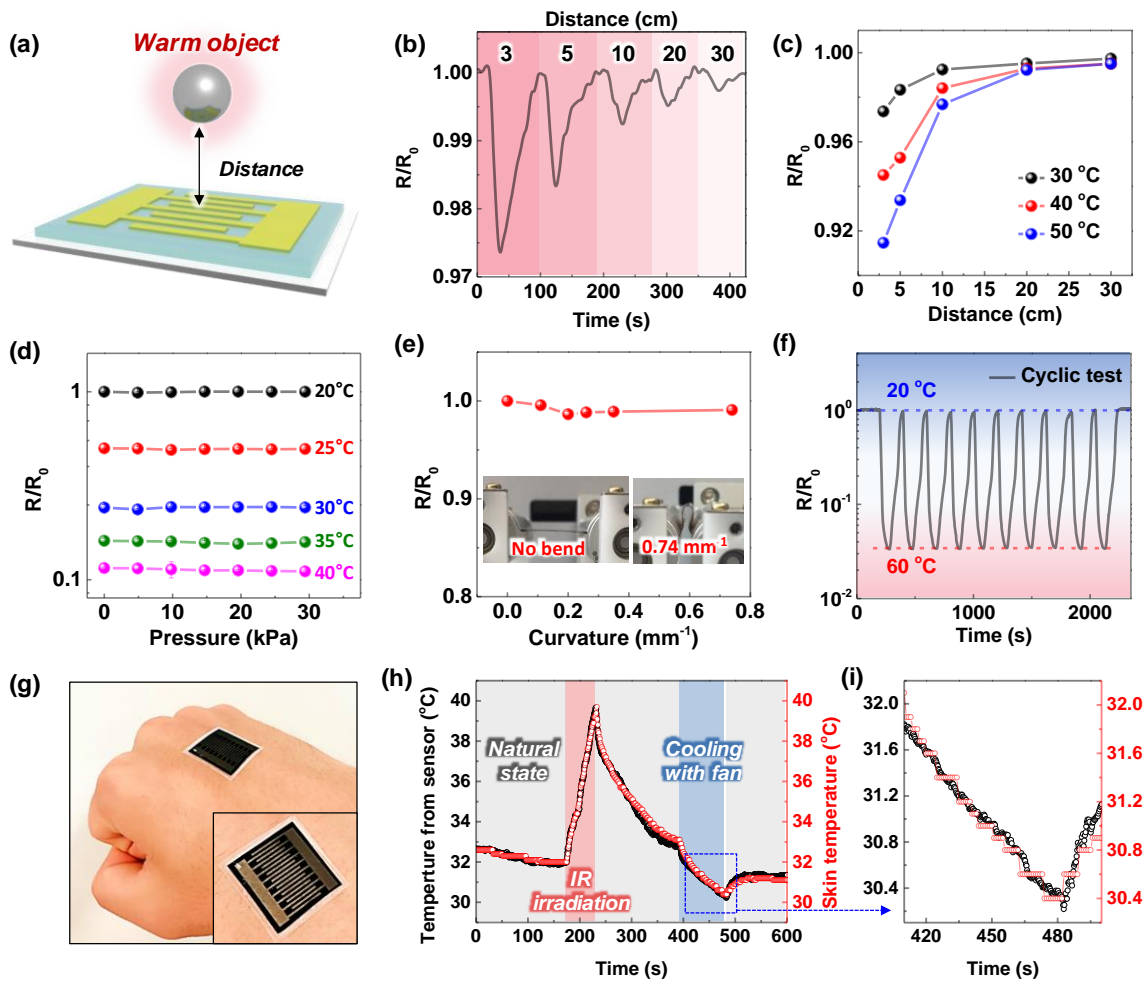


Figure 6.12. Temperature-sensing performances in the presence of a warm object at a distance and deformation-insensitive behavior of temperature sensors for wearable application. (a) Schematic illustration of temperature sensing in the presence of a warm object at a distance. (b) Changes in relative resistance of temperature sensors when a warm object at 30 °C was located at a varying distance from the temperature sensors. (c) Relative resistance of temperature sensors as a function of the distance from the warm object; the measurements were repeated when the temperature of the warm object was set to different values. (d) Relative resistance of temperature sensors with different temperature as a function of pressure. (e) Relative resistance of temperature sensors as a function of the bending curvature. (f) Cycling stability of temperature sensors under repetitive temperature change from 20 to 60 °C. (g) A photograph of deformation-insensitive flexible temperature sensor attached on the back of hand. The inset shows enlarged photograph of temperature sensor. (h) Body temperature change detected by the wearable temperature sensor (black) and surface thermometer (red). (i) Enlarged plot in Figure 4h showing temperature accuracy of our temperature sensor and surface thermometer.

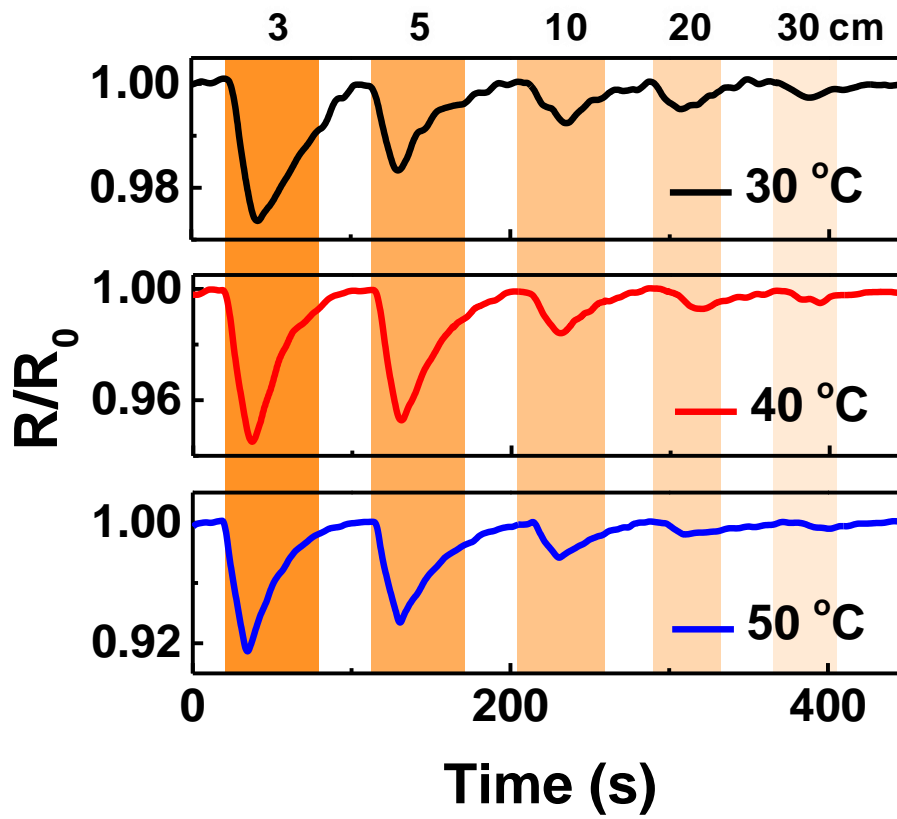


Figure 6.13. Real-time monitoring of relative resistance of temperature sensors when the warm objects with temperature of 30, 40, and 50 °C were located at a distance of 3 to 30 cm.

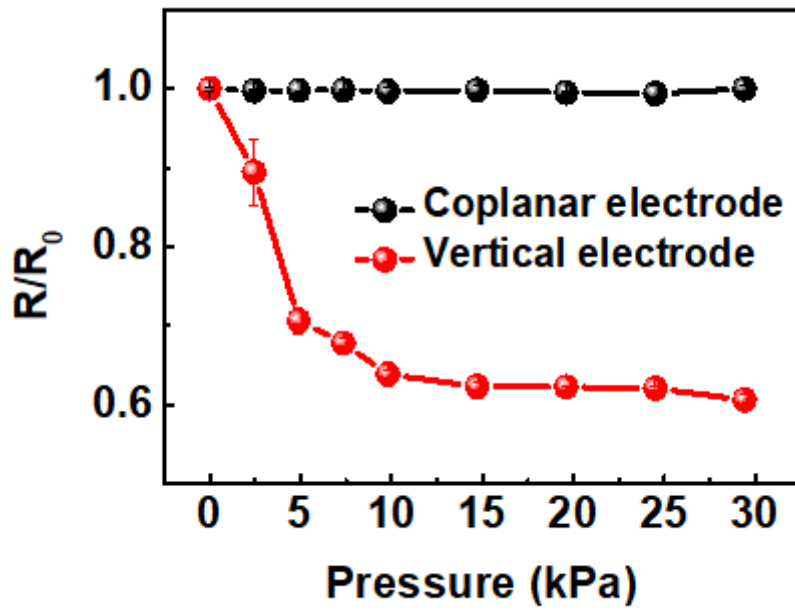


Figure 6.14. Pressure sensitivity of temperature sensors with different electrode designs.

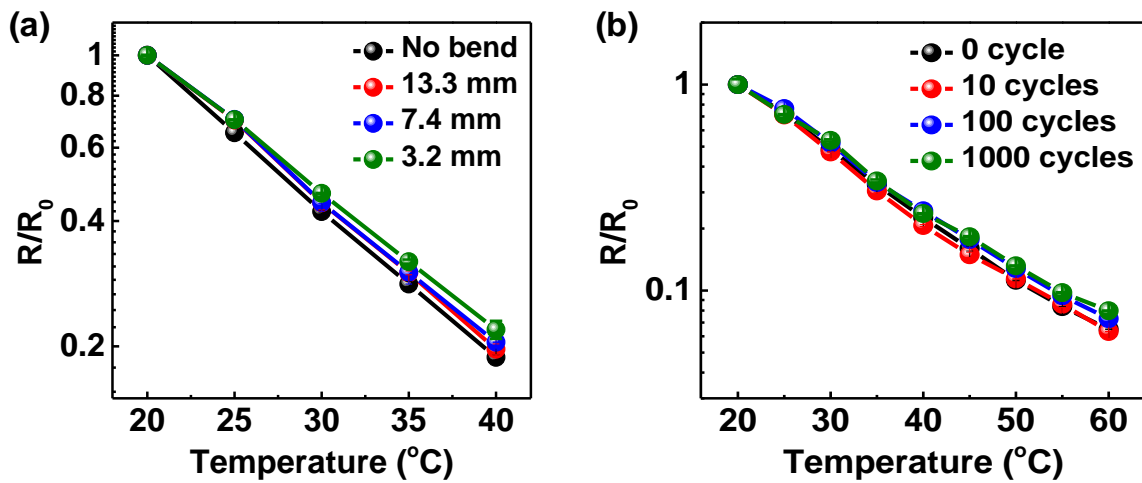


Figure 6.15. (a) Temperature-sensing performances of temperature sensors in different bending states. (b) Relative resistance as a function of temperature of temperature sensors after 0–1000 bending cycles.

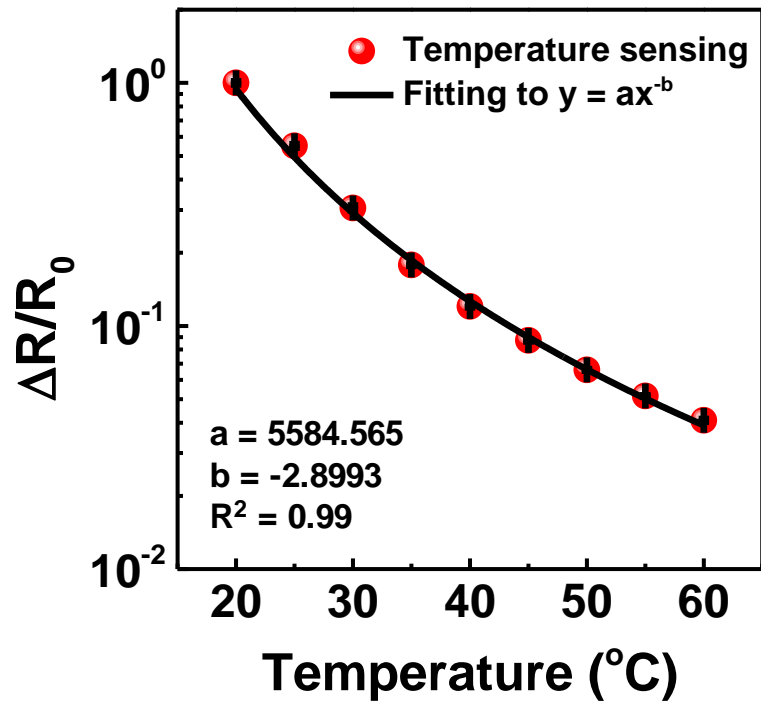


Figure 6.16. Relative resistance as a function of temperature of a temperature sensor. The data was fitted with a power-law equation, $y = ax^{-b}$, where a is 11264.48 and b is -3.11 .

Dual-mode temperature sensor with simultaneous electrical and colorimetric temperature detection capabilities is advantageous in the simultaneous detection of an accurate temperature value from electric signals and the location of temperature variation from color changes. To prepare dual-mode temperature sensor, the pyroresistive temperature sensor was encapsulated with thermochromic composite film (Figure 6.17a). Thermochromic materials, which undergo a color change in response to temperature variation, enable the intuitive visualization of different temperatures. We fabricated thermochromic composite films by mixing PDMS with thermochromic inks. To obtain a wide temperature-sensing range, we used three thermochromic inks of three different colors and three different response temperatures (Figure 6.18). The color changes of the thermochromic composite films in response to temperature variations were evaluated by red–green–blue (RGB) analysis and color coordination (Figure 6.17b,c and 6.19). Both analysis techniques showed clear differences in color as the temperature was changed in steps of 1 °C, demonstrating the high temperature sensitivity of our thermochromic composite films over a wide temperature range. The changes in color with different temperatures can be easily perceived by the naked eye, enabling direct visualization of temperature changes even without any special analytical devices (Figure 6.17d).

To further demonstrate the dual-mode temperature-sensing functionality of our temperature sensor, we investigated the electrical and colorimetric response to the time-dependent temperature variations during natural cooling of a water droplet on the dual-mode temperature sensor. Figure 6.17e shows the relative resistance of the pyroresistive temperature sensor. When warm water droplets with temperatures of 30, 40, and 50 °C were released onto the dual-mode temperature sensor, the relative resistance sharply decreased owing to the heat transfer from each water droplet to the sensor. The resistance then recovered to the original value owing to the natural cooling of the water droplets. These resistance variations exactly matched the temperature variations detected by an infrared (IR) camera. The enlarged plot in Figure 6.17e (Figure 6.17f) shows that the temperature variations detected by the IR camera matched the resistance variations detected by the sensor, demonstrating their fast and reliable operation. The dual-mode temperature sensor could be also operated as a thermochromic temperature sensor for direct visualization of temperature changes. Figure 6.17g shows the color changes of thermochromic composite films and temperature mapping images obtained by the IR camera for temperature variations of a warm water droplet on the sensor. The temperatures obtained from the color images of thermochromic composite films (Figure 6.17d and 6.17g) match well with the temperatures obtained by the IR camera. An RGB analysis of Figure 4g indicates the time-dependent color sensing of our temperature sensor (Figure 6.20).

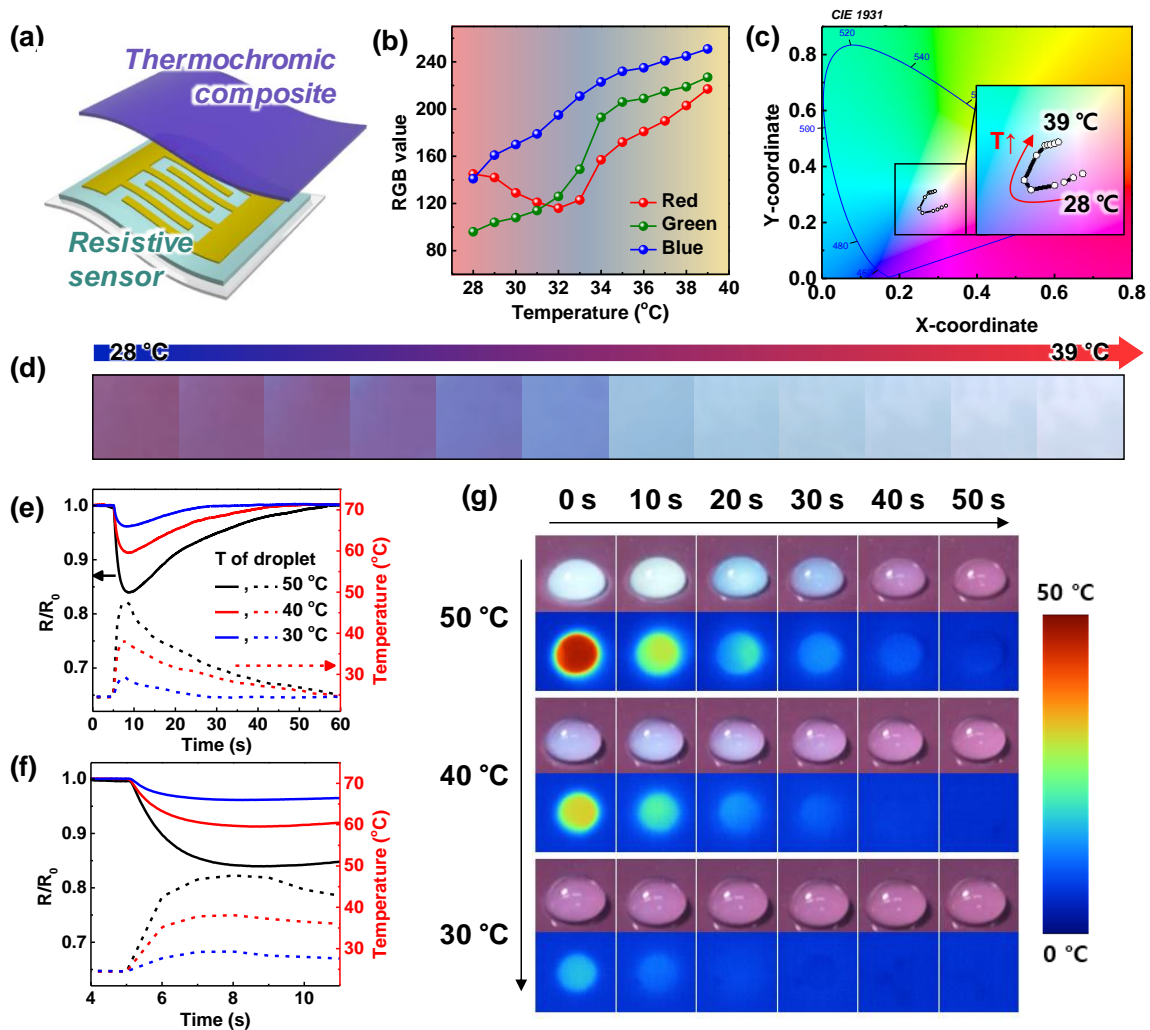


Figure 6.17. Dual-mode temperature sensors for electrical and colorimetric temperature sensing. (a) Schematic illustration of dual-mode temperature sensors. (b) Intensities of the color components (red, green, blue) as a function of temperature of thermochromic composite films. (c) Changes in the CIE 1931 color space chromaticity diagrams of thermochromic composite films when the temperature was changed from 28 to 39 °C in steps of 1 °C. (d) Photographs of the thermochromic composite films in 1 °C increments. (e) Time-dependent relative resistance of pyroresistive temperature sensors after the release of a warm water droplet and temperature variation of warm water droplet, obtained by infrared camera. (f) Magnified variations in relative resistance and temperature shown in (e). (g) Color changes of thermochromic composite films after the release of a warm water droplet and temperature mapping images, obtained by infrared camera, of warm water droplet.

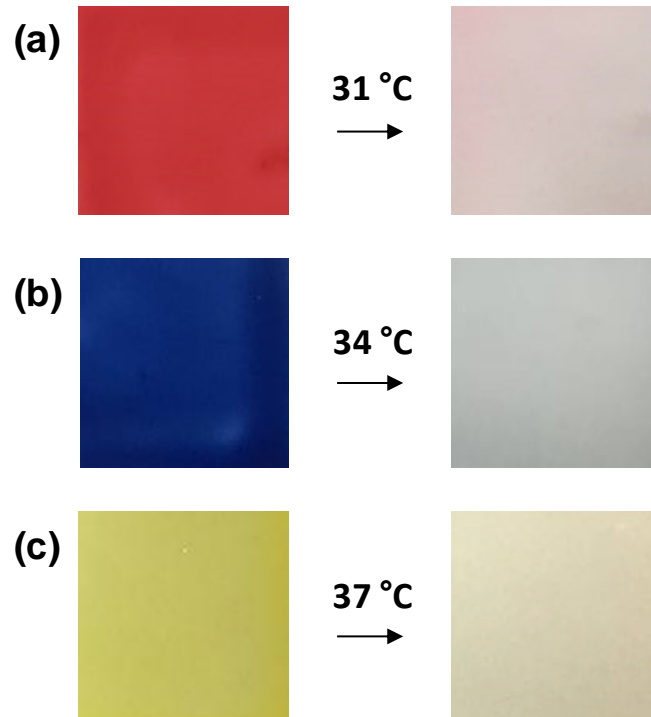


Figure 6.18. (a–c) Thermochromic color change of three thermochromic inks with different color and response temperature.

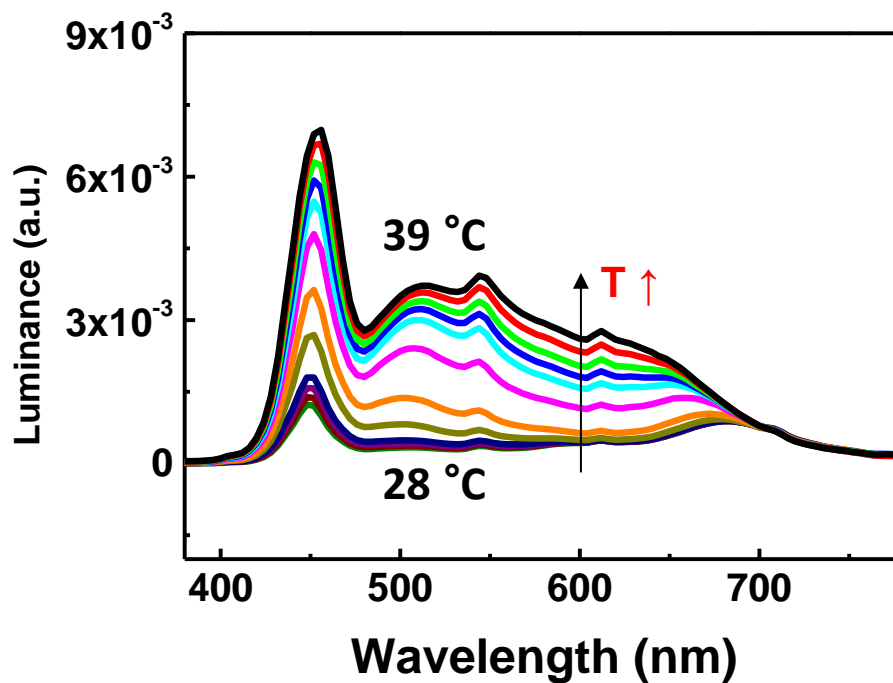


Figure 6.19. Luminance as a function of wavelength for thermochromic composite film as the temperature was changed from 28 to 39 °C in steps of 1 °C.

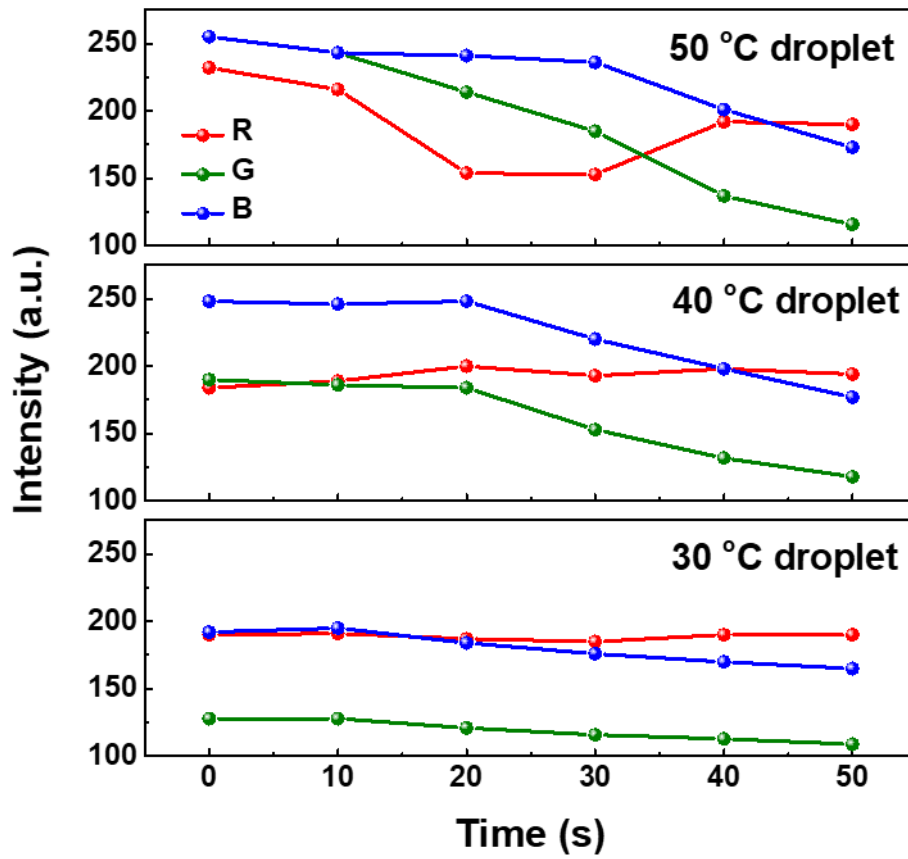


Figure 6.20. RGB values of thermochromic composite films when warm water droplets with temperature of 50, 40, and 30 °C were released on the film surface.

Although colorimetric temperature analysis provides information on the location as well as approximate temperatures, we fabricated flexible pyroresistive temperature sensors in 8×8 pixel arrays to perceive the exact temperature with location information. Figure 6.21a shows a schematic illustration of 8×8 pixel arrays of temperature sensors on a polyethylene naphthalate (PEN) substrate. The vertical and horizontal electrodes were composed of evaporated-Au-film/Ag-nanowire hybrid layers for stable operation under bending states, and the overlapping areas between two electrodes were separated by a parylene layer to avoid direct electrical contact between the electrode lines (Figure 6.21b and 6.22). Figure 6.21c shows the fabricated flexible temperature sensors in 8×8 pixel arrays. We evaluated the temperature-sensing performance of the 8×8 pixel arrays in the temperature range of 20–60 °C (blue line), and the detected signals agree well with the signals from a single temperature sensor (red line) (Figure 6.21d,e). After encapsulation of the pyroresistive temperature-sensor arrays with thermochromic composite films, the dual-mode temperature-sensor arrays could differentiate the heated local regions from others, demonstrating the ability of the temperature-sensor arrays to sense any spatial temperature distribution. Various types of heated metal plates with different temperatures (30, 32, and 40 °C) were loaded on the dual-mode temperature-sensor arrays. The corresponding map of the pyroresistive sensor arrays exactly matches the color map of the thermochromic composite (Figure 6.21f–h). When compared with the values of relative resistance obtained from the non-linear power fitting (Figure 6.16), the average values of detected pyroresistive signals from the three mapping images are close to the fitted relative resistance values at 30, 32, and 40 °C, with errors of 2.8%, 3.7%, and 3.4%, respectively.

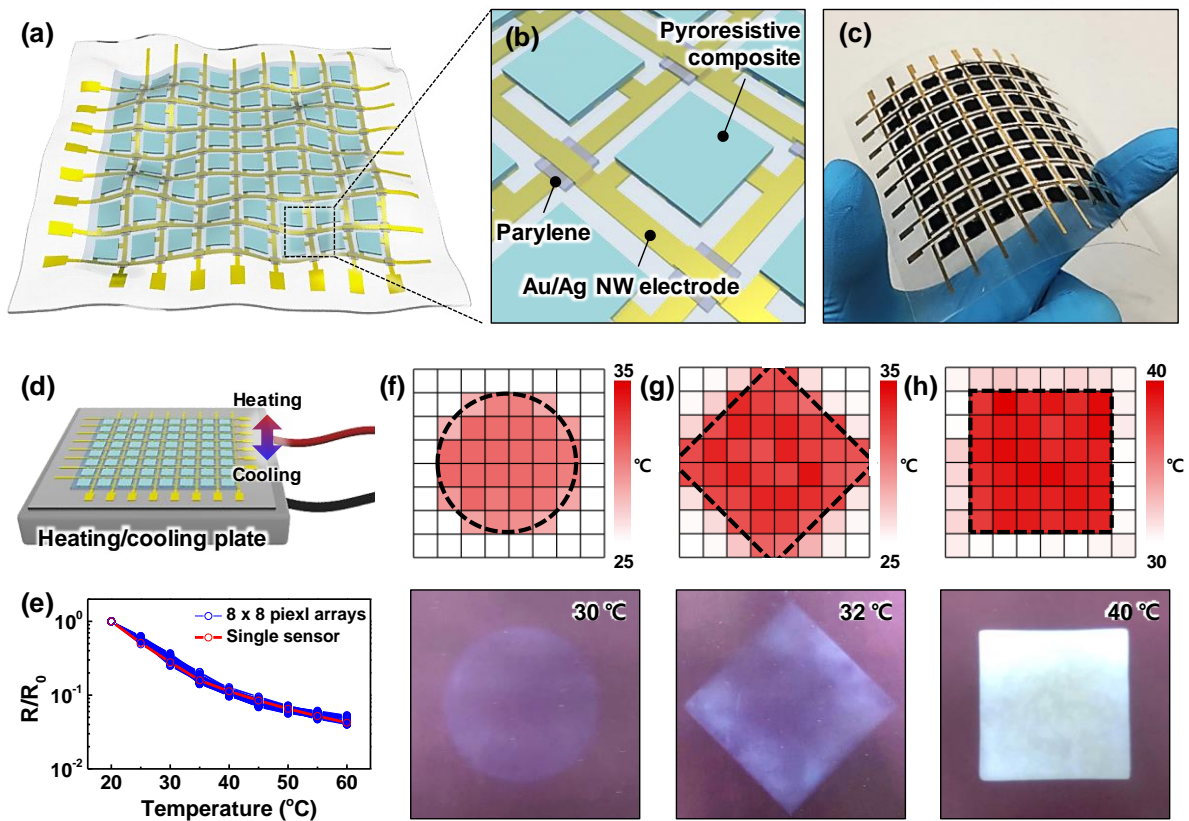


Figure 6.21. 8 × 8 dual-mode temperature-sensor arrays. (a) Schematic illustration of 8 × 8 pixel arrays of temperature sensors. (b) Magnified schematic illustration showing components of temperature-sensor arrays. (c) Photograph of flexible pyroresistive temperature sensors in 8 × 8 pixel arrays. (d) Scheme for the temperature-measurement setup of temperature sensors in 8 × 8 pixel arrays on the heating–cooling plate. (e) Relative resistance of 8 × 8 pixel arrays (blue) and a single temperature sensor (red) as the temperature was changed from 20 to 60 °C. (f–h) Pyroresistive temperature mapping images of three metal plates with temperatures of 30, 32, and 40 °C and photographs of corresponding color mapping of the thermochromic composite film.

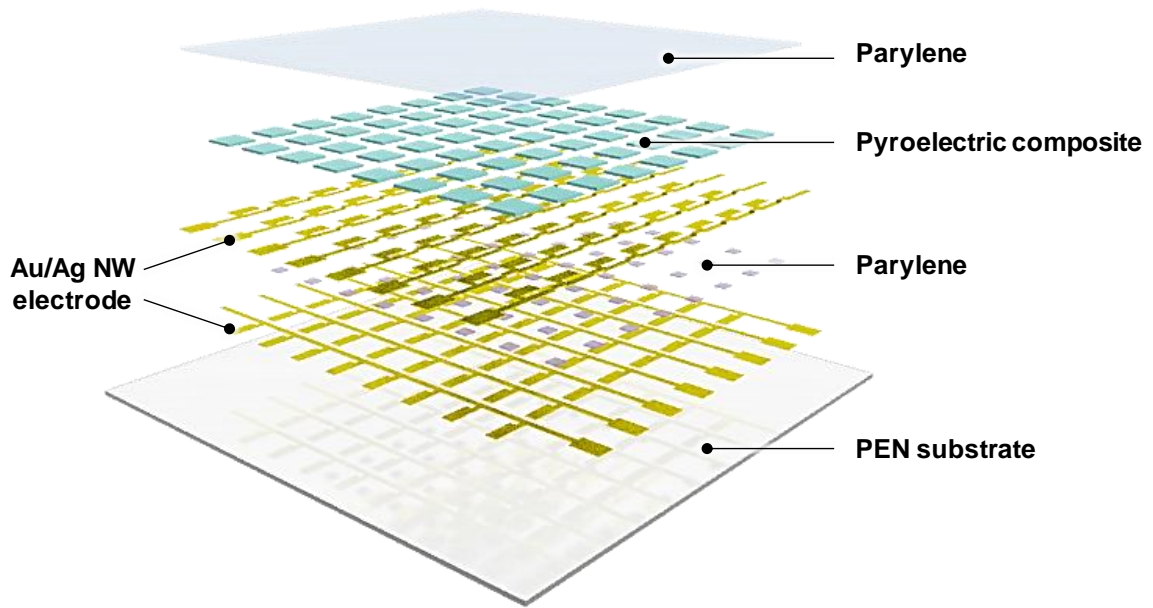


Figure 6.22. Layer-by-layer schematic illustration of 8×8 pixel arrays of temperature sensors.

6.4 Conclusion

We demonstrated a flexible and highly sensitive temperature sensors based on a thermoresponsive rGO–PEO–PVDF composite. The melt-induced volume expansion of semi-crystalline PEO microdomains, as well as the NTC effect of rGO, yielded an ultrahigh TCR of $6.94\% \text{ } ^\circ\text{C}^{-1}$ and high temperature-sensing accuracy of $0.1 \text{ } ^\circ\text{C}$. The ultralow thickness of our flexible temperature sensor enabled highly stable and deformation-insensitive operation under pressure and bending, which facilitates the application of wearable skin temperature sensor with high accuracy ($< 0.1 \text{ } ^\circ\text{C}$). In addition, we fabricated dual-mode temperature-sensor arrays with electrical and colorimetric temperature-sensing performances by combining pyroresistive temperature sensors with thermochromic composite films, enabling simultaneous and accurate sensing of temperature and spatial temperature distribution. Our temperature sensors are expected to be suitable for various applications that require precise temperature measurement and visualization, such as wearable healthcare devices, electronic skins, and intelligent robots.

Chapter 7. Summary and Future Perspective

7.1 Summary

Mimicking the structures and functions of human and biological skins, we suggested bioinspired e-skins with great progress in sensor performances and multifunctionality. Human skin, which is an ideal sensory organ, can sensitively perceive various tactile stimuli (normal, shear, tensile, bending stimuli) and thermal stimuli by transducing them into electrical signals in the mechanoreceptors. In this process, interlocked microstructures between dermal and epidermal layers, owing to the effective stress concentration between dermal and epidermal layers with different moduli. In this thesis, we emulated specialized sensory functions and structures of human skin for high-performance e-skins with high sensitivity, multidirectional force sensing capability, linear response to stimuli, and broad working range. In addition, the unique structures and functionalities of biological skins have provided us a great inspiration for novel designs of e-skins. Inspired by responsive color change in biological skins (such as cephalopods, chameleons, and turkeys), we developed highly sensitive colorimetric skins, which display tactile information by change in color. Furthermore, we demonstrated highly sensitive temperature sensor mimicking snake skin that have ultrahigh sensitivity in temperature change. These bioinspired e-skins have found broad application in wearable healthcare devices or equipment with accurate sensing and reliable actuation systems.

In chapter 2, inspired by the interlocked microstructures found in epidermal–dermal ridges in human skin, piezoresistive interlocked microdome arrays are employed for stress-direction-sensitive, stretchable electronic skins. Here we show that these arrays possess highly sensitive detection capability of various mechanical stimuli including normal, shear, stretch, bending, and twisting forces. Furthermore, the unique geometry of interlocked microdome arrays enables the differentiation of various mechanical stimuli because the arrays exhibit different levels of deformation depending on the direction of applied forces, thus providing different sensory output patterns. In addition, we show that the electronic skins attached on human skin in the arm and wrist areas are able to distinguish various mechanical stimuli applied in different directions and can selectively monitor different intensities and directions of air flows and vibrations. Stretchable electronic skins with multidirectional force-sensing capabilities are of great importance in robotics, prosthetics, and rehabilitation devices.

In chapter 3, we introduced interlocked microdome multilayer system for highly sensitive and ultra-large dynamic range e-skins with linear response. Our e-skins possess high sensitivity (47.7 kPa^{-1} , 1.3 Pa minimum detection) under the static/dynamic pressure due to stress concentration between interlocked microdome arrays and increased contact area change in multilayer system. In addition,

stress distribution between stacked layers enables linear and ultra-large range pressure sensing (0.0013 – 353 kPa), maintaining their high sensitivity upto several hundreds of kPa. Flexible pressure sensors with a high sensitivity over a broad linear range can simplify the wearable sensing systems without additional signal processing for the linear output, enabling device miniaturization and low power consumption. For proof-of-concept demonstrations, highly sensitive e-skins are applied to precise detection of acoustic sound, respiration, and pulse pressure in weak pressure-regime. In addition, wide range pressure sensing ability is employed for the plantar pressure monitoring in high pressure-regime.

In chapter 4, we demonstrated a highly-sensitive and linearly-responsive flexible pressure sensor by multi-layering PEDOT:PSS/PUD composites with interlocked structures. The multi-layer with gradient conductivity enabled regulation of saturation behavior of composite resistance in response to applied pressure. Further, the multi-layered pressure sensor could linearly perceive pressure over a broad working pressure range (0.8 Pa to 100 kPa) with an extremely high sensitivity of $3.8 \times 10^5 \text{ kPa}^{-1}$, which is the highest reported value for pressure sensors. In addition, the sensor indicated a rapid response time of 130 ms, a relaxation time of 11 ms, and high durability during 5000 repetitive cycles of pressure application (20 kPa). Finally, the pressure sensor could distinguish weak gas flows characterized by different densities, subtle manipulation of objects, and different pulse rates of the carotid artery and the internal jugular vein.

In chapter 5, we reported a hierarchical nanoparticle-in-micropore (NP-MP) architecture in porous mechanochromic polymers to enhance the mechanosensitivity and stretchability of mechanochromic electronic skins (e-skins). The hierarchical NP-MP structure results in stress concentration-induced mechanochemical activation of mechanophores, significantly improving the mechanochromic sensitivity to both tensile strain and normal force (critical tensile strain: 50% and normal force: 1 N). Furthermore, the porous mechanochromic composites exhibit a reversible mechanochromism under a strain of 250%. This architecture enables a dual-mode mechanochromic e-skin for detecting static/dynamic forces via mechanochromism and triboelectricity. The hierarchical NP-MP architecture provides a general platform to develop mechanochromic composites with high sensitivity and stretchability.

In chapter 6, we demonstrated a deformation-insensitive, flexible, and highly sensitive resistive-type temperature sensor that is made of a polymer nanocomposite with semi-crystalline polymer microdomains. Unlike previously reported resistive temperature sensors, whose temperature sensitivity is mainly affected by the temperature coefficients of resistance (TCR) of conductive fillers, our sensor shows an extremely large change in resistance due to the melt-induced expansion in volume of the semi-crystalline poly(ethylene oxide) microphase, as well as the TCR of reduced graphene oxide. The optimized temperature sensor exhibits an ultrahigh temperature sensitivity of $6.94\% \text{ }^\circ\text{C}^{-1}$, high

temperature-sensing accuracy of 0.1 °C, stable operation under mechanical stimuli, and accurate skin temperature monitoring performance. As a proof-of-concept prototype, dual-mode 8 × 8 pixel arrays of temperature sensors are encapsulated by thermochromic composite films, and they demonstrate simultaneous and accurate detection of temperature and spatial temperature distribution.

In summary, this thesis covers various types of e-skins inspired by human and biological skins. The biomimicry of human and biological skins has become a great inspiration for realizing novel wearable electronic systems with exceptional multifunctionality (static/dynamic force sensing, multidirectional force sensing, self-powered sensing, visualization of stimuli, IR sensing from far object) as well as advanced sensory functions (ultrahigh sensitivity, linear response, broad working range, fast response, durability). Benefitting from their high-performances and multifunctionalities, the suggested bioinspired e-skins were successfully applied to various fields, including wearable motion sensor, wearable healthcare sensor, acoustic sensor, and cosmetics. Through those studies, we believe that our bioinspired e-skins provide a great potential of electronic skins for next-generation sensor systems in wearable and soft electronics.

7.2 Future perspective

For the applications of e-skins in wearable and implantable electronics, several important factors are still needed to be considered such as signal processing, power supply, integration, and biocompatibility (Figure 7.1). In this section, we briefly introduce these factors for the realization of next-generation skin electronics and recent outcomes for addressing these challenges.

Linear sensitivity over wide pressure range: The e-skin with linear sensitivity over a wide pressure range is beneficial for obtaining accurate sensor-output information without additional complex signal processing. In addition, the simplified process can meet the increasing demand for device miniaturization and low power consumption. Typically, conventional e-skins have shown a trade-off between sensitivity and pressure-sensing range, due to limited deformability or a nonlinear variation of contact area in a single film. Recent reports addressed this issue via novel geometrical approaches. For example, our group demonstrated a ferroelectric skin with a multilayer interlocked microdome geometry for ultrahigh pressure sensitivity and linear response over a wide pressure range.¹²² Cho and co-workers demonstrated a piezoresistive pressure sensor with a linear output by introducing a hierarchically structured graphene/PDMS film.¹²³ Besides pressure sensors, several studies have focused on strain sensors with linear sensitivity based on PDMS-infused conductive (PEDOT:PSS/cellulose nanofibrils aerogel²⁹⁰ and tough hydrogels with PANI and poly(acrylamide-*co*-hydroxyethyl methyl acrylate) (P-(AAM-*co*-HEMA) network.²⁹¹

Self-powered system: To realize wearable electronics, a sustainable electrical power supply is necessary for sensor operation, signal processing, and transmission. In this regard, self-powered systems that can harvest renewable energy by various mechanical and thermal stimuli have recently emerged.²⁹² The self-powered system can generate electrical power from various body motions or from surrounding environmental sources (wind, vibration, and solar), providing great possibility of device operation without the help of any external power source and the miniaturization of electronic devices. Self-powered e-skins are largely based on four types of signal-transduction modes; piezoelectric, triboelectric, pyroelectric, and thermoelectric.

Piezoelectric e-skin can produce electric charges in response to mechanical stress based on inorganic materials such as ZnO,²⁴ lead zirconium titanate (PZT),²⁹³ and BaTiO₃,²⁹⁴ and organic materials such as PVDF,²² PVDF-based copolymers,²⁹⁵ poly-l-lactide,²⁹⁶ MoS₂,²⁹⁷ and non-synthetic biocompatible protein.²⁹⁸ To further improve the piezoelectric performance, surface micropatterns (e.g., dome, pyramid, and pillar)^{22,24,295} and bioinspired structures (e.g., interlocking, hierarchical, porous)^{24,299-300} have been used to greatly improve the piezopotentials, resulting from a large localized stress and large surface area. Triboelectric e-skins convert mechanical energy to electrical energy through a conjugation of triboelectrification and electrostatic induction, caused by various contact

motions such as vertical touch, shear friction from sliding motion, and torsional stress. Since the triboelectric output critically relies on differences in triboelectric polarity between two contacting materials and contacting surface areas, a rational design of material and structure is important to demonstrate high-performance triboelectric e-skin. For a structural approach, uniquely designed micro/nanoscale structures such as surface micropatterns, micropore, nanoscale assembly, and hierarchical nanoporous and interlocked micro-ridge structures²⁸ have been suggested, which enables the increases in surface area and stress-induced deformability, thereby producing enhanced power up to a few tens of milliwatts. In addition, chemically modified surface charge by self-assembled monolayers using an end-fluorine terminated group,³⁰¹⁻³⁰² thiol with a different head group,³⁰³ and atomic-level halogens and amines³⁰⁴ influences the surface potential and surface-charge density, enabling control of triboelectric output.

In addition to mechanical-energy harvesting devices, ambient-heat variation can be converted into electrical energy by pyroelectric and thermoelectric effects. While the pyroelectric effect harvests thermal energy by spontaneous polarization in certain anisotropic solids as a result of temperature fluctuation, the thermoelectric effect induces the diffusion of charge carriers following the thermal gradient in the materials (Seebeck effect).³⁰ For the pyroelectric nanogenerator, various ferroelectric materials such as P(VDF-TrFE),³¹ ZnO,³² PZT,³³ and BaTiO₃³⁴ have been introduced, but relatively low power density restrict the application for self-powered e-skins. For thermoelectric devices, various materials including conductive polymers such as PANI,³⁵ polypyrrole,³⁶ and PEDOT:PSS,^{37,266,305} inorganic materials (such as Bi₂Te₃, Sb₂Te₃, and Bi_{0.5}Sb_{1.5}Te₃),³⁸ and even ionic polymer solution³⁹ have been introduced. Ionic skin is capable of generating an electrical potential by mechanical-deformation-induced mobile charged ions, which have recently attracted much attention for self-powered e-skin.³⁰⁶ The ionic materials can also be used for highly transparent, stretchable, and biocompatible conducting and dielectric materials, which provide great potential applications for transparent pressure sensors,³⁰⁷ ionic loudspeakers,³⁰⁸ and energy harvesting devices.³⁰⁹

Integrated system with flexible and stretchable properties: The integration of various sensors with electronic elements and the attainment of mechanical flexibility and stretchability are essential to the further development and wider adoption of skin-attachable and wearable electronics. One approach to address these issues is the geometrical approach integrating the multiple electronic elements with uniquely designed interconnects such as serpentine, wavy, and buckling configurations.^{78,310-311} Another one is the fabrication of highly stretchable and conformable sensor-matrix networks with high-density 3D-integrated multiple sensors using meandering interconnects,⁶¹ where sensing elements are adjustable by stretching and expanding the meandering interconnects. The use of intrinsically stretchable materials to electronic components has been also introduced.³¹²⁻³¹³ This approach enables simultaneous achievement of both the intrinsic advantages of excellent electrical conductivity of fillers

and stretchability of elastomers by simple fabrication methods. In addition, stretchable semiconducting polymers by molecular design to promote dynamic noncovalent crosslinking,³¹⁴ has been employed to construct intrinsically stretchable transistor arrays, for which all electronic conductor, semiconductor, and dielectric components are composed of intrinsically stretchable polymers.³¹⁵

Biocompatible or biodegradable materials and systems: For wearable electronics mounted onto skin or an organ, it is necessary to use biocompatible materials for reducing immune reaction.³¹⁶⁻³¹⁷ Although various biocompatible dielectric polymers have been developed for biomedical applications, demonstrating biocompatible semiconductor and conductor materials for high-performance electronics is still challenged. Recent report demonstrated biocompatible semiconducting polymers incorporated with conjugated polymer (diketopyrrolopyrrole) with reversible imine bonds, which can be easily decomposed under acidic conditions.³¹⁸ For the biocompatible conductor, a highly stretchable conductor based on Ag–Au nanowire and poly(styrene-butadiene-styrene) composite have been suggested,³¹⁸ such conductors would enable soft wearable and implantable bioelectronics for monitoring electrophysiological signals and electrical and thermal stimulations. In addition, a new type of biocompatible e-skin patch based on conductive Au nanomesh has been demonstrated.³¹⁹ Compared with conventional plastic and elastomer films with lower gas permeability, the Au nanomesh conductor significantly reduces the risk of inflammation caused by an on-skin sensor due to its large gas-permeability and light-weight properties. In addition, direct skin-attachable property, high electrical stability, and excellent mechanical durability of the conductive nanomesh enables the accurate monitoring of touch, temperature, pressure and electromyograms.

Recently, a concept of “transient electronics” has been introduced based on silicon complementary metal-oxide semiconductor (CMOS) consisting of water-dissolvable materials.³²⁰ In such a system, all the components—such as transistors, diodes, inductors, capacitors, and resistors—consist of inorganic materials (e.g., Mg, MgO, SiO₂ and silicon-based nanomembranes), and all components are completely dissolved by hydrolysis. Furthermore, this platform of transient electronics can be applied to biodegradable silicon electronic sensors in combination with silicon-based sensing elements,³²¹ which can detect fluid, flow, motion, pH, or thermal stimuli. Biodegradable organic materials such as poly(glycerol sebacate),³²² poly(lactic-co-glycolic acid),³²³⁻³²⁴ and poly-L-lactide²⁹⁶ have been used in various biodegradable sensor systems. Bao and co-workers demonstrated a fully biodegradable capacitive sensor capable of independent sensing of strain and pressure.³²⁵ The combination of tunable biodegradability with multifunctional-sensing capability is expected to provide great opportunities for biomedical applications, including orthopedic, rehabilitation monitoring, cardiovascular patches, and reconstructive surgery.

In this thesis, we found that recent electronic skins have accomplished a great achievements in

terms of improving sensor performance, energy harvesting, and multi-functionality, furthermore practical applications in current key technologies including smart electronics, wearable and healthcare devices. With a great demand for the next generation technologies such as Internet of Things (IoT), human-machine interfaces (HMI), virtual reality (VR), artificial intelligent (AI), an importance of interactive platform between the electronic devices/sensors and human or surrounding objects have been considerably increased. Key enabling technologies of interactive system include signal transmission, perception, and display of sensing information. Constructing the wireless-communication devices facilitates a remote monitor/control and a data collection from various sensors, which results in the applications for the personalized and real-time physiological and clinical diagnosis, and various interface devices.³²⁶ In addition, the study on perception mechanism of deep-learning and machine-learning by pattern recognition, modeling, and developing intelligence will be essential factor for artificial intelligent robots, and advanced healthcare and wearable electronics.³²⁷ Furthermore, the display of tactile information by actuator and visualization will provide a great potential for haptic interface, and virtual reality application.³²⁸ Combined with these components with electronic sensor devices, electronic skin will change our lifestyle and will experience a technological innovation for futuristic applications.

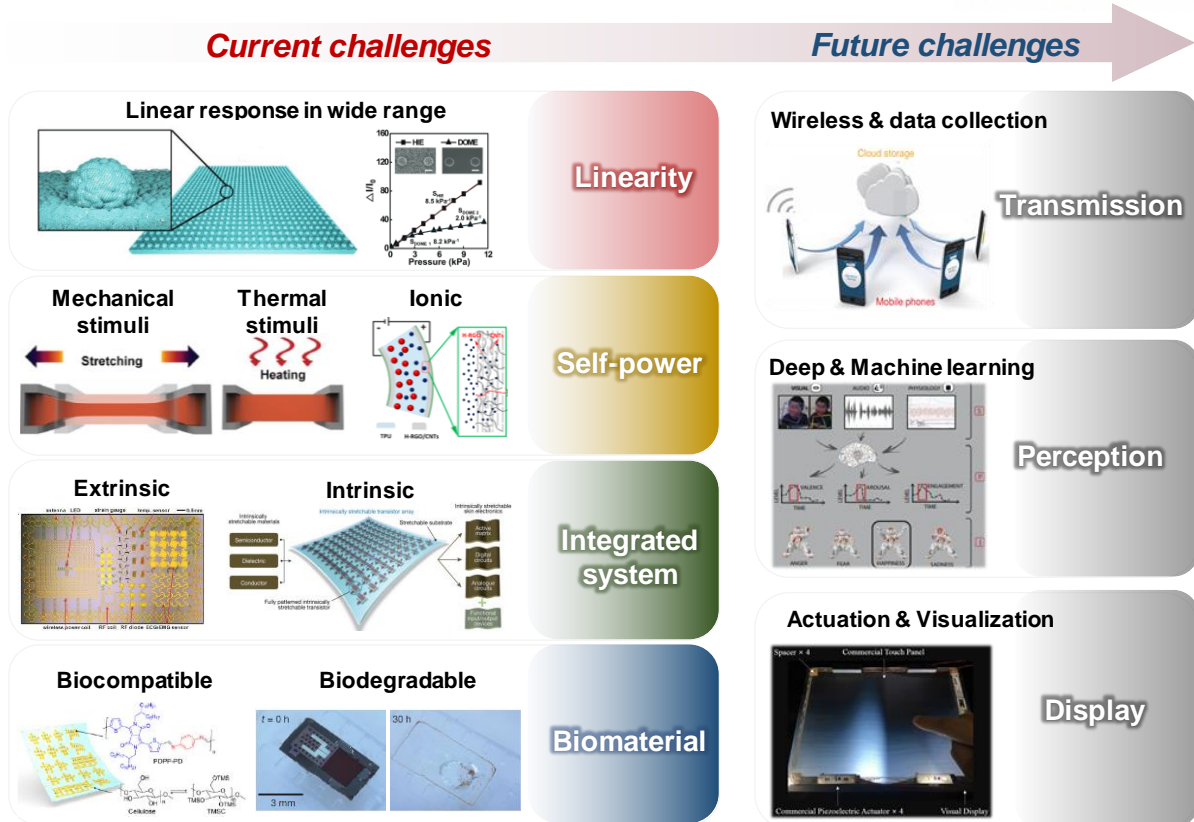


Figure 7.1. Current and Future challenges for the demonstration of skin electronics. Current challenges: Linearity controlled by macroscopic and microscopic structure modification. (Bae et al. *Adv. Mater.* **2016**, *28*, 5300-5306). Self-powered e-skins based on piezoelectric, triboelectric, pyroelectric, thermoelectric and ionic properties. (Lee et al. *Adv. Mater.* **2014**, *26*, 765, Zhao et al. *Nat. Commun.* **2017**, *8*, 14214). Integration with stretchable electronic components controlled by extrinsically modified structure and intrinsically modified materials. (Kim et al. *Science* **2011**, *333*, 838, Wang et al. *Nature* **2018**, *555*, 83). Biocompatible and biodegradable electronics. (Lei et al. *Proc. Natl. Acad. Sci. U.S.A.* **2017**, *114*, 5107, Kange et al. *Nature* **2016**, *530*, 71). **Future challenges:** Transmission. (Gao et al. *Nature* **2016**, *529*, 509) Perception. (Rudovic. Et al. *Sci. Robot.* **2018**, *3*, eaao6760). Display. (Ryu et al. *Sci. Rep.* **2018**, *8*, 4555).

References

- (1) Trung, T. Q.; Lee, N. E., Flexible and stretchable physical sensor integrated platforms for wearable human-activity monitoring and personal healthcare. *Adv. Mater.* **2016**, *28*, 4338-4372.
- (2) Wortmann, F.; Flüchter, K., Internet of things. *Bus. Inf. Syst. Eng.* **2015**, *57*, 221-224.
- (3) Whitmore, A.; Agarwal, A.; Da Xu, L., The Internet of Things—A survey of topics and trends. *Inf. Syst. Front.* **2015**, *17*, 261-274.
- (4) Xu, K.; Lu, Y.; Takei, K., Multifunctional Skin-Inspired Flexible Sensor Systems for Wearable Electronics. *Adv. Mater. Technol.* **2019**, *4*, 1800628.
- (5) Chang, T. H.; Li, K.; Yang, H.; Chen, P. Y., Multifunctionality and Mechanical Actuation of 2D Materials for Skin-Mimicking Capabilities. *Adv. Mater.* **2018**, *30*, 1802418.
- (6) Lou, Z.; Wang, L.; Shen, G., Recent Advances in Smart Wearable Sensing Systems. *Adv. Mater. Technol.* **2018**, *3*, 1800444.
- (7) Park, J.; Lee, Y.; Ha, M.; Cho, S.; Ko, H., Micro/nanostructured surfaces for self-powered and multifunctional electronic skins. *J. Mater. Chem. B* **2016**, *4*, 2999-3018.
- (8) Boutry, C. M.; Negre, M.; Jorda, M.; Vardoulis, O.; Chortos, A.; Khatib, O.; Bao, Z., A hierarchically patterned, bioinspired e-skin able to detect the direction of applied pressure for robotics. *Sci. Robot.* **2018**, *3*, eaau6914.
- (9) Wang, T.; Zhang, Y.; Liu, Q.; Cheng, W.; Wang, X.; Pan, L.; Xu, B.; Xu, H., A self-healable, highly stretchable, and solution processable conductive polymer composite for ultrasensitive strain and pressure sensing. *Adv. Funct. Mater.* **2018**, *28*, 1705551.
- (10) Choe, A.; Yeom, J.; Shanker, R.; Kim, M. P.; Kang, S.; Ko, H., Stretchable and wearable colorimetric patches based on thermoresponsive plasmonic microgels embedded in a hydrogel film. *NPG Asia Mater.* **2018**, *1*.
- (11) Han, S.; Liu, C.; Xu, H.; Yao, D.; Yan, K.; Zheng, H.; Chen, H.-J.; Gui, X.; Chu, S.; Liu, C., Multiscale nanowire-microfluidic hybrid strain sensors with high sensitivity and stretchability. *NPJ Flexible Electron.* **2018**, *2*, 16.
- (12) Theodosiou, T.; Saravanos, D., Numerical investigation of mechanisms affecting the piezoresistive properties of CNT-doped polymers using multi-scale models. *Compos. Sci. Technol.* **2010**, *70*, 1312-1320.
- (13) Obitayo, W.; Liu, T., A review: Carbon nanotube-based piezoresistive strain sensors. *Journal*

of *Sensors* **2012**, 2012.

- (14) Jiang, M.-J.; Dang, Z.-M.; Xu, H.-P., Giant dielectric constant and resistance-pressure sensitivity in carbon nanotubes/rubber nanocomposites with low percolation threshold. *Appl. Phys. Lett.* **2007**, *90*, 042914.
- (15) Park, J.; Lee, Y.; Hong, J.; Ha, M.; Jung, Y.-D.; Lim, H.; Kim, S. Y.; Ko, H., Giant tunneling piezoresistance of composite elastomers with interlocked microdome arrays for ultrasensitive and multimodal electronic skins. *ACS Nano* **2014**, *8*, 4689-4697.
- (16) Schwartz, G.; Tee, B. C.-K.; Mei, J.; Appleton, A. L.; Kim, D. H.; Wang, H.; Bao, Z., Flexible polymer transistors with high pressure sensitivity for application in electronic skin and health monitoring. *Nat. Commun.* **2013**, *4*, 1859.
- (17) Lee, Y.; Park, J.; Choe, A.; Cho, S.; Kim, J.; Ko, H., Mimicking Human and Biological Skins for Multifunctional Skin Electronics. *Adv. Funct. Mater.* **2019**, 1904523.
- (18) Lovinger, A. J., Ferroelectric polymers. *Science* **1983**, *220*, 1115-1121.
- (19) Ling, Q.-D.; Liaw, D.-J.; Zhu, C.; Chan, D. S.-H.; Kang, E.-T.; Neoh, K.-G., Polymer electronic memories: Materials, devices and mechanisms. *Prog. Polym. Sci.* **2008**, *33*, 917-978.
- (20) Karan, S. K.; Bera, R.; Paria, S.; Das, A. K.; Maiti, S.; Maitra, A.; Khatua, B. B., An approach to design highly durable piezoelectric nanogenerator based on self-poled PVDF/AlO-rGO flexible nanocomposite with high power density and energy conversion efficiency. *Adv. Energy Mater.* **2016**, *6*, 1601016.
- (21) Su, S.; Zuo, R.; Lu, S.; Xu, Z.; Wang, X.; Li, L., Poling dependence and stability of piezoelectric properties of Ba (Zr_{0.2}Ti_{0.8})O₃-(Ba_{0.7}Ca_{0.3})TiO₃ ceramics with huge piezoelectric coefficients. *Curr. Appl. Phys.* **2011**, *11*, S120-S123.
- (22) Park, J.; Kim, M.; Lee, Y.; Lee, H. S.; Ko, H., Fingertip skin-inspired microstructured ferroelectric skins discriminate static/dynamic pressure and temperature stimuli. *Sci. Adv.* **2015**, *1*, e1500661.
- (23) Garain, S.; Sinha, T. K.; Adhikary, P.; Henkel, K.; Sen, S.; Ram, S.; Sinha, C.; Schmeißer, D.; Mandal, D., Self-poled transparent and flexible UV light-emitting cerium complex-PVDF composite: a high-performance nanogenerator. *ACS Appl. Mater. Interfaces* **2015**, *7*, 1298-1307.
- (24) Ha, M.; Lim, S.; Park, J.; Um, D. S.; Lee, Y.; Ko, H., Bioinspired interlocked and hierarchical design of ZnO nanowire arrays for static and dynamic pressure-sensitive electronic skins. *Adv. Funct. Mater.* **2015**, *25*, 2841-2849.

- (25) Wang, Z. L., Triboelectric nanogenerators as new energy technology for self-powered systems and as active mechanical and chemical sensors. *ACS Nano* **2013**, *7*, 9533-9557.
- (26) Ha, M.; Park, J.; Lee, Y.; Ko, H., Triboelectric generators and sensors for self-powered wearable electronics. *ACS Nano* **2015**, *9*, 3421-3427.
- (27) Kim, M. P.; Lee, Y.; Hur, Y. H.; Park, J.; Kim, J.; Lee, Y.; Ahn, C. W.; Song, S. W.; Jung, Y. S.; Ko, H., Molecular structure engineering of dielectric fluorinated polymers for enhanced performances of triboelectric nanogenerators. *Nano Energy* **2018**, *53*, 37-45.
- (28) Ha, M.; Lim, S.; Cho, S.; Lee, Y.; Na, S.; Baig, C.; Ko, H., Skin-inspired hierarchical polymer architectures with gradient stiffness for spacer-free, ultrathin, and highly sensitive triboelectric sensors. *ACS Nano* **2018**, *12*, 3964-3974.
- (29) Mukhopadhyay, S. C., *Wearable electronics sensors: For safe and healthy living*. Springer: 2015; Vol. 15.
- (30) Wang, Z. L.; Zhu, G.; Yang, Y.; Wang, S.; Pan, C., Progress in nanogenerators for portable electronics. *Mater. Today* **2012**, *15*, 532-543.
- (31) Lee, J. H.; Lee, K. Y.; Gupta, M. K.; Kim, T. Y.; Lee, D. Y.; Oh, J.; Ryu, C.; Yoo, W. J.; Kang, C. Y.; Yoon, S. J., Highly stretchable piezoelectric-pyroelectric hybrid nanogenerator. *Adv. Mater.* **2014**, *26*, 765-769.
- (32) Yang, Y.; Guo, W.; Pradel, K. C.; Zhu, G.; Zhou, Y.; Zhang, Y.; Hu, Y.; Lin, L.; Wang, Z. L., Pyroelectric nanogenerators for harvesting thermoelectric energy. *Nano Lett.* **2012**, *12*, 2833-2838.
- (33) Zhang, Y.; Xie, M.; Roscow, J.; Bao, Y.; Zhou, K.; Zhang, D.; Bowen, C. R., Enhanced pyroelectric and piezoelectric properties of PZT with aligned porosity for energy harvesting applications. *J. Mater. Chem. A* **2017**, *5*, 6569-6580.
- (34) Cho, S.; Lee, J. S.; Jang, J., Enhanced Crystallinity, Dielectric, and Energy Harvesting Performances of Surface-Treated Barium Titanate Hollow Nanospheres/PVDF Nanocomposites. *Adv. Mater. Interfaces* **2015**, *2*, 1500098.
- (35) Yao, Q.; Chen, L.; Zhang, W.; Liufu, S.; Chen, X., Enhanced thermoelectric performance of single-walled carbon nanotubes/polyaniline hybrid nanocomposites. *ACS Nano* **2010**, *4*, 2445-2451.
- (36) Kemp, N.; Kaiser, A.; Liu, C. J.; Chapman, B.; Mercier, O.; Carr, A.; Trodahl, H.; Buckley, R.; Partridge, A.; Lee, J., Thermoelectric power and conductivity of different types of polypyrrole. *J. Polym. Sci., Part B: Polym. Phys.* **1999**, *37*, 953-960.

- (37) Taroni, P. J.; Santagiuliana, G.; Wan, K.; Calado, P.; Qiu, M.; Zhang, H.; Pugno, N. M.; Palma, M.; Stingelin-Stutzman, N.; Heeney, M., Toward Stretchable Self-Powered Sensors Based on the Thermoelectric Response of PEDOT: PSS/Polyurethane Blends. *Adv. Funct. Mater.* **2018**, *28*, 1704285.
- (38) Son, S.; Shin, E.; Kim, B.-S., Light-responsive micelles of spiropyran initiated hyperbranched polyglycerol for smart drug delivery. *Biomacromolecules* **2014**, *15*, 628-634.
- (39) Zhao, D.; Fabiano, S.; Berggren, M.; Crispin, X., Ionic thermoelectric gating organic transistors. *Nat. Commun.* **2017**, *8*, 14214.
- (40) Wang, C.; Hwang, D.; Yu, Z.; Takei, K.; Park, J.; Chen, T.; Ma, B.; Javey, A., User-interactive electronic skin for instantaneous pressure visualization. *Nat. Mater.* **2013**, *12*, 899.
- (41) Yokota, T.; Zalar, P.; Kaltenbrunner, M.; Jinno, H.; Matsuhisa, N.; Kitano, H.; Tachibana, Y.; Yukita, W.; Koizumi, M.; Someya, T., Ultraflexible organic photonic skin. *Sci. Adv.* **2016**, *2*, e1501856.
- (42) Pan, C.; Dong, L.; Zhu, G.; Niu, S.; Yu, R.; Yang, Q.; Liu, Y.; Wang, Z. L., High-resolution electroluminescent imaging of pressure distribution using a piezoelectric nanowire LED array. *Nat. Photonics* **2013**, *7*, 752.
- (43) White, M. S.; Kaltenbrunner, M.; Głowacki, E. D.; Gutnichenko, K.; Kettlgruber, G.; Graz, I.; Aazou, S.; Ulbricht, C.; Egbe, D. A.; Miron, M. C., Ultrathin, highly flexible and stretchable PLEDs. *Nat. Photonics* **2013**, *7*, 811.
- (44) Somani, P. R.; Radhakrishnan, S., Electrochromic materials and devices: present and future. *Mater. Chem. Phys.* **2003**, *77*, 117-133.
- (45) Lee, H. Y.; Cai, Y.; Velioglu, S.; Mu, C.; Chang, C. J.; Chen, Y. L.; Song, Y.; Chew, J. W.; Hu, X. M., Thermochromic ionogel: a new class of stimuli responsive materials with super cyclic stability for solar modulation. *Chem. Mater.* **2017**, *29*, 6947-6955.
- (46) Jeong, S. M.; Song, S.; Lee, S. K.; Ha, N. Y., Color manipulation of mechanoluminescence from stress-activated composite films. *Adv. Mater.* **2013**, *25*, 6194-6200.
- (47) Arsenault, A. C.; Clark, T. J.; von Freymann, G.; Cademartiri, L.; Sapienza, R.; Bertolotti, J.; Vekris, E.; Wong, S.; Kitaev, V.; Manners, I., From colour fingerprinting to the control of photoluminescence in elastic photonic crystals. *Nat. Mater.* **2006**, *5*, 179.
- (48) Larson, C.; Peele, B.; Li, S.; Robinson, S.; Totaro, M.; Beccai, L.; Mazzolai, B.; Shepherd, R., Highly stretchable electroluminescent skin for optical signaling and tactile sensing. *Science* **2016**, *351*, 1071-1074.

- (49) Gossweiler, G. R.; Hewage, G. B.; Soriano, G.; Wang, Q.; Welshofer, G. W.; Zhao, X.; Craig, S. L., Mechanochemical activation of covalent bonds in polymers with full and repeatable macroscopic shape recovery. *ACS Macro Lett.* **2014**, *3*, 216-219.
- (50) Davis, D. A.; Hamilton, A.; Yang, J.; Cremer, L. D.; Van Gough, D.; Potisek, S. L.; Ong, M. T.; Braun, P. V.; Martínez, T. J.; White, S. R., Force-induced activation of covalent bonds in mechanoresponsive polymeric materials. *Nature* **2009**, *459*, 68.
- (51) Chen, H.; Yang, F.; Chen, Q.; Zheng, J., A Novel Design of Multi-Mechanoresponsive and Mechanically Strong Hydrogels. *Adv. Mater.* **2017**, *29*, 1606900.
- (52) Zeng, S.; Zhang, D.; Huang, W.; Wang, Z.; Freire, S. G.; Yu, X.; Smith, A. T.; Huang, E. Y.; Nguon, H.; Sun, L., Bio-inspired sensitive and reversible mechanochromisms via strain-dependent cracks and folds. *Nat. Commun.* **2016**, *7*, 11802.
- (53) Raisch, M.; Genovese, D.; Zaccheroni, N.; Schmidt, S. B.; Focarete, M. L.; Sommer, M.; Gualandi, C., Highly Sensitive, Anisotropic, and Reversible Stress/Strain-Sensors from Mechanochromic Nanofiber Composites. *Adv. Mater.* **2018**, *30*, 1802813.
- (54) Imato, K.; Kanehara, T.; Ohishi, T.; Nishihara, M.; Yajima, H.; Ito, M.; Takahara, A.; Otsuka, H., Mechanochromic dynamic covalent elastomers: quantitative stress evaluation and autonomous recovery. *ACS Macro Lett.* **2015**, *4*, 1307-1311.
- (55) Wang, Z.; Ma, Z.; Wang, Y.; Xu, Z.; Luo, Y.; Wei, Y.; Jia, X., A novel mechanochromic and photochromic polymer film: when rhodamine joins polyurethane. *Adv. Mater.* **2015**, *27*, 6469-6474.
- (56) Takei, K.; Takahashi, T.; Ho, J. C.; Ko, H.; Gillies, A. G.; Leu, P. W.; Fearing, R. S.; Javey, A., Nanowire active-matrix circuitry for low-voltage macroscale artificial skin. *Nat. Mater.* **2010**, *9*, 821.
- (57) Someya, T.; Sekitani, T.; Iba, S.; Kato, Y.; Kawaguchi, H.; Sakurai, T., A large-area, flexible pressure sensor matrix with organic field-effect transistors for artificial skin applications. *Proc. Natl. Acad. Sci. U.S.A.* **2004**, *101*, 9966-9970.
- (58) Tee, B. C.; Wang, C.; Allen, R.; Bao, Z., An electrically and mechanically self-healing composite with pressure- and flexion-sensitive properties for electronic skin applications. *Nat. Nanotech.* **2012**, *7*, 825.
- (59) Low, Z. W. K.; Li, Z.; Owh, C.; Chee, P. L.; Ye, E.; Kai, D.; Yang, D. P.; Loh, X. J., Using Artificial Skin Devices as Skin Replacements: Insights into Superficial Treatment. *Small* **2019**, *15*, 1805453.

- (60) Park, J.; Lee, Y.; Hong, J.; Lee, Y.; Ha, M.; Jung, Y.; Lim, H.; Kim, S. Y.; Ko, H., Tactile-direction-sensitive and stretchable electronic skins based on human-skin-inspired interlocked microstructures. *ACS Nano* **2014**, *8*, 12020-12029.
- (61) Hua, Q.; Sun, J.; Liu, H.; Bao, R.; Yu, R.; Zhai, J.; Pan, C.; Wang, Z. L., Skin-inspired highly stretchable and conformable matrix networks for multifunctional sensing. *Nat. Commun.* **2018**, *9*, 244.
- (62) Son, D.; Kang, J.; Vardoulis, O.; Kim, Y.; Matsuhisa, N.; Oh, J. Y.; To, J. W.; Mun, J.; Katsumata, T.; Liu, Y., An integrated self-healable electronic skin system fabricated via dynamic reconstruction of a nanostructured conducting network. *Nat. Nanotech.* **2018**, *13*, 1057.
- (63) Lee, G. H.; Choi, T. M.; Kim, B.; Han, S. H.; Lee, J. M.; Kim, S.-H., Chameleon-inspired mechanochromic photonic films composed of non-close-packed colloidal arrays. *ACS Nano* **2017**, *11*, 11350-11357.
- (64) Lee, H.; Um, D. S.; Lee, Y.; Lim, S.; Kim, H. j.; Ko, H., Octopus-inspired smart adhesive pads for transfer printing of semiconducting nanomembranes. *Adv. Mater.* **2016**, *28*, 7457-7465.
- (65) Pikul, J.; Li, S.; Bai, H.; Hanlon, R.; Cohen, I.; Shepherd, R., Stretchable surfaces with programmable 3D texture morphing for synthetic camouflaging skins. *Science* **2017**, *358*, 210-214.
- (66) Kang, D.; Pikhitsa, P. V.; Choi, Y. W.; Lee, C.; Shin, S. S.; Piao, L.; Park, B.; Suh, K.-Y.; Kim, T.-i.; Choi, M., Ultrasensitive mechanical crack-based sensor inspired by the spider sensory system. *Nature* **2014**, *516*, 222.
- (67) Sykes, B.; Puddle, B.; Francis, M.; Smith, R., The estimation of two collagens from human dermis by interrupted gel electrophoresis. *Biochem. Biophys. Res. Commun.* **1976**, *72*, 1472-1480.
- (68) Dargahi, J.; Najarian, S., Human tactile perception as a standard for artificial tactile sensing—A review. *Int. J. Med. Rob. Comp. Assist. Surg.* **2004**, *1*, 23-35.
- (69) Delmas, P.; Hao, J.; Rodat-Despoix, L., Molecular mechanisms of mechanotransduction in mammalian sensory neurons. *Nat. Rev. Neurosci.* **2011**, *12*, 139.
- (70) Busam, K. J., *Dermatopathology E-Book: A Volume in the Series: Foundations in Diagnostic Pathology*. Elsevier Health Sciences: 2014.
- (71) Svechtarova, M. I.; Buzzacchera, I.; Toebes, B. J.; Lauko, J.; Anton, N.; Wilson, C. J., Sensor devices inspired by the five senses: A review. *Electroanalysis* **2016**, *28*, 1201-1241.

- (72) Lumpkin, E. A.; Caterina, M. J., Mechanisms of sensory transduction in the skin. *Nature* **2007**, *445*, 858.
- (73) Fernandes, A. M.; Albuquerque, P. B., Tactual perception: a review of experimental variables and procedures. *Cogn. Process.* **2012**, *13*, 285-301.
- (74) Abraira, V. E.; Ginty, D. D., The sensory neurons of touch. *Neuron* **2013**, *79*, 618-639.
- (75) Hayward, V., A brief overview of the human somatosensory system. In *Musical Haptics*, Springer, Cham: 2018; pp 29-48.
- (76) Pang, C.; Lee, G.-Y.; Kim, T.-i.; Kim, S. M.; Kim, H. N.; Ahn, S.-H.; Suh, K.-Y., A flexible and highly sensitive strain-gauge sensor using reversible interlocking of nanofibres. *Nat. Mater.* **2012**, *11*, 795.
- (77) Su, B.; Gong, S.; Ma, Z.; Yap, L. W.; Cheng, W., Mimosa-inspired design of a flexible pressure sensor with touch sensitivity. *Small* **2015**, *11*, 1886-1891.
- (78) Kim, D.-H.; Lu, N.; Ma, R.; Kim, Y.-S.; Kim, R.-H.; Wang, S.; Wu, J.; Won, S. M.; Tao, H.; Islam, A., Epidermal electronics. *Science* **2011**, *333*, 838-843.
- (79) Zhao, S.; Zhu, R., Electronic skin with multifunction sensors based on thermosensation. *Adv. Mater.* **2017**, *29*, 1606151.
- (80) Jin, M. L.; Park, S.; Lee, Y.; Lee, J. H.; Chung, J.; Kim, J. S.; Kim, J. S.; Kim, S. Y.; Jee, E.; Kim, D. W., An ultrasensitive, visco-poroelastic artificial mechanotransducer skin Inspired by piezo2 protein in mammalian merkel cells. *Adv. Mater.* **2017**, *29*, 1605973.
- (81) Jones, L. A.; Lederman, S. J., *Human hand function*. Oxford University Press: 2006.
- (82) Cartmill, M., The volar skin of primates: its frictional characteristics and their functional significance. *Am. J. Phys. Anthropol.* **1979**, *50*, 497-509.
- (83) Manfredi, L. R.; Saal, H. P.; Brown, K. J.; Zielinski, M. C.; Dammann III, J. F.; Polashock, V. S.; Bensmaia, S. J., Natural scenes in tactile texture. *J. Neurophysiol.* **2014**, *111*, 1792-1802.
- (84) Cao, Y.; Li, T.; Gu, Y.; Luo, H.; Wang, S.; Zhang, T., Fingerprint-Inspired Flexible Tactile Sensor for Accurately Discerning Surface Texture. *Small* **2018**, *14*, 1703902.
- (85) Chun, S.; Choi, I. Y.; Son, W.; Bae, G. Y.; Lee, E. J.; Kwon, H.; Jung, J.; Kim, H. S.; Kim, J. K.; Park, W., A Highly Sensitive Force Sensor with Fast Response Based on Interlocked Arrays of Indium Tin Oxide Nanosprings toward Human Tactile Perception. *Adv. Funct. Mater.* **2018**, *28*, 1804132.
- (86) Reeder, J. T.; Kang, T.; Rains, S.; Voit, W., 3D, Reconfigurable, Multimodal Electronic

Whiskers via Directed Air Assembly. *Adv. Mater.* **2018**, *30*, 1706733.

- (87) Wang, Q.; Gossweiler, G. R.; Craig, S. L.; Zhao, X., Cephalopod-inspired design of electro-mechano-chemically responsive elastomers for on-demand fluorescent patterning. *Nat. Commun.* **2014**, *5*, 4899.
- (88) Chou, H.-H.; Nguyen, A.; Chortos, A.; To, J. W.; Lu, C.; Mei, J.; Kurosawa, T.; Bae, W.-G.; Tok, J. B.-H.; Bao, Z., A chameleon-inspired stretchable electronic skin with interactive colour changing controlled by tactile sensing. *Nat. Commun.* **2015**, *6*, 8011.
- (89) Oh, J.-W.; Chung, W.-J.; Heo, K.; Jin, H.-E.; Lee, B. Y.; Wang, E.; Zueger, C.; Wong, W.; Meyer, J.; Kim, C., Biomimetic virus-based colourimetric sensors. *Nat. Commun.* **2014**, *5*, 3043.
- (90) Morin, S. A.; Shepherd, R. F.; Kwok, S. W.; Stokes, A. A.; Nemiroski, A.; Whitesides, G. M., Camouflage and display for soft machines. *Science* **2012**, *337*, 828-832.
- (91) Kim, E. H.; Cho, S. H.; Lee, J. H.; Jeong, B.; Kim, R. H.; Yu, S.; Lee, T.-W.; Shim, W.; Park, C., Organic light emitting board for dynamic interactive display. *Nat. Commun.* **2017**, *8*, 14964.
- (92) Cho, S.; Kang, S.; Pandya, A.; Shanker, R.; Khan, Z.; Lee, Y.; Park, J.; Craig, S. L.; Ko, H., Large-area cross-aligned silver nanowire electrodes for flexible, transparent, and force-sensitive mechanochromic touch screens. *ACS Nano* **2017**, *11*, 4346-4357.
- (93) Autumn, K.; Liang, Y. A.; Hsieh, S. T.; Zesch, W.; Chan, W. P.; Kenny, T. W.; Fearing, R.; Full, R. J., Adhesive force of a single gecko foot-hair. *Nature* **2000**, *405*, 681.
- (94) Pang, C.; Kim, T. i.; Bae, W. G.; Kang, D.; Kim, S. M.; Suh, K. Y., Bioinspired Reversible Interlocker Using Regularly Arrayed High Aspect-Ratio Polymer Fibers. *Adv. Mater.* **2012**, *24*, 475-479.
- (95) Yang, S. Y.; O'Carbhaill, E. D.; Sisk, G. C.; Park, K. M.; Cho, W. K.; Villiger, M.; Bouma, B. E.; Pomahac, B.; Karp, J. M., A bio-inspired swellable microneedle adhesive for mechanical interlocking with tissue. *Nat. Commun.* **2013**, *4*, 1702.
- (96) Kwak, M. K.; Jeong, H. E.; Suh, K. Y., Rational design and enhanced biocompatibility of a dry adhesive medical skin patch. *Adv. Mater.* **2011**, *23*, 3949-3953.
- (97) Pang, C.; Koo, J. H.; Nguyen, A.; Caves, J. M.; Kim, M. G.; Chortos, A.; Kim, K.; Wang, P. J.; Tok, J. B. H.; Bao, Z., Highly skin-conformal microhairy sensor for pulse signal amplification. *Adv. Mater.* **2015**, *27*, 634-640.
- (98) Drotlef, D. M.; Amjadi, M.; Yunusa, M.; Sitti, M., Bioinspired composite microfibers for skin adhesion and signal amplification of wearable sensors. *Adv. Mater.* **2017**, *29*, 1701353.

- (99) Choi, M. K.; Park, O. K.; Choi, C.; Qiao, S.; Ghaffari, R.; Kim, J.; Lee, D. J.; Kim, M.; Hyun, W.; Kim, S. J., Cephalopod-Inspired Miniaturized Suction Cups for Smart Medical Skin. *Adv. Healthcare Mater.* **2016**, *5*, 80-87.
- (100) Amjadi, M.; Turan, M.; Clementson, C. P.; Sitti, M., Parallel microcracks-based ultrasensitive and highly stretchable strain sensors. *ACS Appl. Mater. Interfaces* **2016**, *8*, 5618-5626.
- (101) Luo, C.; Jia, J.; Gong, Y.; Wang, Z.; Fu, Q.; Pan, C., Highly sensitive, durable, and multifunctional sensor inspired by a spider. *ACS Appl. Mater. Interfaces* **2017**, *9*, 19955-19962.
- (102) Liu, Q.; Chen, J.; Li, Y.; Shi, G., High-performance strain sensors with fish-scale-like graphene-sensing layers for full-range detection of human motions. *ACS Nano* **2016**, *10*, 7901-7906.
- (103) Park, J.; Kim, J.; Hong, J.; Lee, H.; Lee, Y.; Cho, S.; Kim, S.-W.; Kim, J. J.; Kim, S. Y.; Ko, H., Tailoring force sensitivity and selectivity by microstructure engineering of multidirectional electronic skins. *NPG Asia Mater.* **2018**, *10*, 163.
- (104) Darabi, M. A.; Khosrozadeh, A.; Mbeleck, R.; Liu, Y.; Chang, Q.; Jiang, J.; Cai, J.; Wang, Q.; Luo, G.; Xing, M., Skin-inspired multifunctional autonomic-intrinsic conductive self-healing hydrogels with pressure sensitivity, stretchability, and 3D printability. *Adv. Mater.* **2017**, *29*, 1700533.
- (105) Park, H.; Kim, D. S.; Hong, S. Y.; Kim, C.; Yun, J. Y.; Oh, S. Y.; Jin, S. W.; Jeong, Y. R.; Kim, G. T.; Ha, J. S., A skin-integrated transparent and stretchable strain sensor with interactive color-changing electrochromic displays. *Nanoscale* **2017**, *9*, 7631-7640.
- (106) Gong, S.; Lai, D. T.; Wang, Y.; Yap, L. W.; Si, K. J.; Shi, Q.; Jason, N. N.; Sridhar, T.; Uddin, H.; Cheng, W., Tattolike polyaniline microparticle-doped gold nanowire patches as highly durable wearable sensors. *ACS Appl. Mater. Interfaces* **2015**, *7*, 19700-19708.
- (107) Guo, Y.; Guo, Z.; Zhong, M.; Wan, P.; Zhang, W.; Zhang, L., A Flexible Wearable Pressure Sensor with Bioinspired Microcrack and Interlocking for Full-Range Human-Machine Interfacing. *Small* **2018**, *14*, 1803018.
- (108) Nichols, W. W., Clinical measurement of arterial stiffness obtained from noninvasive pressure waveforms. *Am. J. Hypertens.* **2005**, *18*, 3S-10S.
- (109) Park, Y.; Shim, J.; Jeong, S.; Yi, G. R.; Chae, H.; Bae, J. W.; Kim, S. O.; Pang, C., Microtopography-guided conductive patterns of liquid-driven graphene nanoplatelet networks for stretchable and skin-conformal sensor array. *Adv. Mater.* **2017**, *29*, 1606453.
- (110) Yang, T.; Jiang, X.; Zhong, Y.; Zhao, X.; Lin, S.; Li, J.; Li, X.; Xu, J.; Li, Z.; Zhu, H., A wearable and highly sensitive graphene strain sensor for precise home-based pulse wave monitoring. *ACS*

Sensors **2017**, *2*, 967-974.

- (111) Majumder, S.; Mondal, T.; Deen, M. J., Wearable sensors for remote health monitoring. *Sensors* **2017**, *17*, 130.
- (112) Hattori, Y.; Falgout, L.; Lee, W.; Jung, S. Y.; Poon, E.; Lee, J. W.; Na, I.; Geisler, A.; Sadhwani, D.; Zhang, Y., Multifunctional skin-like electronics for quantitative, clinical monitoring of cutaneous wound healing. *Adv. Healthcare Mater.* **2014**, *3*, 1597-1607.
- (113) Jeon, J.; Lee, H. B. R.; Bao, Z., Flexible wireless temperature sensors based on Ni microparticle-filled binary polymer composites. *Adv. Mater.* **2013**, *25*, 850-855.
- (114) Trung, T. Q.; Ramasundaram, S.; Hong, S. W.; Lee, N. E., Flexible and transparent nanocomposite of reduced graphene oxide and P (VDF-TrFE) copolymer for high thermal responsivity in a field-effect transistor. *Adv. Funct. Mater.* **2014**, *24*, 3438-3445.
- (115) Oh, J. H.; Hong, S. Y.; Park, H.; Jin, S. W.; Jeong, Y. R.; Oh, S. Y.; Yun, J.; Lee, H.; Kim, J. W.; Ha, J. S., Fabrication of high-sensitivity skin-attachable temperature sensors with bioinspired microstructured adhesive. *ACS Appl. Mater. Interfaces* **2018**, *10*, 7263-7270.
- (116) Farserotu, J.; Baborowski, J.; Decotignie, J.-D.; Dallemagne, P.; Enz, C.; Sebelius, F.; Rosen, B.; Antfolk, C.; Lundborg, G.; Björkman, A. In *Smart skin for tactile prosthetics*, 2012 6th International Symposium on Medical Information and Communication Technology (ISMICT), IEEE: 2012; pp 1-8.
- (117) Ehrsson, H. H.; Spence, C.; Passingham, R. E., That's my hand! Activity in premotor cortex reflects feeling of ownership of a limb. *Science* **2004**, *305*, 875-877.
- (118) Nghiem, B. T.; Sando, I. C.; Gillespie, R. B.; McLaughlin, B. L.; Gerling, G. J.; Langhals, N. B.; Urbanek, M. G.; Cederna, P. S., Providing a sense of touch to prosthetic hands. *Plast. Reconstr. Surg.* **2015**, *135*, 1652-1663.
- (119) Kim, H.-J.; Sim, K.; Thukral, A.; Yu, C., Rubbery electronics and sensors from intrinsically stretchable elastomeric composites of semiconductors and conductors. *Sci. Adv.* **2017**, *3*, e1701114.
- (120) Bu, T.; Xiao, T.; Yang, Z.; Liu, G.; Fu, X.; Nie, J.; Guo, T.; Pang, Y.; Zhao, J.; Xi, F., Stretchable triboelectric–photonic smart skin for tactile and gesture sensing. *Adv. Mater.* **2018**, *30*, 1800066.
- (121) Osborn, L. E.; Dragomir, A.; Betthausen, J. L.; Hunt, C. L.; Nguyen, H. H.; Kaliki, R. R.; Thakor, N. V., Prosthesis with neuromorphic multilayered e-dermis perceives touch and pain. *Sci. Robot.* **2018**, *3*, eaat3818.

- (122) Lee, Y.; Park, J.; Cho, S.; Shin, Y.-E.; Lee, H.; Kim, J.; Myoung, J.; Cho, S.; Kang, S.; Baig, C.; Ko, H., Flexible ferroelectric sensors with ultrahigh pressure sensitivity and linear response over exceptionally broad pressure range. *ACS Nano* **2018**, *12*, 4045-4054.
- (123) Bae, G. Y.; Pak, S. W.; Kim, D.; Lee, G.; Kim, D. H.; Chung, Y.; Cho, K., Linearly and highly pressure-sensitive electronic skin based on a bioinspired hierarchical structural array. *Adv. Mater.* **2016**, *28*, 5300-5306.
- (124) Hammock, M. L.; Chortos, A.; Tee, B. C. K.; Tok, J. B. H.; Bao, Z., 25th anniversary article: the evolution of electronic skin (e-skin): a brief history, design considerations, and recent progress. *Adv. Mater.* **2013**, *25*, 5997-6038.
- (125) Dahiya, R. S.; Metta, G.; Valle, M.; Sandini, G., Tactile sensing—from humans to humanoids. *IEEE Trans. Robot.* **2009**, *26*, 1-20.
- (126) Edin, B. B.; Johansson, N., Skin strain patterns provide kinaesthetic information to the human central nervous system. *J. Physiol.* **1995**, *487*, 243-251.
- (127) Birznieks, I.; Jenmalm, P.; Goodwin, A. W.; Johansson, R. S., Encoding of direction of fingertip forces by human tactile afferents. *J. Neurosci.* **2001**, *21*, 8222-8237.
- (128) Dobrzynska, J. A.; Gijs, M., Polymer-based flexible capacitive sensor for three-axial force measurements. *J. Micromech. Microeng.* **2012**, *23*, 015009.
- (129) Lee, H.-K.; Chung, J.; Chang, S.-I.; Yoon, E., Real-time measurement of the three-axis contact force distribution using a flexible capacitive polymer tactile sensor. *J. Micromech. Microeng.* **2011**, *21*, 035010.
- (130) Surapaneni, R.; Guo, Q.; Xie, Y.; Young, D.; Mastrangelo, C., A three-axis high-resolution capacitive tactile imager system based on floating comb electrodes. *J. Micromech. Microeng.* **2013**, *23*, 075004.
- (131) Sekitani, T.; Yokota, T.; Zschieschang, U.; Klauk, H.; Bauer, S.; Takeuchi, K.; Takamiya, M.; Sakurai, T.; Someya, T., Organic nonvolatile memory transistors for flexible sensor arrays. *Science* **2009**, *326*, 1516-1519.
- (132) Yamada, T.; Hayamizu, Y.; Yamamoto, Y.; Yomogida, Y.; Izadi-Najafabadi, A.; Futaba, D. N.; Hata, K., A stretchable carbon nanotube strain sensor for human-motion detection. *Nat. Nanotech.* **2011**, *6*, 296.
- (133) Cohen, D. J.; Mitra, D.; Peterson, K.; Maharbiz, M. M., A highly elastic, capacitive strain gauge based on percolating nanotube networks. *Nano Lett.* **2012**, *12*, 1821-1825.

- (134) Mannsfeld, S. C.; Tee, B. C.; Stoltenberg, R. M.; Chen, C. V. H.; Barman, S.; Muir, B. V.; Sokolov, A. N.; Reese, C.; Bao, Z., Highly sensitive flexible pressure sensors with microstructured rubber dielectric layers. *Nat. Mater.* **2010**, *9*, 859.
- (135) Lipomi, D. J.; Vosgueritchian, M.; Tee, B. C.; Hellstrom, S. L.; Lee, J. A.; Fox, C. H.; Bao, Z., Skin-like pressure and strain sensors based on transparent elastic films of carbon nanotubes. *Nat. Nanotech.* **2011**, *6*, 788.
- (136) Persano, L.; Dagdeviren, C.; Su, Y.; Zhang, Y.; Girardo, S.; Pisignano, D.; Huang, Y.; Rogers, J. A., High performance piezoelectric devices based on aligned arrays of nanofibers of poly (vinylidene fluoride-co-trifluoroethylene). *Nat. Commun.* **2013**, *4*, 1633.
- (137) Wu, W.; Wen, X.; Wang, Z. L., Taxel-addressable matrix of vertical-nanowire piezotronic transistors for active and adaptive tactile imaging. *Science* **2013**, *340*, 952-957.
- (138) Fan, F.-R.; Lin, L.; Zhu, G.; Wu, W.; Zhang, R.; Wang, Z. L., Transparent triboelectric nanogenerators and self-powered pressure sensors based on micropatterned plastic films. *Nano Lett.* **2012**, *12*, 3109-3114.
- (139) Zhang, X.-S.; Han, M.-D.; Wang, R.-X.; Zhu, F.-Y.; Li, Z.-H.; Wang, W.; Zhang, H.-X., Frequency-multiplication high-output triboelectric nanogenerator for sustainably powering biomedical microsystems. *Nano Lett.* **2013**, *13*, 1168-1172.
- (140) Yeo, W. H.; Kim, Y. S.; Lee, J.; Ameen, A.; Shi, L.; Li, M.; Wang, S.; Ma, R.; Jin, S. H.; Kang, Z., Multifunctional epidermal electronics printed directly onto the skin. *Adv. Mater.* **2013**, *25*, 2773-2778.
- (141) Son, D.; Lee, J.; Qiao, S.; Ghaffari, R.; Kim, J.; Lee, J. E.; Song, C.; Kim, S. J.; Lee, D. J.; Jun, S. W., Multifunctional wearable devices for diagnosis and therapy of movement disorders. *Nat. Nanotech.* **2014**, *9*, 397.
- (142) Xu, L.; Gutbrod, S. R.; Bonifas, A. P.; Su, Y.; Sulkin, M. S.; Lu, N.; Chung, H.-J.; Jang, K.-I.; Liu, Z.; Ying, M., 3D multifunctional integumentary membranes for spatiotemporal cardiac measurements and stimulation across the entire epicardium. *Nat. Commun.* **2014**, *5*, 3329.
- (143) Kim, D.-H.; Lu, N.; Ghaffari, R.; Kim, Y.-S.; Lee, S. P.; Xu, L.; Wu, J.; Kim, R.-H.; Song, J.; Liu, Z., Materials for multifunctional balloon catheters with capabilities in cardiac electrophysiological mapping and ablation therapy. *Nat. Mater.* **2011**, *10*, 316.
- (144) Harada, S.; Honda, W.; Arie, T.; Akita, S.; Takei, K., Fully printed, highly sensitive multifunctional artificial electronic whisker arrays integrated with strain and temperature sensors. *ACS Nano* **2014**, *8*, 3921-3927.

- (145) Hou, C.; Wang, H.; Zhang, Q.; Li, Y.; Zhu, M., Highly Conductive, Flexible, and Compressible All-Graphene Passive Electronic Skin for Sensing Human Touch. *Adv. Mater.* **2014**, *26*, 5018-5024.
- (146) Tien, N. T.; Jeon, S.; Kim, D. I.; Trung, T. Q.; Jang, M.; Hwang, B. U.; Byun, K. E.; Bae, J.; Lee, E.; Tok, J. B. H., A flexible bimodal sensor array for simultaneous sensing of pressure and temperature. *Adv. Mater.* **2014**, *26*, 796-804.
- (147) Vogt, D. M.; Park, Y.-L.; Wood, R. J., Design and characterization of a soft multi-axis force sensor using embedded microfluidic channels. *IEEE Sens. J.* **2013**, *13*, 4056-4064.
- (148) Viry, L.; Levi, A.; Totaro, M.; Mondini, A.; Mattoli, V.; Mazzolai, B.; Beccai, L., Flexible three-axial force sensor for soft and highly sensitive artificial touch. *Adv. Mater.* **2014**, *26*, 2659-2664.
- (149) Gong, S.; Schwalb, W.; Wang, Y.; Chen, Y.; Tang, Y.; Si, J.; Shirinzadeh, B.; Cheng, W., A wearable and highly sensitive pressure sensor with ultrathin gold nanowires. *Nat. Commun.* **2014**, *5*, 3132.
- (150) Cauna, N., Nature and functions of the papillary ridges of the digital skin. *Anat. Rec.* **1954**, *119*, 449-468.
- (151) Gerling, G. J.; Thomas, G. W. In *The effect of fingertip microstructures on tactile edge perception*, First Joint Eurohaptics Conference and Symposium on Haptic Interfaces for Virtual Environment and Teleoperator Systems. World Haptics Conference, IEEE: 2005; pp 63-72.
- (152) Ko, H.; Lee, J.; Schubert, B. E.; Chueh, Y.-L.; Leu, P. W.; Fearing, R. S.; Javey, A., Hybrid core-shell nanowire forests as self-selective chemical connectors. *Nano Lett.* **2009**, *9*, 2054-2058.
- (153) Ko, H.; Zhang, Z.; Chueh, Y. L.; Ho, J. C.; Lee, J.; Fearing, R. S.; Javey, A., Wet and Dry Adhesion Properties of Self-Selective Nanowire Connectors. *Adv. Funct. Mater.* **2009**, *19*, 3098-3102.
- (154) Collins, D. F.; Refshauge, K. M.; Todd, G.; Gandevia, S. C., Cutaneous receptors contribute to kinesthesia at the index finger, elbow, and knee. *J. Neurophysiol.* **2005**, *94*, 1699-1706.
- (155) Amjadi, M.; Pichitpajongkit, A.; Lee, S.; Ryu, S.; Park, I., Highly stretchable and sensitive strain sensor based on silver nanowire-elastomer nanocomposite. *ACS Nano* **2014**, *8*, 5154-5163.
- (156) Yan, C.; Wang, J.; Kang, W.; Cui, M.; Wang, X.; Foo, C. Y.; Chee, K. J.; Lee, P. S., Highly stretchable piezoresistive graphene-nanocellulose nanopaper for strain sensors. *Adv. Mater.* **2014**, *26*, 2022-2027.

- (157) Xiao, X.; Yuan, L.; Zhong, J.; Ding, T.; Liu, Y.; Cai, Z.; Rong, Y.; Han, H.; Zhou, J.; Wang, Z. L., High-strain sensors based on ZnO nanowire/polystyrene hybridized flexible films. *Adv. Mater.* **2011**, *23*, 5440-5444.
- (158) Zhou, J.; Gu, Y.; Fei, P.; Mai, W.; Gao, Y.; Yang, R.; Bao, G.; Wang, Z. L., Flexible piezotronic strain sensor. *Nano Lett.* **2008**, *8*, 3035-3040.
- (159) Cao, J.; Wang, Q.; Dai, H., Electromechanical properties of metallic, quasimetallic, and semiconducting carbon nanotubes under stretching. *Phys. Rev. Lett.* **2003**, *90*, 157601.
- (160) Li, X.; Zhang, R.; Yu, W.; Wang, K.; Wei, J.; Wu, D.; Cao, A.; Li, Z.; Cheng, Y.; Zheng, Q., Stretchable and highly sensitive graphene-on-polymer strain sensors. *Scientific reports* **2012**, *2*, 870.
- (161) Liu, C.-X.; Choi, J.-W., Strain-dependent resistance of PDMS and carbon nanotubes composite microstructures. *IEEE transactions on Nanotechnology* **2010**, *9*, 590-595.
- (162) Yang, Y.; Guo, W.; Qi, J.; Zhang, Y., Flexible piezoresistive strain sensor based on single Sb-doped ZnO nanobelts. *Appl. Phys. Lett.* **2010**, *97*, 223107.
- (163) Takei, K.; Yu, Z.; Zheng, M.; Ota, H.; Takahashi, T.; Javey, A., Highly sensitive electronic whiskers based on patterned carbon nanotube and silver nanoparticle composite films. *Proc. Natl. Acad. Sci. U.S.A.* **2014**, *111*, 1703-1707.
- (164) Lee, H.-K.; Chung, J.; Chang, S.-I.; Yoon, E., Normal and shear force measurement using a flexible polymer tactile sensor with embedded multiple capacitors. *Journal of Microelectromechanical Systems* **2008**, *17*, 934-942.
- (165) Teshigawara, S.; Shimizu, S.; Tadakuma, K.; Aiguo, M.; Shimojo, M.; Ishikawa, M. In *High sensitivity slip sensor using pressure conductive rubber*, SENSORS, 2009 IEEE, IEEE: 2009; pp 988-991.
- (166) Vatani, M.; Engeberg, E. D.; Choi, J.-W., Force and slip detection with direct-write compliant tactile sensors using multi-walled carbon nanotube/polymer composites. *Sensors and Actuators A: physical* **2013**, *195*, 90-97.
- (167) Gleeson, B. T.; Horschel, S. K.; Provancher, W. R., Design of a fingertip-mounted tactile display with tangential skin displacement feedback. *IEEE Transactions on Haptics* **2010**, *3*, 297-301.
- (168) Wang, X.; Gu, Y.; Xiong, Z.; Cui, Z.; Zhang, T., Silk-molded flexible, ultrasensitive, and highly stable electronic skin for monitoring human physiological signals. *Adv. Mater.* **2014**, *26*, 1336-1342.

- (169) Pan, L.; Chortos, A.; Yu, G.; Wang, Y.; Isaacson, S.; Allen, R.; Shi, Y.; Dauskardt, R.; Bao, Z., An ultra-sensitive resistive pressure sensor based on hollow-sphere microstructure induced elasticity in conducting polymer film. *Nat. Commun.* **2014**, *5*, 3002.
- (170) Vallbo, A. B.; Johansson, R. S., Properties of cutaneous mechanoreceptors in the human hand related to touch sensation. *Hum. Neurobiol.* **1984**, *3*, 3-14.
- (171) Wang, X.; Que, M.; Chen, M.; Han, X.; Li, X.; Pan, C.; Wang, Z. L., Full Dynamic-Range Pressure Sensor Matrix Based on Optical and Electrical Dual-Mode Sensing. *Adv. Mater.* **2017**, *29*, 1605817.
- (172) Jung, S.; Kim, J. H.; Kim, J.; Choi, S.; Lee, J.; Park, I.; Hyeon, T.; Kim, D. H., Reverse-micelle-induced porous pressure-sensitive rubber for wearable human-machine interfaces. *Adv. Mater.* **2014**, *26*, 4825-4830.
- (173) Maeno, T.; Kobayashi, K.; Yamazaki, N., Relationship between the structure of human finger tissue and the location of tactile receptors. *JSME Int. J., Ser. C* **1998**, *41*, 94-100.
- (174) William, S.; Hummers, J.; Offeman, R. E., Preparation of graphitic oxide. *J. Am. Chem. Soc.* **1958**, *80*, 1339-1339.
- (175) Kang, D.; Shin, Y. E.; Jo, H. J.; Ko, H.; Shin, H. S., Mechanical Properties of Poly (dopamine)-Coated Graphene Oxide and Poly (vinyl alcohol) Composite Fibers Coated with Reduced Graphene Oxide and Their Use for Piezoresistive Sensing. *Part. Part. Syst. Char.* **2017**, *34*, 1600382.
- (176) Martins, P.; Lopes, A.; Lanceros-Mendez, S., Electroactive phases of poly (vinylidene fluoride): Determination, processing and applications. *Prog. Polym. Sci.* **2014**, *39*, 683-706.
- (177) Zhang, X.-J.; Wang, G.-S.; Cao, W.-Q.; Wei, Y.-Z.; Cao, M.-S.; Guo, L., Fabrication of multi-functional PVDF/RGO composites via a simple thermal reduction process and their enhanced electromagnetic wave absorption and dielectric properties. *RSC Adv.* **2014**, *4*, 19594-19601.
- (178) Choong, C. L.; Shim, M. B.; Lee, B. S.; Jeon, S.; Ko, D. S.; Kang, T. H.; Bae, J.; Lee, S. H.; Byun, K. E.; Im, J., Highly stretchable resistive pressure sensors using a conductive elastomeric composite on a micropylramid array. *Adv. Mater.* **2014**, *26*, 3451-3458.
- (179) Kim, J.; Lee, M.; Shim, H. J.; Ghaffari, R.; Cho, H. R.; Son, D.; Jung, Y. H.; Soh, M.; Choi, C.; Jung, S., Stretchable silicon nanoribbon electronics for skin prosthesis. *Nat. Commun.* **2014**, *5*, 5747.
- (180) Park, H.; Jeong, Y. R.; Yun, J.; Hong, S. Y.; Jin, S.; Lee, S.-J.; Zi, G.; Ha, J. S., Stretchable array of highly sensitive pressure sensors consisting of polyaniline nanofibers and Au-coated

polydimethylsiloxane micropillars. *ACS Nano* **2015**, *9*, 9974-9985.

- (181) Kim, S. Y.; Park, S.; Park, H. W.; Park, D. H.; Jeong, Y.; Kim, D. H., Highly Sensitive and Multimodal All-Carbon Skin Sensors Capable of Simultaneously Detecting Tactile and Biological Stimuli. *Adv. Mater.* **2015**, *27*, 4178-4185.
- (182) Luo, N.; Dai, W.; Li, C.; Zhou, Z.; Lu, L.; Poon, C. C.; Chen, S. C.; Zhang, Y.; Zhao, N., Flexible piezoresistive sensor patch enabling ultralow power cuffless blood pressure measurement. *Adv. Funct. Mater.* **2016**, *26*, 1178-1187.
- (183) Luo, N.; Huang, Y.; Liu, J.; Chen, S. C.; Wong, C. P.; Zhao, N., Hollow-structured graphene-silicone-composite-based piezoresistive sensors: Decoupled property tuning and bending reliability. *Adv. Mater.* **2017**, *29*, 1702675.
- (184) Pang, Y.; Zhang, K.; Yang, Z.; Jiang, S.; Ju, Z.; Li, Y.; Wang, X.; Wang, D.; Jian, M.; Zhang, Y., Epidermis microstructure inspired graphene pressure sensor with random distributed spinosum for high sensitivity and large linearity. *ACS Nano* **2018**, *12*, 2346-2354.
- (185) Chortos, A.; Bao, Z., Skin-inspired electronic devices. *Mater. Today* **2014**, *17*, 321-331.
- (186) Yu, H.; Huang, T.; Lu, M.; Mao, M.; Zhang, Q.; Wang, H., Enhanced power output of an electrospun PVDF/MWCNTs-based nanogenerator by tuning its conductivity. *Nanotechnology* **2013**, *24*, 405401.
- (187) Cretikos, M. A.; Bellomo, R.; Hillman, K.; Chen, J.; Finfer, S.; Flabouris, A., Respiratory rate: the neglected vital sign. *Med. J. Aust.* **2008**, *188*, 657-659.
- (188) Lovett, P. B.; Buchwald, J. M.; Stürmann, K.; Bijur, P., The vexatious vital: neither clinical measurements by nurses nor an electronic monitor provides accurate measurements of respiratory rate in triage. *Ann. Emerg. Med.* **2005**, *45*, 68-76.
- (189) Blacher, J.; Asmar, R.; Djane, S.; London, G. M.; Safar, M. E., Aortic pulse wave velocity as a marker of cardiovascular risk in hypertensive patients. *Hypertension* **1999**, *33*, 1111-1117.
- (190) Spodick, D. H., Survey of selected cardiologists for an operational definition of normal sinus heart rate. *Am. J. Cardiol.* **1993**, *72*, 487-488.
- (191) Razak, A.; Hadi, A.; Zayegh, A.; Begg, R. K.; Wahab, Y., Foot plantar pressure measurement system: A review. *Sensors* **2012**, *12*, 9884-9912.
- (192) Bacarin, T. A.; Sacco, I. C.; Hennig, E. M., Plantar pressure distribution patterns during gait in diabetic neuropathy patients with a history of foot ulcers. *Clinics* **2009**, *64*, 113-120.
- (193) Kimmeskamp, S.; Hennig, E. M., Heel to toe motion characteristics in Parkinson patients

- during free walking. *Clin. Biomech.* **2001**, *16*, 806-812.
- (194) An, J.; Le, T.-S. D.; Huang, Y.; Zhan, Z.; Li, Y.; Zheng, L.; Huang, W.; Sun, G.; Kim, Y.-J., All-graphene-based highly flexible noncontact electronic skin. *ACS Appl. Mater. Interfaces* **2017**, *9*, 44593-44601.
- (195) Trung, T. Q.; Ramasundaram, S.; Hwang, B. U.; Lee, N. E., An all-elastomeric transparent and stretchable temperature sensor for body-attachable wearable electronics. *Adv. Mater.* **2016**, *28*, 502-509.
- (196) Chen, T.; Shi, Q.; Zhu, M.; He, T.; Sun, L.; Yang, L.; Lee, C., Triboelectric self-powered wearable flexible patch as 3D motion control interface for robotic manipulator. *ACS Nano* **2018**, *12*, 11561-11571.
- (197) Garcia-Cordero, E.; Bellando, F.; Zhang, J.; Wildhaber, F.; Longo, J.; Guerin, H.; Ionescu, A. M., Three-Dimensional Integrated Ultra-Low-Volume Passive Microfluidics with Ion-Sensitive Field-Effect Transistors for Multiparameter Wearable Sweat Analyzers. *ACS Nano* **2018**, *12*, 12646-12656.
- (198) Reeder, J.; Kaltenbrunner, M.; Ware, T.; Arreaga-Salas, D.; Avendano-Bolivar, A.; Yokota, T.; Inoue, Y.; Sekino, M.; Voit, W.; Sekitani, T., Mechanically adaptive organic transistors for implantable electronics. *Adv. Mater.* **2014**, *26*, 4967-4973.
- (199) Kaltenbrunner, M.; Sekitani, T.; Reeder, J.; Yokota, T.; Kuribara, K.; Tokuhara, T.; Drack, M.; Schwödiauer, R.; Graz, I.; Bauer-Gogonea, S., An ultra-lightweight design for imperceptible plastic electronics. *Nature* **2013**, *499*, 458.
- (200) Hu, Y.; Liu, X.; Tian, L.; Zhao, T.; Wang, H.; Liang, X.; Zhou, F.; Zhu, P.; Li, G.; Sun, R., Multidimensional Ternary Hybrids with Synergistically Enhanced Electrical Performance for Conductive Nanocomposites and Prosthetic Electronic Skin. *ACS Appl. Mater. Interfaces* **2018**, *10*, 38493-38505.
- (201) Li, X.; Chen, M.; Yu, R.; Zhang, T.; Song, D.; Liang, R.; Zhang, Q.; Cheng, S.; Dong, L.; Pan, A., Enhancing Light Emission of ZnO-Nanofilm/Si-Micropillar Heterostructure Arrays by Piezo-Phototronic Effect. *Adv. Mater.* **2015**, *27*, 4447-4453.
- (202) Koo, J. H.; Jeong, S.; Shim, H. J.; Son, D.; Kim, J.; Kim, D. C.; Choi, S.; Hong, J.-I.; Kim, D.-H., Wearable electrocardiogram monitor using carbon nanotube electronics and color-tunable organic light-emitting diodes. *ACS Nano* **2017**, *11*, 10032-10041.
- (203) Rus, D.; Tolley, M. T., Design, fabrication and control of soft robots. *Nature* **2015**, *521*, 467-475.

- (204) Fu, X.; Dong, H.; Zhen, Y.; Hu, W., Solution-Processed Large-Area Nanocrystal Arrays of Metal–Organic Frameworks as Wearable, Ultrasensitive, Electronic Skin for Health Monitoring. *Small* **2015**, *11*, 3351-3356.
- (205) Wang, X.; Song, W.-Z.; You, M.-H.; Zhang, J.; Yu, M.; Fan, Z.; Ramakrishna, S.; Long, Y.-Z., Bionic single-electrode electronic skin unit based on piezoelectric nanogenerator. *ACS Nano* **2018**, *12*, 8588-8596.
- (206) Wu, Z.; Ding, W.; Dai, Y.; Dong, K.; Wu, C.; Zhang, L.; Lin, Z.; Cheng, J.; Wang, Z. L., Self-Powered Multifunctional Motion Sensor Enabled by Magnetic-Regulated Triboelectric Nanogenerator. *ACS Nano* **2018**, *12*, 5726-5733.
- (207) Lin, Y.; Chen, J.; Tavakoli, M. M.; Gao, Y.; Zhu, Y.; Zhang, D.; Kam, M.; He, Z.; Fan, Z., Printable Fabrication of a Fully Integrated and Self-Powered Sensor System on Plastic Substrates. *Adv. Mater.* **2019**, *31*, 1804285.
- (208) Wang, X.; Dong, L.; Zhang, H.; Yu, R.; Pan, C.; Wang, Z. L., Recent progress in electronic skin. *Adv. Sci.* **2015**, *2*, 1500169.
- (209) Pang, Y.; Tian, H.; Tao, L.; Li, Y.; Wang, X.; Deng, N.; Yang, Y.; Ren, T.-L., Flexible, highly sensitive, and wearable pressure and strain sensors with graphene porous network structure. *ACS Appl. Mater. Interfaces* **2016**, *8*, 26458-26462.
- (210) Lee, D.; Lee, H.; Jeong, Y.; Ahn, Y.; Nam, G.; Lee, Y., Highly Sensitive, Transparent, and Durable Pressure Sensors Based on Sea-Urchin Shaped Metal Nanoparticles. *Adv. Mater.* **2016**, *28*, 9364-9369.
- (211) Jang, K.-I.; Han, S. Y.; Xu, S.; Mathewson, K. E.; Zhang, Y.; Jeong, J.-W.; Kim, G.-T.; Webb, R. C.; Lee, J. W.; Dawidczyk, T. J., Rugged and breathable forms of stretchable electronics with adherent composite substrates for transcutaneous monitoring. *Nat. Commun.* **2014**, *5*, 4779.
- (212) Shuai, X.; Zhu, P.; Zeng, W.; Hu, Y.; Liang, X.; Zhang, Y.; Sun, R.; Wong, C.-p., Highly sensitive flexible pressure sensor based on silver nanowires-embedded polydimethylsiloxane electrode with microarray structure. *ACS Appl. Mater. Interfaces* **2017**, *9*, 26314-26324.
- (213) Yin, F.; Yang, J.; Peng, H.; Yuan, W., Flexible and highly sensitive artificial electronic skin based on graphene/polyamide interlocking fabric. *J. Mater. Chem. C* **2018**, *6*, 6840-6846.
- (214) Yang, C.; Li, L.; Zhao, J.; Wang, J.; Xie, J.; Cao, Y.; Xue, M.; Lu, C., Highly sensitive wearable pressure sensors based on three-scale nested wrinkling microstructures of polypyrrole films. *ACS Appl. Mater. Interfaces* **2018**, *10*, 25811-25818.
- (215) Li, H.; Wu, K.; Xu, Z.; Wang, Z.; Meng, Y.; Li, L., Ultrahigh-Sensitivity Piezoresistive Pressure

- Sensors for Detection of Tiny Pressure. *ACS Appl. Mater. Interfaces* **2018**, *10*, 20826-20834.
- (216) Liu, W.; Liu, N.; Yue, Y.; Rao, J.; Luo, C.; Zhang, H.; Yang, C.; Su, J.; Liu, Z.; Gao, Y., A flexible and highly sensitive pressure sensor based on elastic carbon foam. *J. Mater. Chem. C* **2018**, *6*, 1451-1458.
- (217) Pu, J.-H.; Zha, X.-J.; Tang, L.-S.; Bai, L.; Bao, R.-Y.; Liu, Z.-Y.; Yang, M.-B.; Yang, W., Human skin-inspired electronic sensor skin with electromagnetic interference shielding for the sensation and protection of wearable electronics. *ACS Appl. Mater. Interfaces* **2018**, *10*, 40880-40889.
- (218) Kim, S.; Sanyoto, B.; Park, W. T.; Kim, S.; Mandal, S.; Lim, J. C.; Noh, Y. Y.; Kim, J. H., Purification of PEDOT: PSS by Ultrafiltration for Highly Conductive Transparent Electrode of All-Printed Organic Devices. *Adv. Mater.* **2016**, *28*, 10149-10154.
- (219) Wei, Q.; Mukaida, M.; Naitoh, Y.; Ishida, T., Morphological change and mobility enhancement in PEDOT: PSS by adding co-solvents. *Adv. Mater.* **2013**, *25*, 2831-2836.
- (220) Shi, J.; Wang, L.; Dai, Z.; Zhao, L.; Du, M.; Li, H.; Fang, Y., Multiscale hierarchical design of a flexible piezoresistive pressure sensor with high sensitivity and wide linearity range. *Small* **2018**, *14*, 1800819.
- (221) Gillespie, P. G.; Walker, R. G., Molecular basis of mechanosensory transduction. *Nature* **2001**, *413*, 194.
- (222) Hickenboth, C. R.; Moore, J. S.; White, S. R.; Sottos, N. R.; Baudry, J.; Wilson, S. R., Biasing reaction pathways with mechanical force. *Nature* **2007**, *446*, 423.
- (223) Caruso, M. M.; Davis, D. A.; Shen, Q.; Odom, S. A.; Sottos, N. R.; White, S. R.; Moore, J. S., Mechanically-induced chemical changes in polymeric materials. *Chem. Rev.* **2009**, *109*, 5755-5798.
- (224) Li, J.; Nagamani, C.; Moore, J. S., Polymer mechanochemistry: from destructive to productive. *Acc. Chem. Res.* **2015**, *48*, 2181-2190.
- (225) Chen, Y.; Spiering, A.; Karthikeyan, S.; Peters, G. W.; Meijer, E.; Sijbesma, R. P., Mechanically induced chemiluminescence from polymers incorporating a 1, 2-dioxetane unit in the main chain. *Nat. Chem.* **2012**, *4*, 559.
- (226) Piermattei, A.; Karthikeyan, S.; Sijbesma, R. P., Activating catalysts with mechanical force. *Nat. Chem.* **2009**, *1*, 133.
- (227) Diesendruck, C. E.; Steinberg, B. D.; Sugai, N.; Silberstein, M. N.; Sottos, N. R.; White, S. R.;

- Braun, P. V.; Moore, J. S., Proton-coupled mechanochemical transduction: a mechanogenerated acid. *J. Am. Chem. Soc.* **2012**, *134*, 12446-12449.
- (228) Lenhardt, J. M.; Ong, M. T.; Choe, R.; Evenhuis, C. R.; Martinez, T. J.; Craig, S. L., Trapping a diradical transition state by mechanochemical polymer extension. *Science* **2010**, *329*, 1057-1060.
- (229) Larsen, M. B.; Boydston, A. J., Successive mechanochemical activation and small molecule release in an elastomeric material. *J. Am. Chem. Soc.* **2014**, *136*, 1276-1279.
- (230) Hong, G.; Zhang, H.; Lin, Y.; Chen, Y.; Xu, Y.; Weng, W.; Xia, H., Mechanoresponsive healable metallosupramolecular polymers. *Macromolecules* **2013**, *46*, 8649-8656.
- (231) Lee, C. K.; Davis, D. A.; White, S. R.; Moore, J. S.; Sottos, N. R.; Braun, P. V., Force-induced redistribution of a chemical equilibrium. *J. Am. Chem. Soc.* **2010**, *132*, 16107-16111.
- (232) Rifaie-Graham, O.; Apebende, E. A.; Bast, L. K.; Bruns, N., Self-reporting fiber-reinforced composites that mimic the ability of biological materials to sense and report damage. *Adv. Mater.* **2018**, *30*, 1705483.
- (233) Li, Z. a.; Toivola, R.; Ding, F.; Yang, J.; Lai, P. N.; Howie, T.; Georgeson, G.; Jang, S. H.; Li, X.; Flinn, B. D., Highly sensitive built-in strain sensors for polymer composites: Fluorescence turn-on response through mechanochemical activation. *Adv. Mater.* **2016**, *28*, 6592-6597.
- (234) Kryger, M. J.; Munaretto, A. M.; Moore, J. S., Structure–mechanochemical activity relationships for cyclobutane mechanophores. *J. Am. Chem. Soc.* **2011**, *133*, 18992-18998.
- (235) Beiermann, B. A.; Kramer, S. L.; May, P. A.; Moore, J. S.; White, S. R.; Sottos, N. R., The effect of polymer chain alignment and relaxation on force-induced chemical reactions in an elastomer. *Adv. Funct. Mater.* **2014**, *24*, 1529-1537.
- (236) Beiermann, B. A.; Davis, D. A.; Kramer, S. L.; Moore, J. S.; Sottos, N. R.; White, S. R., Environmental effects on mechanochemical activation of spiropyran in linear PMMA. *J. Mater. Chem.* **2011**, *21*, 8443-8447.
- (237) Chen, Y.; Zhang, H.; Fang, X.; Lin, Y.; Xu, Y.; Weng, W., Mechanical activation of mechanophore enhanced by strong hydrogen bonding interactions. *ACS Macro Lett.* **2014**, *3*, 141-145.
- (238) Jiang, S.; Zhang, L.; Xie, T.; Lin, Y.; Zhang, H.; Xu, Y.; Weng, W.; Dai, L., Mechanoresponsive PS-PnBA-PS triblock copolymers via covalently embedding mechanophore. *ACS Macro Lett.* **2013**, *2*, 705-709.

- (239) Yan, H.; Yang, F.; Pan, D.; Lin, Y.; Hohman, J. N.; Solis-Ibarra, D.; Li, F. H.; Dahl, J. E.; Carlson, R. M.; Tkachenko, B. A., Sterically controlled mechanochemistry under hydrostatic pressure. *Nature* **2018**, *554*, 505.
- (240) Zhang, H.; Chen, Y.; Lin, Y.; Fang, X.; Xu, Y.; Ruan, Y.; Weng, W., Spiropyran as a mechanochromic probe in dual cross-linked elastomers. *Macromolecules* **2014**, *47*, 6783-6790.
- (241) Filonenko, G. A.; Lugger, J. A.; Liu, C.; van Heeswijk, E. P.; Hendrix, M. M.; Weber, M.; Müller, C.; Hensen, E. J.; Sijbesma, R. P.; Pidko, E. A., Tracking Local Mechanical Impact in Heterogeneous Polymers with Direct Optical Imaging. *Angew. Chem.* **2018**, *130*, 16623-16628.
- (242) Sagara, Y.; Karman, M.; Verde-Sesto, E.; Matsuo, K.; Kim, Y.; Tamaoki, N.; Weder, C., Rotaxanes as mechanochromic fluorescent force transducers in polymers. *J. Am. Chem. Soc.* **2018**, *140*, 1584-1587.
- (243) Berto, F.; Lazzarin, P., Recent developments in brittle and quasi-brittle failure assessment of engineering materials by means of local approaches. *Mater. Sci. Eng. R Rep.* **2014**, *75*, 1-48.
- (244) Gao, H.; Ji, B.; Jäger, I. L.; Arzt, E.; Fratzl, P., Materials become insensitive to flaws at nanoscale: lessons from nature. *Proc. Natl. Acad. Sci. U.S.A.* **2003**, *100*, 5597-5600.
- (245) Lakes, R., Materials with structural hierarchy. *Nature* **1993**, *361*, 511.
- (246) Lin, Y.; Barbee, M. H.; Chang, C.-C.; Craig, S. L., Regiochemical Effects on Mechanophore Activation in Bulk Materials. *J. Am. Chem. Soc.* **2018**, *140*, 15969-15975.
- (247) Barbee, M. H.; Mondal, K.; Deng, J. Z.; Bharambe, V.; Neumann, T. V.; Adams, J. J.; Boechler, N.; Dickey, M. D.; Craig, S. L., Mechanochromic stretchable electronics. *ACS Appl. Mater. Interfaces* **2018**, *10*, 29918-29924.
- (248) Chun, J.; Kim, J. W.; Jung, W.-s.; Kang, C.-Y.; Kim, S.-W.; Wang, Z. L.; Baik, J. M., Mesoporous pores impregnated with Au nanoparticles as effective dielectrics for enhancing triboelectric nanogenerator performance in harsh environments. *Energy & Environmental Science* **2015**, *8*, 3006-3012.
- (249) Kazem, N.; Bartlett, M. D.; Majidi, C., Extreme toughening of soft materials with liquid metal. *Adv. Mater.* **2018**, *30*, 1706594.
- (250) Rice, R., Limitations of pore-stress concentrations on the mechanical properties of porous materials. *Journal of Materials Science* **1997**, *32*, 4731-4736.
- (251) Sen, D.; Buehler, M. J., Structural hierarchies define toughness and defect-tolerance despite simple and mechanically inferior brittle building blocks. *Scientific reports* **2011**, *1*, 35.

- (252) Li, M.; Zhang, Q.; Zhu, S., Photo-inactive divinyl spiropyran mechanophore cross-linker for real-time stress sensing. *Polymer* **2016**, *99*, 521-528.
- (253) Kang, S.; Lee, J.; Lee, S.; Kim, S.; Kim, J. K.; Algadi, H.; Al-Sayari, S.; Kim, D. E.; Kim, D.; Lee, T., Highly sensitive pressure sensor based on bioinspired porous structure for real-time tactile sensing. *Advanced Electronic Materials* **2016**, *2*, 1600356.
- (254) Klajn, R., Spiropyran-based dynamic materials. *Chem. Soc. Rev.* **2014**, *43*, 148-184.
- (255) Dübner, M.; Spencer, N. D.; Padeste, C., Light-responsive polymer surfaces via postpolymerization modification of grafted polymer-brush structures. *Langmuir* **2014**, *30*, 14971-14981.
- (256) Lee, C. K.; Beiermann, B. A.; Silberstein, M. N.; Wang, J.; Moore, J. S.; Sottos, N. R.; Braun, P. V., Exploiting force sensitive spiropyran as molecular level probes. *Macromolecules* **2013**, *46*, 3746-3752.
- (257) Kang, S.; Cho, S.; Shanker, R.; Lee, H.; Park, J.; Um, D.-S.; Lee, Y.; Ko, H., Transparent and conductive nanomembranes with orthogonal silver nanowire arrays for skin-attachable loudspeakers and microphones. *Sci. Adv.* **2018**, *4*, eaas8772.
- (258) Chen, S. W.; Cao, X.; Wang, N.; Ma, L.; Zhu, H. R.; Willander, M.; Jie, Y.; Wang, Z. L., An ultrathin flexible single-electrode triboelectric-nanogenerator for mechanical energy harvesting and instantaneous force sensing. *Adv. Energy Mater.* **2017**, *7*, 1601255.
- (259) Kosuge, T.; Imato, K.; Goseki, R.; Otsuka, H., Polymer-inorganic composites with dynamic covalent mechanochromophore. *Macromolecules* **2016**, *49*, 5903-5911.
- (260) Göstl, R.; Sijbesma, R., π -extended anthracenes as sensitive probes for mechanical stress. *Chemical science* **2016**, *7*, 370-375.
- (261) Zhang, H.; Gao, F.; Cao, X.; Li, Y.; Xu, Y.; Weng, W.; Boulatov, R., Mechanochromism and mechanical-force-triggered cross-linking from a single reactive moiety incorporated into polymer chains. *Angew. Chem. Int. Ed.* **2016**, *55*, 3040-3044.
- (262) Robb, M. J.; Kim, T. A.; Halmes, A. J.; White, S. R.; Sottos, N. R.; Moore, J. S., Regioisomer-specific mechanochromism of naphthopyran in polymeric materials. *J. Am. Chem. Soc.* **2016**, *138*, 12328-12331.
- (263) Khan, Y.; Ostfeld, A. E.; Lochner, C. M.; Pierre, A.; Arias, A. C., Monitoring of vital signs with flexible and wearable medical devices. *Adv. Mater.* **2016**, *28*, 4373-4395.
- (264) Liu, H.; Sun, W.; Xu, S., An extremely simple thermocouple made of a single layer of metal.

Adv. Mater. **2012**, *24*, 3275-3279.

- (265) Yokota, T.; Inoue, Y.; Terakawa, Y.; Reeder, J.; Kaltenbrunner, M.; Ware, T.; Yang, K.; Mabuchi, K.; Murakawa, T.; Sekino, M., Ultraflexible, large-area, physiological temperature sensors for multipoint measurements. *Proc. Natl. Acad. Sci. U.S.A.* **2015**, *112*, 14533-14538.
- (266) Zhang, F.; Zang, Y.; Huang, D.; Di, C.-a.; Zhu, D., Flexible and self-powered temperature–pressure dual-parameter sensors using microstructure–frame-supported organic thermoelectric materials. *Nat. Commun.* **2015**, *6*, 8356.
- (267) Someya, T.; Kato, Y.; Sekitani, T.; Iba, S.; Noguchi, Y.; Murase, Y.; Kawaguchi, H.; Sakurai, T., Conformable, flexible, large-area networks of pressure and thermal sensors with organic transistor active matrixes. *Proc. Natl. Acad. Sci. U.S.A.* **2005**, *102*, 12321-12325.
- (268) Li, Q.; Zhang, L. N.; Tao, X. M.; Ding, X., Review of flexible temperature sensing networks for wearable physiological monitoring. *Adv. Healthcare Mater.* **2017**, *6*, 1601371.
- (269) Kim, D. H.; Wang, S.; Keum, H.; Ghaffari, R.; Kim, Y. S.; Tao, H.; Panilaitis, B.; Li, M.; Kang, Z.; Omenetto, F., Thin, flexible sensors and actuators as ‘instrumented’ surgical sutures for targeted wound monitoring and therapy. *Small* **2012**, *8*, 3263-3268.
- (270) Lee, C.-Y.; Lin, C.-H.; Lo, Y.-M., Fabrication of a flexible micro temperature sensor for micro reformer applications. *Sensors* **2011**, *11*, 3706-3716.
- (271) Hong, S. Y.; Lee, Y. H.; Park, H.; Jin, S. W.; Jeong, Y. R.; Yun, J.; You, I.; Zi, G.; Ha, J. S., Stretchable active matrix temperature sensor array of polyaniline nanofibers for electronic skin. *Adv. Mater.* **2016**, *28*, 930-935.
- (272) Shin, Y.-E.; Lee, J.-E.; Park, Y.; Hwang, S.-H.; Chae, H. G.; Ko, H., Sewing machine stitching of polyvinylidene fluoride fibers: programmable textile patterns for wearable triboelectric sensors. *J. Mater. Chem. A* **2018**, *6*, 22879-22888.
- (273) Barton, A. M., *Handbook of Polymer-Liquid Interaction Parameters and Solubility Parameters*. Routledge: 2018.
- (274) Bottino, A.; Capannelli, G.; Munari, S.; Turturro, A., Solubility parameters of poly (vinylidene fluoride). *J. Polym. Sci., Part B: Polym. Phys.* **1988**, *26*, 785-794.
- (275) Zoller, P.; Fakhreddine, Y. A., Pressure—volume—temperature studies of semi-crystalline polymers. *Thermochim. Acta* **1994**, *238*, 397-415.
- (276) Chen, Z.; Hsu, P.-C.; Lopez, J.; Li, Y.; To, J. W.; Liu, N.; Wang, C.; Andrews, S. C.; Liu, J.; Cui, Y., Fast and reversible thermoresponsive polymer switching materials for safer batteries. *Nat.*

Energy **2016**, *1*, 15009.

- (277) Honda, W.; Harada, S.; Ishida, S.; Arie, T.; Akita, S.; Takei, K., High-Performance, Mechanically Flexible, and Vertically Integrated 3D Carbon Nanotube and InGaZnO Complementary Circuits with a Temperature Sensor. *Adv. Mater.* **2015**, *27*, 4674-4680.
- (278) Yan, C.; Wang, J.; Lee, P. S., Stretchable graphene thermistor with tunable thermal index. *ACS Nano* **2015**, *9*, 2130-2137.
- (279) Biver, T.; Criscitiello, F.; Di Francesco, F.; Minichino, M.; Swager, T.; Pucci, A., MWCNT/perylene bisimide water dispersions for miniaturized temperature sensors. *RSC Adv.* **2015**, *5*, 65023-65029.
- (280) Ren, X.; Pei, K.; Peng, B.; Zhang, Z.; Wang, Z.; Wang, X.; Chan, P. K., A low-operating-power and flexible active-matrix organic-transistor temperature-sensor array. *Adv. Mater.* **2016**, *28*, 4832-4838.
- (281) Wu, J.; Han, S.; Yang, T.; Li, Z.; Wu, Z.; Gui, X.; Tao, K.; Miao, J.; Norford, L. K.; Liu, C., Highly stretchable and transparent thermistor based on self-healing double network hydrogel. *ACS Appl. Mater. Interfaces* **2018**, *10*, 19097-19105.
- (282) Bae, G. Y.; Han, J. T.; Lee, G.; Lee, S.; Kim, S. W.; Park, S.; Kwon, J.; Jung, S.; Cho, K., Pressure/temperature sensing bimodal electronic skin with stimulus discriminability and linear sensitivity. *Adv. Mater.* **2018**, *30*, 1803388.
- (283) Hobbs, J. K.; Farrance, O. E.; Kailas, L., How atomic force microscopy has contributed to our understanding of polymer crystallization. *Polymer* **2009**, *50*, 4281-4292.
- (284) Elashmawi, I.; Gaabour, L., Raman, morphology and electrical behavior of nanocomposites based on PEO/PVDF with multi-walled carbon nanotubes. *Results Phys.* **2015**, *5*, 105-110.
- (285) Matthäus, C.; Chernenko, T.; Quintero, L.; Miljković, M.; Milane, L.; Kale, A.; Amiji, M.; Torchilin, V.; Diem, M., Raman micro-spectral imaging of cells and intracellular drug delivery using nanocarrier systems. In *Confocal Raman Microscopy*, Springer: 2010; pp 137-163.
- (286) Jurado, J. F.; Vargas Hernandez, C.; VARGAS, R. A., Preparation of zinc oxide and polyethylene oxide composite membranes and their phase relationship. *Dyna* **2012**, *79*, 79-85.
- (287) Eda, G.; Fanchini, G.; Chhowalla, M., Large-area ultrathin films of reduced graphene oxide as a transparent and flexible electronic material. *Nat. Nanotech.* **2008**, *3*, 270.
- (288) Simoes, R.; Job, A.; Chinaglia, D. L.; Zucolotto, V.; Camargo-Filho, J.; Alves, N.; Giacometti, J. A.; Oliveira Jr, O.; Constantino, C., Structural characterization of blends containing both

- PVDF and natural rubber latex. *Journal of Raman Spectroscopy: An International Journal for Original Work in all Aspects of Raman Spectroscopy, Including Higher Order Processes, and also Brillouin and Rayleigh Scattering* **2005**, *36*, 1118-1124.
- (289) Gracheva, E. O.; Ingolia, N. T.; Kelly, Y. M.; Cordero-Morales, J. F.; Hollopeter, G.; Chesler, A. T.; Sánchez, E. E.; Perez, J. C.; Weissman, J. S.; Julius, D., Molecular basis of infrared detection by snakes. *Nature* **2010**, *464*, 1006.
- (290) Zhou, J.; Hsieh, Y.-L., Conductive Polymer Protonated Nanocellulose Aerogels for Tunable and Linearly Responsive Strain Sensors. *ACS Appl. Mater. Interfaces* **2018**, *10*, 27902-27910.
- (291) Wang, Z.; Chen, J.; Cong, Y.; Zhang, H.; Xu, T.; Nie, L.; Fu, J., Ultrastretchable strain sensors and arrays with high sensitivity and linearity based on super tough conductive hydrogels. *Chem. Mater.* **2018**, *30*, 8062-8069.
- (292) Fan, F. R.; Tang, W.; Wang, Z. L., Flexible nanogenerators for energy harvesting and self-powered electronics. *Adv. Mater.* **2016**, *28*, 4283-4305.
- (293) Dagdeviren, C.; Su, Y.; Joe, P.; Yona, R.; Liu, Y.; Kim, Y.-S.; Huang, Y.; Damadoran, A. R.; Xia, J.; Martin, L. W., Conformable amplified lead zirconate titanate sensors with enhanced piezoelectric response for cutaneous pressure monitoring. *Nat. Commun.* **2014**, *5*, 4496.
- (294) Park, K. I.; Lee, M.; Liu, Y.; Moon, S.; Hwang, G. T.; Zhu, G.; Kim, J. E.; Kim, S. O.; Kim, D. K.; Wang, Z. L., Flexible nanocomposite generator made of BaTiO₃ nanoparticles and graphitic carbons. *Adv. Mater.* **2012**, *24*, 2999-3004.
- (295) Lee, J. H.; Yoon, H. J.; Kim, T. Y.; Gupta, M. K.; Lee, J. H.; Seung, W.; Ryu, H.; Kim, S. W., Micropatterned P (VDF-TrFE) film-based piezoelectric nanogenerators for highly sensitive self-powered pressure sensors. *Adv. Funct. Mater.* **2015**, *25*, 3203-3209.
- (296) Curry, E. J.; Ke, K.; Chorsi, M. T.; Wrobel, K. S.; Miller, A. N.; Patel, A.; Kim, I.; Feng, J.; Yue, L.; Wu, Q., Biodegradable piezoelectric force sensor. *Proc. Natl. Acad. Sci. U.S.A.* **2018**, *115*, 909-914.
- (297) Park, M.; Park, Y. J.; Chen, X.; Park, Y. K.; Kim, M. S.; Ahn, J. H., MoS₂-based tactile sensor for electronic skin applications. *Adv. Mater.* **2016**, *28*, 2556-2562.
- (298) Kim, K.; Ha, M.; Choi, B.; Joo, S. H.; Kang, H. S.; Park, J. H.; Gu, B.; Park, C.; Park, C.; Kim, J., Biodegradable, electro-active chitin nanofiber films for flexible piezoelectric transducers. *Nano Energy* **2018**, *48*, 275-283.
- (299) Mao, Y.; Zhao, P.; McConohy, G.; Yang, H.; Tong, Y.; Wang, X., Sponge-like piezoelectric polymer films for scalable and integratable nanogenerators and self-powered electronic systems.

Adv. Energy Mater. **2014**, *4*, 1301624.

- (300) Xu, S.; Yeh, Y.-w.; Poirier, G.; McAlpine, M. C.; Register, R. A.; Yao, N., Flexible piezoelectric PMN–PT nanowire-based nanocomposite and device. *Nano Lett.* **2013**, *13*, 2393-2398.
- (301) Song, G.; Kim, Y.; Yu, S.; Kim, M.-O.; Park, S.-H.; Cho, S. M.; Velusamy, D. B.; Cho, S. H.; Kim, K. L.; Kim, J., Molecularly engineered surface triboelectric nanogenerator by self-assembled monolayers (METS). *Chem. Mater.* **2015**, *27*, 4749-4755.
- (302) Shin, S.-H.; Kwon, Y. H.; Kim, Y.-H.; Jung, J.-Y.; Lee, M. H.; Nah, J., Triboelectric charging sequence induced by surface functionalization as a method to fabricate high performance triboelectric generators. *ACS Nano* **2015**, *9*, 4621-4627.
- (303) Wang, S.; Zi, Y.; Zhou, Y. S.; Li, S.; Fan, F.; Lin, L.; Wang, Z. L., Molecular surface functionalization to enhance the power output of triboelectric nanogenerators. *J. Mater. Chem. A* **2016**, *4*, 3728-3734.
- (304) Shin, S.-H.; Bae, Y. E.; Moon, H. K.; Kim, J.; Choi, S.-H.; Kim, Y.; Yoon, H. J.; Lee, M. H.; Nah, J., Formation of triboelectric series via atomic-level surface functionalization for triboelectric energy harvesting. *ACS Nano* **2017**, *11*, 6131-6138.
- (305) Khan, Z. U.; Edberg, J.; Hamed, M. M.; Gabrielsson, R.; Granberg, H.; Wågberg, L.; Engquist, I.; Berggren, M.; Crispin, X., Thermoelectric polymers and their elastic aerogels. *Adv. Mater.* **2016**, *28*, 4556-4562.
- (306) Zhao, J.; Han, S.; Yang, Y.; Fu, R.; Ming, Y.; Lu, C.; Liu, H.; Gu, H.; Chen, W., Passive and space-discriminative ionic sensors based on durable nanocomposite electrodes toward sign language recognition. *ACS Nano* **2017**, *11*, 8590-8599.
- (307) Lee, K. Y.; Chun, J.; Lee, J. H.; Kim, K. N.; Kang, N. R.; Kim, J. Y.; Kim, M. H.; Shin, K. S.; Gupta, M. K.; Baik, J. M., Hydrophobic sponge structure-based triboelectric nanogenerator. *Adv. Mater.* **2014**, *26*, 5037-5042.
- (308) Keplinger, C.; Sun, J.-Y.; Foo, C. C.; Rothemund, P.; Whitesides, G. M.; Suo, Z., Stretchable, transparent, ionic conductors. *Science* **2013**, *341*, 984-987.
- (309) Parida, K.; Kumar, V.; Jiangxin, W.; Bhavanasi, V.; Bendi, R.; Lee, P. S., Highly transparent, stretchable, and self-healing ionic-skin triboelectric nanogenerators for energy harvesting and touch applications. *Adv. Mater.* **2017**, *29*, 1702181.
- (310) Sun, Y.; Choi, W. M.; Jiang, H.; Huang, Y. Y.; Rogers, J. A., Controlled buckling of semiconductor nanoribbons for stretchable electronics. *Nat. Nanotech.* **2006**, *1*, 201.

- (311) Kim, D. H.; Rogers, J. A., Stretchable electronics: materials strategies and devices. *Adv. Mater.* **2008**, *20*, 4887-4892.
- (312) Sekitani, T.; Nakajima, H.; Maeda, H.; Fukushima, T.; Aida, T.; Hata, K.; Someya, T., Stretchable active-matrix organic light-emitting diode display using printable elastic conductors. *Nat. Mater.* **2009**, *8*, 494.
- (313) Sekitani, T.; Noguchi, Y.; Hata, K.; Fukushima, T.; Aida, T.; Someya, T., A rubberlike stretchable active matrix using elastic conductors. *Science* **2008**, *321*, 1468-1472.
- (314) Oh, J. Y.; Rondeau-Gagné, S.; Chiu, Y.-C.; Chortos, A.; Lissel, F.; Wang, G.-J. N.; Schroeder, B. C.; Kurosawa, T.; Lopez, J.; Katsumata, T., Intrinsically stretchable and healable semiconducting polymer for organic transistors. *Nature* **2016**, *539*, 411.
- (315) Wang, S.; Xu, J.; Wang, W.; Wang, G.-J. N.; Rastak, R.; Molina-Lopez, F.; Chung, J. W.; Niu, S.; Feig, V. R.; Lopez, J., Skin electronics from scalable fabrication of an intrinsically stretchable transistor array. *Nature* **2018**, *555*, 83.
- (316) Nishizawa, M., Soft, wet and ionic microelectrode systems. *Bull. Chem. Soc. Jpn.* **2018**, *91*, 1141-1149.
- (317) Stauss, S.; Honma, I., Biocompatible batteries—materials and chemistry, fabrication, applications, and future prospects. *Bull. Chem. Soc. Jpn.* **2018**, *91*, 492-505.
- (318) Choi, S.; Han, S. I.; Jung, D.; Hwang, H. J.; Lim, C.; Bae, S.; Park, O. K.; Tschabrunn, C. M.; Lee, M.; Bae, S. Y., Highly conductive, stretchable and biocompatible Ag–Au core–sheath nanowire composite for wearable and implantable bioelectronics. *Nat. Nanotech.* **2018**, *1*.
- (319) Miyamoto, A.; Lee, S.; Cooray, N. F.; Lee, S.; Mori, M.; Matsuhisa, N.; Jin, H.; Yoda, L.; Yokota, T.; Itoh, A., Inflammation-free, gas-permeable, lightweight, stretchable on-skin electronics with nanomeshes. *Nat. Nanotech.* **2017**, *12*, 907.
- (320) Hwang, S.-W.; Tao, H.; Kim, D.-H.; Cheng, H.; Song, J.-K.; Rill, E.; Brenckle, M. A.; Panilaitis, B.; Won, S. M.; Kim, Y.-S., A physically transient form of silicon electronics. *Science* **2012**, *337*, 1640-1644.
- (321) Kang, S.-K.; Murphy, R. K.; Hwang, S.-W.; Lee, S. M.; Harburg, D. V.; Krueger, N. A.; Shin, J.; Gamble, P.; Cheng, H.; Yu, S., Bioresorbable silicon electronic sensors for the brain. *Nature* **2016**, *530*, 71.
- (322) Boutry, C. M.; Nguyen, A.; Lawal, Q. O.; Chortos, A.; Rondeau-Gagné, S.; Bao, Z., A sensitive and biodegradable pressure sensor array for cardiovascular monitoring. *Adv. Mater.* **2015**, *27*, 6954-6961.

- (323) Wang, Y.; Ameer, G. A.; Sheppard, B. J.; Langer, R., A tough biodegradable elastomer. *Nat. Biotechnol.* **2002**, *20*, 602.
- (324) Zheng, Q.; Zou, Y.; Zhang, Y.; Liu, Z.; Shi, B.; Wang, X.; Jin, Y.; Ouyang, H.; Li, Z.; Wang, Z. L., Biodegradable triboelectric nanogenerator as a life-time designed implantable power source. *Sci. Adv.* **2016**, *2*, e1501478.
- (325) Boutry, C. M.; Kaizawa, Y.; Schroeder, B. C.; Chortos, A.; Legrand, A.; Wang, Z.; Chang, J.; Fox, P.; Bao, Z., A stretchable and biodegradable strain and pressure sensor for orthopaedic application. *Nature Electronics* **2018**, *1*, 314.
- (326) Gao, W.; Emaminejad, S.; Nyein, H. Y. Y.; Challa, S.; Chen, K.; Peck, A.; Fahad, H. M.; Ota, H.; Shiraki, H.; Kiriya, D., Fully integrated wearable sensor arrays for multiplexed in situ perspiration analysis. *Nature* **2016**, *529*, 509.
- (327) Rudovic, O.; Lee, J.; Dai, M.; Schuller, B.; Picard, R. W., Personalized machine learning for robot perception of affect and engagement in autism therapy. *Sci. Robot.* **2018**, *3*, 19.
- (328) Ryu, S.; Pyo, D.; Lim, S.-C.; Kwon, D.-S., Mechanical Vibration Influences the Perception of Electro vibration. *Scientific reports* **2018**, *8*, 4555.

*Chapter 2 is reproduced in part with permission of “Tactile-Direction-Sensitive and Stretchable Electronic Skins Based on Human-Skin-Inspired Interlocked Microstructures, *ACS Nano*, 2014, *8*, 12020-12029”. Copyright 2014, American Chemical Society

*Chapter 3 is reproduced in part with permission of “Flexible Ferroelectric Sensors with Ultrahigh Pressure Sensitivity and Linear Response over Exceptionally Broad Pressure Range, *ACS Nano*, 2018, *12*, 4045-4054”. Copyright 2018 American Chemical Society

*Chapter 5 is reproduced in part with permission of “A Hierarchical Nanoparticle-in-Micropore Architecture for Enhanced Mechanosensitivity and Stretchability in Mechanochromic Electronic Skins, *Adv. Mater.*, 2019, *31*, 1808148”. Copyright 2017 Wiley-VCH.

Appendix A: List of Achievements

The results of this dissertation have been published in: (†: equal contribution)

1. Jonghwa Park†, **Youngoh Lee† (co-first author)**, Jaehyung Hong, Youngsu Lee, Minjeong Ha, Youngdo Jung, Hyuneui Lim, Sung Youb Kim, and Hyunhyub Ko, Tactile-Direction-Sensitive and Stretchable Electronic Skins Based on Human-Skin-Inspired Interlocked Microstructures, *ACS Nano*, **2014**, 8, 12020-12029
2. **Youngoh Lee†**, Jonghwa Park†, Soo won Cho, Young-Eun Shin, Hochan Lee, Jinyoung Kim, Jinyoung Myoung, Seungse Cho, Saewon Kang, Chunggi Baig, and Hyunhyub Ko, Flexible Ferroelectric Sensors with Ultrahigh Pressure Sensitivity and Linear Response over Exceptionally Broad Pressure Range, *ACS Nano*, **2018**, 12, 4045-4054
3. Jonghwa Park†, **Youngoh Lee† (co-first author)**, Meredith H. Barbee†, Soowon Cho†, Seungse Cho, Ravi Shanker, Jinyoung Kim, Jinyoung Myoung, Minsoo P. Kim, Chunggi Baig, Stephen L. Craig, and Hyunhyub Ko, A Hierarchical Nanoparticle-in-Micropore Architecture for Enhanced Mechanosensitivity in Mechanochromic Electronic Skins, *Adv. Mater.*, **2019**, 31, 1908148.
4. **Youngoh Lee†**, Jonghwa Park†, Ayoung Choe, Seungse Cho, Jinyoung Kim, and Hyunhyub Ko, Mimicking Human and Biological Skins for Multifunctional Skin Electronics, *Adv. Funct. Mater.*, **2019**, 29, 1904523.

The other related results have been published in:

1. **Youngoh Lee†**, Jiwon Lee†, Tae Kyung Lee†, Jonghwa Park, Minjung Ha, Sang Kyu Kwak, and Hyunhyub Ko, Particle-on-Film Gap Plasmons on Antireflective ZnO Nanocone Arrays for Molecular-Level Surface-Enhanced Raman Scattering Sensors, *ACS Appl. Mater. Interfaces*, **2015**, 7, 26421.
2. Minsoo P. Kim†, **Youngoh Lee† (co-first author)**, Yoon Hyung Hur†, Jonghwa Park, Jinyoung Kim, Youngsu Lee, Chang Won Ahn, Seung Won Song, Yeon Sik Jung, and Hyunhyub Ko, Molecular structure engineering of dielectric fluorinated polymers for enhanced performances of triboelectric nanogenerators, *Nano Energy* **2018**, 53, 37.
3. Jonghwa Park, **Youngoh Lee**, Jaehyung Hong, Minjeong Ha, Young-Do Jung, Hyuneui Lim, Sung Youb Kim, and Hyunhyub Ko, Giant tunneling piezoresistance of composite elastomers with

- interlocked microdome array for ultrasensitive and multimodal electronic skins, *ACS Nano*, **2014**, *8*, 4689.
4. Jonghwa Park, **Youngoh Lee**, Seongdong Lim, Youngsu Lee, Youngdo Jung, Hyuneui Lim, and Hyunhyub Ko, Ultrasensitive piezoresistive pressure sensors based on interlocked micropillar arrays, *Bionanosci.*, **2014**, *4*, 349.
 5. Jonghwa Park[†], Marie Kim[†], **Youngoh Lee**, Heon-Sang Lee, and Hyunhyub Ko, Fingertip skin-inspired microstructured ferroelectric skins discriminate static/dynamic pressure and temperature stimuli, *Sci. Adv.*, **2015**, *1*, e1500661
 6. Minjeong Ha, Seongdong Lim, Jonghwa Park, Doo-Seung Um, **Youngoh Lee**, and Hyunhyub Ko, Bioinspired Interlocked and Hierarchical Design of ZnO Nanowire Arrays for Static and Dynamic Pressure-Sensitive Electronic Skins, *Adv. Funct. Mater.*, **2015**, *25*, 2841.
 7. Saewon Kang[†], Taehyo Kim[†], Seungse Cho, **Youngoh Lee**, Ayoung Choe, Bright Walker, Seo-Jin Ko, Jin Young Kim, and Hyunhyub Ko, Capillary Printing of Highly Aligned Silver Nanowire Transparent Electrode for High-Performance Optoelectronic Devices, *Nano Lett.* **2015**, *15*, 7933.
 8. Minjeong Ha, Jonghwa Park, **Youngoh Lee**, and Hyunhyub Ko, Triboelectric Generators and Sensors for Self-Powered Wearable Electronics, *ACS Nano*, **2015**, *9*, 3421. [Perspective]
 9. Jonghwa Park, **Youngoh Lee**, Minjeong Ha, Seungse Cho, and Hyunhyub Ko, Micro/nanostructured surfaces for self-powered and multifunctional electronic skins, *J. Mater. Chem. B*, **2016**, *4*, 2999. [Advance Article]
 10. Minjeong Ha, Seongdong Lim, Soowon Cho, **Youngoh Lee**, Sangyun Na, Chunggi Baig, and Hyunhyub Ko, Skin-Inspired Hierarchical Polymer Architectures with Gradient Stiffness for Spacer-Free, Ultrathin, and Highly Sensitive Triboelectric Sensors, *ACS Nano* **2018**, *12*, 3964.
 11. Jonghwa Park[†], Jinyoung Kim[†], Jaehyung Hong[†], Hochan Lee, **Youngoh Lee**, Seungse Cho, Sung Youb Kim, and Hyunhyub Ko, Tailoring Force Sensitivity and Selectivity by Microstructure Engineering of Multidirectional Electronic Skins, *NPG. Asia Mater.* **2018**, DOI 10.1038/s41427-018-0031-8
 12. Sung-Woo Kim, **Youngoh Lee**, Jonghwa Park, Seungmok Kim, Heeyoung Chae, Hyunhyub Ko, Jae Joon Kim, A Triple-Mode Flexible E-Skin Sensor Interface for Multi-Purpose Wearable Applications, *Sensors*, **2018**, *18*, 78.
 13. Saewon Kang[†], Seungse Cho[†], Ravi Shanker, Hochan Lee, Jonghwa Park, Doo-Seung Um, **Youngoh Lee**, and Hyunhyub Ko, Transparent and conductive nanomembranes with orthogonal

- silver nanowire arrays for skin-attachable loudspeakers and microphones, *Sci. Adv.* **2018**, 4, eaas8772.
14. Kwangmuk Lee, Hee Young Chae, Kyeonghwan Park, **Youngoh Lee**, Seungse Cho, Hyunhyub Ko, and Jae Joon Kim, A Multi-Functional Physiological Hybrid Sensing E-Skin Integrated Interface for Wearable IoT Applications, *IEEE Trans. Biomed. Circuits Syst.*, **2019**, DOI 10.1109/TBCAS.2019.2946875.
 15. Jonghwa Park, Minjeong Ha, **Youngoh Lee**, and Hyunhyub Ko, Polymer-Based Electronic Skins and Wearable Sensors, *Polymer Science and Technology (Korea)*, **2015**, 26, 274.
 16. **Youngoh Lee**, Jonghwa Park, and Hyunhyub Ko, Bioinspired Electronic Skins with High Sensitivity and Multifunctionality, *Polymer Science and Technology (Korea)*, **2019**, 30, 14.

Conference Presentation:

1. **Youngoh Lee**, Jonghwa Park, Ayoung Choe, Young-Eun Shin and Hyunhyub Ko, “Deformation-Insensitive Flexible and Wearable Temperature Sensors based on Thermoresponsive Semi-Crystalline Polymer Microdomains”, *The Korean Society for Composite Materials 2019*, Korea
2. **Youngoh Lee**, Jonghwa Park, Ayoung Choe, Young-Eun Shin and Hyunhyub Ko, “Deformation-Insensitive Flexible Temperature Sensor based on Thermoresponsive Semi-Crystalline Polymer Microdomains”, *The Polymer Society of Korea 2019*, Korea
3. **Youngoh Lee**, Jonghwa Park, Ayoung Choe, Young-Eun Shin and Hyunhyub Ko, “Deformation-Insensitive Flexible and Highly Sensitive Dual-Mode Temperature Sensors”, *Nano Korea 2019*, Korea
4. **Youngoh Lee**, Jonghwa Park, Young-Eun Shin and Hyunhyub Ko, “Interlocked Microdome Multilayer Electronic Skins for Linear and Ultra-Large Dynamic Range Pressure Sensors”, *The Polymer Society of Korea 2018*, Korea
5. **Youngoh Lee**, Jonghwa Park and Hyunhyub Ko, “Interlocked Microdome Multilayer Electronic Skins for Linear and Ultra-Large Dynamic Range Pressure Sensors”, *International Union of Materials Research Society-International Conference on Electronic Materials (IUMRS-ICEM) 2018*, Korea
6. **Youngoh Lee**, Jonghwa Park, Soowon Cho, Young-Eun Shin, Chunggi Baig and Hyunhyub Ko, “Flexible Ferroelectric Electronic Skins with Ultrahigh Pressure Sensitivity and Linear Response over Exceptionally Broad Pressure Range”, *Fall MRS Meeting 2018*, Boston, USA

7. **Youngoh Lee**, Jonghwa Park, Soowon Cho, Young-Eun Shin, Chunggi Baig and Hyunhyub Ko, “Flexible Ferroelectric Electronic Skins with multilayer geometry for highly sensitive, linear and broad range pressure sensing” *The 5th International Conference on Electronic Materials and Nanotechnology for Green Environment (ENGE) 2018*, Korea (selected as best poster award)
8. **Youngoh Lee**, Jonghwa Park and Hyunhyub Ko, “Interlocked Microdome Multilayer Electronic Skins for Linear and Ultra-Large Dynamic Range Pressure Sensors”, *The polymer Society of Korea 2017*, Korea
9. **Youngoh Lee**, Jiwon Lee, Tae Kyung Lee, Jonghwa Park, Minjeong Ha, Sang Kyu Kwak, and Hyunhyub Ko, “Particle-on-Film Gap Plasmons on Antireflective ZnO Nanocone Arrays as Ultrasensitive SERS Sensors”, *Spring MRS Meeting 2016*, Phoenix, USA (selected as the best poster award)
10. Jonghwa Park, **Youngoh Lee**, and Hyunhyub Ko, “Fingertip Skin-Inspired Multimodal Electronic Skins Discriminating Static/Dynamic Pressure and Temperature Stimuli”, *The 4th International Conference on Electronic Materials and Nanotechnology for Green Environment (ENGE) 2016*, Korea
11. **Youngoh Lee**, Jiwon Lee, Jonghwa Park, Minjeong Ha, Hyunhyub Ko, “Particle-on-Film Gap Plasmons on Antireflective ZnO Nanocone Arrays for Ultrasensitive SERS Sensors”, *The polymer Society of Korea 2015*, Korea
12. **Youngoh Lee**, Jiwon Lee, Jonghwa Park, Minjeong Ha, Hyunhyub Ko, “Particle-on-Film Gap Plasmons on Antireflective ZnO Nanocone Arrays for Ultrasensitive SERS Sensors”, *The 3rd International Conference on Advanced Electromaterials (ICAE) 2015*, Korea
13. **Youngoh Lee**, Jiwon Lee, Jonghwa Park, Minjeong Ha, Hyunhyub Ko, “ZnO Nanocone Array: Facile Synthesis and Applications in Plasmonic Sensors” *Fall MRS Meeting 2014*, Boston, USA

Honors and Awards:

1. ENGE Outstanding Graduate student Award in UNIST, Ulsan National Institute of Science and Technology, 2018
2. Best poster Award, The Korean Institute of Metals and Materials, 2018
3. Best poster Award, MRS spring meeting in Phoenix, 2016
4. Global Ph.D Fellowship, National Research Foundation of Korea, 2014-2019

Acknowledgements

I would like to begin by expressing my heartfelt gratitude to Prof. Hyunhyub Ko who is my principal investigator during my combined master's and doctoral course. I am very grateful for his tireless support, encouragement, and his words of wisdom, which have helped me not only in successfully completing Ph.D course but in making me a better human being. Without his guidance and constant feedback, this Ph.D would not have been achievable. I consider myself to be extremely privileged to have been his student and I would like to say my professor, "You are the reason why I decided to go to pursue a career in research and I really respect you. Thank you."

And, I would like to extend my gratitude to the committee members, Prof. Jae Joon Kim, Prof. Chunggi Baig, Prof. Sang Kyu Kwak and Prof. Jiseok Lee, *Ulsan National Institute of Science and Technology (UNIST)*, for their helpful career advice and constructive comments. I am very grateful to committee professors for their valuable comments to improve my thesis and for all their investing time for me. I felt proud and honoured that you have accepted to be on my committee members.

I would like to thank all of FNL members; my previous colleagues Dr. Jiwon Lee, Dr. Doo-Seung Um, Dr. Saewon Kang, Sehee Ahn, Dr. Ziyauddin Khan, Dr. Ravi Shanker, Dr. Seongdong Lim, Dr. Minjeong Ha, Dr. Seungyoung Park and current members Dr. Minsoo Kim, Dr. Jonghwa Park, Dr. Sujoy Kumar Ghosh, Young-Eun Shin, Young-Ryul Kim, Hochan Lee, Youngsu Lee, Ayoung Choe, Seungse Cho, Jeonghee Yeom, Jinyoung Kim, Jinyoung Myoung, Yoojeong Park, Sangyun Na, and Donghee Kang, Yeju Kwon, Hyejin Lee, Seungjae Lee, Yujung Ko, Geonyoung Jeong. Especially, I feel great thanks to my team members, Jonghwa Park, *my mentor and role model*, Jinyoung Kim, *my older senior and advisor*, Jinyoung Myoung, *my first baby and real honesty*, and Seungjae Lee, *my new baby*. Without their support, I might not be able to finish the Ph.D course successfully. In addition, I also specially thank to Jiwon, *the purest and first lab leader*, Doo-Seung, *my research mentor*, Saewon, *mimi*, Sehee, *straight shooter*, Hochan, *the funniest LG man*, Youngsu, *my oldest friend in UNIST*, AYoung, *the second straight shooter*, Seungse, *machine learner*, Young-Ryul, *lonely guy*, Yoojeong, *Yoovely*, Donghee, *pizza boy*. Further, I always thanks to Jonghwa who is my second advisor. He always devoted his time to support me like a real brother. He was and remains my best role model for a scientist and mentor.

Lastly, I would like to appreciate my parents and sistor for their love, immense support and encouragement. Their perpanent love have encouraged me to go ahead in my study and career. they were my source of energy and my inspiration during my Ph.D course. I would never be able to pay back

the love and affection shown upon by my family. Thank you.

The present thesis, resulting of six years of research, would not have been possible without guidance, encouragements, and support of many people. I thank all of them and I present them all my gratitude.

Youngoh Lee

